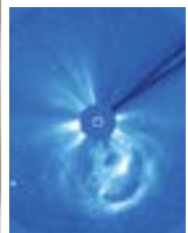
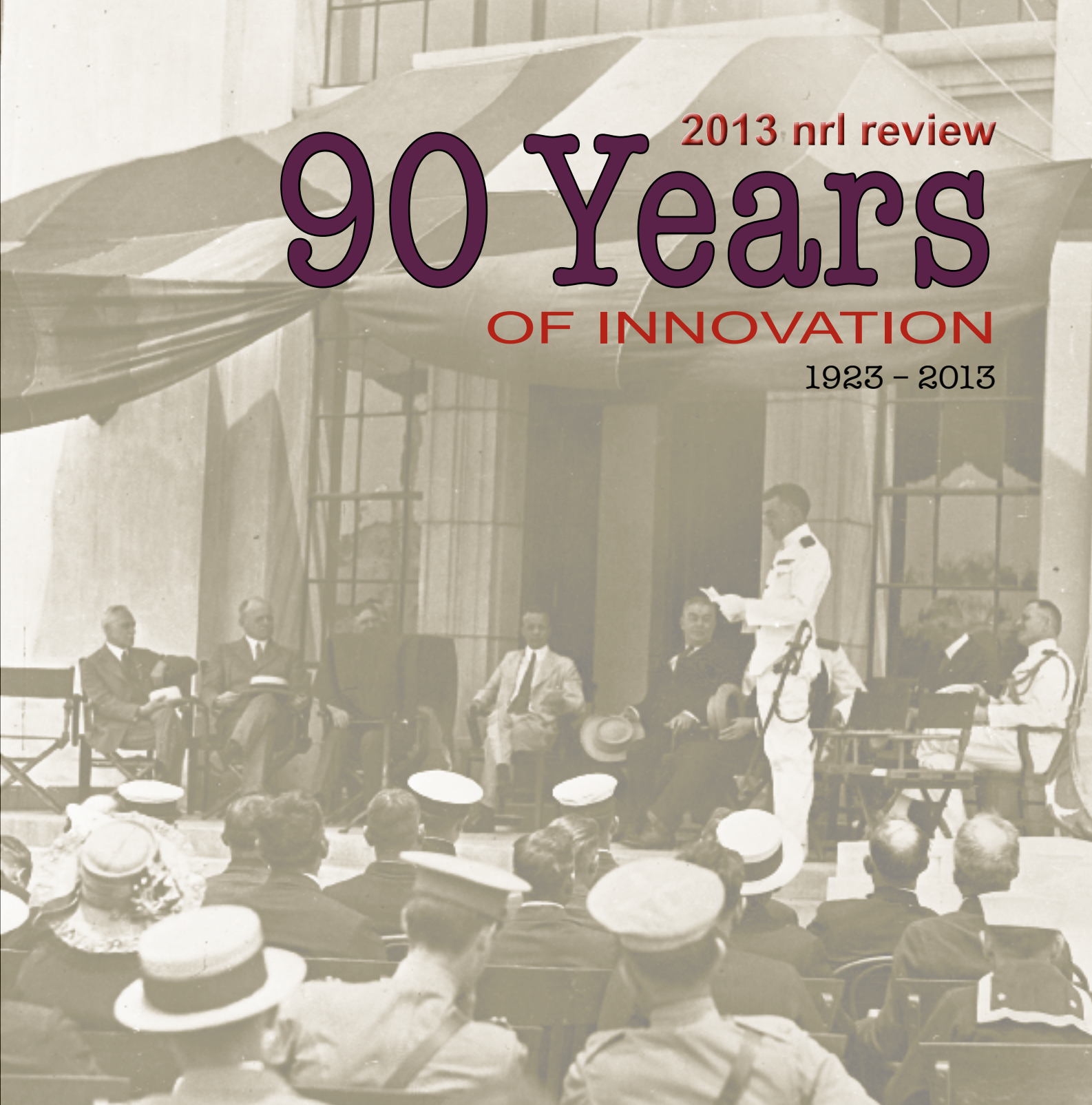


2013 nrl review

90 Years

OF INNOVATION

1923 - 2013



NAVAL RESEARCH LABORATORY
Washington, DC

NRL's MISSION

To conduct a broadly based multidisciplinary program of scientific research and advanced technological development directed toward maritime applications of new and improved materials, techniques, equipment, systems, and ocean, atmospheric, and space sciences and related technologies.

The Naval Research Laboratory provides primary in-house research for the physical, engineering, space, and environmental sciences; broadly based applied research and advanced technology development programs in response to identified and anticipated Navy and Marine Corps needs; broad multidisciplinary support to the Naval Warfare Centers; and space and space systems technology, development, and support.



NRL REVIEW STAFF

SENIOR SCIENCE EDITOR

John D. Bultman

COORDINATOR

Jonna Atkinson

CONSULTANT

Kathy Parrish

DESIGN, LAYOUT, AND GRAPHIC SUPPORT

Jonna Atkinson

EDITORIAL ASSISTANCE

Saul Oresky

Kathy Parrish

Claire Peachey

PHOTOGRAPHIC PRODUCTION

Jamie Hartman

James Marshall

Gayle Fullerton



COMMANDING OFFICER

CAPT Anthony J. Ferrari, USN



DIRECTOR OF RESEARCH

Dr. John A. Montgomery

REVIEWED AND APPROVED

NRL/PU/3430--14-577

RN: 14-1231-1938

June 2014

Anthony J. Ferrari, Captain, USN

Commanding Officer

90 Years

OF INNOVATION

1923 – 2013

The Naval Research Laboratory celebrated its 90th anniversary in 2013. The world is quite different today than it was 90 years ago, but NRL's early 20th century founders knew, as we do today, the importance of science and technology in maintaining naval power and preserving national security. NRL began operations in 1923 as the United States Navy's first modern research institution, and it continues today as one of the Navy's premier R&D resources.

During the years since World War II, the Laboratory has conducted basic and applied research pertaining to the Navy's environments of Earth, sea, sky, space, and cyberspace. Investigations have ranged widely—from monitoring the Sun's behavior, to analyzing marine atmospheric conditions, to measuring parameters of the deep oceans. Detection and communication capabilities have benefited by research that has exploited new portions of the electromagnetic spectrum, extended ranges to outer space, and provided a means of transferring information reliably and securely, even through massive jamming.

Submarine habitability, lubricants, shipbuilding materials, firefighting, and the study of sound in the sea have remained steadfast concerns, to which have been added recent explorations within the fields of virtual reality, superconductivity, biomolecular science and engineering, and nanotechnology.

The Laboratory has pioneered naval research into space—from atmospheric probes with captured V-2 rockets, through direction of the Vanguard project (America's first satellite program), to inventing and developing the first satellite prototypes of the Global Positioning System (GPS). Today, NRL is the Navy's lead laboratory in space systems research, as well as in fire research, tactical electronic warfare, microelectronic devices, and artificial intelligence.

The Laboratory is now focusing its research efforts on new Navy strategic interests in the 21st century, a period marked by global terrorism, shifting power balances, and irregular and asymmetric warfare. NRL scientists and engineers are working to give the Navy the special knowledge, capabilities, and flexibility to succeed in this dynamic environment. While continuing its programs of basic research that help the Navy anticipate and meet future needs, NRL also moves technology rapidly from concept to operational use when high-priority, short-term needs arise—for pathogen detection, lightweight body armor, contaminant transport modeling, and communications interoperability, for example. The interdisciplinary and wide-ranging nature of NRL's work keeps this "great research laboratory" at the forefront of discovery and innovation, solving naval challenges and benefiting the nation as a whole.

(Photo: Aerial of the Naval Research Laboratory, circa 1923.)

2013 NRL REVIEW



NRL'S INVOLVED!

- 2 Our People Make a Big Difference
- 7 NRL Celebrates 90th Birthday
- 8 Dr. George Carruthers Honored with National Medal of Technology and Innovation
- 10 NRL Hosts Its Second Annual Karles Invitational Conference
- 12 The Fleet's First Radar Turns 75
- 14 Naval Research Laboratory Dedicates Marine Meteorology Center
- 16 NRL Scientist Builds Model of LASR Facility: One LEGO at a Time

THE NAVAL RESEARCH LABORATORY

- 20 NRL – Our Heritage
- 21 Highlights of NRL Research in 2012
- 33 NRL Today

FEATURED RESEARCH

- 80 **CIGS: A Healthy Habit for Flexible PVs**
Sputtered Thin-Film Absorbers for Flexible Photovoltaics
- 87 **We've Got You Covered, Topsides...**
Single-Component Polysiloxane Coating for Navy Topsides
- 95 **With Graphene Tunnel Barriers, Resistance Is Not Futile**
Graphene as a Tunnel Barrier
- 105 **Assessing the Microbial Enemy's Antibiotic Defenses on the Genetic Level...with Next-day Service**
Molecular Epidemiology of Global Antimicrobial Resistance

- 113 **NRL Has a Flare for Studying CMEs: Staring into the Sun to See the "Rosetta Stone" of Flux Rope Formation**
The Stuff Coronal Mass Ejections Are Made Of
- 120 **Doing the Locomotion...with a Microrobot Powered by a Microbial Fuel Cell**
Low Power Microrobotics Utilizing Biologically Inspired Energy Generation

RESEARCH ARTICLES

acoustics

- 128 Controlling Sonar Clutter via Higher-Order Statistics
- 130 Transition and Optimization of a Fast Broadband Pulse Propagation Algorithm for Fleet Use
- 132 Range-Dependent Seismo-Acoustics

atmospheric science and technology

- 136 High-Altitude Flight Control of a Micro Air Vehicle Using Only Two Sensors
- 138 The Navy Global Environmental Model
- 140 Long-Range, Low-Frequency, Atmospheric Sound Propagation Physics
- 143 Smart Voyage Planning — Saving Fuel by Using Environmental Forecasts to Aid in Ship Routing

chemical/biochemical research

- 148 Barnacle Adhesion Two-Step
- 150 Pulsed Electron Beam Driven Chemistry

electronics and electromagnetics

- 154 High Frequency Vector Sensor Design and Testing
- 156 Intrinsically Switched Varactor-Tuned Filters and Filter Banks
- 159 Thermoelectroelastic Simulation of GaN Devices

information technology and communications

- 164 Stable Throughput Tradeoffs in Cognitive Radio Networks
- 165 X-Band Airborne Satellite Communications
- 168 GLADIS Hosted Payload Demonstrates Nanosatellite Technology
- 169 Dynamic Network Analysis for Mobile (DyNAMo) Adaptation
- 171 Frequency Position Modulation

materials science and technology

- 176 The Physics of the Unconfined Deflagration-to-Detonation Transition
- 178 Failure of Classical Elasticity
- 180 Synfuel from Seawater
- 181 Relationship of Grain Boundary Microchemistry to Stress Corrosion Susceptibility in Aircraft Aluminum Alloys
- 183 A New Annealing Technique: Multicycle Rapid Thermal Annealing (MRTA)

nanoscience technology

- 188 Measuring Protein Secretions from Individual Live Cells
- 190 A Micromechanical Analogue to Optical Lasers

ocean science and technology

- 194 Turbulence Production by Nonbreaking Waves
- 196 A Target Depth Classification Method for Autonomous Passive Acoustic Surveillance Systems in Littorals
- 199 Maximizing Effectiveness of Autonomous Underwater Vehicles
- 201 WAVEWATCH III® Transition to Naval Operations

optical sciences

- 206 A Panoramic Shortwave Infrared Hyperspectral Sensor for Maritime Sensing
- 208 Spatiotemporal-Multiplexed Quantum Dot Biosensors

remote sensing

- 212 Electrochemical Detection of Nitroenergetics for Long Term Monitoring
- 214 Remote Sensing Signatures of Breaking Waves from Multi-Instrument Field Experiment on FLIP
- 216 Surprising Discoveries in Reflectance Properties of Complex Granular Sediments

simulation, computing, and modeling

- 220 Robotic Multiaxial Testing and Constitutive Characterization of Composites
- 222 How Clutter and Expertise Affect Search in Geospatial Displays

space research and satellite technology

- 228 Ground-Based Investigation of Near-Earth Space Plasma Processes in the NRL Space Physics Simulation Chamber
- 229 Artificial Ionospheric Plasma Clouds Using HAARP
- 232 Maritime Detection of Radiological/Nuclear Threats
- 233 RAIDER-M: Transitioning Space Systems Knowledge to Terrestrial Remote Sensing
- 235 Morphing Satellite Reflector Antennas Using Tensegrity Structures

SPECIAL AWARDS AND RECOGNITION

- 240 Special Awards and Recognition
- 255 Alan Berman Research Publication and NRL Edison (Patent) Awards
- 259 NRC/ASEE Postdoctoral Research Publication Awards

PROGRAMS FOR PROFESSIONAL DEVELOPMENT

- 262 Programs for NRL Employees — Graduate Programs, Continuing Education, Professional Development, Equal Employment Opportunity (EEO) Programs, and Other Activities
- 264 Programs for Non-NRL Employees — Postdoctoral Research Associateships, Faculty Member Programs, Professional Appointments, and Student Programs
- 266 NRL Employment Opportunities

GENERAL INFORMATION

- 268 Technical Output
- 269 Key Personnel
- 270 Contributions by Divisions, Laboratories, and Departments
- 273 Subject Index
- 276 Author Index
- 277 Map/Quick Reference Telephone Numbers

NRL's Involved!

2 Our People Make a Big Difference

7 NRL Celebrates 90th Birthday

8 Dr. Carruthers Honored with National Medal of Technology and Innovation

10 NRL Hosts Its Second Annual Karles Invitational Conference

12 The Fleet's First Radar Turns 75

14 Naval Research Laboratory Dedicates Marine Meteorology Center

16 NRL Scientist Builds Model of LASR Facility: One LEGO at a Time

NRL Celebrates 90th Birthday



The Naval Experimental and Research Laboratory (the name was shortened to Naval Research Laboratory in 1926) was formally commissioned on **July 2, 1923**, by the Assistant Secretary of the Navy, Theodore Roosevelt, Jr. (seated fourth from left in the photo above). The Laboratory's Director, CAPT Edward L. Bennett, USN (standing), is shown accepting the completed Laboratory. The commissioning ceremonies were held in front of Building 1.

Dr. George Carruthers Honored with National Medal of Technology and Innovation



President Barack Obama congratulates Dr. George Carruthers on receiving the National Medal of Technology and Innovation.



NRL Space Science Division (SSD) scientist Dr. George Carruthers has received the 2012 National Medal of Technology and Innovation. This is the nation's highest honor for technology achievement, and it is bestowed by the president of the United States on America's leading innovators. The award ceremony was held at the White House on February 1, 2013.

Dr. Carruthers grew up during the space race and was intrigued with space science. While still a boy, he began building telescopes and model rockets and was an enthusiastic reader at the local libraries. His love for space science extended through his youth and eventually led him to pursue degrees in aeronautical, nuclear, and astronomical engineering from the University of Illinois.

Following his graduate studies, he accepted a position at NRL in 1964 after receiving a fellowship in Rocket Astronomy from the National Science Foundation. Throughout his tenure in the NRL SSD, Dr. Carruthers has focused his atten-

tion on far-ultraviolet observations of the Earth's upper atmosphere and of astronomical phenomena. In 1969, he received a patent for his pioneering instrumentation, "Image Converter for Detecting Electromagnetic Radiation Especially in Short Wave Lengths," which detected electromagnetic radiation in short wave lengths.

In 1972, Dr. Carruthers' Far Ultraviolet Camera Spectrograph, the first Moon-based space observatory, was sent to the Moon with the Apollo 16 mission. This 50-lb, gold-plated camera system allowed researchers to take readings of and understand objects and elements in space that are unrecognizable to the naked eye and gave them views of stars and the solar systems thousands of miles away. His NRL camera still sits on the surface of the Moon. A second version of this camera was sent on the 1974 Skylab space flight to study comets and was used to observe Halley's Comet, among others.

He has been the principal investigator for numerous NASA and DoD-sponsored space



The first observatory ever operated by man from a fixed platform outside the earth was this gold-plated ultra-violet camera/spectrograph. It was placed on the moon by the Apollo 16 astronauts in April 1972. George Carruthers is right and William Conway is left.

instruments, including a 1986 rocket instrument that obtained ultraviolet images of Comet Halley. His experiment on the DoD Space Test Program Advanced Research and Global Observation Satellite (ARGOS) captured an image of a Leonid shower meteor entering the Earth's atmosphere, the first time a meteor has been imaged in the far ultraviolet from a spaceborne camera.

In announcing the National Medal recipients, President Barak Obama said, "I am proud to honor these inspiring American innovators. They represent the ingenuity and imagination that has long made this Nation great—and they remind us of the enormous impact a few good ideas can have when these creative qualities are unleashed in an entrepreneurial environment."

The National Medal of Science was created by statute in 1959 and is administered for the White House by the National Science Foundation. Awarded annually, the medal recognizes individuals who have made outstanding contributions to science and engineering. A committee of Presidential appointees selects nominees on the basis of their extraordinary knowledge in and contributions to chemistry, engineering, computing, mathematics, or the biological, behavioral/social, and physical sciences.

Then the National Medal of Technology and Innovation was created by statute in 1980 and is administered for the White House by the U.S. Department of Commerce's Patent and Trademark Office. The award recognizes those who have made lasting contributions to America's competitiveness and quality of life and helped strengthen the Nation's technological workforce. National Medal of Technology and Innovation nominees are selected by a distinguished independent committee representing the private and public sectors.

Geospace research led by Dr. George Carruthers, which this award celebrates, is contributing outstandingly to improving our ability to understand and forecast space weather at Earth that can affect military and civilian space and communication systems.



Artist's drawing of an astronaut on the Moon with Dr. Carruthers' Far Ultraviolet Camera Spectrograph.

NRL Hosts Its Second Annual

KARLES INVITATIONAL CONFERENCE

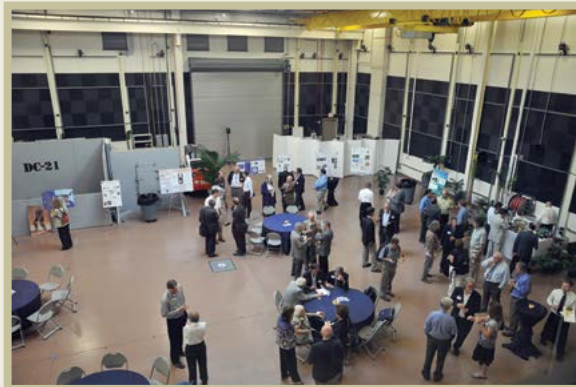
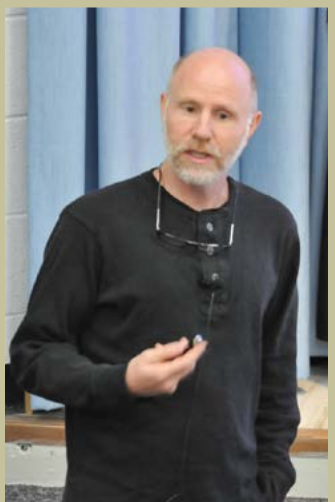
AUGUST 27–28, 2012



QUANTUM INFORMATION SCIENCE & TECHNOLOGY

The professional contributions of Dr. Jerome Karle, 1985 Nobel Laureate in Chemistry, and Dr. Isabella Karle, a 1993 Bower Award Laureate and 1995 recipient of the National Medal of Science, were critical in enabling the resolution of the molecular structure and function of complex macromolecules. While fundamental in nature, the Karles' contributions continue to have a significant impact on the basic and applied physical, chemical, metallurgical, geological, and biological sciences. In commemoration of their achievements and broad scientific impact, the U.S. Naval Research Laboratory in Washington, DC, has initiated an annual invitational conference that will convene the leading authorities and innovators from scientific disciplines that are on the verge of producing contributions with similar reach and impact. The selected topic in 2012 was Quantum Information Science and Technology.

Quantum Information Science and Technology is an exciting new field of exceptional potential that has become one of the most active areas of scientific research around the world. It takes advantage of the full power of quantum mechanics by creating new scientific concepts and making possible entirely new technologies that have the potential to change both society and military capabilities. In recent years, the development of new nanoscience techniques and fast lasers have made it possible to control single quantum objects, such as photons or spins, coherently. This has made possible the exploration of novel phenomena and concepts based upon the principles of quantum mechanics. The timeliness of this conference is evidenced by noting important advances that have been made recently in implementing stationary quantum bits (qubits) in atomic, semiconducting, and superconducting systems and in connecting them coherently using photonic flying qubits. New algorithms have also recently been developed for factoring large numbers and for searching large data sets, and concepts involving the roles of entanglement in new technologies have been proposed. These advances have opened new fields ranging from quantum computing and secure communications to code breaking, imaging, and navigation. Technology opportunities being explored in areas of importance to the Navy and the nation include ultrasecure codes and communications, fast processing of large data sets, and high-resolution imaging, to mention but a few.



The Fleet's First Radar Turns 75

December 2013 marks the 75th anniversary of one of the Naval Research Laboratory's most important contributions to technology development and national defense: the Fleet's first shipboard radar.

NRL's XAF radar, fondly known as the "flying bedspring," was the prototype that showed the Navy what this new radio detecting and ranging system – not yet called radar – was capable of doing. In December 1938, the XAF radar was installed aboard USS *New York* (BB 34) in preparation for Fleet exercises in the Caribbean in early 1939. During the at-sea exercises, the 200 MHz XAF system successfully spotted aircraft at distances up to 48 miles and ships at 10 miles, and could even follow 14-inch shells in flight. It also detected and pinpointed destroyers making nighttime simulated torpedo attacks. NRL physicist Robert M. Page, one of the developers of the XAF system and inventor of many other radar technologies, was aboard *New York* and later described the reaction after the mock attacks:

These performances were at night, with no possibility of seeing the destroyers. Their lights were out. That really impressed the officers. From then on they were sold on the stuff and they would give us anything we wanted.



XAF on the battleship USS *New York*, 1938–1939.

Admiral A.W. Johnson, Commander, Atlantic Squadron, reported after witnessing the demonstrations:

The equipment is one of the most important military developments since the advent of radio itself. Its value as a defensive instrument of war and as an instrument for avoidance of collisions at sea justifies the Navy's unlimited development of the equipment.

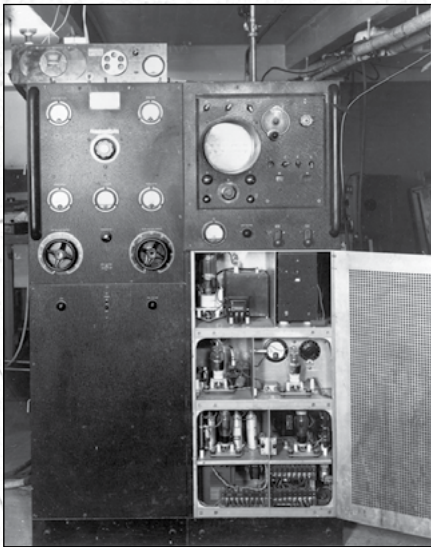
XAF's capabilities resulted in the recommendation for immediate procurement of "10 to 20 of the devices in their present form" for installation on Fleet vessels.

The NRL system went rapidly to production by RCA as the CXAM and CXAM-1 models, and by the time the United States entered World War II, these radar units were installed on 20 Navy vessels, mainly heavy cruisers, carriers, and battleships. Radar surged in importance, and NRL, which had a wide-ranging program of radio research, developed prototypes of air and submarine radars that were also used during the war. Today, NRL continues to be a leading center for research and development of radar systems.

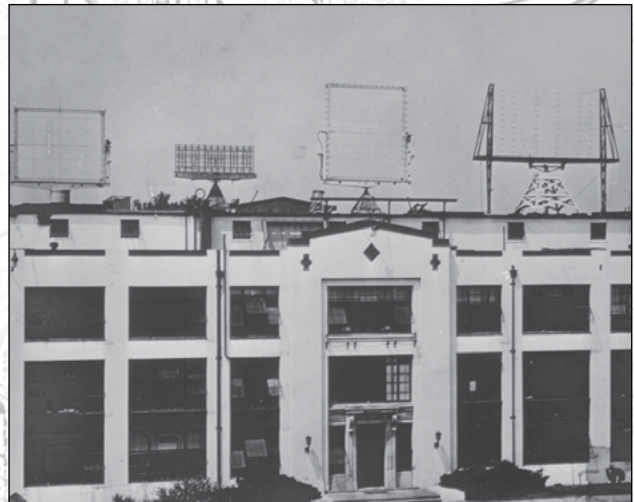
The XAF radar is still around for its 75th: the deteriorating equipment recently underwent conservation treatment and is on display at the National Electronics Museum in Linthicum, Maryland.

Sources and further reading:

- D.K. Allison, "New Eye for the Navy: The Origin of Radar at the Naval Research Laboratory," NRL Report 8466, Sept. 29, 1981. See especially Ch. 7, "From Model to Operational Equipment (1936–1940)," pp. 99–112, and references therein.
- M.A. Simons, "The Flying Bedspring: Restoring the US Navy's XAF Radar," 2011 IEEE MTT-S International Microwave Symposium, June 5–10, 2011, Baltimore, MD.
- "U.S. Navy Shipboard Radars – XAF," Naval History and Heritage Command web site: <http://www.history.navy.mil/photos/weapon/radar/us/xaf.htm>.
- "Bedspring Antenna 'Retires' to Museum," *NRL Labstracts* No. 32, Aug. 7, 1964.
- "Flying Mattress' Comes to Rest," *The Washington Post*, Aug. 21, 1964, p. A16.



The XAF transceiver, ca. 1938.



XAF and other early radar antennas on the roof of Building 12 (undated photo, probably 1930s–1940s).



XAF antenna on display at NRL, ca. 1952.



Mr. Louis Gebhard, NRL “plank owner” and pioneer of radio electronics research and development, stands in front of the XAF antenna at the Washington Navy Yard, ca. 1980. An amusing article in a 1964 issue of *NRL Labstracts* documents moving XAF to the new Naval Historical Display Center at the Navy Yard: “Moving the 1,500-pound antenna from its resting place adjacent to Bldg. 50A proved to be a problem more formidable than truckers or even the Marines could solve.” The antenna was too tall to travel by truck over the DC highways and posed too much of a hazard to be carried by Marine chopper. Finally, it was taken to the NRL pier, loaded onto a 70-foot pontoon barge, and floated upriver to the Navy Yard pier. This event made the pages of the *Washington Post*.



The XAF antenna today, on display at the National Electronics Museum, Linthicum, Maryland. A panel display inside the museum tells the story of the radar. (Photo courtesy of the National Electronics Museum.)

Naval Research Laboratory Dedicates Marine Meteorology Center

October 12, 2012



NRL's Marine Meteorology Center located in Monterey, California.

NRL senior officials were joined by The Honorable Sam Farr, U.S. Representative for California's 17th Congressional District, for the dedication and ribbon cutting ceremony of the Naval Research Laboratory Monterey Marine Meteorology Division's (MMD) new 15,000-square-foot Marine Meteorology Center research facility on Friday, October 12.

This new \$10 million laboratory will consolidate the Meteorological Applications Development Branch; which includes the Satellite Meteorological Applications, On-Demand Systems, and Aerosol and Radiation Sections; and Division Administration — now in three different buildings — into a single location.



From left to right, Mr. Peter Dausen representing Naval Support Activity Monterey; CAPT Erica Sauer, Commanding Officer, Fleet Numerical Meteorology and Oceanography Center; The Honorable Sam Farr; Dr. John A. Montgomery, NRL Director of Research; Dr. Simon Chang, Superintendent, NRL Marine Meteorology Division; Dr. Edward R. Franchi, NRL Associate Director of Research, Ocean and Atmospheric Science and Technology Directorate; and CAPT Anthony J. Ferrari, NRL Commanding Officer.



The building dedication was celebrated with a ceremonial cake cutting. From left to right: Dr. John A. Montgomery, NRL Director of Research; Dr. Edward R. Franchi, NRL Associate Director of Research, Ocean and Atmospheric Science and Technology Directorate; The Honorable Sam Farr; Dr. Simon Chang, Superintendent, NRL Marine Meteorology Division; CAPT Anthony J. Ferrari, NRL Commanding Officer; and CAPT Erica Sauer, Commanding Officer, Fleet Numerical Meteorology and Oceanography Center.

This environmentally engineered laboratory can provide state-of-the-art research facilities for more than 60 NRL MMD meteorologists, physicists, mathematicians, and other researchers investigating air/sea interaction effects on operations, data assimilation techniques, global/regional forecasting, tactical database development, meteorological tactical decision aids, and other atmospheric research in direct support of the U.S. Navy and Marine Corps. NRL MMD's research not only supports the warfighter, but also has been successfully transitioned to the civilian-forecasting sector, providing weather and hurricane/tropical cyclone prediction tools.

This consolidation will foster increased collaboration between NRL MMD researchers and colleagues at the Naval Postgraduate School and NOAA's National Weather Service, and primary operational customer the Fleet Numerical Meteorology and Oceanographic Center (FNMOC) who use environmental prediction systems developed by NRL. High-speed fiber optic connectivity to the FNMOC Computer Center will permit efficient access to NRL's Dedicated High Performance Computer (HPC) Project Investment (DHPI) Cray Supercomputer and Navy Operational computer systems. This will allow research on a fast computer system and development on the same high-speed computers of the future operational systems.

A rooftop observation platform and aerosol/radiation laboratory will host a suite of state-of-the-art instruments to collect atmospheric aerosol optical and radiation properties for the Monterey Bay area. This will complement the weather and climatological meteorological observations made by the adjacent National Weather Service Forecast Office.

NRL's Marine Meteorology Center is a Green building with LEED Gold, and possibly Platinum Certification, which features rooftop photovoltaic panels, a rainwater recovery system, zoned environmental controls, low-water usage landscaping, and a bicycle storage facility to encourage further reduction of the carbon footprint.



Dr. Simon Chang, Superintendent, NRL Marine Meteorology Division, gives a tour of the new 15,000-square-foot research facility. From left to right: CAPT Anthony J. Ferrari, NRL Commanding Officer; Dr. John A. Montgomery, NRL Director of Research; The Honorable Sam Farr; and Dr. Simon Chang.

NRL Scientist Builds Model of LASR Facility: One LEGO at a Time



NRL's William Adams with his completed LEGO model of the newly opened Laboratory for Autonomous Systems Research.

For his daytime job, Mr. William Adams works in the Navy Center for Applied Research in Artificial Intelligence at NRL, supporting research in human-robot interaction, sensing, and autonomy. He manages the resources of the Center's robot lab, and keeps the Center's Mobile, Dexterous, Social (MDS) robots — Octavia, Isaac, and Lucas — operating and configured to meet research needs.

It was in April of 2012 that NRL opened the brand-new Laboratory for Autonomous Systems Research facility. The building and opening of that one-of-a-kind facility sparked an idea in William's mind that led to a LEGO model. For those of us who enjoyed simple LEGO projects as children or with our children, the scope of this project is beyond our imagination.

Here's how William describes the project:

How long did it take you to build the LEGO model of LASR?

It took approximately 120 hours, working a few evenings a week, over the course of 3 months. It also took seven trips to the three local LEGO stores to buy additional bricks.

Do you know how many pieces are used in the model?

It wasn't practical to keep an accurate tally during construction, but I have made a rather detailed post-construction estimate of 13,400 pieces.

Tell us about the details from inside some of the LASR rooms. Were you able to build all of the actual LASR environments in your Lego model?

Limitations on time and brick (the community's collective term for LEGO pieces) prevented a

complete interior, but I tried to represent most of the spaces. The Reconfigurable Prototyping High Bay, Littoral High Bay, Desert High Bay, Tropical High Bay, Power and Energy Lab, two Human-System Interaction Labs, the Machine Shop, Electrical Shop, and changing room all have full interiors.

What sparked the idea for you to attempt making this model?

LEGO recently released a line of architectural kits, all in a very small scale. I had some aging LEGO models in my office that needed replacing and figured that I could build a model of the LASR building. Then I thought about the larger models sometimes seen on display and decided to build it larger for the opening of the LASR facility (a deadline which I ended up missing). Building to a larger scale, approximately 1:60, allowed for detailed interiors while keeping it slightly under LEGO figure (“minifig”) scale, approximately 1:48, cut the brick demands in half and kept it transportable.

Have you built other models of this scale and complexity?

Not really. When we were kids, my siblings and I would build custom castles on the dining room table and lay siege, according to a well thought out set of rules inspired by various board games. My brother and I built a model of the National Cathedral that rose with different color strata as we exhausted our brick supply of each. Several years ago, I built a set of detailed models with the theme of a medieval shipyard, each showing a particular trade or technology, but those models were much smaller and could have all fit within the LASR model’s large high bay.

Where is the model located now? Will you keep it as a permanent model?

The model is on display in the front area of the LASR facility, where it will stay until either the LASR Director needs the space, or I need the brick for recycling into a new model. It will probably be there through the holidays this year.

How and when did you start working with LEGOs?

I remember I was 5, in 1975, and my father took us to the toy store and bought us the Moon landing kit; that’s #565 for the AFOLs. Since it kept us kids occupied, LEGO became standard fare for birthday and Christmas presents. After a high school and college hiatus, I picked up the habit again, although now we “kids” never really get the time to build together.

(EDITOR’S NOTE: “AFOL” refers to “Adult Fan of LEGO” and describes those adult hobbyists who build or collect LEGOs.)

Have you started a new LEGO project yet?

I don’t have any specific plans for another LEGO project. I’ll be adding to the LASR model to keep it up to date and keep it interesting.

The model shows the Human-System Interaction Labs, which overlook the Prototyping High Bay looking through glass walls. The Vicomotion capture cameras and audio array speakers are located along the walls.



The model depicts one of the Mobile, Dexterous, Social robots. Using these robots, NRL scientists study embodied cognition, voice, and gesture recognition, and dynamic autonomy. This scene shows the MDS robot “Octavia” working with a human team leader to detect and extinguish a fire in a mockup of a ship space for the Damage Control for the 21st Century (DC-21) project.



The model displays a replica of the LASR’s Littoral High Bay, which includes tanks and pools that can support autonomous systems research in water environments. In this view, the NRL Deformable Fin UUV is in the pool.



The model has a replica of the LASR’s Desert High Bay, which provides sand and rock for evaluating autonomous systems designed for those challenging environments.



The model has a replica of the LASR’s Tropical High Bay, which simulates a southeastern Asian rainforest.



The model shows the Prototyping High bay, which measures 150 feet by 75 feet by 30 feet high in real life. The LASR’s JLG lift and Bobcat are modeled, along with a menagerie of NRL’s ground and flying autonomous vehicles.





The Naval Research Laboratory

- 20** NRL – Our Heritage
- 21** Highlights of NRL Research in 2012
- 33** NRL Today
- 34** NRL Research Divisions
- 72** Research Support Facilities
- 74** Other Research Sites

NRL — OUR HERITAGE

The early 20th century founders of the Naval Research Laboratory (NRL) knew the importance of science and technology in building naval power and protecting national security. They knew that success depended on taking the long view, focusing on the long-term needs of the Navy through fundamental research. NRL began operations on July 2, 1923, as the United States Navy's first modern research institution, and it continues today as one of the Navy's premier research and development centers.

Thomas Edison's Vision: The first step came in May 1915, a time when Americans were deeply worried about the great European war. Thomas Edison, when asked by a *New York Times* correspondent to comment on the conflict, argued that the Nation should look to science. "The Government," he proposed in a published interview, "should maintain a great research laboratory....In this could be developed...all the technique of military and naval progression without any vast expense." Secretary of the Navy Josephus Daniels seized the opportunity created by Edison's public comments to enlist Edison's support. He agreed to serve as the head of a new body of civilian experts — the Naval Consulting Board — to advise the Navy on science and technology. The Board's most ambitious plan was the creation of a modern research facility for the Navy. Congress allocated \$1.5 million for the institution in 1916, but wartime delays and disagreements within the Naval Consulting Board postponed construction until 1920.

The Laboratory's two original divisions — Radio and Sound — pioneered in the fields of high-frequency radio and underwater sound propagation. They produced communications equipment, direction-finding devices, sonar sets, and perhaps most significant of all, the first practical radar equipment built in this country. They also performed basic research, participating, for example, in the discovery and early exploration of the ionosphere. Moreover, the Laboratory was able to work gradually toward its goal of becoming a broadly based research facility. By the beginning of World War II, five new divisions had been added: Physical Optics, Chemistry, Metallurgy, Mechanics and Electricity, and Internal Communications.

World War II Years and Growth: Total employment at the Laboratory jumped from 396 in 1941 to 4400 in 1946, expenditures from \$1.7 million to \$13.7 million, the number of buildings from 23 to 67, and the number of projects from 200 to about 900. During WWII, scientific activities necessarily were

concentrated almost entirely on applied research. New electronics equipment — radio, radar, sonar — was developed. Countermeasures were devised. New lubricants were produced, as were antifouling paints, luminous identification tapes, and a sea marker to help save survivors of disasters at sea. A thermal diffusion process was conceived and used to supply some of the ^{235}U isotope needed for one of the first atomic bombs. Also, many new devices that developed from booming wartime industry were type tested and then certified as reliable for the Fleet.

Post-WWII Reorganization: The United States emerged into the postwar era determined to consolidate its significant wartime gains in science and technology and to preserve the working relationship between its armed forces and the scientific community. While the Navy was establishing its Office of Naval Research (ONR) as a liaison with and supporter of basic and applied scientific research, it was also encouraging NRL to broaden its scope and become, in effect, its corporate research laboratory. There was a transfer of NRL to the administrative oversight of ONR and a parallel shift of the Laboratory's research emphasis to one of long-range basic and applied investigation in a broad range of the physical sciences.

However, rapid expansion during WWII had left NRL improperly structured to address long-term Navy requirements. One major task — neither easily nor rapidly accomplished — was that of reshaping and coordinating research. This was achieved by transforming a group of largely autonomous scientific divisions into a unified institution with a clear mission and a fully coordinated research program. The first attempt at reorganization vested power in an executive committee composed of all the division superintendents. This committee was impracticably large, so in 1949, a civilian director of research was named and given full authority over the program. Positions for associate directors were added in 1954, and the laboratory's 13 divisions were grouped into three directorates: Electronics, Materials, and Nucleonics.

The Breadth of NRL: During the years since World War II, the Laboratory has conducted basic and applied research pertaining to the Navy's environments of Earth, sea, sky, space, and cyberspace. Investigations have ranged widely — from monitoring the Sun's behavior, to analyzing marine atmospheric conditions, to measuring parameters of the deep oceans. Detection and communication capabilities have benefited by research that has exploited new portions of the elec-

tromagnetic spectrum, extended ranges to outer space, and provided a means of transferring information reliably and securely, even through massive jamming. Submarine habitability, lubricants, shipbuilding materials, firefighting, and the study of sound in the sea have remained steadfast concerns, to which have been added recent explorations within the fields of virtual reality, superconductivity, biomolecular science and engineering, and nanotechnology.

The Laboratory has pioneered naval research into space — from atmospheric probes with captured V-2 rockets, through direction of the Vanguard project (America's first satellite program), to inventing and developing the first satellite prototypes of the Global Positioning System (GPS). Today, NRL is the Navy's lead laboratory in space systems research, as well as in fire research, tactical electronic warfare, microelectronic devices, and artificial intelligence.

The consolidation of NRL and the Naval Oceanographic and Atmospheric Research Laboratory, with centers at Bay St. Louis, Mississippi, and Monterey, California, added critical new strengths to the Laboratory. NRL now is additionally the lead Navy center

for research in ocean and atmospheric sciences, with special strengths in physical oceanography, marine geosciences, ocean acoustics, marine meteorology, and remote oceanic and atmospheric sensing.

The Twenty-First Century: The Laboratory is focusing its research efforts on new Navy strategic interests in the 21st century, a period marked by global terrorism, shifting power balances, and irregular and asymmetric warfare. NRL scientists and engineers are working to give the Navy the special knowledge, capabilities, and flexibility to succeed in this dynamic environment. While continuing its programs of basic research that help the Navy anticipate and meet future needs, NRL also moves technology rapidly from concept to operational use when high-priority, short-term needs arise — for pathogen detection, lightweight body armor, contaminant transport modeling, and communications interoperability, for example. The interdisciplinary and wide-ranging nature of NRL's work keeps this "great research laboratory" at the forefront of discovery and innovation, solving naval challenges and benefiting the nation as a whole.

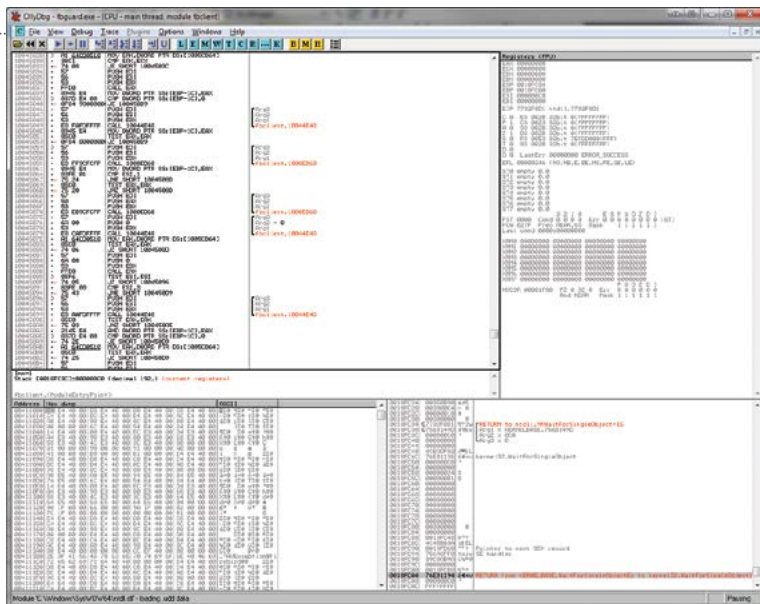
HIGHLIGHTS OF NRL RESEARCH IN 2012

The scientific community at NRL conducts innovative research across a wide spectrum of technical areas, much of it detailed in the *NRL Review* chapters ahead. This section presents a few highlights from the year.



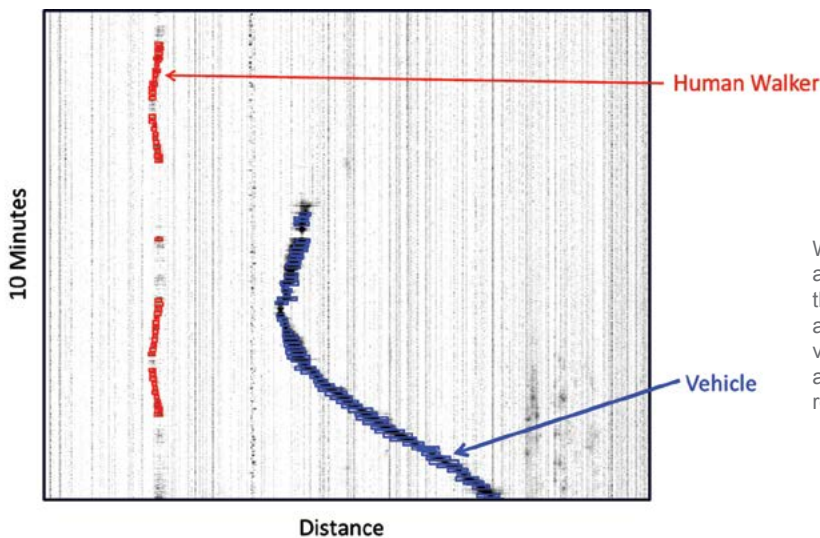
NRL high-frequency electromagnetic vector sensor.

Six-Axis Electromagnetic Vector Sensor: The NRL Radar Division has successfully designed, fabricated, and tested a six-axis electromagnetic vector sensor (EMVS). The novel, high-frequency (HF) EMVS, sponsored by the Intelligence Advanced Research Projects Activity (IARPA), enables simultaneous measurement of the complete electric and magnetic field vectors at a single point. Increased knowledge of HF propagating signals enables advanced signal processing techniques and leads to improved performance. Three loops and three dipoles with actively-matched balun circuits are employed in the NRL design. The dual-loop construction enables structurally sound dipole integration and improved loop signal strength. Active circuits for the electrically small antenna components enable a 10:1 physical sensor size reduction depending on frequency. Field experiments with the EMVS have verified capability for signal direction of arrival estimation in azimuth and elevation as well as signal polarization orientation and ellipticity for ionospherically propagated HF signals. Ongoing research with the NRL EMVS model shows significant improvement over previous vector sensor design endeavors.



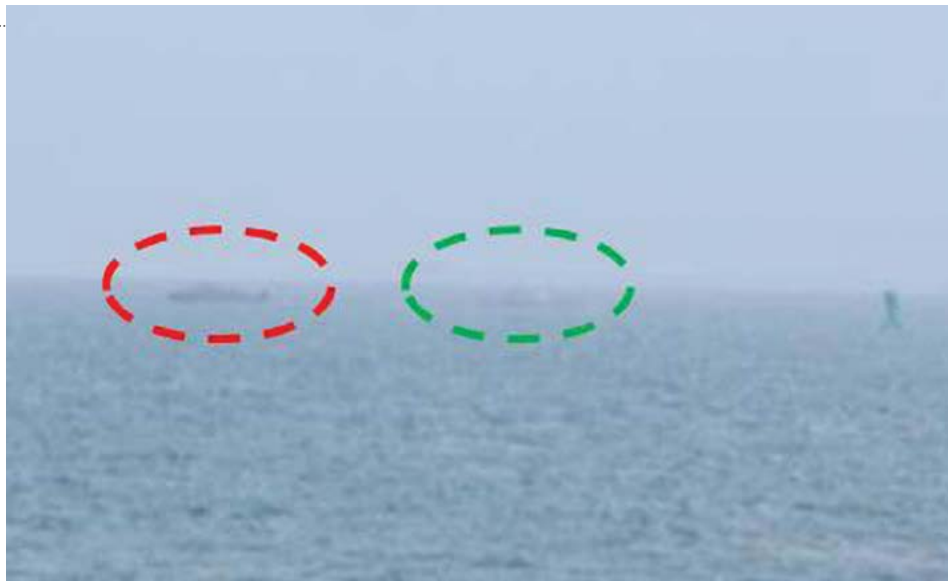
Sample representations of malware analysis methods.

Joint Malware Catalog: In compliance with Chairman of the Joint Chiefs of Staff Manual 6510.01A, the Department of Defense (DoD) shall create a central repository for the storage and sharing of malicious software artifacts among members of the Computer Network Defense (CND) community. The National Security Agency (NSA) Information Assurance Division contracted NRL to be the principal investigator in developing the Joint Malware Catalog (JMC). Since 2010, NRL has worked with malware analysts from the DoD CND community to develop operational requirements and to build and test a centralized platform for malware submission, sharing, and automated analysis of submitted files accessible via web portal. JMC serves as an information repository for malware analysts to share their knowledge and custom analysis tools to allow users to collaborate on the analysis of malicious software discovered on DoD networks.



Waterfall display showing the seismo-acoustic activity in gray scale along the length of the virtual fence. Human and vehicle activity near the fiber optic virtual fence is automatically detected and classified as shown in red and blue respectively.

Fiber-Optic Terrestrial Sensor Border Monitoring: The NRL is working with the Department of Homeland Security to develop an automated fiber optic distributed sensor system for border monitoring applications. The optical sensing mechanism, which turns a standard commercial off-the-shelf (COTS) fiber optic cable into a sensitive distributed seismo-acoustic sensor, was developed in the NRL's Optical Sciences Division. A prototype system has been deployed in an engineering testbed to gather real-world signature data for targets of interest including people, animals, vehicles, helicopters, and fixed wing aircraft. The gathered signature data was used to develop detection routines to trigger on, and classify events of interest while ignoring environmental and nuisance events. The system demonstrated nearly 100% detection of known targets in simulated border crossing testing performed in May.



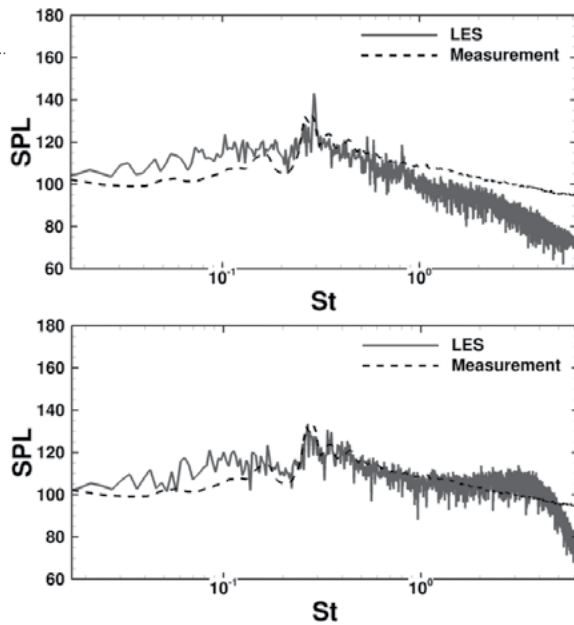
At-sea comparison of the old RCB paint scheme (red oval) to the new paint scheme (green oval).

Improved Survivability for Navy Coastal Riverine Forces: NRL Tactical Electronic Warfare Division researchers performed an analysis for the Navy Expeditionary Combat Command (NECC) of paint schemes designed to counter the detection of Navy riverine craft by hostile threats. The analysis was done for two types of craft with different missions, the Riverine Command Boat (RCB), which mostly operates offshore, and the Riverine Patrol Boat (RPB), which operates upriver. Based on NRL-led field evaluations of the design on a prototype riverine combat command craft, this paint scheme is now being applied to additional craft.



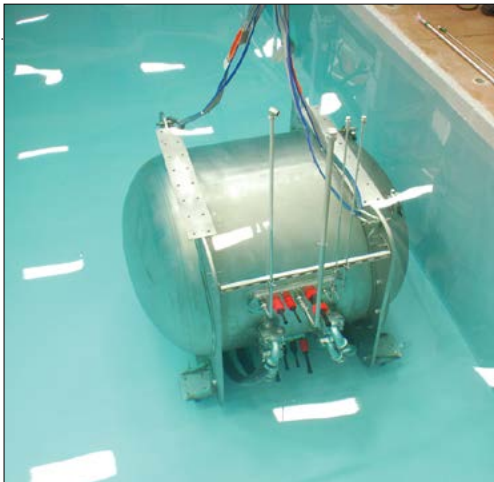
Fueled by liquid hydrogen, the Ion Tiger unmanned aerial vehicle completes a record flight time of 48 hours and 1 minute. The same aircraft was used in autonomous soaring experiments, using atmospheric motion to double battery-only endurance from 1 hour to 2.13 hours.

Innovative Solutions for Dynamic Performance Enhancements: NRL's Ion Tiger unmanned aerial vehicle (UAV) flew two endurance enhancement technologies in FY2012: a liquid hydrogen (LH₂) tank that holds promise for 3-day tactical UAV flight endurance, and an autonomous soaring algorithm that enables a UAV to soar like a bird. In 2009, Ion Tiger flew 26.1 hr on compressed gaseous hydrogen (GH₂). However, LH₂ has approximately 3 times the energy density of GH₂, providing significant opportunity for improvements in endurance. A custom Dewar tank was designed, constructed, bench tested, and integrated into the Ion Tiger aircraft. From 16 to 18 April 2012, a demonstration flight with the LH₂ tank in Ion Tiger lasted 48 hr 1 min, approximately twice the endurance available from GH₂. In parallel, NRL adapted autonomous soaring technologies for Ion Tiger. In FY2008–FY2010, an NRL 6.2 program developed and demonstrated autonomous soaring algorithms that searched for, identified, and provided guidance to stay within thermal updrafts for atmospheric energy extraction. These algorithms were modified to include electric propulsion energy input terms and to operate within the constraints of a communications relay mission, closing a traditional gap between soaring research and tactical application. A test flight demonstrated 2.13 hr endurance using the soaring algorithms, doubling Ion Tiger's nominal 1 hr battery flight time, with all endurance improvements coming from energy extracted from the atmosphere.



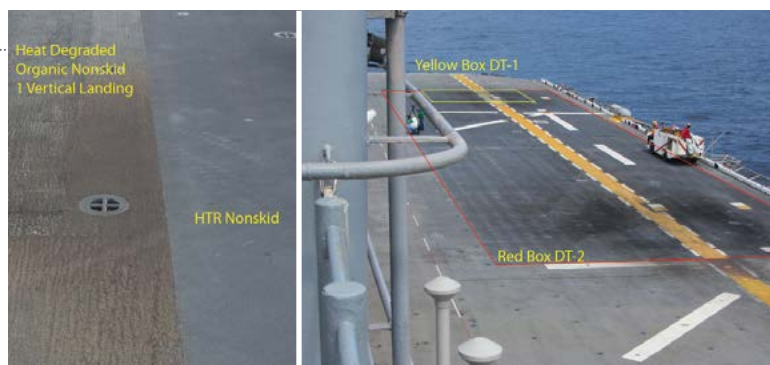
Sound pressure level (SPL) distributions at $1.5 d$ (d = exhaust nozzle exit diameter). St is the Strouhal number. LES stands for large-eddy simulation. Top: Inflow turbulence level is 0.4% of the jet velocity. Bottom: Inflow turbulence level is 2.0% of the jet velocity.

Impact of Inflow Turbulence on Noise from Military Aircraft Jets: NRL has demonstrated that the turbulence inside the exhaust nozzle of a supersonic jet impacts the jet's noise generation, and this impact varies with the jet operating conditions. Since turbulence levels inside a full-scale exhaust nozzle can be drastically different from those observed in a clean nozzle used in a laboratory model test, the jet noise reduction techniques developed based on jet flows from exhaust nozzles with clean inlet flows may not always be effective in actual engine applications. In this work, we have numerically investigated the impact of inflow turbulence at several supersonic jet conditions by using large-eddy simulations. Two techniques were used to control the turbulence level at the nozzle exit. These techniques included employing random perturbations to the flow field inside the nozzle and imposing wall roughness onto the nozzle surface. It was found that if the turbulence level is sufficiently high, a thicker shear layer is observed, the shock-cell sizes are altered, and the far-field noise level is reduced to some extent, especially in the direction upstream of the nozzle, where the shock-associated noise dominates. In addition, it was found that the overexpanded jet conditions, which are the engine operating conditions during flight takeoff and landing on an aircraft carrier deck, are more sensitive to the inflow turbulence level than the underexpanded jet conditions.



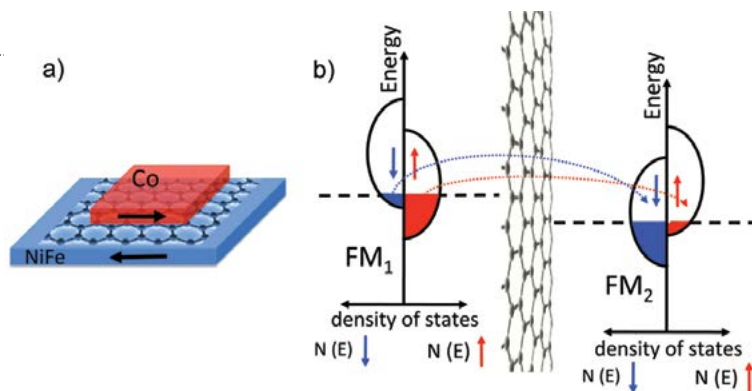
Photograph of the air-independent fuel cell system in the pool at NRL's LASR facility.

Air-Independent Automotive Fuel Cell for Unmanned Undersea Vehicle Propulsion: The Naval Research Laboratory, Naval Surface Warfare Center-Carderock, University of Hawaii, and General Motors Company have completed the successful air-independent operation of an automotive fuel cell system. The automotive fuel cell system was integrated by the Navy fuel cell team to operate in a closed environment under automated control. The accomplishment proves that such commercial fuel cell systems are a viable electric-power solution for propulsion in the Navy's next generation of undersea systems. Funding is provided by the Office of Naval Research.



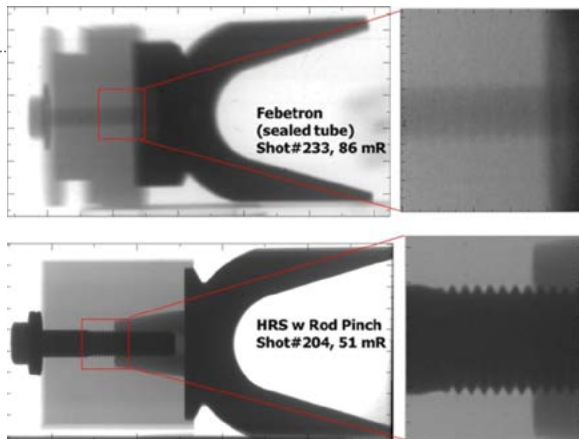
Left: The high temperature resistant (HTR) nonskid decking material outperforms the legacy organic nonskid. During a single vertical descent by an F-35B aircraft, the organic nonskid showed significant degradation, while the adjacent HTR nonskid sustained no damage. Right: The two separate demonstration patches, 900 ft² (DT-1) and 8000 ft² (DT-2). The black staining is simply exhaust soot from the AV-8B landings.

High Temperature Resistant Nonskid for STOVL Joint Strike Fighter (F-35B): Flight-deck nonskid decking material was determined by the Naval Sea Systems Command (NAVSEA) to be a high-risk area in the integration of the standard takeoff and vertical landing (STOVL) Joint Strike Fighter (F-35B) on amphibious ships, since operational temperatures during vertical landings were expected to exceed decomposition temperatures of traditional Navy organic nonskid. Given no alternative materials for decking had previously been identified, the Naval Research Laboratory, via Future Naval Capabilities Enterprise Platform Enablers program under the Office of Naval Research, reviewed and thoroughly evaluated technologies to meet the Navy's operational needs. During the first F-35B Shipboard Compatibility tests in 2011 aboard USS Wasp (LHD 1), NRL successfully demonstrated on landing spot #9 (900 ft²) an aluminum-ceramic thermal spray decking material, which exhibited no degradation during F-35B landings. This material was further enhanced, scaled up, and optimized in 2012 through 2013 by NRL based on lessons learned to support the second round of F-35B compatibility testing on a larger scale (8,000 ft² application in 2013); the high temperature resistant nonskid was subjected to 95 vertical landings during second round of shipboard testing. Beyond the Joint Strike Fighter landings, the NRL nonskid material also successfully performed during 381 combined vertical landings by MV-22 (OSPREY), AV-8B (HARRIER), and other helicopter platforms, resulting in over 450 vertical landing. This successful development and demonstration of an inorganic decking material has provided the U.S. Navy with a viable means of retaining nonskid decking requirements while sustainably surviving F-35B operations, which would not have been possible using current nonskid decking products. Currently, additional efforts are still proceeding by NRL to improve production rate by advancing application robotic systems and processes as well as some additional coating optimization.



Graphene provides a new paradigm for tunnel junctions. (a) Schematic of a magnetic tunnel junction fabricated using single layer graphene as a tunnel barrier between two ferromagnetic metal films, cobalt and permalloy (NiFe). The resistance is higher when the magnetizations are antiparallel (shown), and lower when they are parallel. (b) Simplified spin-dependent energy diagram illustrating spin-polarized electrons tunneling from one ferromagnetic metal, through the graphene tunnel barrier, and into the second ferromagnetic metal for the antiparallel state.

Breakthrough in Tunnel Barrier Technology for Electronic Devices: Scientists in NRL's Materials Science and Technology and Electronics Science and Technology Divisions have demonstrated, for the first time, the use of graphene as a tunnel barrier — an electrically insulating barrier between two conducting materials through which electrons tunnel quantum mechanically. The researchers report fabrication of magnetic tunnel junctions using graphene, a single atom thick sheet of carbon atoms arranged in a honeycomb lattice, between two ferromagnetic metal layers in a fully scalable photolithographic process. Their results demonstrate that single-layer graphene can function as an effective tunnel barrier for both charge- and spin-based devices, and enable realization of more complex graphene-based devices for highly functional nanoscale circuits, such as tunnel transistors, nonvolatile magnetic memory, and reprogrammable spin logic.



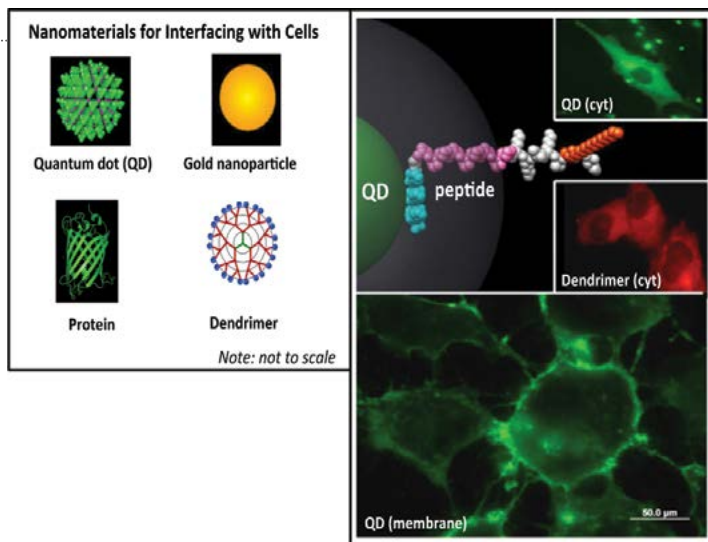
A comparison between the commercially available Febetron unit (top) and the NRL-developed Hybrid Radiation Source (HRS) (bottom). The smaller spot size on the NRL unit enables the imaging of much finer detail than the commercial source, as evidenced by the bolt threads in the radiograph.

Enhanced Flash Radiography for DoD Applications: A variety of applications, such as equation-of-state modeling, fragmentation-warhead development, and target-interaction studies, rely on radiographic images to diagnose processes that occur on the microsecond time scale in destructive tests. Traditional radiographic units, such as the 1 MV Febetron, are used with commercial X-ray diode heads that are optimized for long life and not for performance quality. Los Alamos National Laboratory (LANL) tasked NRL with the development of an improved unit to support Department of Energy studies on explosively strained material tests. The resulting unit combined the casing and Marx capacitor bank of a Febetron with an NRL-designed front end that allowed the use of a much smaller anode on the vacuum diode. The resulting radiographs have demonstrated a 10× increase in radiographic figure of merit. NRL successfully filed a patent on the diode in 2010, and is working with DoD partners to apply the technology to DoD user needs. These include diagnosis of electromagnetic railguns, high-velocity impacts, shock physics, advanced energetics, and armor penetrators.



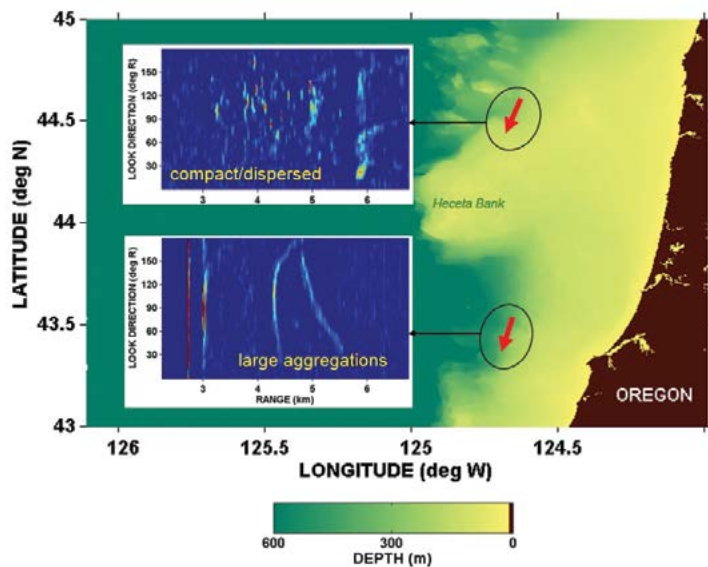
The high-efficiency, flexible solar panels developed by NRL have been integrated into the U.S. Marine Corps Marine Austere Patrolling System (MAPS), which was field-tested by Marines at the Bridgeport Mountain Training Area. Pictured here are two Marines in camp during the MAPS exercise with the solar arrays deployed. During this exercise, the solar panels were able to keep the batteries of a rifle squad, 13 Marines, charged during the entire 4-day mission, thereby eliminating the need to pack replacement batteries or for resupply.

Mobile Solar Power: The military's need to reduce both fuel and battery resupply is a real-time requirement for increasing combat effectiveness and decreasing vulnerability. Mobile photovoltaics are a technology that can address these needs by leveraging emerging flexible space photovoltaic technology. NRL has developed and produced a semirigid, lightweight, efficient solar blanket with the ability to mount on or stow in a backpack and recharge a BB-2590 lithium-ion battery. The blanket consists of a 10×3 solar array of 20 cm^2 , triple-junction, epitaxial lift-off (ELO) solar cells manufactured by Microlink Devices, which have efficiency of approximately 25% under AM1.5 illumination and capable of producing up to approximately 18W.



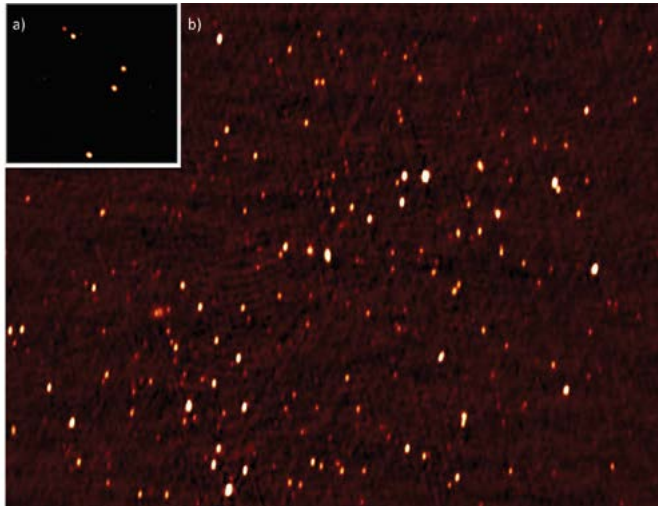
Cellular delivery of disparate nanoparticle (NP) materials facilitated by multifunctional peptides. NP materials for use in cellular applications include semiconductor quantum dots (QDs), gold, proteins and dendrimers (left panel). Highly fluorescent QDs and dendrimeric NPs are targeted to the cytosol (cyt) and membrane using peptides developed at NRL (right panel).

Peptide-Mediated Cytosolic Delivery of Nanomaterials: Delivering nanomaterials including labels, probes, and drugs to cells continues to be a major focus in nanotechnology. The major hurdle to this goal is the resulting sequestration in the endolysosomal system. NRL's Center for Bio/Molecular Science and Engineering has shown that a palmitoylated peptide (Palm-1) can facilitate nanoparticle endosomal escape and delivery to the cellular cytosol over the course of 48 hours with minimal cytotoxicity. We performed an extensive structure/function analysis of this peptide to better understand the mechanism of action and to develop more efficient peptides for cellular delivery. We demonstrated the cytosolic delivery of CdSe/ZnS core/shell quantum dots (QDs) to multiple cell lines and a developing chick embryo, as well as cytosolic delivery of proteins, dendrimers, and gold nanoparticles. Codelivery of multiple cargoes and multifunctional labeling demonstrate the potential use of this peptide for a myriad of applications including in vivo labeling, nanoparticle-mediated drug delivery, and intracellular biosensing.



Spatial characteristics of long-range coherent echoes from fish collected with a towed mid-frequency (1–10 kHz) sonar — ship tracks in red — observed in two littoral areas off the Oregon coast. In the southern site, the echo patterns extend over most receiver look directions, while in the northern site, the echoes are more discrete and “clutter like,” i.e., they would present false targets to a sonar detector. Significantly, in each case, the echo variability was consistent with in situ observations of the spatiotemporal behavior of the two primary fish species (near-surface sardines and mid-water hake), thus providing a physical basis for ASW clutter prediction.

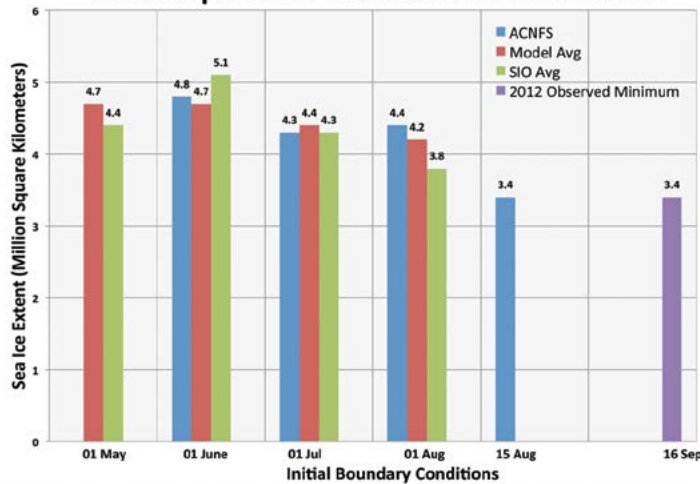
Characterizing Sonar Clutter Due to Fish Aggregations: Active sonar systems use acoustic sources and receivers coupled with signal processing to detect, classify, and track underwater targets. However, acoustic interaction with biologics can severely limit sonar performance by masking desired target echoes or creating false target detections (“clutter”). Under the auspices of an ONR Basic Research Challenge (BRC) program, in the summer of 2012, researchers in the NRL Acoustics Division led a successful littoral experiment off the coast of Oregon to conduct low- and mid-frequency sonar studies of biological sources of attenuation and clutter, specifically fish. By focusing on the physics of interactions of acoustic signals with aggregations of fish, this work provides a scientific foundation for improving active sonar antisubmarine warfare (ASW) performance in the littoral, where biologics are commonplace.



Images of the radio sky as seen with the new VLA VHF receivers. (a) First light image from the new system taken in May 2012 using five of the VHF receivers on the VLA. This image shows five distant radio galaxies. (b) Image of the sky from August 2013 using 23 of the VLA's 27 new VHF receivers. The more recent image using the nearly complete system shows a much larger number of distant radio galaxies that are powered by supermassive black holes.

Scientists Bring Low Frequency “First Light” to the Jansky Very Large Array: Remote sensing of the Earth’s ionosphere and astrophysical objects within and beyond the solar system relies on having state-of-the-art receivers on the world’s most powerful radio interferometric telescopes. NRL’s Remote Sensing Division worked closely with the National Radio Astronomy Observatory to develop very high frequency (VHF) receivers for the Karl G. Jansky Very Large Array (VLA). These new VHF receivers will enable observations on the VLA at frequencies below 1 GHz. These receivers are currently fully deployed on the VLA, and initial commissioning data was used to meet an important milestone in May 2012 when the first light astrophysical image at 337 MHz was made using the new VHF receiver system. The receivers are currently operational for use by the community and are providing NRL with state-of-the-art measurements of astrophysical sources as well as ionospheric waves and turbulence.

2012 September Sea Ice Extent Estimates



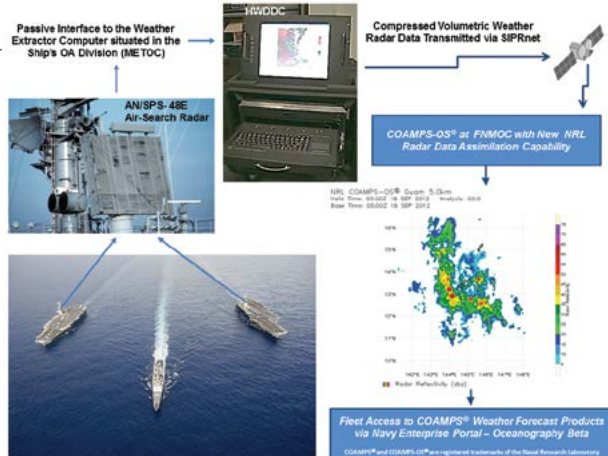
The September 2012 minimum sea ice extent estimates from ACNFS (blue), average of all numerical models participating in SIO (red), and SIO overall average (green) based on initial conditions from early (May) to late (Aug) in the season. An additional ACNFS forecast ensemble starting from 15 August initial conditions is also included. An intense storm in early August contributed to the Arctic reaching a record minimum ice extent on 16 Sept 2012 (3.4 Mkm² - purple), well below the long-term average minimum (6.7 Mkm²).

The Navy’s First Seasonal Ice Forecasts: The Arctic Cap Nowcast/Forecast System (ACNFS) was used to produce long-term seasonal forecasts of ice extent in the northern hemisphere as part of the 2012 Sea Ice Outlook (SIO) project, an international effort to provide a community-wide summary of the expected September Arctic sea ice minimum. ACNFS seasonal projections were made using an ensemble of model simulations from 2003 to 2011. Each model simulation was initialized from an ACNFS analysis field from 01 June, 01 July, 01 August, and 15 August 2012 and integrated through September with atmospheric forcing from the Navy Operational Global Atmospheric Prediction System for each year. The ice extent was averaged for each day in the month of September, with the mean representing the NRL ice extent for September 2012. This was the first time the Navy produced long-term seasonal forecasts of Arctic ice conditions. This new capability could prove to be beneficial in future strategic mission planning.



The GHub CISView is being used to display enemy alerts and tracks during an exercise at Bogue Airfield, North Carolina. The alerts and tracks are automatically generated from UAV video, persisted in the GHub, and visualized using CISView in a real-time or forensic mode.

The NRL Geospatial Hub and CISView for Multi-INT WAAS Exploitation: The NRL Geospatial Hub (GHub) and Common Information Space Viewer (CISView) address the problems of video and track exploitation and data management for the Marine Corps' Wide Field of View Plane Array Camera (WFPAC), a long-endurance, high-resolution Wide Area Airborne Sensor (WAAS) capability. Used in a force protection scenario, the capability captures motion imagery on an unmanned airborne system and is combined with real-time forensic analytics to produce vehicle tracks and derived behavior alerts. GHub solves the problem of providing a common data space for both raw and derived products, as well as a layered spatiotemporal visualization tool. It provides unique technologies for managing discovery and dissemination in a network-challenged scenario. Also, it serves as a common integration framework for analytics in a tactical cloud environment. The Marine Corps WFPAC program employs the Geospatial Hub as its key enabling technology to expose intelligence to the wider DoD enterprise.



Aircraft carriers USS *George Washington* and USS *John C. Stennis* are shown departing the Valiant Shield 2012 experiment area with the guided-missile cruiser USS *Mobile Bay* on September 20, 2012. These SPS-48E/HWDDC equipped carriers provided near-real-time weather radar data to FNMOC that were assimilated hourly with NEXRAD weather radar data from Guam (an example unclassified NEXRAD-only analysis is shown) and conventional atmospheric and oceanic observations into COAMPS® during the 12-day experiment. The radar data provided improved storm structure and wind forecasts compared to control forecasts that excluded radar data.

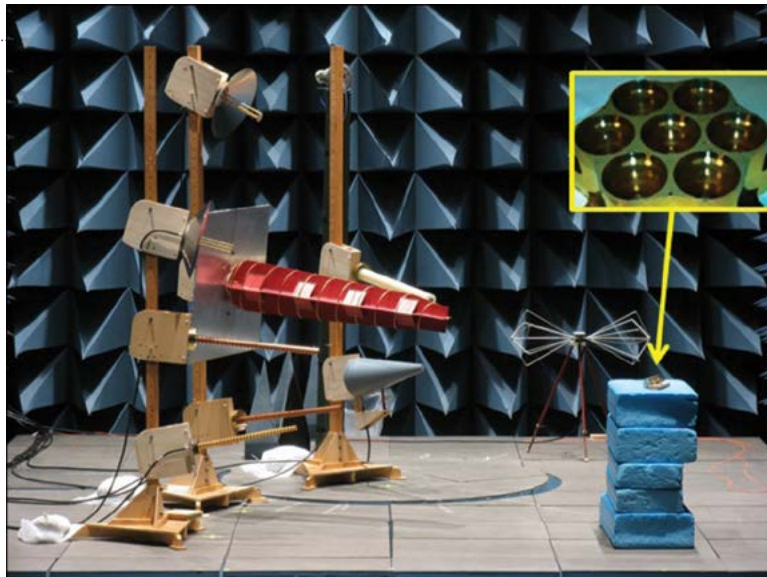
Improved Tactical-Scale Forecasting by Assimilating Operational Navy Shipboard Radar Through-the-Sensor Data with COAMPS®:

NRL, in collaboration with the Space and Naval Warfare Systems Command (SPAWAR) and Fleet Numerical Meteorology and Oceanography Center (FNMOC), has for the first time successfully demonstrated the capability to automatically obtain and assimilate Navy operational "through-the-sensor" tactical radar data into the Coupled Ocean/Atmosphere Mesoscale Prediction System (COAMPS®). The demonstration project, called the Hazardous Weather Decision Aid (HWDA), was selected by the Trident Warrior fleet experimentation program to participate during the Rim of the Pacific (RIMPAC) and Valiant Shield 2012 exercises. HWDA is an automated meteorology and oceanography (METOC) forecast/nowcast system based on the COAMPS - On Demand System (COAMPS-OS®) that fuses conventional weather and ocean observations with shipboard AN/SPS-48E air defense radar data and ground-based NEXRAD weather radar data within the COAMPS forecast model at FNMOC. The SPS-48E tactical data are processed on board by the Hazardous Weather Detection and Display Capability (HWDDC) to extract the weather signal and transmit the results to FNMOC for assimilation. The HWDA demonstration system at FNMOC continuously produced an updated suite of products depicting anticipated atmospheric and oceanographic conditions which were accessible to the Fleet via the Navy Enterprise Portal - Oceanography (NEP-Oc) Beta website.



Photograph of an LCU-2000 target ship with a hidden radiation source as seen by the SuperMISTI system. The reconstructed radiation source position is overlaid as the dark blue rectangle.

SuperMISTI: Improved detection of weapons of mass destruction is one of the science and technology priorities of the Secretary of Defense for fiscal years 2013–2017. Unfortunately, the remote detection of special nuclear materials is difficult because the materials are not very radioactive, the radiation signatures decrease rapidly with distance, and faint sources of radiation can be obscured by naturally occurring and manmade radioactive sources. Researchers from NRL's Space Science Division (Radiation Detection Section, High Energy Space Environment Branch) developed the SuperMISTI standoff detection system for maritime environments. The instrument was deployed at Norfolk Naval Station in July 2012 to determine the on-water performance of the system.



The risk reduction model (inset, right) of the GPS III Laser Retroreflector Array, developed and tested by the Naval Center for Space Technology (NCST) at NRL, is shown under test in an NCST anechoic chamber.

GPS III Laser Retroreflective Array: After completing studies of materiel and concept of operations (CONOPS) solutions, and briefing the Senior Advisory Group from NASA, Air Force Space Command, National Geospatial-Intelligence Agency, National Nuclear Security Agency, Department of State, and STRATCOM, NRL kicked off the GPS III Laser Retroreflector Array (LRA) Prototype Development Program. The LRA Prototype Requirements Review was completed in September 2012. The goal of the program is to begin the development of a prototype LRA to be hosted on GPS III satellites, and to architect CONOPS to support achieving a stable reference frame with 10 times better accuracy over projected user needs for positioning, navigation, and timing.



TacSat-4 ready for encapsulation in the Minotaur IV+ fairing.

TacSat-4 Flight Operations and Successful Military Experimentation and Assessment: On September 27, 2011, the TacSat-4 satellite was launched into orbit. TacSat-4 is an Ultra High Frequency (UHF) research and development satellite that provides up to five UHF channels for bent-pipe satellite communications (SATCOM) operations. TacSat-4 was designed to augment existing SATCOM and to allow users to experiment with advanced communications capabilities, technologies, and CONOPS. NRL leads the flight operations team and NRL's Blossom Point Tracking Facility performs command and control. User experimentation and Military Utility Assessments (MUA) were performed during the first year of operations. Formal assessments were performed by multiple parties and summarized in the Operationally Responsive Space (ORS) Office's Joint MUA report, which found utility and recommends transition, and was sent to STRATCOM. The Navy's formal assessment was performed during Trident Warrior 2012 (TW-12). The TW-12 final report, authored by the Navy Warfare Development Command, established that TacSat-4 was capable of supporting operational forces, and recommended that TacSat-4 be made available to operational forces to establish data on how a satellite in its orbit can best be used. This information on operational use will inform future satellite acquisition decisions.

NRL TODAY

ORGANIZATION AND ADMINISTRATION

The Naval Research Laboratory is a field command under the Chief of Naval Research, who reports to the Secretary of the Navy via the Assistant Secretary of the Navy for Research, Development and Acquisition.

Heading the Laboratory with joint responsibilities are CAPT Anthony J. Ferrari, USN, Commanding Officer, and Dr. John A. Montgomery, Director of Research. Line authority passes from the Commanding Officer and the Director of Research to three Associate Directors of Research, the Director of the Naval Center for Space Technology, and the Associate Director for Business Operations. Research divisions are organized under the following functional directorates:

- Systems
- Materials Science and Component Technology
- Ocean and Atmospheric Science and Technology
- Naval Center for Space Technology

The *NRL Fact Book*, published every two years, contains information on the structure and functions of the directorates and divisions.

NRL operates as a Navy Working Capital Fund (NWCF) Activity. All costs, including overhead, are charged to various research projects. Funding in FY12 came from the Chief of Naval Research, the Naval Systems Commands, and other Navy sources; government agencies such as the U.S. Air Force, the Defense Advanced Research Projects Agency, the Department of Energy, and the National Aeronautics and Space Administration; and several nongovernment activities.

PERSONNEL DEVELOPMENT

At the end of FY12, NRL employed 2791 persons — 33 officers, 47 enlisted, and 2711 civilians. In the research staff, there are 869 employees with doctorate degrees, 352 with master's degrees, and 447 with bachelor's degrees. The support staff assists the research staff by providing administrative support, computer-aided design, machining, fabrication, electronic construction, publication and imaging, personnel development, information retrieval, large mainframe computer support, and contracting and supply management services.

Opportunities for higher education and other professional training for NRL employees are available through several programs offered by the Employee Relations Branch. These programs provide for graduate work leading to advanced degrees, advanced training, college course work, short courses, continuing education, and

career counseling. Graduate students, in certain cases, may use their NRL research for thesis material.

For non-NRL employees, several postdoctoral research programs exist. There are also agreements with several universities for student opportunities, as well as summer and part-time employment programs. Summer and interchange programs for college faculty members, professional consultants, and employees of other government agencies are also available. These programs are described in the *NRL Review* chapter "Programs for Professional Development."

NRL has active chapters of Women in Science and Engineering (WISE), Sigma Xi, Toastmasters International, and the Federal Executive and Professional Association. An amateur radio club, a drama group, and several sports clubs are also active. NRL has a Recreation Club that provides gymnasium and weight-room facilities. NRL also has an award-winning Community Outreach Program. See "Programs for Professional Development" for details on all these programs and activities.

NRL has its very own credit union. Established in 1946, NRL Federal Credit Union (NRLFCU) is a sound financial institution that serves about 20,000 members including NRL employees, contractors, select employee groups and their families as well as consumers via the American Consumer Council. Focusing on its mission of Trusted Partners for Life, NRLFCU provides many free and low-cost products and services, including free checking with free bill pay, Visa CheckCard, and mobile banking with remote deposit and great rates on auto and personal loans, credit cards, mortgages and more. Plus, NRLFCU offers the convenience of direct deposit, online access, and local branches (including one located in Bldg. 222, one in Waldorf, MD, and one coming soon to Alexandria, VA), nationwide access via the National Shared Branching Network with over 28,000 surcharge-free ATMs, and personalized full-service investment and brokerage services. For more information, call 301-839-8400 or visit nrlfcu.org.

Public transportation to NRL is provided by Metrobus. Metrorail service is three miles away.

SITES AND FACILITIES

NRL's main campus in Washington, D.C., consists of 89 main buildings on about 131 acres. NRL also maintains 15 other research sites, including a vessel for fire research and a Flight Support Detachment. The many diverse scientific and technological research and support facilities are described here. More details can be found in the *NRL Major Facilities* publication at www.nrl.navy.mil.

Institute for Nanoscience



NRL researchers working in the Institute for Nanoscience clean room.

The revolutionary opportunities available in nanoscience and nanotechnology led to a National Nanotechnology Initiative in 2001. In that same year, the NRL Institute for Nanoscience was established with a current annual budget of \$11 million in core research funds. The prospect for nanoscience to provide a dramatic change in the performance of materials and devices was the rationale for identifying this emerging field as one of the DoD strategic research areas for basic research funding on a long-term basis.

The mission of the NRL Institute for Nanoscience is to conduct highly innovative, interdisciplinary research at the intersections of the fields of materials, electronics, chemistry, and biology in the nanometer size domain. The Institute exploits the broad multidisciplinary character of the Naval Research Laboratory to bring together scientists with disparate training and backgrounds to pursue common goals at the intersection of their respective fields in systems at this length scale. The Institute provides the Navy and DoD with scientific leadership in this complex, emerging area and

identifies opportunities for advances in future defense technology. NRL's nanoscience research programs and accomplishments directly impact nearly all Naval S&T focus areas.

The Institute's current research program emphasizes multidisciplinary, cross-division efforts in a wide range of science and technology applications:

- Ultra-low-power electronics
- Quantum information processing
- Chemical signaling
- Energy conversion/storage
- Photonics/plasmonics
- Multifunctional materials
- Biomimetics
- Bio/inorganic hybrid materials

The Institute for Nanoscience building, opened in October 2003, provides NRL scientists access to state-of-the-art laboratory space and fabrication facilities. The building has 5000 ft² of Class 100 clean room space for device fabrication, 4000 ft² of "quiet" lab space with temperature controlled to ± 0.5 °C, acoustic isolation at the NC35 standard (35 dB at 1 kHz), floor vibration isolation to <150 $\mu\text{m/s}$ rms at 10 to 100 Hz and <0.3

mOe magnetic noise at 60 Hz, and 1000 ft² of “ultra-quiet” laboratory space with temperature controlled to ± 0.1 °C and acoustic isolation at the NC25 standard (25 dB at 1 kHz). Clean room equipment includes a complete suite of fabrication tools including deposition and etch systems; optical mask aligners; two electron beam writers; a focused ion beam writer; an optical pattern generator for mask making; a plasma-enhanced atomic layer deposition system; a laser machining tool; a wide variety of characterization tools; and more.



Metrology.



Transmission electron microscopy.



The Institute for Nanoscience research building.

Radar



The AMRFC testbed, located at NRL's CBD, was developed as a proof-of-principle demonstration system that is capable of simultaneously transmitting and receiving multiple beams from common transmit and receive array antennas for radar, electronic warfare, and communications.

NRL has gained worldwide renown as the “birthplace of U.S. radar,” and for more than half a century has maintained its reputation as a leading center for radar-related research and development. A number of facilities managed by NRL’s Radar Division continue to contribute to this reputation.

A widely used major facility is the Compact Antenna Range (operated jointly with the Space Systems Development Department) for antenna design and development and radar cross section measurements. The range is capable of simulating far-field conditions from 1 to 110 GHz, with a quiet zone approximately 7 ft in diameter and 8 ft in length. Instrumentation covers from 1 to 95 GHz. The range was recently upgraded to include a 20 ft × 12 ft near-field scanner supporting near-field antenna measurements up to 110 GHz. Another strong division capability is in the Computational Electromagnetics (CEM) Facility, which has capabilities for complex electromagnetic modeling, including radar target and antenna structures. The Radar Signature Calculation Facility produces detailed computations of radar cross sections of various targets, primarily ships. The CEM facility includes multiple-CPU supercomputers that are

also used to design phased array radar antennas. The tremendous synergism between the CEM group and the Compact Antenna Range Facility provides the ability to design in the CEM environment, to test in the compact range, and have immediate feedback between the theoretical and experimental aspects to shorten the development cycle for novel and new designs.

In support of airborne radar applications, the division operates a supercomputer-based Radar Imaging Facility and an inverse synthetic aperture radar (ISAR) capable of being deployed in the air, ground, or shipboard for collecting radar imaging data. A P-3 aircraft equipped with the AN/APS-145 radar and cooperative engagement capability is also available to support experiments.

In support of ship-based radar applications, the division operates the Radar Test Facility at the Chesapeake Bay Detachment (CBD) near Chesapeake Beach,

Maryland. The site has radars for long-range air search and surface search functions and features the W-band Advanced Radar for Low Observable Control (WARLOC), a fully operational high-power coherent millimeter-wave radar operating at 94 GHz. The WARLOC transmitter is capable of producing a variety of waveforms suitable for precision tracking and imaging of targets at long range. Waveforms with a bandwidth of 600 MHz can be transmitted at full power. A 6 ft Cassegrain antenna is mounted on a precision pedestal and achieves 62 dB of gain. An S-band waveform development testbed is under development that will incorporate a 20 ft Cassegrain antenna with > 43 dB gain supporting bandwidths up to 400 MHz.

The Advanced Multifunction Radio Frequency Concept (AMRFC) testbed is an installation at CBD operated by the Radar Division, with significant contributions by other NRL divisions. The goal of the AMRFC program is to demonstrate the integration of multiple shipboard RF functions, including radar, electronic warfare (EW), and communications, by utilizing a common set of broadband array antennas, signal and data processing, and signal generation and display hardware. The testbed consists of separate active transmit and receive arrays that operate over the 6 to 18 GHz band. Functionality of the testbed includes a multimode navigation/surface surveillance Doppler radar, multiple communication links (line-of-sight and satellite), and passive and active EW capabilities. The arrays are mounted on a 15° tilt-back overlooking the Chesapeake Bay, emulating a shipboard installation. Currently, the AMRFC testbed site is being enlarged and modified to accommodate additional equipment in support of the Integrated Topside (InTop) program. The InTop program, sponsored by ONR, has a similar set of goals as AMRFC, but is broader in scope, covering RF functions across the spectrum from HF through Ka band.

The division also has access to other radar systems: the Microwave Microscope (MWM); the Navy's relocatable over-the-horizon radar (AN/TPS-71); and an experimental Cooperative Aircraft Identification system. The internally developed MWM has a high-resolution (2 cm) ultrawideband capability that is used to investigate backscatter from surface and volumetric clutter, has through-wall detection capability, and characterizes the impulse responses of scattering objects. The division provides direct technical support for AN/TPS-71 and has direct access to data. The Cooperative Aircraft Identification system is used to explore system concepts and engineering developments in connection with target identification.



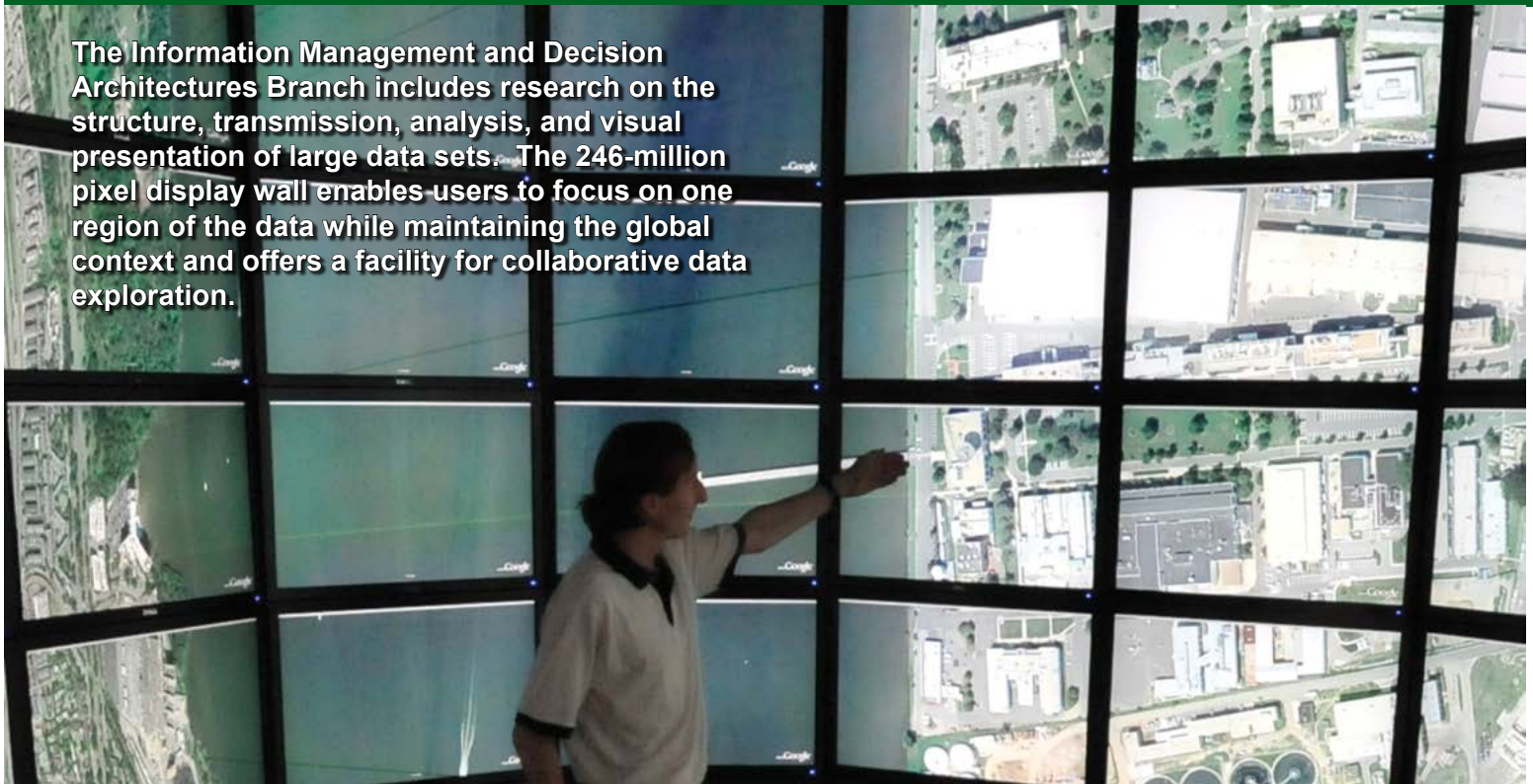
Compact Range Facility.



Radar antennas in front of and on the roof of the Radar Test Facility.

Information Technology

The Information Management and Decision Architectures Branch includes research on the structure, transmission, analysis, and visual presentation of large data sets. The 246-million pixel display wall enables users to focus on one region of the data while maintaining the global context and offers a facility for collaborative data exploration.



NRL's Information Technology Division (ITD) conducts basic research, exploratory development, and advanced technology demonstrations in the collection, transmission, processing, dissemination, and presentation of information. ITD's research program spans the areas of artificial intelligence (AI), autonomous systems, high assurance systems, tactical and strategic computer networks, large data systems, modeling and simulation, virtual and augmented reality, visual analytics, human/computer interaction, communication systems, transmission technology, and high performance computing.

NRL's RF Communications Laboratory conducts research in satellite communications systems and modulation techniques, develops advanced systems for line-of-sight communications links, and conducts designs for the next generation of airborne relays. A Voice Communication Laboratory supports the development of tactical voice technology, a Mobile Network Modeling Laboratory supports modeling, emulation, development, and scenario-based performance evaluation of both tactical network and Mobile Ad Hoc Networking (MANET) capabilities, and a Dynamic

Spectrum Allocation/Cognitive Radio Technology Test Lab provides the capability to analyze, test, and develop dynamic, cognitive, networked tactical wireless communications capabilities that efficiently share and exploit the spectrum. A Freespace Laser Communications Laboratory supports the design and development of prototype technical solutions for Naval laser communications requirements.

The Center for Computational Science (CCS) hosts the High Performance Computing (HPC) and Communications efforts at NRL. CCS participates in the DoD HPC Affiliated Research Center (ARC) program providing supercomputer research access to NRL and DoD customers. For high-performance networking, the Center runs the Advanced Technology Demonstration Network (ATDnet) in the Washington, D.C., metro area that provides dark fiber access to research partners. Other research supports high-speed connections (10s to 100s of Gbps) of supercomputer assets to NRL's corporate IT network as well as the global Defense Research and Engineering Network (DREN). Current efforts range from mapping traditional large shared memory (SHMEM) problems onto scalar computing systems to emerging cloud architectures to extremely large storage (petabytes and beyond).

The Cryptographic Technology Laboratory supports the development of certifiable Communications

Security (COMSEC) and Information Assurance (IA) products, including programmable cryptographic devices, cryptographic applications, and high assurance cross-domain solutions. The Naval Key Management Laboratory investigates electronic key management and networked key distribution technologies for the Navy and DoD. The Cyber Defense Development Laboratory provides direct support to the Fleet in the areas of computer network defense and visualization, cross-domain solutions, and reverse code analysis.

The Autonomous Systems and Robotics Laboratory provides the ability to develop and evaluate intelligent software and interfaces for autonomous vehicles. The Immersive Simulation Laboratory utilizes a collection of commercial off-the-shelf and specially developed components to support R&D in interfaces for virtual simulators, ranging from fully immersive to desktop simulations. The AI Center's Audio Laboratory combines a state-of-the-art 3D sound environment and multitask test bed for basic and applied human performance studies and Navy information display

research. The Warfighter Human System Integration Laboratory maintains a range of virtual environment interface technologies as well as wearable, Wi-Fi physiological monitors and associated real-time processing algorithms for use in adaptive operational and training support technologies. The core of the new Visual Analytics Laboratory is a display wall composed of LCD tiles, which enable teams of analysts to explore massive, diverse streams of data, supporting research into the science of analytical reasoning facilitated by visual interfaces. The Service Oriented Architecture Laboratory is used to investigate, prototype, and evaluate flexible, loosely coupled Web services that can be rapidly combined to meet dynamically changing warfighter needs. The Behavioral Detection Laboratory supports the development of algorithms, processes, and sensor suites associated with behavioral indicators of deception.



Scientist using the Dynamic Spectrum Allocation/Cognitive Radio Technology Test Lab facility to prepare a WNaN radio network for RF Spectrum Sharing field testing.



Technicians and scientists in the Mobile Network Modeling Laboratory (top) prepare and run a scenario-based, tactical network emulation using the NRL-developed EMANE system (bottom).

Optical Sciences

The Advanced Optical Materials Fabrication Laboratory, a state-of-the-art high vacuum cluster system, consists of a series of interconnected chambers allowing vacuum deposition of complex, multilayer films to be deposited and patterned without breaking vacuum during processing.



The Optical Sciences Division has a broad program of basic and applied research in optics and electro-optics. Areas of concentration include fiber optics and fiber-optic sensing, materials and sensors for the visible and infrared (IR) spectral regions, integrated optical devices, signal processing, optical information processing, panchromatic and hyperspectral imaging for surveillance and reconnaissance, and laser development.

The division occupies some of the most modern optical facilities in the country. The newest facility in Optical Sciences is the Advanced Optical Materials Fabrication Laboratory, a state-of-the-art cluster system for vacuum deposition of thin films. The facility consists of a series of interconnected high vacuum chambers, allowing complex, multilayer films to be

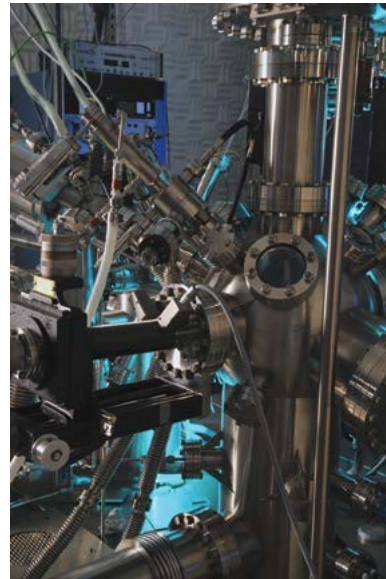
deposited without breaking vacuum during processing. The system includes a glove box, sample distribution robot, sputtering chambers for chalcogenide materials and oxides, evaporators for metals and dielectrics, and a mask changing module to enable layers to be patterned in situ while eliminating interface effects that result from exposure to air. Three other recently added facilities include the Optical Fiber Preform Fabrication Facility for making doped and undoped, multimode, single-mode, multicore, and photonic crystal glass preforms at temperatures as high as 2300 °C; the Surface Characterization Facility for ultraviolet and X-ray photoemission spectroscopy, atomic force and scanning tunneling microscopy (STM), and STM-induced light emission measurements; and the molecular beam epitaxial growth system dedicated to infrared lasers and detectors based on GaSb/InAs/AlSb quantum well and superlattice structures. In addition, an extensive set of laboratories

exists to develop and test new laser and nonlinear frequency conversion concepts and to evaluate non-destructive test and evaluation techniques. Fiber-optic sensor testing stations include acoustic test cells and a three-axis magnetic sensor test cell. There is also an Ultralow-loss Infrared Fiber-Optic Waveguide Facility using high-temperature IR glass technology. The facilities for ceramic optical materials include powder preparation, vacuum presses, and a 50-ton hot press for sintering. The Focal Plane Array Evaluation Facility

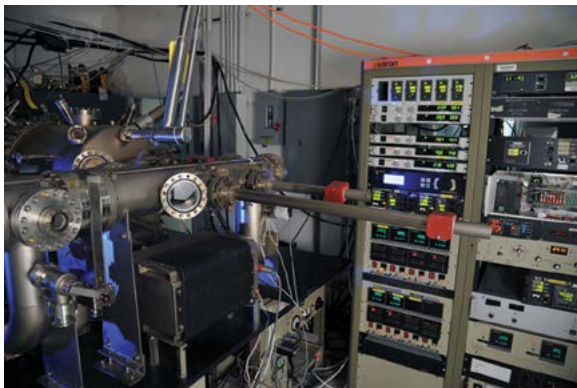
allows measurement of the optical and electrical characteristics of infrared focal plane arrays being developed for advanced Navy sensors. The IR Missile-Seeker Evaluation Facility performs open-loop measurements of the susceptibilities of IR tracking sensors to optical countermeasures. An ultra-high-vacuum multichamber deposition apparatus is used for fabrication of electro-optical devices and can be interlocked with the Surface Characterization Facility.



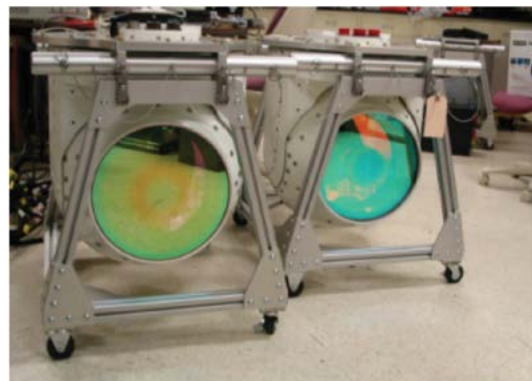
The Optical Fiber Preform Fabrication Facility includes computer control of the glass composition and standard fiber-optic dopants as well as rare earths, aluminum, and other components for specialty fibers.



The Optical Sciences Surface Characterization Facility includes instrumentation for ultraviolet and X-ray photo-emission spectroscopy (UPS and XPS), atomic force and scanning tunneling microscopy (AFM and STM), and STM-induced light emission (STM-LE) measurements.



Molecular beam epitaxy (MBE) system dedicated to quantum confined GaSb/InAs/AlSb structures for midwave infrared laser development.



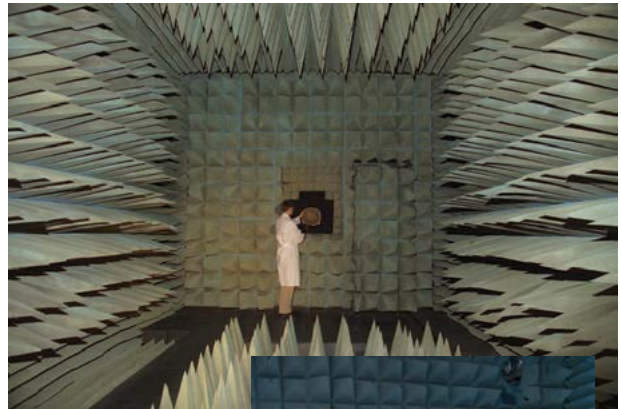
MX-20SW hyperspectral sensors.

Tactical Electronic Warfare

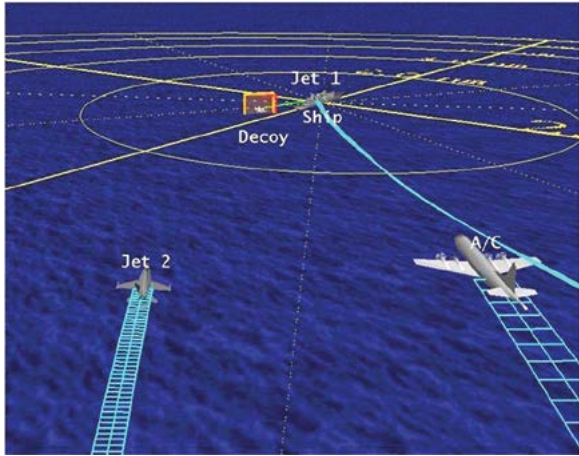


Learjet with simulators during RIMPAC exercises.

The Tactical Electronic Warfare (TEW) Division's program for electronic warfare (EW) research and development covers the entire electromagnetic spectrum. The program includes technology research and advanced developments and their applicability to producing EW products for the Fleet. The range of ongoing activities includes components, techniques, and subsystems development as well as system conceptualization, design, and EW effectiveness evaluation. The focus on the research activities extends across the entire breadth of the battlespace. These activities emphasize providing the methods and means to detect and counter enemy hostile actions via threat neutralization—from the beginning, when enemy forces are being mobilized for an attack, through to the final stages of the engagement. In conducting this program, the TEW Division employs an extensive array of special research and development laboratories, anechoic chambers, and modern computer systems used for modeling and simulation. Dedicated field sites and airborne platforms allow for the conduct of field experiments and operational trials. This combination of scientists, engineers, and specialized facilities also supports the innovative use of all Fleet defensive and offensive EW assets currently available to operational forces.



Radio Frequency Countermeasures anechoic chamber for EW testing.



TEWD develops and implements advanced visualization tools to support EW systems development and analysis.



The Central Target Simulation Facility is a high-performance, hardware-in-the-loop simulator for real-time closed-loop testing and evaluation of electronic warfare systems and techniques to counter the antiship missile threats.



EATES — Electronic Attack Technique Evaluation System, a stand-alone portable EA testing system.



Deployed EW subsystem to improve emitter detection and classification based on conceptualization and development performed in TEWD.

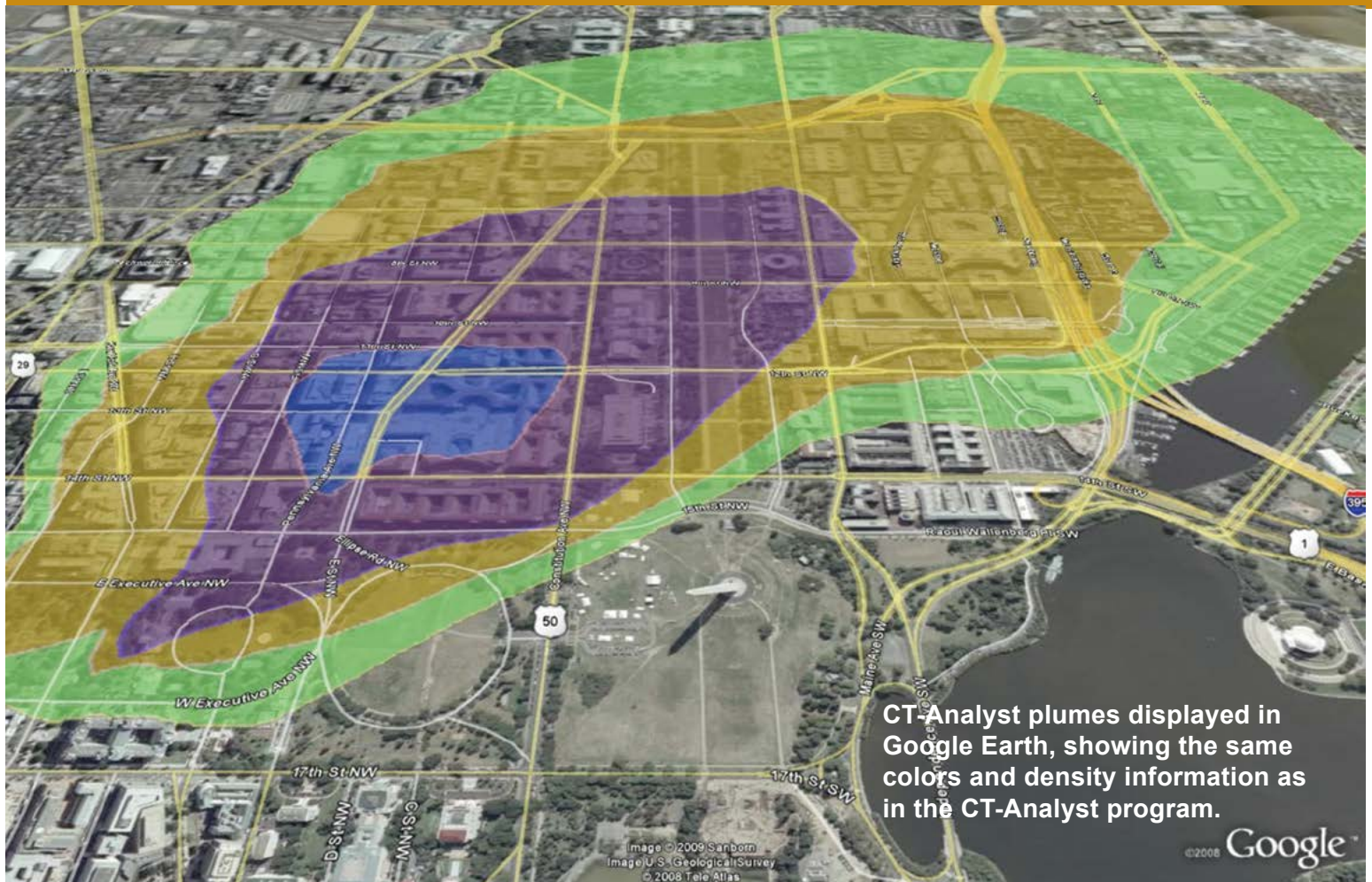


XFC (Experimental Fuel Cell) UAV — tube launch sequence.



XFC prototype in flight under fuel cell power.

Laboratories for Computational Physics and Fluid Dynamics



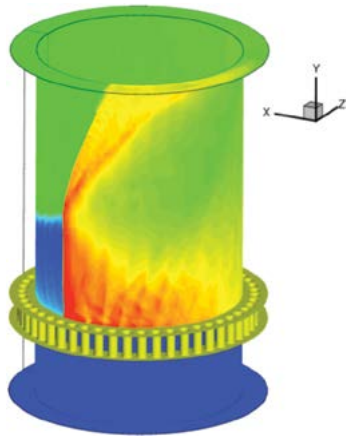
The Laboratories for Computational Physics and Fluid Dynamics (LCP&FD) is staffed by physicists, engineers, and computer scientists who develop software and use high-performance computers to solve priority problems for the Navy, the DoD, and the nation when existing capabilities and available commercial software prove inadequate to the application. For example, the LCP&FD developed the CT-Analyst crisis management software (figure above) so that first responders can have instant predictions of an airborne contaminant spread in an urban environment.

The LCP&FD maintains a very powerful collection of computer systems applied to a broad collection of work. There are currently 256 shared memory Itanium processors, 2948 clustered x86_64 cores, and their associated support systems. In addition there are over

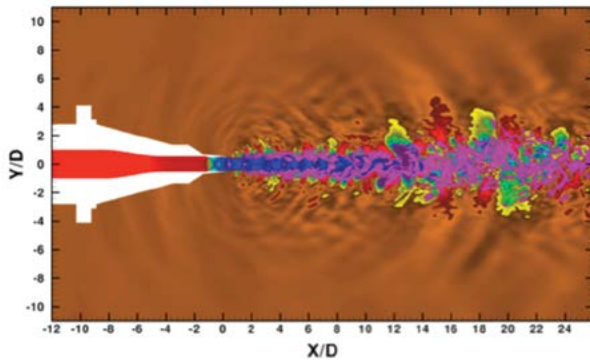
40 Apple workstations in the group, most of which are capable of large calculations both independently and in parallel ad hoc clusters.

There are four 64-bit x86 multi-core distributed memory clusters, each well coupled with Infiniband high-speed switched interconnect. The GPU cluster is comprised of 88 NVIDIA Fermi GPUs tightly coupled to 35 x86_64 multi-core processor nodes.

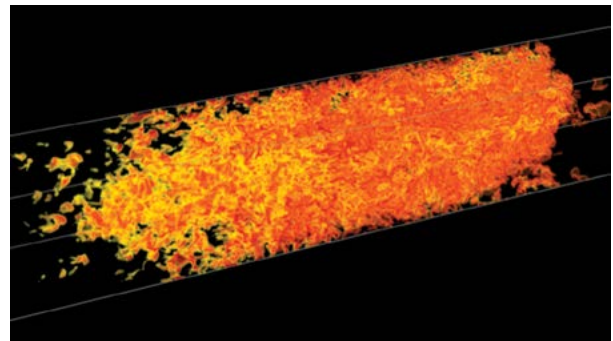
All systems share 200 terabytes of storage for use during a simulation and at least one gigabyte of memory per processor core. All unclassified systems share a common disk space for home directories as well as 2.8 terabytes of AFS space that can be used from any AFS-capable system throughout the allowed Internet.



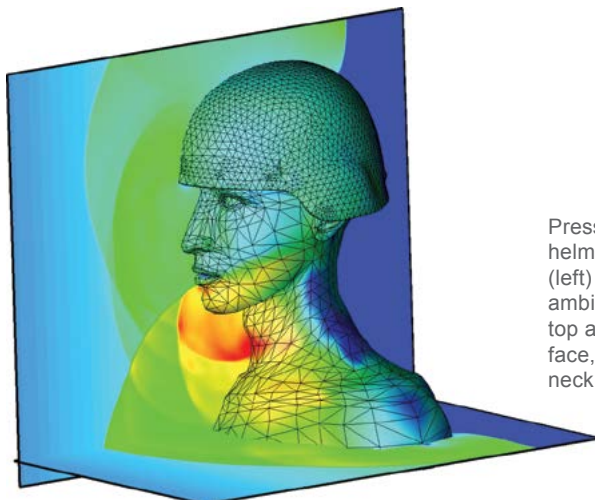
The computed flow field inside a rotating detonation engine with mixture plenum (bottom), injector plate and injectors (center), and combustion chamber (top). This new class of engines has been investigated computationally and been shown to have the potential to reduce fuel consumption by 25% while providing the same performance as current gas-turbine engines.



The computed exhaust from a supersonic jet aircraft showing the density fluctuations and near-field acoustic waves (noise). Computations are being used to develop and assess various means of reducing the exhaust jet noise during take-off and landing on aircraft carriers.



Accelerating unconfined turbulent flame in a methane-air mixture shortly before a spontaneous transition to a detonation. Shown is the volume rendering of the reaction rate in a fully resolved numerical simulation of the flame interaction with the driven, homogeneous, isotropic and high-speed turbulence.



Pressure contours resulting from blast interaction with a helmeted head. The shock wave approaches from the front (left) and envelops the geometry; the boundary between ambient (dark blue) and post-shock (green) air is seen at the top and bottom right. Interacting shock reflections from the face, helmet, and torso generate high pressures (red) on the neck below the chin.

Chemistry



The Chemistry Division's new NanoIR combines an atomic force microscope for topographic imaging with infrared chemical analysis and mapping with submicron spatial resolution.

NRL has been a major center for chemical research in support of naval operational requirements since the late 1920s. The Chemistry Division continues this tradition. The Chemistry Division conducts basic research, applied research, and development studies in the broad fields of diagnostics, dynamics, synthesis, materials, surface/interfaces, environment, corrosion, combustion, and fuels. Specialized programs currently within these fields include the synthesis and characterization of organic and inorganic materials, coatings, composites, nondestructive evaluation, surface/interface modification and characterization, nanometer structure science/technology, chemical vapor processing, tribology, solution and electrochemistry, mechanisms and kinetics of chemical processes, analytical chemistry, theoretical chemistry, decoy materials, radar-absorbing materials/radar-absorbing structures (RAM/RAS) technology, chemical/biological warfare defense, atmosphere analysis and control,

environmental remediation and protection, corrosion science and engineering, marine coatings, personnel protection, and safety and survivability. The Division has several research facilities.

Chemical analysis facilities include a wide range of modern photonic, phononic, magnetic, electronic, and ionic-based spectroscopic/microscopic techniques for bulk and surface analysis.

The Magnetic Resonance Facility includes advanced high-resolution solid-state nuclear magnetic resonance (NMR) spectroscopy techniques to observe nuclei across much of the periodic table and provides detailed structural and dynamical information.

The Nanometer Characterization/Manipulation Facility includes fabrication and characterization capability based on scanning tunneling microscopy/spectroscopy, atomic force microscopy, and related techniques.

The Materials Synthesis/Property Measurement Facility has special emphasis on polymers, surface-film processing, and directed self-assembly.

The Chemical Vapor and Plasma Deposition Facility is designed to study and fabricate materials such as diamond using in situ diagnostics, laser machining, and plasma deposition reactors.

The Navy Fuel Research Facility performs basic and applied research to understand the underlying chemistry that impacts the use, handling, and storage of current and future Navy mobility fuels.

Fire research facilities include a 11,400 ft³ fire research chamber (Fire I) and the 457 ft ex-USS *Shadwell* (LSD 15) advanced fire research ship. Commensurate support has been devoted to survivability of the new classes of ships, DDX, LPD 17, LCS, CVNX, and LHA(R).

The Marine Corrosion and Coatings Facility located on Fleming Key at Key West, Florida, offers a “blue” ocean environment and unpolluted, flowing seawater for studies of environmental effects on materials. Equipment is available for experiments involving accelerated corrosion and weathering, general corrosion, long-term immersion and alternate immersion, fouling, electrochemical phenomena, coatings applica-

tion and characterization, cathodic protection design, ballast water treatment, marine biology, and corrosion monitoring.

The Chemistry Division has focused on force protection/homeland defense (FP/HD) since September 11, 2001, especially on the development of improved detection techniques for chemical, biological, and explosive threats. As part of a multidivisional program to develop new technology systems, the Chemistry Division is a major contributor to the NRL Institute for Nanoscience. Nanoscience complements FP/HD in that nanoscience is expected to provide dramatic improvements to chemical/biological detection, protection, and neutralization. Chemistry will approach the nanoscale from the bottom up — building smaller atoms and molecules into nanostructures with new properties and developing the directed assembly of nanostructures into hierarchical systems. The NRL Nanoscience building is linked directly into the Chemistry building to provide controlled access and auxiliary space for work not requiring a “low noise” environment.



DNA Sequencer: High-throughput sequencer providing over >35 million bases per run with sequence reads averaging 450 bases in length.

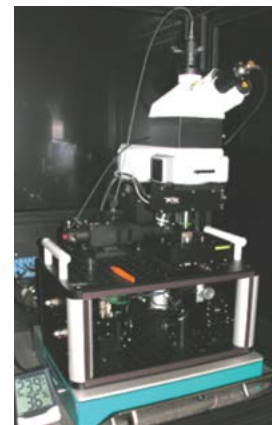


The Division's new Glow Discharge – Optical Emission Spectrometer performs high precision elemental analyses and correlates these elemental analyses with depth profiles.



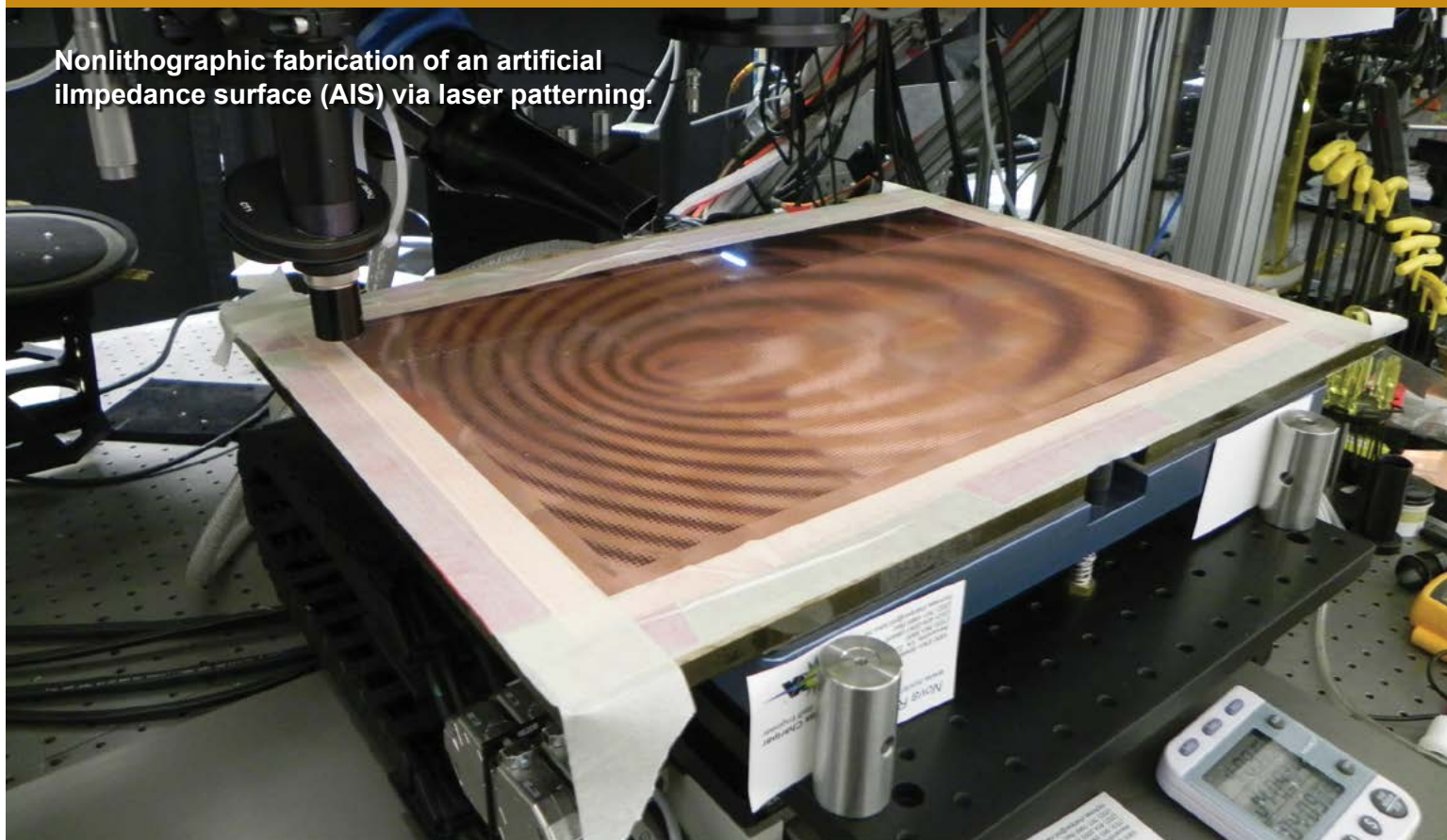
Genetic Analyzer: The Genetic Analyzer allows for presequencing sample screening and low cost fragment analysis by Length Heterogeneity-Polymerase Chain Reaction.

The Division's new near-field scanning optical microscope is capable of 1) diffraction-limited Raman and fluorescence spectroscopy, 2) correlated optical and structural images using atomic force microscopy, 3) sub-diffraction limit resolution (~100 nm resolution), and 4) 3D scanning.



Materials Science and Technology

Nonlithographic fabrication of an artificial impedance surface (AIS) via laser patterning.



The Materials Science and Technology Division at NRL provides expertise and facilities to foster materials innovation.

The Division houses many specialized and unique facilities for carrying out basic and applied materials synthesis and characterization research.

The Magnetolectronics Fabrication Facility consists of a Class 1000 clean room equipped with tools for lithographic construction of magnetolectronic and spintronic devices. It provides pattern definition, metallization, dielectric layer deposition, and both reactive and Ar⁺ ion etching of wafers and small pieces.

The Electrical, Magnetic, and Optical Measurement Facility contains several complementary instruments that allow for the magnetic, electrical, optical, and heat capacity characterization of materials and devices. The SQUID (superconducting quantum interference device) uses magnetometry and vibrating sample magnetometry to determine important properties of superconducting, paramagnetic, diamagnetic, and ferromagnetic materials. The transport properties of materials, namely the temperature- and magnetic-field-

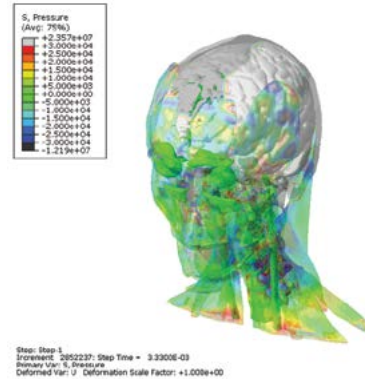
dependent resistivity combined with heat-capacity measurements, allow for a fundamental physical understanding of electronic properties.

The Materials Processing Facility includes apparatuses for powder production by fluid atomization, thermal evaporation, and arc erosion, and a physical vapor deposition system designed to produce and coat submicron powders in situ. Facilities to process powder into bulk specimens by hot and cold isostatic pressing permit a variety of consolidation possibilities. The isothermal heat treatment facility and quenching dilatometer permit alloy synthesis and single crystal growth. Bulk alloys can be prepared by induction melting, while rapidly solidified metals of thin cross section can be made by splat quenching and melt spinning. Ceramic and ceramic-matrix composites processing facilities include a wide variety of conventional, controlled atmospheric furnaces, hot presses, a ball milling apparatus, particle size determination capability, and sol-gel and organometallic coating processing capabilities.

The Mechanical Characterization Facility consists of various testing systems, many with automated computer control and data acquisition, for determining the mechanical response of materials under controlled



Electron backscatter diffraction inverse pole figure map shows the grain orientations of the ferrite and austenite phases in a duplex stainless steel 2205 alloy.



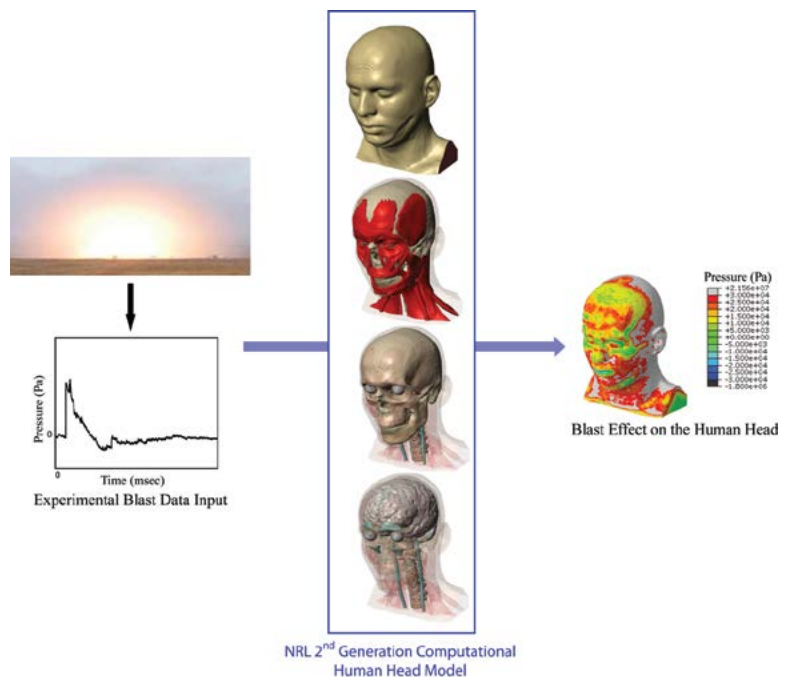
Head dynamic response to front blast pressure wave; translucent image of pressure levels in the head.

loading/deformation and environmental conditions. Basic capabilities include quasistatic tensile and fracture testing, dynamic storage and loss moduli as a function of frequency and temperature, cyclic fatigue crack growth and corrosion fatigue testing, and stress-corrosion cracking testing.

The Thin-Film Materials Synthesis and Processing Facility provides users a wide variety of techniques for growth and processing of thin films (thickness 1 μm or less). Sputter deposition offers a versatile method of depositing metallic and dielectric films and is a primary tool of this facility. Thermal evaporation of metals is implemented in both high-vacuum and ultra-high-vacuum systems. Pulsed laser deposition (PLD) with variable stage temperature and controlled atmosphere allows growth of oxides. Electrolytic deposition offers efficient growth of gold and silver films. Laser direct-write ablation and deposition processes provide unique methods for imposing CAD-defined features via ablation of a substrate film and ablative mass transfer to a substrate.

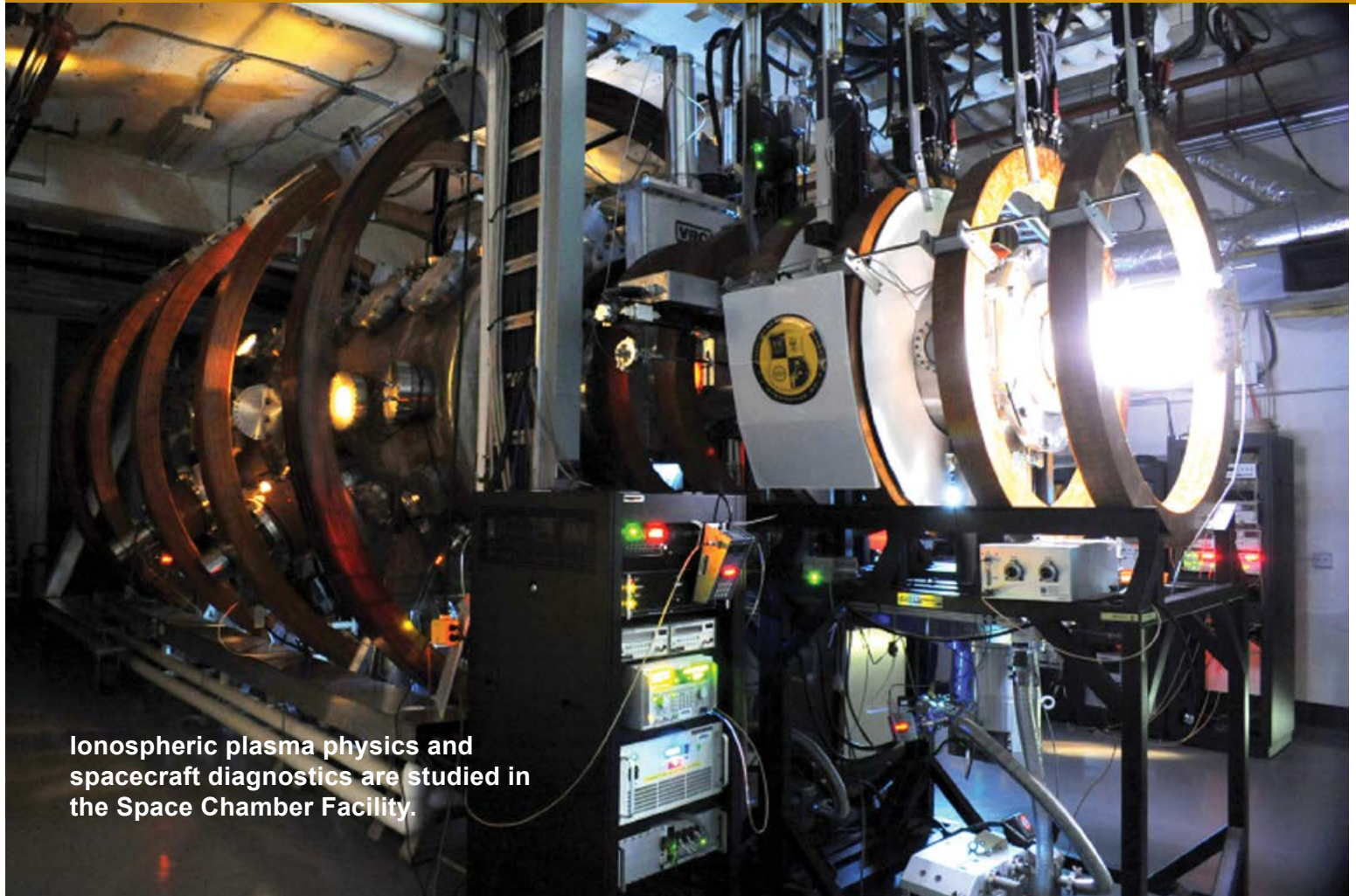
The Micro/Nanostructure Characterization Facility is capable of performing transmission electron microscopy (TEM), scanning transmission electron microscopy (STEM), atomic resolution transmission electron microscopy (ARTEM), electron energy loss spectroscopy (EELS), Z-contrast imaging, and spectral imaging through the use of a JEOL 2010F transmission electron microscope, an FEI Tecnai G² 30 analytical transmission electron

microscope, and a JEOL JSM-7001F Variable Pressure scanning electron microscope with secondary and backscattered electron imaging capabilities, as well as energy dispersive spectrometry (EDS) and electron backscatter diffraction (EBSD). In addition, this field-emission microscope operates in low-vacuum mode, which allows for high-resolution imaging of nonconductive materials without coatings or any additional preparation. Other standard microstructure characterization instruments are also available.



High-fidelity modeling of the human head under blast loading.

Plasma Physics



Ionospheric plasma physics and spacecraft diagnostics are studied in the Space Chamber Facility.

The Plasma Physics Division conducts basic and applied research in space plasmas; inertial confinement fusion (ICF); ultra-short pulse laser interactions; directed energy; railguns; pulsed-power and intense particle beams; materials processing; advanced diagnostics; radiation-atomic physics; and nonlinear dynamics.

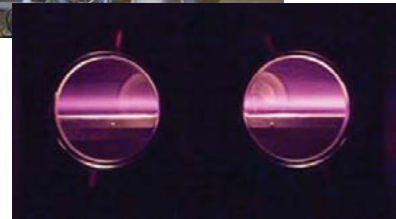
The Space Physics Simulation Chamber generates near-Earth plasma environments for studying space plasma phenomena and spacecraft diagnostic development and testing. Nike and Electra are major KrF laser facilities for ICF research, studying ICF target physics and developing repetitively pulsed KrF technologies, respectively. The Ultrashort-Pulse, High-Intensity Laser facility has both a 10 Hz (15 TW) and kilohertz (0.45 TW) Ti:Sapphire laser to investigate laser-driven

acceleration and nonlinear laser-plasma interactions. Directed energy research is performed in the High Energy Laser Lab, which has four multikilowatt fiber lasers to study laser propagation, incoherent beam combining, and power beaming. The Materials Testing Facility houses a 6-meter-long railgun used to study the materials issues of electromagnetic launch for the Navy and DoD's multimission railgun program. A new small caliber railgun will fire repetitively and expand our knowledge of materials, pulsed power, and energy storage. The Division has two large, high-voltage, pulsed-power devices, Gamble II and Mercury, which are used to produce intense electron and ion beams, flash X-ray sources, and high-density plasmas for application to nuclear weapons effects testing, radiography, and active detection of nuclear materials. The Division uses both microwaves and plasmas for materials processing applications. The microwave materials processing laboratory includes a 20 kW, CW, 83 GHz gyrotron.

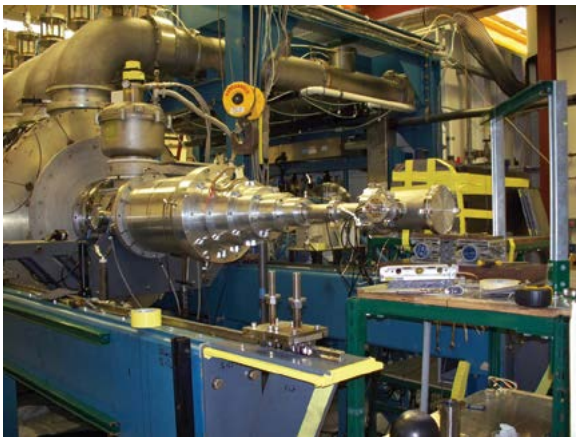
The Large Area Plasma Processing System (LAPPS) generates ultra low-temperature plasmas for studying the modification of energy sensitive materials such as polymers, graphene, and biologicals. Two atmospheric discharge systems are used to study plasma processing and synthesis, plasma biology, and plasma aerodynamics.



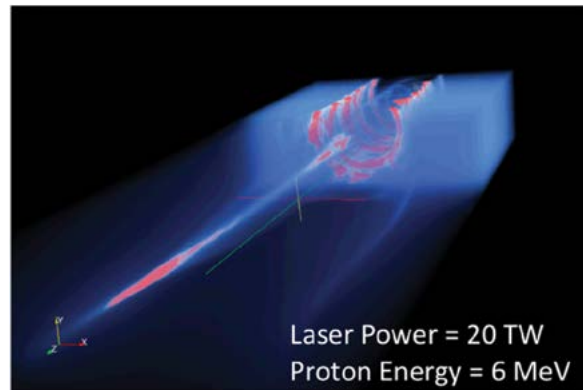
The Materials Testing Facility railgun studies the physics and material science of electromagnetic launch.



The Large Area Plasma Processing Source (LAPPS) is used to develop, characterize, and study plasma-based processing of energy sensitive materials.



Tapered front-end of Mercury accelerator (6 MV, 360 kA, 50 ns) for dual-axis down-hole radiography.



TURBOWAVE simulation proton acceleration from a hydrogen gas target driven by an ultrashort pulse laser.



Electron beam pump Electra repetitively pulsed (KrF) laser for inertial fusion energy, materials modification, and waste remediation, and biofuel production

Electronics Science and Technology



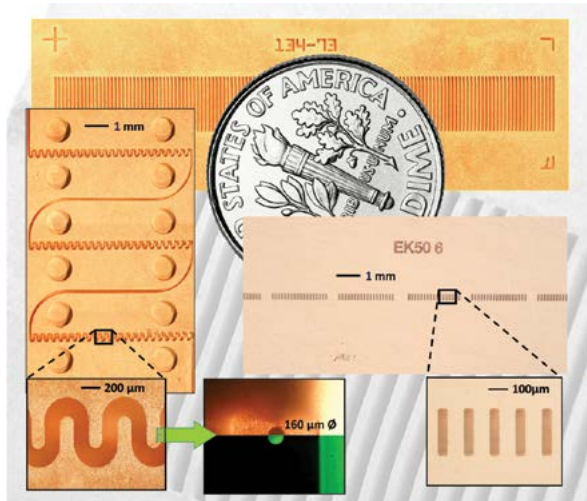
The Electronics Science and Technology Division's Advanced Silicon Carbide Epitaxial Research Laboratory (ASCERL).

The Electronics Science and Technology Division conducts a multi-disciplinary basic and applied research program in solid-state electronics; electronic materials including growth, theory, and characterization of semiconductors and heterostructures; surface and interface science; microwave and millimeter-wave components and techniques; microelectronic device research and fabrication; nanoelectronics science and technologies; vacuum electronics; power electronics; photovoltaics and optoelectronics; and process modeling and simulation.

The Division operates 13 major facilities: Ultrafast Laser Facility (ULF), Solar Cell Characterization Laboratory (SCCL), Compound Semiconductor Processing Facility (CSPF), Laboratory for Advanced Materials Synthesis (LAMS), Center for Advanced Materials Epitaxial Growth and Characterization (Epicenter), Ultra-Violet Photolithography Laboratory for Submillimeter-Wave Devices (UV-PL), Millimeter-Wave Vacuum Electronics Fabrication Facility (MWVEFF), Advanced Silicon Carbide Epi-

taxial Research Laboratory (ASCERL), Optoelectronic Scanning Electron Characterization Facility (OSECF), Infrared Materials and Detectors Characterization Laboratory (IR Characterization Lab), Atomic Layer Deposition System (ALD), Atomic Layer Epitaxy System, and High Pressure Multi-Anvil System (HP-MAS).

The CSPF processes compound semiconductor structures on a service basis, especially if advanced fabrication equipment such as electron beam lithography for reactive ion etching is required. But most fabrication can be hands-on by NRL scientists to assure personal process control and history. The LAMS uses metallorganic chemical vapor deposition to synthesize a wide range of thin films, particularly wide bandgap semiconductors such as gallium nitride (GaN) and related alloys. The Epicenter (a joint activity of the Electronics Science and Technology, Materials Science and Technology, Optical Sciences, and Chemistry Divisions) is dedicated to the growth of multilayer nanostructures by molecular beam epitaxy (MBE). Current research involves the growth and etching of conventional III-V semiconductors, ferromagnetic semiconductor materials, 6.1 Å III-V semiconductors, and II-VI semiconductors. The structures grown in this facility are analyzed via in situ scanning tunneling microscopy and angle-resolved electron microscopy. The ASCERL is the focal point of NRL



Microfabricated circuits for vacuum electronic amplifiers made using UV-LIGA (ultraviolet lithography, electroplating, and molding). NRL's UV Photolithography Laboratory for Submillimeter-Wave Devices has developed unique techniques to create free-standing, all-copper structures with height-to-width aspect ratios up to 10:1. Clockwise from the top: 220 GHz grating structure designed for a sheet-beam traveling-wave amplifier; 670 GHz multicavity extended interaction klystron; 160 μm diameter beam tunnel fabricated using an NRL-proprietary monofilament technique; and 220 GHz serpentine waveguide circuits designed to generate >50 W with 15 GHz bandwidth.

The NRL sheet electron beam device developed for a 10 kW W-band (94 GHz) amplifier. A thin sheet beam (0.3 mm x 4 mm) is generated by a unique electron gun (20 kV, 3.5 A, inset right) and is focused by an 8 kG uniform magnetic field supplied by the permanent magnet structure that comprises the lower 2/3 of the main photo. A sheet beam can carry much higher current than a conventional cylindrical beam of the same voltage, so this W-band amplifier can produce 5 to 10 times the power of comparable state-of-the-art amplifiers. NRL's award-winning computer code, MICHELLE, was instrumental in designing the electron optics (inset upper left). Over 98% of the electron current emitted from the gun is transported through the beam tunnel, in excellent agreement with MICHELLE simulations.



efforts to develop thin-film heterostructure materials needed for high-voltage, high-power silicon carbide (SiC) power electronic components in future naval systems. ASCERL uses an EPIGRESS reactor capable of growing thick, low-defect, ultra-high-purity SiC epitaxial layers. The SCCL studies new and emerging solar cell technologies for tactical applications including terrestrial and space environments. The ULF is optimized for the characterization of photophysical and photochemical processes on a timescale of tens of femtoseconds. It includes a synchronously pumped dye laser system for simulating the effects of charge deposited in semiconductors characteristic of space radiation. The UV-PL and MWVEFF are key laboratories for developing precision, all-metal structures for electron optics, electron beam-wave interaction (e.g.,

amplifiers and oscillators), and passive electromagnetic devices. The UV-PL uses lithographic techniques and chemical electroforming to create high height-to-width aspect ratio structures (up to 10:1) with feature sizes as small as 5 μm. These dimensions are compatible with devices that can produce coherent electromagnetic radiation at submillimeter wavelengths. The MWVEFF contains a computer numerically controlled (CNC) milling machine and a CNC precision lathe capable of fabricating intricate millimeter-wave vacuum electronic components and a wire electric discharge machining (EDM) tool for fabrication of millimeter-wave and submillimeter-wave components that cannot be fabricated by conventional rotary cutting tools. EDM offers a noncontact process for both hard and soft metals as well as SiC and doped silicon.

Center for Bio/Molecular Science and Engineering



Bio-inspired underwater vehicle developed using fish fins as a model.

The Center for Bio/Molecular Science and Engineering conducts cross-disciplinary, bio-inspired research and development to address problems relevant to the Navy and the DoD by exploiting biology's well-known ability for developing effective materials and sensing systems. The primary goal is to translate cutting-edge, bio-based discoveries into useful materials, sensors, and prototypes that can be scaled up, are robust, and lead to enhanced capabilities in the field. The challenges include identifying biological approaches with the greatest potential to solve Navy problems and provide new capabilities while focusing on bio-inspired solutions to problems that have not otherwise been solved by conventional means.

Studies involve biomaterial development for chemical/biological warfare defense, structural and functional applications, and environmental quality/cleanup. Program areas include optical biosensors, nanoscale manipulations, genomics and proteomics, bio/molecular and cellular arrays, surface modification,

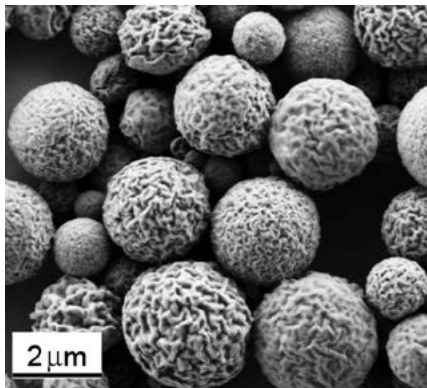
energy harvesting, systems biology, viral particles as scaffolds, and bioorganic materials from self-assembly.

The staff of the Center is an interdisciplinary team with expertise in biochemistry, surface chemistry, biophysics, molecular and cell biology, organic synthesis, materials science, and engineering. The Center also collaborates throughout NRL and with other government laboratories, universities, and industry.

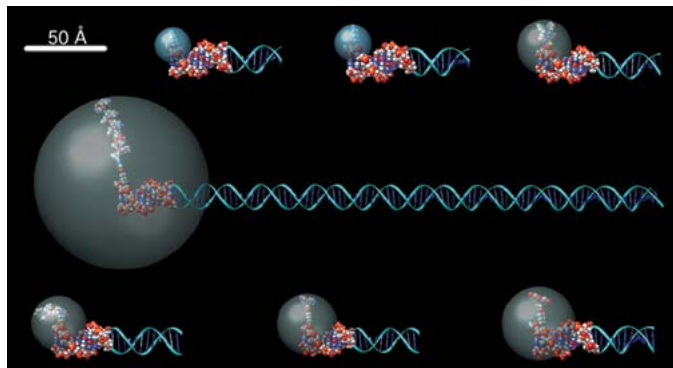
The Center's modern facilities include laboratories for research in chemistry, biochemistry, systems biology, and physics. Specialized areas include controlled-access laboratories for cell culture and molecular biology, an electron microscope facility, a scanning probe microscope laboratory, instrument rooms with access to a variety of spectrophotometers, a multichannel surface plasmon resonance (SPR) sensor, and an optical microscope facility including polarization, fluorescence, and confocal microscopes. Additional laboratories accommodate nuclear magnetic resonance (NMR) spectroscopy, liquid chromatography-mass spectrometry (LCMS), and fabrication of microfluidic and micro-optical systems in polymers. The Center maintains a state-of-the-art X-ray diffraction system including a MicroSTAR-H X-ray generator. In com-

bination with new detectors and components, the system is ideal for data collection on proteins or very small single crystals of organic compounds and is also capable of collecting data on films and powders. Additional core facilities have recently been established for

fluorescence activated cell sorting (FACS), microarray analysis, next generation sequencing, circular dichroism (CD) spectroscopy, and 3D printing and rapid prototyping.



Organic nanoparticles with textured morphology to incorporate multifunctionality.



Model of the fluorescent dye CY5 coupled to the 5' end of DNA. The first 10 base pairs are represented by a space-filling (i.e., CPK) model and the rest is a ribbon. The translucent sphere shows the area accessible to the fluorescent dye.



Seabed energy harvesting devices to power underwater Navy sensors.



Moored and autonomous underwater vehicle (AUV) deployment of immunosensor systems.

Acoustics

NRL's "Reliant" unmanned undersea vehicle with towed acoustic array being deployed during a long range active acoustics experiment.



The Acoustics Division's research program spans the domains of quantum and classical physics. It addresses spatial scales from nanometers to hundreds of kilometers and temporal scales from less than microseconds to the seasonal and long-term variability of the oceans. The Division's research topics include:

- 1) The study of the impact of riverine, ocean, and atmospheric fluid dynamics on the phase coherent properties of acoustic signals with the objective of predicting the performance variability of tactical and strategic naval acoustic systems including autonomous unmanned underwater systems and their underwater acoustic communications networks;
- 2) The continued development, expansion, and adaptation of linear and nonlinear full physics underwater acoustic propagation and scattering theories.

The use of numerical simulations to estimate the uncertainty in the calculated acoustic fields that is caused by limited spatial and temporal sampling of the initialization and updating sound speed fields;

- 3) The measurement and theoretical description of the spatial/temporal variability of the deterministic/statistical properties of acoustic signals scattered from marine organisms, the near-surface ocean volume, the air-sea interface and the sea bottom/subbottom with the objective of reducing the impact of non-target acoustic signal clutter on naval mine countermeasures and antisubmarine warfare system performance;
- 4) The prediction and measurement of the angle and frequency dependence of acoustic signals scattered and radiated by complex three-dimensional structures with application to advanced manned and unmanned mine countermeasures and antisubmarine warfare detection concepts;
- 5) The design from first principles of microelectromechanical and nanotechnology-based structures

(e.g., metamaterials and sensors) that have unique sound transmission, reflection, and transduction properties.

The experimental and computational components of the Division's research program require the utilization of high-performance computers, the Naval Research Laboratory Institute for Nanoscience experimental facilities, the University-National Oceanographic Laboratory System's ships and measurement systems, and the design and use of state-of-the-art laboratory, underwater, and atmospheric research instrumentation.

At-Sea Research: The Division uses autonomous unmanned vehicles, fixed autonomous moorings, and measurement systems attached to ships.

Undersea acoustic propagation and ambient noise measurements are made with a fully autonomous acoustic data acquisition suite composed of two 80 m, 32-channel vertical hydrophone arrays, two 600 m, 96-channel horizontal hydrophone arrays, and two 50% duty cycle programmable acoustic sources operating at center frequencies of 300 and 500 Hz. Data (synced with atomic clocks) are acquired by two 32-channel and one 96-channel recording systems that continuously acquire 24-bit data (5 kHz sample rate) for a minimum of 30 days.

Ship-attached instruments are used to investigate the four-dimensional properties of acoustic signals scattered from the ocean's surface, bottom, and volume. They include two flex-tensional XF-4 and one ITC 2077 sound sources; a towable, vertically directional source array operating in the 1.5 to 9.5 kHz frequency band and a 64-channel broadband (500 to 3500 Hz) time reversal source-receiver array.

A 53 cm diameter Bluefin autonomous underwater vehicle (AUV), which is instrumented with single crystal transducers, multielement receiving arrays for synthetic aperture data acquisition, a horizontal towed array, and an onboard data acquisition and processing system, is used to test autonomous unmanned mine countermeasures and antisubmarine warfare concepts.

Underwater acoustic communications network research defines future network capacity by simultaneously deploying eight moored Benthos modems, two Iver-2 58 in. expandable AUVs, and two 8-channel moored/towed remotely controlled acoustic communications data acquisition modems in a variety of protocol geometries.

Laboratory Facilities: The Acoustics Division has several nationally unique laboratory facilities.

The Laboratory for Structural Acoustics supports experimental research where acoustic radiation, scatter-

ing, and surface vibration measurements of fluid-loaded and non-fluid-loaded structures are performed. The 3.7 million liter in-ground pool facility (17 m dia. \times 15 m deep) has vibration and temperature control, anechoic interior walls, and automated three-dimensional scattering cross section measurement capabilities. Instrumentation includes compact range scattering, nearfield holography, and scanning laser Doppler vibrometry capabilities. Ultra-high-precision measurements are conducted in this pristine laboratory environment using submarine hull backing impedance simulators, torpedoes, scale-model submarine structures, and deactivated mine targets.

A structural acoustics in-air measurement facility supports experimental research where broadband acoustic radiation, reflection, transmission, and surface vibration measurements are required. Typically, ultra-high-precision, highly spatially sampled measurements are conducted on satellite payload fairings, active and passive material systems for sound control, and new transducer and sensor systems. The large, acoustically treated facility is 50 \times 40 ft and 38 ft high and is instrumented with robotic scanners capable of generating nearfield acoustic holography (NAH) radiation, reflection, and transmission databases.

Marine sediments are replicated in tanks to study the impact of sediment burial on the structural response of mines or improvised explosive devices.

A salt water tank (6 m \times 6 m \times 3.5 m) facility is designed to study a variety of physical phenomena under both saline and nonsaline conditions. These include air-sea interface and subsurface bubble acoustic signal absorption and scatter studies; characterization of sound generated by laser pulses; and the effectiveness of acoustic metamaterials. The tank has twelve 1.2 \times 2.4 m windows for optical access.

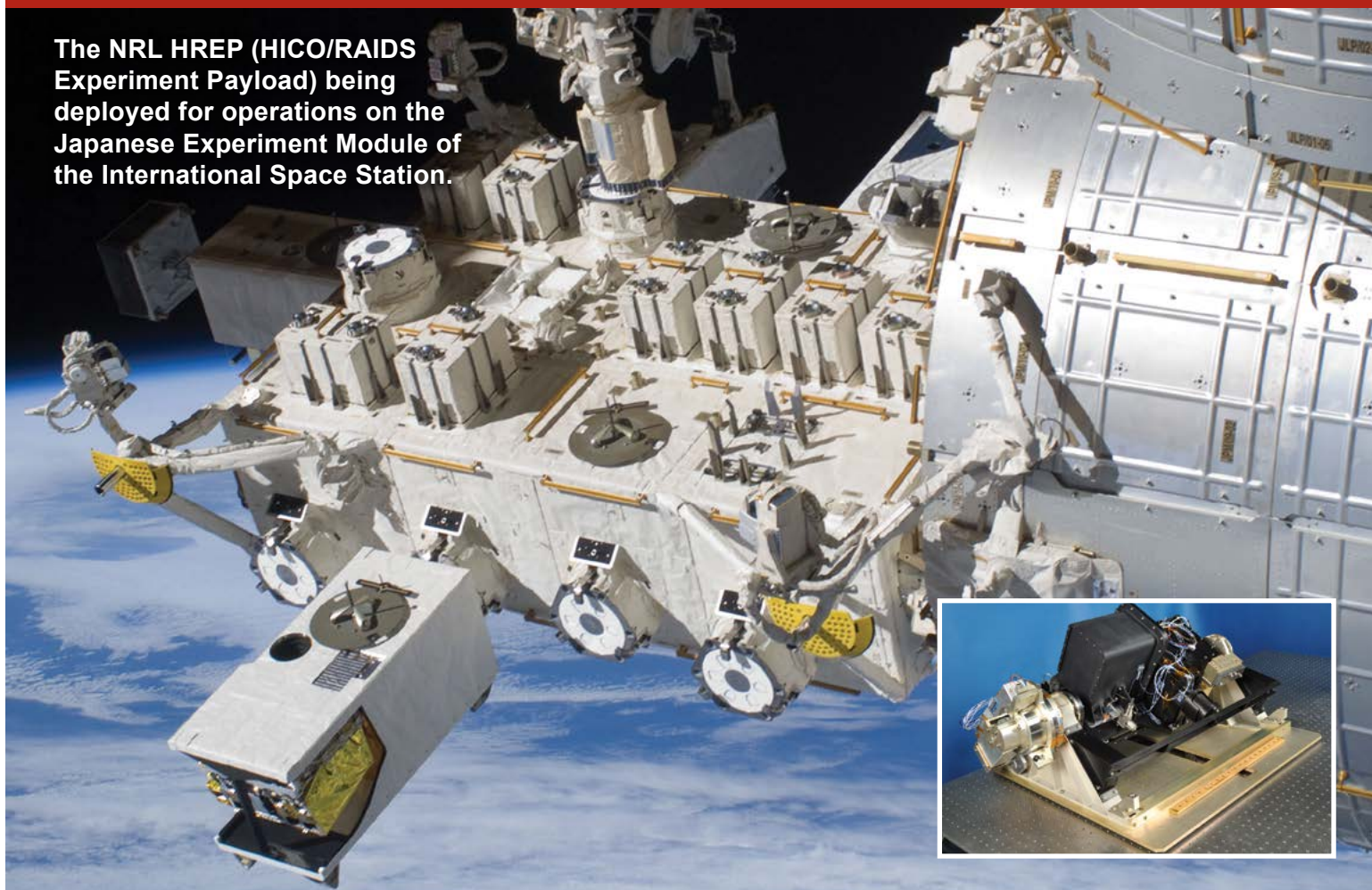
A sonomagnetic measurement facility is equipped with a vibration-insulating optical table constructed from nonmagnetic materials and a single three-axis magnetometer capable of measuring fields up to ± 100 μ T with a 1 nT noise floor at 1 kHz.

An ultrasonic measurements laboratory is used for small-scale acoustics experiments designed to measure the effectiveness of acoustic metamaterials. Two 1.2 m cubic water tanks are equipped with overhead X-Y-Z positioning systems and LabVIEW-based data acquisition systems.

A fabrication workshop equipped with a Haas Mini-Mill and an Objet Connex 500 3-D rapid prototyping machine support the laboratory research facilities.

Remote Sensing

The NRL HREP (HICO/RAIDS Experiment Payload) being deployed for operations on the Japanese Experiment Module of the International Space Station.



The Remote Sensing Division is the Navy's center of excellence for remote sensing research and development, conducting a broad program of basic and applied research across the full electromagnetic spectrum using active and passive techniques from ground-, air-, and space-based platforms. Current applications include Earth, ocean, atmospheric, astronomy, astrometry, and astrophysical science, and surveillance/reconnaissance activities including maritime domain awareness, antisubmarine warfare, and mine warfare. Special emphasis is given to developing space-based platforms and exploiting existing space systems.

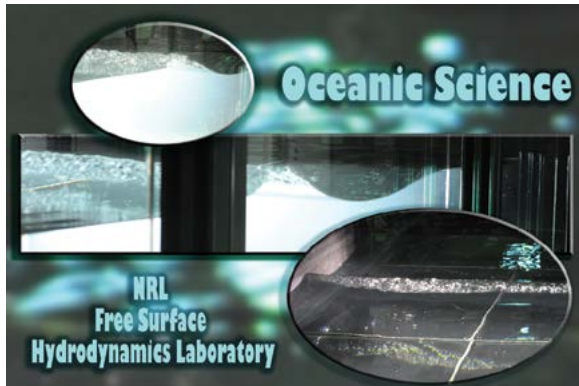
Research in ocean and Earth science includes maritime hyperspectral imaging, radar measurements of the ocean surface for the remote sensing of waves and currents, model- and laboratory-based hydrodynamics, and land-based trafficability studies.

Current airborne sensors used for characterization of the littoral environment include visible/near-IR and shortwave hyperspectral imagers, a broadband, visible polarimetric sensor, long- and midwave IR thermal cameras, and an X-band, 2-channel interferometric synthetic aperture radar. As an outgrowth of our airborne sensing program, the Division developed the Hyperspectral Imager for the Coastal Ocean (HICO), the world's first spaceborne hyperspectral sensor specifically designed for coastal maritime environmental observations. HICO was launched to the International Space Station in September 2009 and is currently providing scientific imagery of varied coastal types worldwide. Ground-based instruments for maritime sensing include the NRL Focused Phased Array Imaging Radar (NRL FOPAIR), an X-band, high-frame-rate polarimetric radar system. New research areas include the exploitation of polarized hyperspectral imaging, and active (lidar-based) sensing of the water column.

For radiometric and spectral calibration of the visible and IR imaging sensors, the Division operates a Calibration Facility that includes a NIST-traceable

integrating sphere and a set of gas emission standards for wavelength calibration.

The Division's Free Surface Hydrodynamics Laboratory (FSHL) supports ocean remote sensing research. The lab consists of a 10 m wave tank equipped with a computer-controlled wave generator and a compre-



Snapshots of breakers generated in the Free Surface Hydrodynamics Laboratory. At lower right, a wave traveling toward the viewer is seen breaking across the width (approx. 3 m) of the tank. In the upper images, waves traveling from left to right are breaking and forming surface turbulence.

hensive set of diagnostic tools. Recent work focuses on the physics of breaking waves, their infrared signature, and their role in producing aerosols. Experiments conducted in the FSHL are also used to test and validate numerical results and analytical theories dealing with the physics of the ocean's free surface.

Current atmospheric science research areas include the measurement of ocean surface winds and middle atmospheric research. NRL (in a collaboration between the Naval Center for Space Technology (NCST) and the Remote Sensing Division) also developed the first spaceborne polarimetric microwave radiometer, WindSat, launched in January 2003 and still operational. Its primary mission was to demonstrate the capability to remotely sense the ocean surface wind vector with a passive system. WindSat provides major risk reduction for development of the microwave imager for the next-generation DoD operational environmental satellite program. WindSat data are processed at the Navy Fleet Numerical Meteorology and Oceanography Center (FNMOC), and operationally assimilated into the Navy's global weather model, as well as that of several civilian weather agencies worldwide. In addition, the Remote Sensing Division is exploiting WindSat's unique data set for other environmental parameters such as sea surface temperature, soil moisture, and sea ice concentration.

The Water Vapor Millimeter-wave Spectrometer (WVMS) is a ground-based instrument designed to measure water vapor in the middle atmosphere. It is part of the international ground-based Network for Detection of Atmospheric Composition Change (NDACC), with sensors based in Lauder, New Zealand, Mauna Loa, Hawaii, and Table Mountain, California.

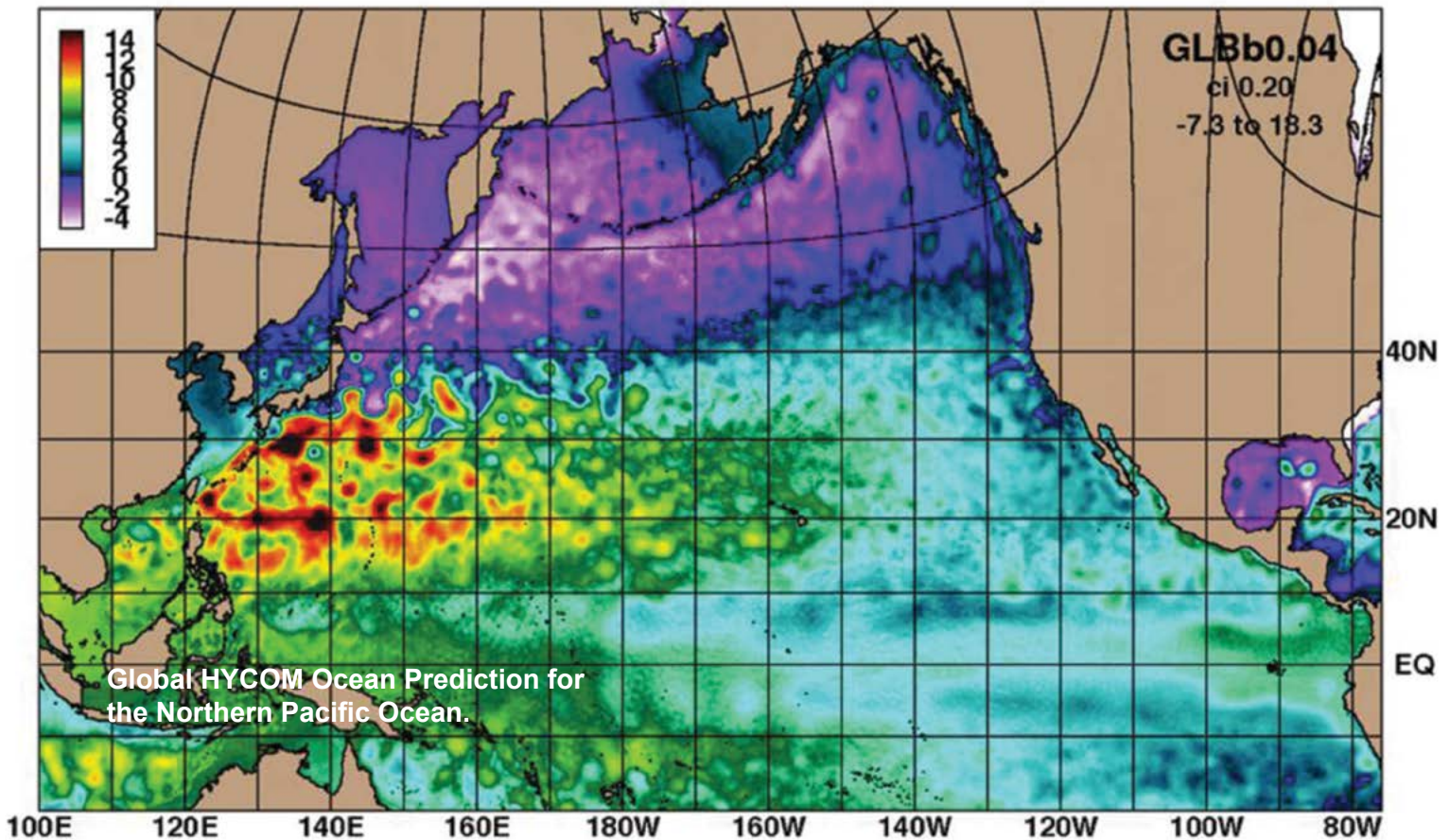
The Division has research programs in astronomy and astrophysics ranging in wavelength from the optical to longwave radio (HF), with an emphasis on interferometric imaging. Facilities include the Navy Optical Interferometer (NOI), located near Flagstaff, Arizona, a joint project between the U.S. Naval Observatory and the NRL Remote Sensing Division. The NOI is used for optical astrometry, to investigate unfilled aperture imaging technologies, and to conduct astrophysical research. When completed, it will be the highest-resolution ground-based optical telescope in the world. The Division is also at the forefront of research in low-frequency (<100 MHz) radio astronomy and associated instrumentation and interferometric imaging techniques. The Division developed and installed VHF receivers on the National Radio Astronomy Observatory's Very Large Array (VLA), has designed the next-generation HF receiver system for the EVLA (Expanded VLA), and developed imaging techniques necessary to correct for ionospheric phase disturbances, important at HF frequencies. The Division is also collaborating with the University of New Mexico and New Mexico Tech on the Long Wavelength Array, a prototype, next-generation, HF imaging array ultimately with 200 to 300 km baselines.

The Division operates the NRL SEALAB (Sensor Exploitation Lab), which is the primary conduit of Division research to the operational community.



The NRL WindSat polarimetric radiometer prior to spacecraft integration.

Oceanography



The Oceanography Division is the major center for in-house Navy research and development in oceanography. It is known nationally and internationally for its unique combination of theoretical, numerical, experimental, and remotely sensed approaches to oceanographic problems. The Division's modeling focus is on a truly integrated global-to-coastal modeling strategy, from deep water up to the coast including straits, harbors, bays, inlets, and rivers. This requires emphasis on both ocean circulation and wave/surf prediction, with additional focus on coupling the ocean models to atmospheric, biological, optical, and sediment models. This includes processing and analysis of satellite and in-water observations, development of numerical model systems, and assimilation for predicting the ocean environment. This modeling is conducted on the Navy's and DoD's most powerful vector and parallel processing machines. The Division's in-house Ocean Dynamics and Prediction Computational Network Facility provides computer services to scientists for program development, graphics, data pro-

cessing, storage, and backup. It also provides network connectivity to other Navy sites, to the DoD High Performance Computing centers, and to the Internet. The computational system enables leading-edge oceanographic numerical prediction research applicable to Navy operations affected by environmental variations at scales of meters to hundreds of kilometers and time scales of seconds to weeks. To study the results of this intense modeling effort, the Division operates a number of highly sophisticated graphic systems to visualize ocean and coastal dynamic processes. Problems addressed cover a wide scope of physics including parameterization of oceanic processes, construction and analysis of ocean models and forecast systems, basic and applied research of ocean dynamics, surface waves, thermohaline circulation, nearshore circulation, estuarine and riverine modeling, arctic ice modeling, internal waves, and ocean/atmosphere coupling. Additional emphasis is on optimization of underwater, airborne, and satellite observing systems, representation of ocean processes affecting temperature, salinity, and mixed-layer depth, uncertainty analysis in coupled systems, ensemble and probabilistic ocean forecasting,

targeting ocean observations, representing probability in ocean/acoustic systems, and satellite-observed surface heat fluxes. The end goal is to build cutting-edge technology systems that transition to operational forecast centers.

The Division's Ocean Sciences Branch conducts basic and applied research in ocean physics, air-sea interaction, ocean optics, and marine microbially influenced corrosion. Emphasis of this research is on understanding the oceans' physical processes and their interactions with the atmosphere and biological/chemical systems at scales ranging from basin-scale to microscale. Numerical and analytical models are developed and tested in laboratory and field experiments. The results of this research support the Navy's operational capability for predictions of oceanic atmospheric exchanges, acoustic propagation/detection, light transmission/emission, and influences of microbes on marine corrosion. The seagoing experimental programs of the Division range worldwide. Unique measurement systems include a wave measurement system to acquire in situ spatial properties of water waves; a salinity mapper that acquires images of spatial and temporal sea surface salinity variabilities in littoral regions; an integrated absorption cavity and optical profiler system, and towed optical hyperspectral array for studying

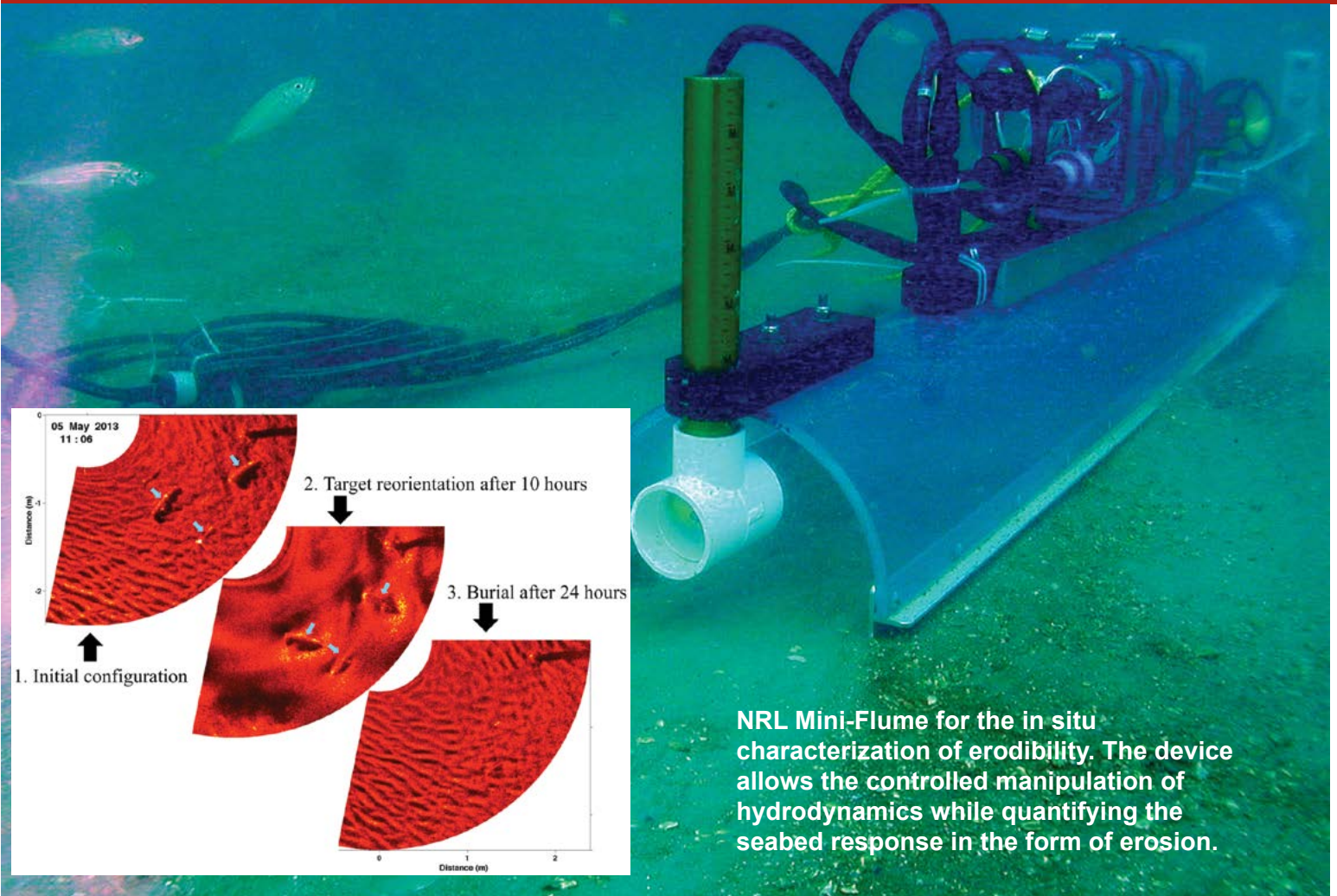
ocean optical characteristics; self-contained, bottom-mounted, upward-looking acoustic Doppler current profilers (ADCPs) for measuring ocean variability; and a Shallow water Environmental Profiler in Trawl-safe, Real-time configuration (SEPTR). Newly acquired Rayleigh Bernard Convective Tank and a Hybrid Underwater Camera support the Division's ocean optics programs providing object detection and identification in extremely turbid underwater environments. Instruments for sensing the littoral environment include a Vertical Microstructure Profiler (VMP), a Scanfish, and four Slocum Gliders.

The Division's remote sensing research focuses on radiative transfer theory, optical ocean instrumentation, lasers and underwater imaging and vision, satellite and aircraft remote sensing, remote sensing of bio-optical signatures, and coupled physical bio-optical modeling. The research includes applying aircraft and satellite ocean color and thermal infrared signatures for understanding the bio-geo-chemical cycles in the surface ocean. Additional emphasis is on algorithm and model development using satellite and aircraft data (SeaWiifs, MODIS, MERIS, AVHRR, VIIRS, OCM, GOCI, HICO, and CASI) to address the spatial and temporal variability of coastal optical properties.



Ice lead opening off the coast of Barrow, Alaska as observed from aircraft in March 2013.

Marine Geosciences



NRL Mini-Flume for the in situ characterization of erodibility. The device allows the controlled manipulation of hydrodynamics while quantifying the seabed response in the form of erosion.

The Marine Geosciences Division is the major Navy in-house center for research and development in marine geology, geophysics, geodesy, geoacoustics, geotechnology, and geo-spatial information and systems, with its research focused in three thrust areas:

Characterization and Prediction in Seafloor and Terrestrial Regions. Research subthrusts: (1) This year's airborne work has included developing methods to utilize a prototype ultra-wideband, low-frequency synthetic aperture radar (SAR) for application to the airborne detection of improvised explosive devices and for foliage penetration in densely forested regions. (2) The Division developed an advanced, bias-free geotectonic modeling technique using realistic geologic and geophysical constraints to improve gravity anomaly estimation. The technique was demonstrated for the

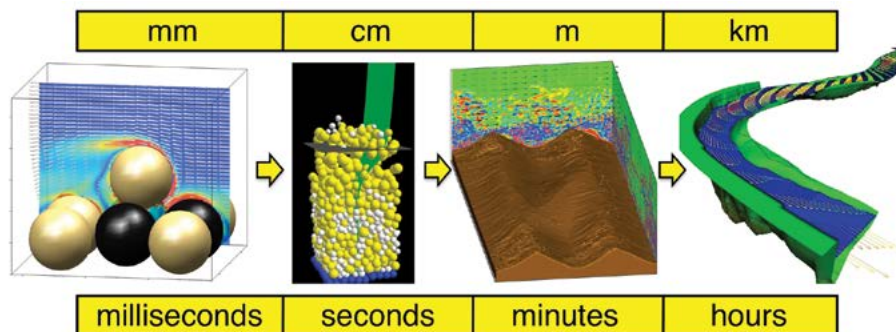
eastern area of Afghanistan, where the mountains are too high to safely conduct airborne surveys and almost no ground station gravity data are available. The predicted gravity compares favorably with predictions from the suitably altitude-adjusted GOCO02S gravity model and with measured airborne gravity along a track through the eastern region. This new modeling technique will improve Earth gravity and geoid models that will better support advanced inertial navigation systems. (3) In a major at-sea experiment, scientists conducted a seismic oceanography investigation across the Agulhas Return Current off South Africa (with Oceanography Division). Analyses reveal clearly visible reflections (temperature contrasts) that are most prominent and concentrated at the strongest portion of the frontal zone, with some reflections that can be traced at tens of meters resolution over distances of tens of kilometers. The observations place new, hard constraints on details of frontal zone mixing that are

now grossly parameterized. (4) As part of the new Carbon Flux Project, recently acquired data from the Bering Sea have been analyzed with seismic waveform inversion techniques to quantify gas and gas hydrate in the deep-water Aleutian Basin. Each of the large, super chimneys in the area is estimated to hold 0.01 to 0.014 gigatons of carbon (GtC) in the form of methane. There are as many as 1000 super chimneys, holding as much as 14 GtC; by comparison, the atmosphere holds 3.8 GtC as methane.

Dynamic Littoral and Riverine Processes. The Division continued its development of the predictive model for the mechanical strength and erodibility of soft, cohesive sediments by detailed characterization of the physicochemical, micromechanical, and bulk mechanical responses of cohesive sediment constituents under controlled manipulation of variables including hydrodynamics, salinity, and organic matter speciation. Research subthrusters: (1) The Division continued its modeling of sediment transport phenomena that spans many orders of magnitude, from the discrete particle scale (in which individual sand grains are simulated) to the continuum scale (in which the flow of rivers is resolved). Modeling the relevant physics of the problem at each scale and identifying links between the adjacent scales is crucial to developing the operational forecasts needed by Navy warfighters. (2) Scientists have conducted a series of field experiments with investigators funded by the Office of Naval Research to assess technologies for operational use towards tactical identification of navigational hazards and related environmental conditions. These riverine conditions, which include flow velocity, water surface level, and bathymetry, were obtained at high resolution using a variety of

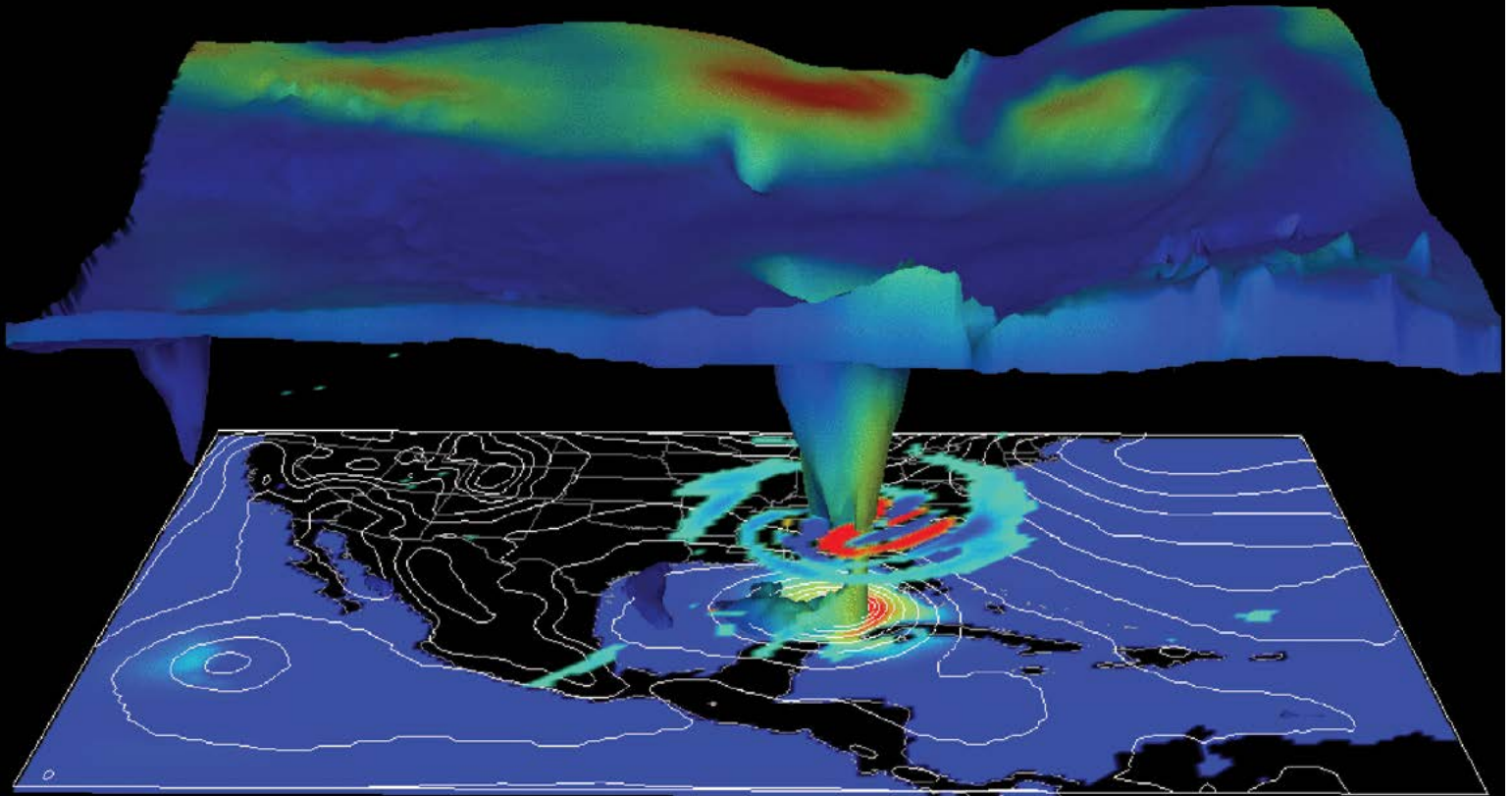
sensing approaches including acoustic Doppler current profilers, single-beam and multibeam sonars, inexpensive GPS-based drifters, and AUV-based sampling. (3) Division scientists developed a modified constitutive law on shear strain dependence of strength of soft clays and muds, applicable to a wide range of strain rates, including extension to the never before modeled high strain-rate region. (4) Research included marine biogeochemists studying the impact of the hypoxic zones in the Gulf of Mexico on benthic communities and on surficial sediment characteristics.

Geospatial Sciences and Technology. NRL computer scientists developed and hosted advanced geospatial services for the National Geospatial-Intelligence Agency, Marine Corps, Army, and Air Force in the Division's 1400 ft² geospatial services laboratory. The Division's Geospatial Hub (GHUB) is a content management system that provides an automatically synchronized, Web-based means of organizing and distributing all types of geospatial information including imagery, maps, and weather and scientific data. In 2012, the Division supported security efforts at the summer Olympics by hosting detailed maps of the Olympic venues for security forces. NRL mapping systems have features not found in civilian systems. These include NRL-patented, high-speed data management technology and support for an unlimited number of different data layers. Scientists delivered new software (EPMA Build 3.0.1) to the Naval Oceanographic Office for use in the Littoral Combat Ship Mine Countermeasures Mission Module to utilize on-scene data/information to update environmental databases and reduce timelines for detecting minelike changes on the seabed.



In the Marine Geosciences Division, scientists model sediment transport phenomena that span many orders of magnitude, from the discrete particle scale (far left) where individual grains are simulated, up to the continuum scale (far right) where the flow in rivers is resolved. The goal is to develop reliable forecasting models for operational length and time scales. Consequently, we must simulate the relevant physics of the problem at each scale and identify links between adjacent scales (arrows). Pictures from left to right: a fully resolved simulation of the entrainment of an individual particle into a turbulent boundary layer; simulation of sheet flow transport using a discrete particle model; simulation of sand ripple evolution using mixture theory (SedMix3D); and simulation of flow in a reach of the Kootenai River, Idaho.

Marine Meteorology



3D depiction of Hurricane Katrina 2005 by NRL's high-resolution operational mesoscale model, COAMPS®-TC (Coupled Ocean/Atmosphere Mesoscale Prediction System–Tropical Cyclone).

The Marine Meteorology Division, located in Monterey, California, conducts basic and applied research in atmospheric sciences. The Division develops meteorological analysis and prediction systems and other products to support Navy, DoD, and other customers operating at theater, operational, and tactical levels. It is collocated with the Fleet Numerical Meteorology and Oceanography Center (FNMOC), the Navy's operational production center for numerical weather prediction (NWP) and satellite imagery interpretation.

The Division's Environmental Prediction System Development Laboratory is built around multiple LINUX clusters supported by approximately 1500 TB of RAID storage and a tape library capable of expansion to about 10 PB. The Division also maintains over 100

LINUX servers, including a unique Global Ocean Data Assimilation Experiment (GODAE) server hosting data sets suitable for research and development of ocean and atmospheric data assimilation capabilities. In 2012, the DoD HPC Modernization Office (HPCMO) Dedicated HPC Project Investment (DHPI) awarded the Division a Cray XE6m supercomputer consisting of 5376 cores, 10,752 gigabytes of memory, and 65 teraflops of peak performance. These systems, in combination with offsite DoD Supercomputing Resource Centers (DSRC) and FNMOC assets, enable the Division to efficiently develop, improve, and transition numerical weather analysis and prediction systems and coupled air/ocean/ice systems to operational use, producing guidance that is used by Fleet forces around the globe. These systems also support basic research and conduct real-time demonstrations in atmospheric processes such as air-sea-ice interaction, atmospheric dynamics, and cloud/aerosol physics, as well as development of environmental applications, decision aids, and probabilistic prediction products.

The Division's state-of-the-art Satellite Data Processing Laboratory allows the direct downlink of real-time NOAA geostationary (GEO) information (GOES-WEST/EAST) and data relays from five other geostationary satellites. Data from numerous low Earth orbiting (LEO) platforms are also received in near real time via collaborative interagency agreements. NRL-Monterey processes digital satellite data from 27 LEO sensors and seven GEO platforms to conduct research and development of multisensor data fusion products to support a variety of DoD operations. These activities range from monitoring and analyzing tropical cyclone characteristics to providing special meteorological products in support of combat operations in Southwest Asia.

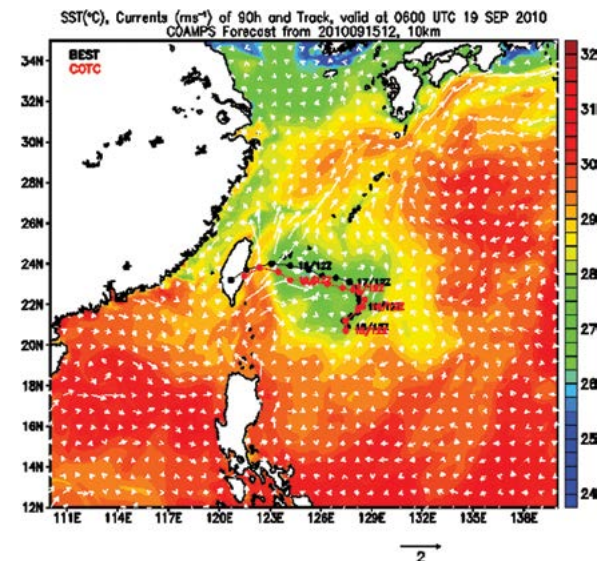


MAARCO is designed as a stand-alone facility for basic atmospheric research and the collection of data to assist in validating aerosol and weather models. Its purpose is to enable research on atmospheric aerosols, gases, and radiation (visible and IR light) in areas of key interest, including remote areas, overseas locales, and aboard ships. This complete mobile laboratory facilitates deployment in areas with limited facilities, and provides maximum flexibility for integration of additional instrumentation.



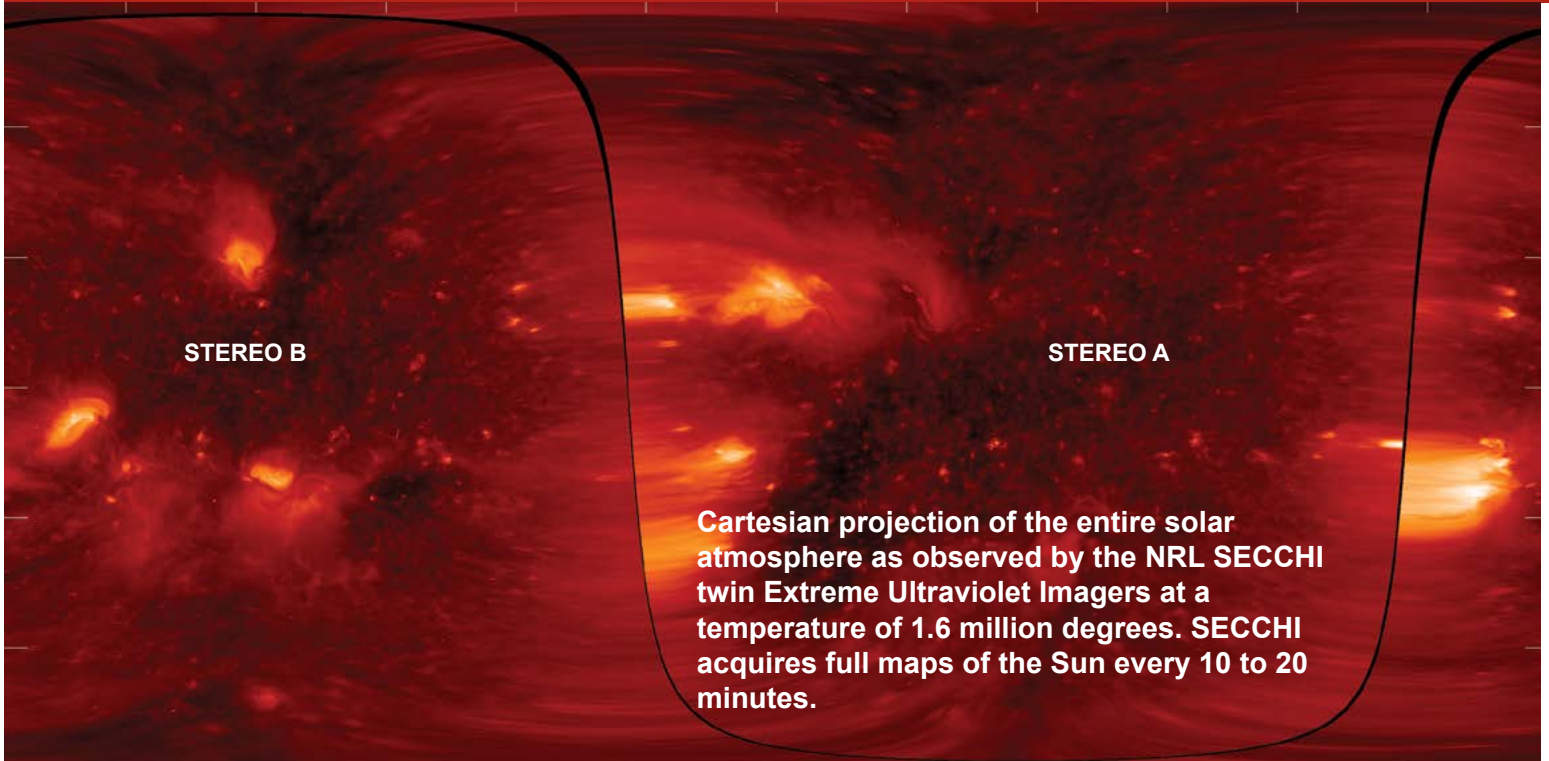
NRL's Marine Meteorology Division processes satellite data from 27 LEO sensors and seven geostationary platforms and uses that data to conduct research and development of multisensor data fusion products to support a variety of DoD operations.

The Mobile Atmospheric Aerosol and Radiation Characterization Observatories (MAARCO) are a pair of mobile laboratories housed in climate-controlled modified shipping containers with integrated suites of meteorological, aerosol, gas, and radiation instruments. MAARCO can be deployed to operate in strategic areas around the globe, including remote regions, overseas locales, and aboard ships at sea. For added flexibility in field data collection, the modular instruments can be removed and mounted on aircraft and are used to investigate boundary layer meteorology, aerosol microphysics, aerosol and cloud radiative properties, and electro-optical propagation.



The sea surface temperature (shaded, in °C) and surface currents (vectors, ms^{-1}) at 90 hour of the coupled COAMPS®-TC forecast starting at 1200 UTC 15 Sept. 2010, overlaid with the model track (red dots) and the BEST track (black dots).

Space Science



Cartesian projection of the entire solar atmosphere as observed by the NRL SECCHI twin Extreme Ultraviolet Imagers at a temperature of 1.6 million degrees. SECCHI acquires full maps of the Sun every 10 to 20 minutes.

The Space Science Division conducts a broad-spectrum RDT&E program in solar-terrestrial physics, astrophysics, upper/middle atmospheric science, and astronomy. Division researchers conceive, plan, and execute scientific research and development programs and transition the results to operational use. They develop instruments to be flown on satellites, sounding rockets, and balloons; and ground-based facilities and mathematical models. The Division's primary objective is to perform foundational discovery research to ensure Navy and Marine Corps access to critical space capabilities and space force enhancement capabilities on the ground, at sea, and in a contested space environment.

The Division's Vacuum Ultraviolet Solar Instrument Test (SIT) facility is an ultra-clean solar instrument test facility designed to satisfy the rigorous contamination requirements of state-of-the-art solar spaceflight instruments. The facility has a 400 ft² Class 10 clean room and a large Solar Coronagraph Optical Test Chamber (SCOTCH). The SIT clean room is ideally suited for assembly and test of contamination-sensitive spaceflight instrumentation. It contains a large vibration-isolated optical bench and a 1-ton capacity overhead crane. The SCOTCH consists of a

large vacuum tank and a precision instrument-pointing table. The Division also maintains extensive facilities for supporting ultraviolet (UV) spectroscopy sounding rocket programs. These facilities include a dedicated Class 1000 instrument clean room, and a gray room area for assembling and testing the rocket payloads that incorporates all of the fixtures required for safe handling of payloads. Further, the Division rocket facilities include a large UV optical test chamber that is additionally equipped with a large vibration- and thermal-isolated optical bench for telescope testing, which allows the laboratory area to be turned into a schlieren facility. The Division also has a unique facility for developing Doppler Asymmetric Spatial Heterodyne (DASH) thermospheric wind sensors, which are currently being developed in support of future space flight missions.

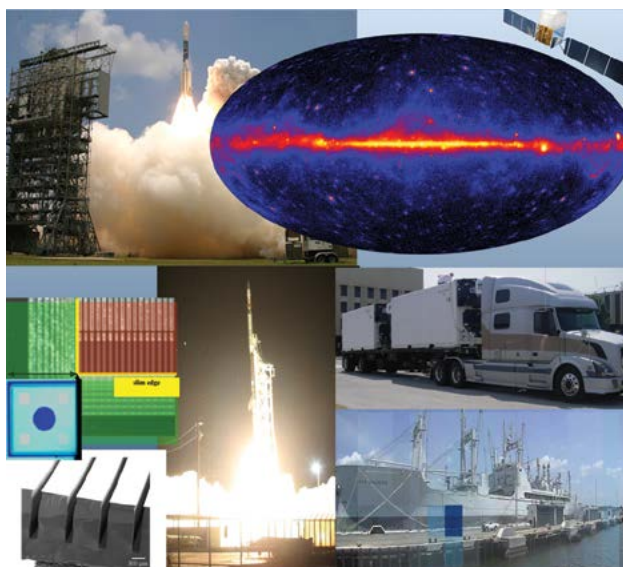
The Division has a wide range of new satellite, rocket, balloon, and ground-based instruments under development. These include the SoloHI heliospheric imager that will image both the quasi-steady flow and transient disturbances in the solar wind when aloft on board the Solar Orbiter mission; the Compact CORonagraph (CCOR), an elegant, externally occulted instrument that uses a single-stage optical design with two lens groups, a polarization analyzer, and a spectral filter to achieve performance comparable to the tra-

ditional three-stage Lyot coronagraph but with significantly lower mass and volume than the traditional design; and the NRL-led SuperMISTI detection system, intended to demonstrate standoff detection, identification and imaging of radiological/nuclear weapons of mass destruction (WMD) in maritime environments. A Division-led thermospheric wind instrument, the Michelson Interferometer for Global High-resolution Thermospheric Imaging (MIGHTI), is being developed for spaceflight onboard the ICON Explorer Mission.

Advanced space-based research is also currently being performed. Division experiments are measuring the Earth's thermosphere and ionosphere to improve space weather forecasting for these near-space atmospheric regions that significantly influence the performance of important operational systems such as GPS navigation, communication, and space debris tracking. The Special Sensor Ultraviolet Limb Imager (SSULI) developed by NRL's Space Science Division and Spacecraft Engineering Department offers a first-of-its-kind technique for remote sensing of the ionosphere and thermosphere from space. Flying on the U.S. Air Force Defense Meteorological Satellite Program (DMSP) satellites, SSULI's characterization of the Earth's upper atmosphere and ionosphere provides necessary scientific data to support military and civil systems. In August 2013, the Fermi Gamma ray Space Telescope, major portions of which were developed and tested by NRL's Space Science Division and Spacecraft Engineering Department, completed five years of successful

operation on orbit. Division scientists have had lead roles in several key scientific discoveries using Fermi, including: confirmation of the long-standing belief that shocks formed from exploding stars are the source of the high-energy cosmic rays seen at Earth; creation of a highly efficient means of discovering new pulsars, the rapidly rotating cores of dead stars that serve as precise astrophysical clocks; and discovery that our Sun accelerates particles to extreme energies even in relatively weak flares, and does so for hours after the impulsive event. Two Space Science Division-led heliophysics space instrument capabilities, the Large Angle Spectrometric and Coronagraphic Telescope (LASCO) on the SOHO Mission and the Sun-Earth Connection Coronal Heliospheric Investigation (SECCHI) on the STEREO Mission, are continuing to advance understanding of the solar corona and the importance of coronal mass ejections in determining space weather at Earth.

Division scientists, using the Division network of computers and workstations and other connected high performance computing assets, develop and maintain physical models in support of their research. These include research to extend the operational Navy Global Environmental Model (NAVGEM) from its current upper boundary to altitudes of ~100 km; and, HiFi, a user-friendly, highly parallel, fully implicit adaptive spectral element code framework designed for model development, magnetohydrodynamics, and multifluid numerical modeling in two- and three-dimensional geometries.



NRL's major role in the Fermi Mission (launch 2008, upper left) has enabled broadly based astrophysical investigations including the gamma ray sky map (upper right) identifying over 1800 point sources and new insight into particle acceleration and radiations from pulsars, supernova remnants, active galactic nuclei and many other topics. Space science research in detector design enabled by NRL's Nanoscience Institute has resulted in three pending patents relating to "slim edge" detectors (middle left) and charge control using atomic layer deposition and three patents on deep reactive ion etching of detectors (lower left). The J-PEX extreme-ultraviolet sounding rocket experiment (lower center) provided unprecedented spectral resolution on White Dwarf stars. Division research in radiological/nuclear Weapons of Mass Destruction (WMD) detection resulted in the dual container SuperMISTI detection system (middle right, in transport to Norfolk maritime testing) providing standoff detection and imaging of WMD. Image (lower right) shows SuperMISTI image of radiation source (blue block) hidden in the hold of the USS *Cape Chalmers*.

Space Systems Development Department

Space Systems Development Department Optical Test Facility transmits laser light at both 1064 nm and 1550 nm for both satellite laser ranging and free space optical communication signals.



The Space Systems Development Department (SSDD) is responsible for the end-to-end definition, design, development, integration, test, and operation of space systems that satisfy naval and national defense requirements.

The total system engineering philosophy employed by the SSDD enables seamless sensor-to-shooter capabilities to be deployed that optimize the interfaces between command and control, on-orbit satellite collection, and onboard and ground processing functions; the dissemination of data to tactical and national users; and the design of tools that provide for the automated correlation and fusion of collected information with other sources.

Research and development is conducted in the areas of space system architectures; advanced mission data processing and data analysis techniques; advanced

information systems concepts, including enterprise and cloud computing and networking of space, air, ground, and subsurface sensors; and mission simulation techniques. Intelligence collection, advanced RF, optical, and laser communication, satellite laser ranging, digital signal processing, data management, and space navigation systems are constantly improved upon to satisfy evolving requirements. These systems are engineered for maximum reuse and interoperability.

Having conceived of and developed the payload for the first Global Positioning System (GPS) satellite, the SSDD continues to be a center of excellence in the research and development of advanced GPS technology. Advanced theoretical and experimental investigations are applied to expanding the design and interoperability of systems used for a wide range of military, space, geodetic, and time dissemination applications. These investigations involve critical precise time generation and measurement technology for passive and

active ranging techniques incorporating advanced data transmission and signal design. Precise time and time interval research conducted involves theoretical and experimental development of atomic time/frequency standards, instrumentation, and timekeeping to support highly precise and accurate timescale systems in scientific and military use. Net-centric systems are critically dependent on highly accurate and stable time/frequency standards coordinated to a common timescale through the diverse dissemination comparison techniques developed within the SSDD.

The PCEF (Precision Clock Evaluation Facility) is one of the major facilities within NRL's Naval Center for Space Technology. The PCEF was developed to support development of high precision clocks for GPS spacecraft and ground applications, primarily atomic standards. Space atomic clocks are evaluated, qualified, and acceptance tested for space flight using the assets of this facility. Testing performed includes long- and short-term performance evaluation, and environmental testing (including shock and vibration). Investigations of on-orbit anomalies are performed within the PCEF to attempt to duplicate similar effects in space-qualified hardware under controlled conditions. The facility was originally developed to evaluate developments in the Global Positioning System concept development program (Block I) and expanded for the dedicated

space clock development conducted during operational system development and deployment. The ability to evaluate and test highly precise atomic clocks, especially in a space environment, requires unique facilities, precise time and frequency references, and precise instrumentation not available anywhere else. The primary time and frequency reference for the PCEF is a specially designed environmental chamber housing a number of hydrogen masers combined with measurement equipment permitting a realization of Universal Coordinated Time (UTC) to be maintained as UTC (NRL) in cooperation with the International Bureau of Weights and Measures (BIPM) for reference and research purposes.

In addition to a wide array of test tools and facilities, the Department operates several field sites including the Midway Research Center satellite calibration facility in Stafford, Virginia; the Blossom Point Satellite Tracking and Command Facility in Welcome, Maryland; and the Chesapeake Bay Detachment Radar Range in Chesapeake Beach, Maryland.



The Naval Center for Space Technology's Precision Clock Evaluation Facility (PCEF).

Spacecraft Engineering Department

Lift-off of TacSat-4 — NRL's 100th satellite.



The Spacecraft Engineering Department (SED) and the Space Systems Development Department, together comprising NRL's Naval Center for Space Technology (NCST), cooperatively develop space systems to respond to Navy, DoD, and national mission requirements with improved performance, capacity, reliability, efficiency, and life cycle cost.

The SED facilities that support this work include integration and test highbays, large and small anechoic radio frequency chambers, varying levels of clean rooms, shock and vibration tables, an acoustic reverberation chamber, large and small thermal/vacuum test chambers, a thermal systems integration and test

laboratory, a spin test facility, a static loads test facility, and a spacecraft robotics engineering and control system interaction laboratory.

Integration and Test Facilities: The department maintains a wide range of specialized RF chambers for test of antennas, receivers, transmitters, electronics, and other flight systems. There are two main anechoic chambers whose main function is the test and verification of antennas and flight systems; the tapered chamber is 31 × 31 × 120 ft, with a 100 ft measurement distance; it is instrumented from 100 MHz to 18 GHz for radiation patterns, and is regularly used for electromagnetic interference (EMI) measurements as well. The rectangular chamber is 10 × 12 × 20 ft, with a 15 ft measurement distance, and is instrumented from 1 to 220 GHz. There is also a 3 × 3 ft millimeter-wave near-field scanner that is instrumented up to 220 GHz, but capable of measurements up to 550 GHz. All the measurement facilities

are computer-controlled and fully automated, allowing multiple antennas and polarizations to be measured at the same time. A third RF chamber is dedicated to electromagnetic interference/radio frequency interference (EMI/RFI) testing. This welded steel chamber measures 23 × 23 × 20 ft and provides as much as 120 dB shielding effectiveness up to 18 GHz and 100 dB from 18 to 50 GHz. The chamber uses a hybrid anechoic material consisting of wideband pyramidal absorbers and ferrite tiles for performance from 20 MHz to 50 GHz. The EMI chamber is equipped with instrumentation to perform the full range of MIL-STD-461 EMI qualification testing. A 10 ft high × 11 ft wide sliding bladder door allows easy access of large test items to the main chamber.

The Laminar Flow Clean Room provides a Class 100 ultraclean environment for the cleaning, assembly, and acceptance testing of contamination-sensitive spacecraft components, and integration of complete spacecraft subsystems. The facility is used primarily to support spacecraft propulsion systems but has been used to support all spacecraft electrical, electronic, and mechanical subsystems.

The Vibration Test Facility, which simulates the various vibration-loading environments present during flight operations and demonstrates compliance to design specifications, consists of the following shakers: Unholtz-Dickie T5000 50K Flb random 2-in. DA stroke, Ling 4022 30K Flb random 2-in. DA stroke, Ling 2022 16K Flb random 2-in. DA stroke, and a Ling 335 16K Flb random 1-in. DA stroke.

The Acoustic Reverberation Simulation Facility is a 10,000 ft³ reverberation chamber that simulates the acoustic environment that spacecraft will experience during launch. The maximum capable sound pressure level is approximately 152 dB.



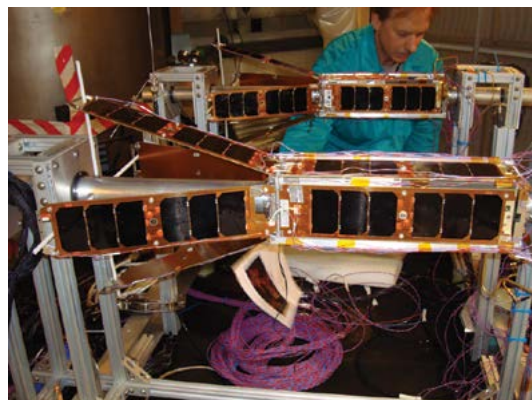
SED's Tapered Anechoic Chamber.

The Thermal Fabrication and Test Facility supports the design, fabrication, installation, and verification of spacecraft thermal control systems. It also provides for the analytical thermal design and analysis of any spacecraft. This includes conceptual design, analytical thermal model development, definition of requirements, worst-case environments and design conditions, and temperature predictions for all cases. The facility provides the means to go from design and analysis to hardware qualification and acceptance testing and then to orbit.

The Spin Test Facility contains two spin balancing machines (one horizontal and one vertical) to handle various types of balancing requirements. Both machines are provided with a plane separation network to obtain correction readings directly in the plane of correction. Moment of inertia (MOI) tables of various capacities are used to verify MOI and center of gravity for units under test.

The Static Loads Test Facility provides the capability to perform modal survey testing on a wide variety of spacecraft and structures. It consists of two 6 ft × 12 ft × 6 in. thick, ~15,500 lb steel plates (attachable) with floating base, six 75 Flb stinger shakers (1/2-in. DA stroke), two 250 Flb stinger shakers (4-in. DA stroke), and a ~300-channel data acquisition system (expandable).

Spacecraft Robotics Engineering and Controls Laboratory: This facility, which is the largest dual-platform motion simulator of its kind, is operated by NCST in collaboration with NRL's Naval Center for Applied Research in Artificial Intelligence. It supports research in the emerging field of space robotics including autonomous rendezvous and capture, remote assembly operations, and machine learning. It allows full-scale, hardware-in-the-loop testing of flight mechanisms, sensors, and logic of space robotic systems.

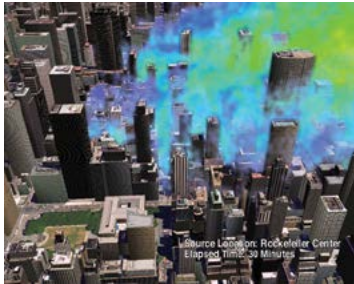


Cubesats being prepared for environmental testing.

RESEARCH SUPPORT FACILITIES

Technology Transfer Office

The NRL Technology Transfer Office (TTO) is responsible for NRL's implementation of the Federal Technology Transfer Act. It facilitates the transfer of NRL's innovative technologies for public benefit by marketing NRL technologies and by negotiating patent license agreements and Cooperative Research and Development Agreements (CRADAs).



NRL's CT-Analyst, which provides instantaneous, 3D predictions of airborne particle transport in urban settings, has been developed for use in specific cities.

TTO markets NRL technology through its Web site, by exhibiting at trade shows and scientific conferences, posting videos on NRL's social media sites, and through DoD-contracted Partnership Intermediaries such as TechLink. It also works with state and local economic development offices to identify small companies manufacturing and selling related technologies.

A license grants a company the right to make, use, and sell NRL technologies commercially in exchange for equitable licensing fees and royalties. Revenue is distributed among inventors and NRL's general fund. TTO reviews the commercialization plan submitted by the potential licensee in support of its application for a license. The plan must provide information on the licensee's capabilities, proposed development expenditures, a time line to commercialization, and an assessment of the planned market.

A license may be exclusive, partially exclusive (exclusive for a particular field of use or geographic area), or non-exclusive. Once a license is executed, TTO monitors the licensee for timely payments and for its diligence in commercializing the licensed invention.

TTO also negotiates Government Purpose Licenses to transition NRL technologies for manufacture and sale solely for Navy and other U.S. Government purposes.

CRADAs provide a vehicle for NRL scientists and engineers to collaborate with their counterparts in industry, academia, and state and local governments. Under a CRADA, a company may provide funding for collaborative work between it and NRL and is granted an exclusive option to license technologies developed under that CRADA's Statement of Work (SOW). TTO works with the NRL scientist to develop a SOW that has sufficient detail to define the scope of the CRADA partner's rights.

Technical Information Services

The Technical Information Services (TIS) Branch combines publication, printing and duplication, graphics, photographic, multimedia, exhibit, and video services into an integrated organization. Publication services include writing, editing, composition, publications consultation and production, and printing management. Our Service Desk provides quick turnaround digital black-and-white and color copying/printing/CD duplicating, as well as passport and ISOPREP photos. TIS uses digital publishing technology to produce scientific and technical reports that can be used for either



Photographer and videographer capture footage for a technical presentation.

print or Web. Graphics support includes technical and scientific illustrations, computer graphics, design services, photographic composites, display posters, and framing. The HP large format printers offer exceptional color print quality up to 1200 dpi and produce indoor posters and signs up to 56 inches. Lamination and mounting are available. Photographic services include digital still camera coverage for data documentation, both at NRL and in the field. Photographic images are captured with state-of-the-art digital cameras and can be output to a variety of archival media. Photofinishing services provide custom printing and quick service color prints from digital files. Video services include producing video reports and technical videos, and capturing presentations of scientific and technical programs. TIS digital video editing equipment allows in-studio and on-location editing. The TIS Exhibits Program works with NRL's scientists and engineers to develop exhibits that best represent a broad spectrum of NRL's technologies and promote these technologies to scientific and nonscientific communities at conferences throughout the United States.

Administrative Services

The Administrative Services Branch is responsible for collecting and preserving the documents that comprise NRL's corporate memory. Archival documents include personal papers and correspondence, laboratory notebooks, and work project files — documents that are appraised for their historical or informational value and considered to be permanently valuable. The



Employees of the Administrative Services Branch working in the mail room.

Branch provides records management services, training, and support for the maintenance of active records, including electronic records, as an important information resource. The Branch is responsible for processing NRL's incoming and outgoing correspondence and provides training and support on correct correspondence formats and practices. The Branch is responsible for NRL's Forms and Reports Management Programs (including designing electronic forms and maintaining a Web site for Lab-wide use of electronic forms), and is responsible for providing NRL postal mail services for first class and accountable mail and for mail pickup and delivery throughout NRL. The Branch also provides NRL Locator Service.

Ruth H. Hooker Research Library

NRL's Ruth H. Hooker Research Library continues to support NRL and ONR scientists in conducting their research by making a comprehensive collection of the most relevant scholarly information available and useable; by providing direct reference and research support; by capturing and organizing the NRL research portfolio; and by creating, customizing, and deploying a state-of-the-art digital library.

Print and digital library resources include extensive technical report, book, and journal collections dating back to the 1800s housed within a centrally located research facility that is staffed by subject specialists and information professionals. The collections include 44,000 books; 54,000 digital books; 80,000 bound

historical journal volumes; more than 3,500 current journal subscriptions; and approximately 2 million technical reports in paper, microfiche, or digital format (classified and unclassified). Research Library staff members provide advanced information consulting; literature searches against all major online databases including classified databases; circulation of materials from the collection including classified literature up to the SECRET level; and retrieval of articles, reports, proceedings, or documents from almost any source around the world. Staff members provide scheduled and on-demand training to help researchers improve productivity through effective use of the library's resources and services.

The Research Library staff has developed and is continuing to expand the NRL Digital Library. The Digital Library currently provides desktop access to thousands of journals, books, and reference sources to NRL-DC, NRL-Stennis, NRL-Monterey, and the Office of Naval Research.

Library systems provide immediate access to scholarly information, including current and archival journals, trade magazines, and conference proceedings that are fully searchable at the researcher's desktop (more than 15,400 titles). Extensive journal archives from all the major scientific publishers and scholarly societies are now available online. The breadth and depth of content available through TORPEDO, NRL's locally loaded digital repository, continues to grow and



Librarians working in the Ruth H. Hooker Research Library.

provides a single point of access to scholarly information by providing full text search against journals, books, conference proceedings, and technical reports from 20 publishers (14.1 million items by November 4, 2013). The NRL Online Bibliography, a Web-based publications information system, is ensuring that the entire research portfolio of written knowledge from all NRL scientists and engineers since the 1920s will be captured, retained, measured, and shared with current and future generations.

OTHER RESEARCH SITES

NRRL has acquired or made arrangements over the years to use a number of major sites and facilities outside of Washington, D.C., for research. The largest facility is located at Stennis Space Center (NRL-SSC) near Bay St. Louis, Mississippi. Others include a facility near the Naval Postgraduate School in Monterey, California (NRL-MRY), and the Chesapeake Bay Detachment (CBD) and Scientific Development Squadron One (VXS-1) in Maryland. Additional sites are located in Virginia, Alabama, and Florida.

Stennis Space Center (NRL-SSC)

The NRL Detachment at Stennis Space Center, Mississippi (NRL-SSC), consists of NRL's Oceanography Division and portions of the Acoustics and Marine Geosciences Divisions. NRL-SSC, a tenant at NASA's John C. Stennis Space Center (SSC), is located in the southwest corner of Mississippi, about 40 miles north-east of New Orleans, Louisiana, and 20 miles from the Mississippi Gulf Coast. NRL-SSC personnel have been located at SSC since the early 1970s, when they were part of the Navy Ocean Research and Development Activity and, later, the Navy Oceanographic and Atmospheric Research Laboratory before becoming an NRL detachment. Other Navy tenants at SSC include the Commander, Naval Meteorology and Oceanography Command (CNMOC), the Naval Oceanographic Office (NAVOCEANO), Naval Oceanography Operations Command, Naval Oceanography Antisubmarine Warfare Center, Naval Oceanography Mine Warfare

Center, Fleet Survey Team, Naval Small Craft Instruction and Technical Training School, Special Boat Team Twenty-two, and Navy Office of Civilian Human Resources Southeast. Other Federal and State agencies at SSC involved in marine-related science and technology include the National Oceanic and Atmospheric Administration (NOAA) National Coastal Data Development Center and the NOAA National Data Buoy Center, the U.S. Geological Survey, the Environmental Protection Agency (EPA) Gulf of Mexico Program and

EPA Environmental Chemistry Laboratory, the Center of Higher Learning, University of Southern Mississippi Department of Marine Science, and Mississippi State University. NRL-SSC benefits from the collocation of CNMOC and NAVOCEANO, which are major opera-



Vertical microstructure profiler.

tional users of the oceanographic, acoustic, and geosciences technology developed by NRL-SSC researchers. NAVOCEANO operates the Navy DoD Supercomputing Resource Center, one of the nation's High Performance Computing Centers, which provides operational support to the warfighter and access to NRL for ocean and atmospheric science and technology.

The Acoustics branch (Code 7180) and Marine Geosciences and Oceanography Divisions occupy more than 175,000

ft² of research, computation, laboratory, administrative, and warehouse space. Facilities include the sediment core laboratory, transmission electron micro-



The JEOL JEM-3010 transmission electron microscope.

scope, moving-map composer facility, underwater navigation control laboratory, computed tomography scanning laboratory, real-time ocean observations and forecast facility, ocean color data receipt and processing facility, environmental microscopy facility, maintenance and calibration systems, Ocean Dynamics & Prediction Computational Network Facility, and numerous laboratories for acoustic, geosciences, and oceanographic computation, instrumentation, analysis, and testing. Special areas are available for constructing, staging, refurbishing, and storing seagoing equipment.

Monterey (NRL-MRY)

The NRL Detachment Monterey is located in Monterey, California, on a 5-acre Navy Annex about one mile from the Naval Postgraduate School (NPS) campus. The Marine Meteorology Division (NRL-MRY) has occupied this site since the early 1970s,



NRL Monterey's new 15,000 ft² Marine Meteorology Center. The building was constructed through the MILCON program, Project P-174, and was dedicated on October 12, 2012.

when the U.S. Navy collocated the meteorological research facility with the operational center, now known as Fleet Numerical Meteorology and Oceanography Center (FNMOC). FNMOC was stood up in Monterey around 1960 to be able to share resources and expertise with NPS. This collocation of research, education, and operations continues to be a winning formula, as FNMOC remains the primary customer for the numerical weather prediction and satellite product systems developed by NRL-MRY. NRL scientists have direct access to FNMOC's large classified supercomputers, allowing advanced development to take place using the real-time, on-site, global atmospheric and oceanographic databases, set in the same computational environment as operations. Such access offers unique advantages for successfully implementing new systems and system upgrades, and allows for rapid integration of new research results into the operational systems. Proximity to NPS also offers unique opportunities for collaborative research, as well as educational and teaching/mentoring opportunities for NRL staff.

The NRL-MRY now occupies portions of three out of the five primary buildings in the Monterey Navy Annex. A \$10.4M MILCON project, the Marine Meteorology Center, was completed and dedicated in October 2012. The new building (B-715) gives the Division a state-of-the-art, "green," LEED certified building that includes an atmospheric aerosol laboratory, classified computer facility, the Meteorology Applications Development Branch (Code 7540), and a Division front office suite. A configurable, cutting-edge aerosol and radiation measuring and observation platform is situated on the roof of B-715 for long-term monitoring of the air quality in Monterey, complementing the standard meteorological observation suite of the regional Forecast Office of the National Weather Service, collocated in the Annex. The Division's Atmospheric Dynamics and Prediction Branch (Code 7530) will vacate B-702 and move into B-704 in FY 2014 while FNMOC moves into B-702 in accordance with the Monterey Navy Annex Building Plan. When completed, NRL-MRY will wholly occupy two buildings in the Annex, the new B-715 and the existing B-704, with a total floor space of approximately 40,000 ft².

Chesapeake Bay Detachment (CBD)

NRL's Chesapeake Bay Detachment (CBD) occupies a 168-acre site near Chesapeake Beach, Maryland, and provides facilities and support services for research in radar, electronic warfare, optical devices, materials, communications, and fire research.

Because of its location high above the western shore of the Chesapeake Bay, unique experiments can be performed in conjunction with the Tilghman

Island site, 16 km across the bay from CBD. Some of these experiments include low-clutter and generally low-background radar measurements. Using CBD's support vessels, experiments are performed that involve dispensing chaff over water and characterizing aircraft and ship radar targets. Basic research is also conducted in radar antenna

properties, testing of radar remote sensing concepts, use of radar to sense ocean waves, and laser propagation. A ship-motion simulator (SMS) that can handle up to 12,000 lb of electronic systems



Aerial view of the Chesapeake Bay Detachment at Randle Cliff (Chesapeake Beach), Maryland.

is used to test and evaluate radar, satellite communications, and line-of-sight RF communications systems under dynamic conditions (various sea states).

CBD also hosts facilities of the Navy Technology Center for Safety and Survivability that are primarily dedicated to conducting experimental studies related to all aspects of shipboard safety, particularly related to flight decks, submarines, interior ship conflagrations, and other field activities that may affect the marine environment. The Center has a variety of specialized facilities including two fully instrumented real-scale fire research chambers for testing small (28 m³) and large (300 m³) volume machinery spaces, a gas turbine engine enclosure and flammable liquid storeroom fire suppression systems; three test chambers (0.3, 5, and 324 m³) for conducting experiments

up to 6 atmospheres of pressure; a 50 ft x 50 ft fire test chamber fitted with a large-scale calorimeter hood rated



CBD's LCM-8 providing test support for electronic warfare research.

up to 3 MW; a 10,000 ft² mini-deck that affords capabilities for studying characteristics and suppression of flight deck fires and suppression techniques; two mobile instrument vans for remote field tests support; and an LCAC gas turbine engine module.

The Radar Range facility at CBD, together with the Maritime Navigation Radar (MNR) Test Range at Tilghman Island, provide the emitters and analysis

tools for developing comprehensive Maritime Domain Awareness capabilities. The MNR consists of dozens of radars that represent a precise cross section of today's actual MNR environment. An integrated suite of advanced sensors has been developed for data collection and processing to identify and classify vessels. A suite of similar sensors and processors has been integrated into a transportable shelter, the Modular Sensor System (MSS), that can be rapidly deployed to ports or other sites for enhanced maritime awareness reporting.

Scientific Development Squadron ONE (VXS-1)

Scientific Development Squadron ONE (VXS-1), located at Naval Air Station (NAS) Patuxent River, MD, is manned by 13 Naval officers, 49 enlisted sailors, and nine civilians. VXS-1 provides airborne Science and Technology (S&T) research platforms to support Naval Research Laboratory and Office of Naval Research (ONR) projects. VXS-1 is the sole airborne S&T squadron in the U.S. Navy and conducts scientific research and advanced technological development for the Department of Defense, the Department of the Navy,



VXS-1 Warlock detachment to Cooperative Security in Comalapa, El Salvador.

Naval Air Systems Command (NAVAIR), the National Science Foundation (NSF), the Missile Defense Agency (MDA), the Joint Improvised Explosive Device Defeat Organization (JIEDDO), the National Oceanic and Atmospheric Administration (NOAA), and many other governmental and nongovernmental agencies. VXS-1 operates and maintains five NP-3D/Cs and two RC-12 research aircraft. In addition, the squadron also serves as the Aircraft Reporting Custodian (ARC) for nine ScanEagle Unmanned Aerial Systems (SE UAS) and the U.S. Navy's only manned airship, the MZ-3A.

VXS-1 routinely conducts a wide variety of S&T missions from remote detachment sites around the globe. In 2013, the squadron completed research detachments to Al Udeid AB, Qatar; Marine Corps Air Station Kaneohe Bay, HI; Cooperative Security

Location Comalapa, El Salvador; NAS Point Mugu, CA; NAS Oceana, VA; Bangor, ME; NAS Fallon, NV; and numerous local flights from NAS Patuxent River, MD. The squadron has provided flight support for a number of diverse research programs: NRL Marine Geosciences Division's Project PERSEUS, sponsored by JIEDDO, performing multiband synthetic aperture radar (MBSAR) counter-IED capabilities expansion research; ONR Code 31's ROUGH WIDOW system,



Scientific Development Squadron ONE personnel.

focused on systems integration, sensor fusion, and performance testing of systems in operational maritime patrol environments; multiple detachments supporting the Missile Defense Agency's testing and experimentation, vital to the success of air- and surface-based missile tracking and interceptor tests; the U.S. Army Joint Land Attack Cruise Missile Elevated Netted Sensor System (JLENS), providing the Airborne Early Warning/Cooperative Engagement Capability platform for sensor and datalink testing; NRL's Tactical Electronic Warfare (TEW) Division, supporting the Navy's electronic warfare requirements; Office of Naval Research's PMR-51 Gimbaled Airborne Tracking Radar II Project sensor development and testing; and multiple RC-12 detachments supporting both NOAA's Gravity for the Redefinition of the American Vertical Datum (GRAV-D) survey and Multiple-Link Common Data Link System (MLCS) testing for NRL Code 5554. The squadron's ongoing contributions to the Naval Research enterprise now total over 71,600 flight hours spanning fifty one years of Class "A" mishap-free operations.

Midway Research Center

The Midway Research Center (MRC) is a world-wide test range that provides accurate, known signals as standards for performance verification, validation, calibration, and anomaly resolution. In this role, the MRC ensures the availability of responsive and coordinated scheduling, transmission, measurement, and reporting of accurate and repeatable signals. The MRC, under the auspices of NRL's Naval Center for Space Technology, provides NRL with state-of-the-art facilities dedicated to Naval communications, navigation, and basic

research. The headquarters and primary site is located on 162 acres in Stafford County, Virginia. The main site consists of three 18.2 m, radome-enclosed precision tracking

antennas and a variety of smaller antennas. The MRC has the capability to transmit precision test signals with multiple modulation types. Its

normal configuration is transmit but can be configured to receive as required. The MRC also provides cross-mission and cross-platform services from worldwide locations using a combination of fixed and transportable resources and a quick-reaction, unique signals capability. Assets include Pulstar Systems (several worldwide locations), a 45 m tracking antenna in Palo Alto, California, and a 25 m tracking antenna system on Guam. The MRC instrumentation suite includes nanosecond-level time reference to the U.S. Naval Observatory, precision frequency standards, accurate RF and microwave power measurement instrumentation, and precision tracking methodologies. The MRC also contains an Optical Test Facility with two specialized suites of equipment: a multipurpose Transportable Research Telescope (TRTEL) used for air-to-ground optical communications and for passive satellite tracking operations, and a satellite laser ranging (SLR) system built around a 1 m telescope as a tool for improving customer ephemeris validation processes.



Midway Research Center satellite calibration facility in Stafford, Virginia.

Pomonkey Facility

The Naval Research Laboratory's Pomonkey Facility is a field laboratory with a variety of ground-based antenna systems designed to support research and development of space-based platforms. Located 25 miles south of Washington, D.C., the facility sits on approximately 140 acres of NRL-owned land, which protect its systems from encroaching ground-based interferers. Among its various precision tracking antennas, the facility hosts the largest high-speed tracking antenna in the United States. Boasting a diameter of 30 m, its range of trackable platforms includes those in low Earth orbit through those designed for deep space missions. The facility's antenna systems are capable of supporting missions at radio frequencies from 50 MHz through 20 GHz and can be easily configured

to meet a variety of mission requirements. The ease of system configuration is due to the facility's stock of multiple antenna feeds, amplifiers, and downconverters. Other facility assets include an in-house ability to design, fabricate, test, and implement a variety of radio frequency components and systems. The facility also hosts a suite of spectrum analysis instrumentation that, when coupled to its antenna systems, provides a unique platform for a variety of research and development missions.



The NRL Pomonkey Facility.

Blossom Point Satellite Tracking and Command Facility

The Blossom Point Tracking and Facility (BPTF) provides engineering and operational support to several complex space systems for the Navy and other sponsors. BPTF provides direct line-of-sight, two-way communications services with spacecraft in multiple bands and multiple orbits including LEO, HEO, GEO, and lunar. Additionally, with BPTF as an external node on the Air Force Satellite Control



Blossom Point Satellite Tracking and Command Facility.

Network (AFSCN), it has the capability to provide coverage worldwide. BPTF consists of a satellite mission operations center, multiple antennas, and an infrastructure capable of providing space system command, control, and management to most on orbit assets worldwide.

Specific BPTF resources include the following:

- *Neptune™/Common Ground Architecture Software (CGA)*: is government-owned software that provides infrastructure and reusable components facilitating construction of command, control, and monitoring systems for space vehicle development, integration,

test, and operations. Neptune™/Common Ground Architecture with Automated Ground Operations (AGO) software allows for 5 × 8 (lights out) operations on 24 × 7 operations. Current missions include 13 satellites with 186 worldwide contacts per day. The GAO-10-55 report dated October 2009, titled *Challenges in Aligning Space Systems Components*, lauds BPTF with Neptune™/Common Ground Architecture as one facility that can control a variety of satellites.

- **Hardware Architecture:** Based on RF, video, and matrix switching with net-centric control and processing, virtually any hardware asset can be “switched” into a path to create the correct capability required for any mission. This architecture supports both classified and unclassified operations and missions, and internal LANs support multiple simultaneous mission operations. Salient resources include antennas; receivers; telemetry, tracking, and command (TT&C); command encoder; front-end processors; operations automatic data processing (ADP) resources; and satellite health and monitoring/engineering.

Marine Coatings Facility

The Chemistry Division’s Marine Coatings Facility located in Key West, Florida, offers a “blue” ocean environment with natural seawater characterized by historically small compositional variation and a stable biomass. This continuous source of stable, natural sea-



Demonstration of the removal of non-skid coating by heat induction at NRL Key West.

water provides a site ideally suited for studies of marine environment effects on materials, including accelerated and long-term exposure testing and materials evaluation. The site maintains capa-

bilities for extensive RDT&E of marine engineering and coatings technologies and supports a wide array of Navy and industrial sponsors. Equipment is available for experiments involving accelerated corrosion and weathering, general corrosion, long-term immersion and alternate immersion, fouling, electrochemical phenomena, coatings application and characterization, cathodic protection design, ballast water treatment,

marine biology, and corrosion monitoring. In 2009, the facility received a comprehensive refurbishment due to hurricane damage.

Ex-USS *Shadwell* Research Platform

The Navy Technology Center for Safety and Survivability has a full-scale test ship, the ex-USS *Shadwell* located at the Joint Maritime Test Detachment (JMTD), Little Sand Island, Mobile, Alabama. The ex-USS *Shadwell* is a 457 ft, 9000 ton dock landing ship (LSD). All ship systems germane to damage control are main-



Moored in Mobile Bay, Alabama, the ex-USS *Shadwell* is regularly set ablaze in a controlled environment to further the safety of operational Navy and civilian firefighting measures.

tained including heating and air conditioning (HVAC), smoke ejection system (SES), one complete Collective Protection System (CPS) (replicating zone two of the DDG 51 class ships), electrical, lighting, and internal communication systems (including wire-free and WLAN communications). Specialized test areas include a hangar bay, flight deck with helicopter mockup, submarine test area, machinery space, shipboard magazine including a PVLS magazine, and well deck/vehicle storage areas. Three damage control lockers are also maintained. The data are collected and displayed via a blown fiber gigabit network that is distributed throughout the ship. In addition, Little Sand Island has a wave tank that is used for in situ burn tests and studies for oil spill containment.

80 Sputtered Thin-Film Absorbers for Flexible Photovoltaics

87 Single-Component Polysiloxane Coating for Navy Topsides

95 Graphene as a Tunnel Barrier

105 Molecular Epidemiology of Global Antimicrobial Resistance

113 The Stuff Coronal Mass Ejections Are Made Of

120 Low Power Microrobotics Utilizing Biologically Inspired Energy Generation

CIGS: A Healthy Habit for Flexible PVs

NRL Optical Sciences Division researchers who have PVs (photovoltaics) in their CVs (curricula vitae) have turned to copper indium gallium diselenide (CIGS) as the most promising candidate thin-film PV material for flexible, lightweight power needs. The Department of Defense (DoD) is a huge consumer of fossil fuels, which have presented unsustainable costs and great risk to personnel, potential loss of supply lines, and reduced force mobility. Photovoltaics, that is, solar power turned into electricity, could provide a much-needed solution, especially for such uses as unmanned aircraft and battery charging in the field. CIGS solar cells are most commonly made by depositing a film on rigid glass substrates, but rigid glass and combat conditions do not mix. Just as a fighting force must be flexible, so must its high-power PV devices. Thin-film PVs provide that flexibility, but flexible thin-film PVs made from amorphous silicon lack the efficiency needed for such high-power applications as foldable, man-portable solar blanket modules. The challenge is then to make CIGS devices on flexible substrates. Co-evaporated from four elemental sources onto flexible polyimide (PI) substrates, CIGS has provided up to a record 20% sunlight-to-electricity efficiency in laboratory settings. However, achieving simultaneous control over all four sources is difficult (copper in particular has a high evaporation temperature), making uniform deposition over large areas an elusive goal. If greater efficiency is to be achieved in mass-manufactured high-power PV devices, another method had to be found.

Sputtering CIGS onto flexible substrates from a single quaternary target that contains all four components (selenium in addition to the metals) seems to do the trick. Just as DVD manufacturers use sputtering to deposit metals over large areas, NRL researchers are using the process to produce CIGS films, achieving efficiencies so far of 11%, with much higher efficiency expected as the technology is refined. This manufacturing-friendly process has produced good results with rigid glass substrates, but total flexibility remaining the goal, PI and Corning Willow Glass (a flexible glass) were tested as substrates. Weight vs performance is being considered in assessing the two materials, but results to date look promising.

Smoking cigarettes is unhealthy, but sputtering CIGS onto flexible substrates seems to be the healthiest power solution for DoD.

Sputtered Thin-Film Absorbers for Flexible Photovoltaics

J.A. Frantz,¹ J.D. Myers,¹ R.Y. Bekele,² V.Q. Nguyen,¹ and J.S. Sanghera¹

¹*Optical Sciences Division*

²*University Research Foundation*

Flexible thin-film photovoltaics (PVs) have been proposed as an appealing power source for applications including unmanned aircraft systems and battery charging in the field. PVs based on silicon and III-V materials typically require thick substrates that add significant weight. Furthermore, their rigidity limits design options, requiring large, flat surfaces. Thin-film PVs offer a potential solution with specific power significantly higher than that of traditional PVs and the potential for flexible devices. Among thin-film PV materials, copper indium gallium diselenide (CIGS) has produced the best laboratory results on rigid glass substrates. Typically, CIGS is deposited by co-evaporation or, alternately, by deposition of the metals with, or followed by, treatment in a selenium environment. We present results from an alternative deposition method that instead uses sputtering from a single quaternary target. This technique is highly manufacturable, and we have already produced devices with conversion efficiencies of over 11%.

INTRODUCTION

The Department of Defense (DoD) is the world's largest organizational user of fossil fuels, with consumption of about 117 million barrels of oil in FY2011.¹ This heavy reliance on petroleum presents significant difficulties, including the vulnerability of supply lines to attack, reduced mobility of forces due to a dependence on supply lines, and loss of life in transporting fuel. The high cost of fuel is also a concern. A 2010 study by the Marine Corps in Afghanistan placed the fully burdened cost of fuel — a measure that includes the cost of personnel, equipment, and force protection required for transportation — at \$9 to \$16 per gallon if delivered by land and \$29 to \$31 for fuel delivered by air.¹ Furthermore, the need for electrical power frequently limits the lifetime and scope of missions for autonomous systems. Generation of some portion of the required electrical power in the field would relieve demands on the supply line, reduce the load carried by an individual soldier, and expand the capabilities of various unmanned platforms.

For these reasons, there has recently been intense interest in solar energy for DoD applications. Traditional PV materials, such as silicon and III-V material systems, are not ideally suited to all DoD needs since they use thick substrates that add significant weight and lack flexibility. Thin-film PVs offer the most promising potential solution, with specific power (measured in W/kg) significantly higher than that of traditional PVs and the potential for flexible devices such as a foldable solar blanket module that can be easily carried in a backpack.

First-generation flexible thin-film PV devices currently in use in the field are based on amorphous silicon PVs that typically provide 6% to 8% efficiency. A module with 20% efficiency would result in more than twice the power for the same size module. Existing thin-film PV technologies do not offer a viable pathway to achieving this efficiency since amorphous silicon PV is believed to be near its upper efficiency limit, and cadmium telluride must be deposited on a rigid glass substrate. PV devices based on copper indium gallium diselenide (CIGS), however, have been demonstrated on flexible polyimide (PI) and metal foil substrates. These materials present the most promising pathway to higher efficiency flexible modules.

The most well-established method of depositing CIGS is by co-evaporation from four independent elemental sources.² This technique has resulted in laboratory devices with record efficiencies of approximately 20%. While this method has produced excellent devices, there are several disadvantages associated with it. As a result of the point source nature of typical evaporation sources, uniform deposition over large areas is difficult. Copper, with the highest evaporation temperature, presents the greatest difficulty. Simultaneous control of all four sources can be challenging, with variations in relative deposition rate potentially leading to incorrect stoichiometry and diminished device performance.

QUATERNARY SPUTTERED CIGS

More recently, there has been interest in deposition by sputtering from a quaternary target — a single

sputtering target that contains Se as well as the metals.³ Sputtering is a well-established technology for large-area deposition. For instance, decorative window glass, the type one might see on an office building, is typically deposited by sputtering as are the coatings on rewritable DVDs. Naval Research Laboratory (NRL) scientists have developed a method that uses sputtering from a single quaternary target (i.e., one that contains all four constituent elements) without additional selenization. We have fabricated working devices using CIGS films that are sputtered in a single step and have demonstrated conversion efficiency as high as 11%. This technique offers the potential for scale-up to large volume manufacturing on flexible substrates.

Figure 1 illustrates the quaternary sputtering process developed at NRL. Bulk CIGS is formed by heating high purity precursors in a vacuum-sealed quartz am-

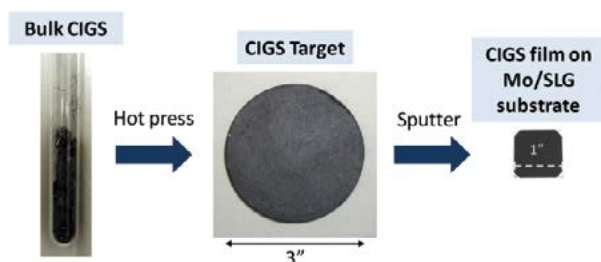


FIGURE 1 Fabrication steps in a quaternary sputtered CIGS process. Bulk material is batched, pressed into a disk, and machined to appropriate dimensions for a target. Thin films are sputtered under high vacuum. SLG = soda lime glass.

poile. The bulk material is ground into a powder inside a nitrogen-purged glovebox, and sputtering targets are formed by hot-pressing the powder into 3 in. diameter disks. The disks are then machined to the proper dimensions and indium-bonded to a copper backing plate. The targets are installed in a sputter deposition system, and 2 μm thick CIGS films are deposited at an elevated temperature of 550 $^{\circ}\text{C}$ onto substrates that were previously coated with a sputtered Mo bottom contact. Figure 2 is a schematic diagram of the structure of a typical CIGS cell. After the p-type CIGS material is deposited, a 50 nm thick layer of n-type CdS is deposited in order to form a junction. Several hundred nanometers of ZnO and $\text{Al}_2\text{O}_3\text{:ZnO}$ (AZO) are deposited by sputtering to serve as a transparent top contact. Finally, patterned grids composed of Ni and Al, which aid in charge collection, are deposited via evaporation. The vacuum deposition steps are performed in a cluster tool in the Optical Sciences Division as shown in Fig. 3. This system includes a glove box, two sputterers (one of which is designed especially for selenium- and sulfur-based compounds), and two evaporators. The system allows a different deposition mask to be applied

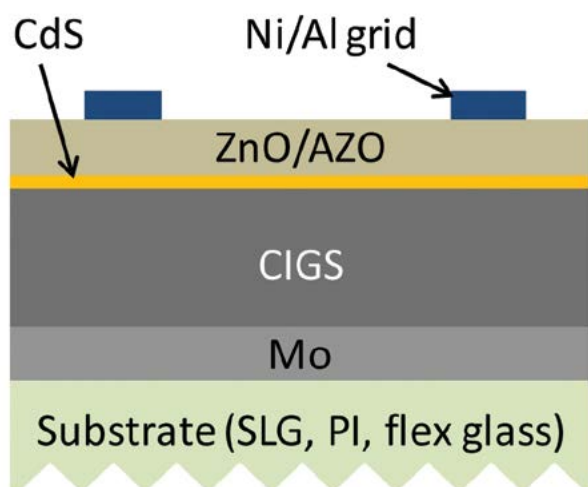


FIGURE 2 Schematic diagram of a typical CIGS cell.



FIGURE 3 Vacuum deposition cluster tool in the Optical Sciences Division. A glove box allows sample loading and manipulation without exposure to air, and robotic transfer moves samples among chambers to build complex, multilayer devices.

for each layer, permitting the fabrication of complex, multilayer devices without ever removing samples to air.

SEM images, shown in Fig. 4, compare the structure of an evaporated film, fabricated externally to NRL, with a quaternary sputtered film. Both deposition methods yield dense films, with 1 μm scale grains at the top surface. One significant difference is the presence in the sputtered film of ~ 100 nm scale grains near the Mo/CIGS interface that coalesce into larger grains near the top surface of the film.

Figure 5 shows device results from a typical 0.5 cm^2 sputtered CIGS device. Light J - V curves were obtained in a solar simulator under one sun, AM1.5G illumination, conditions meant to simulate unconcentrated sunlight on Earth's surface. For this device, the

short circuit current density is 34 mA/cm^2 , the open circuit voltage is 490 mV , the fill factor is 64% , and the sunlight to electricity conversion efficiency is 11% . The inset plot shows the external quantum efficiency (EQE), a measure of the incident photons that produce charge carriers, as a function of wavelength. The EQE is above 80% for short wavelengths, consistent with high-quality absorber material.

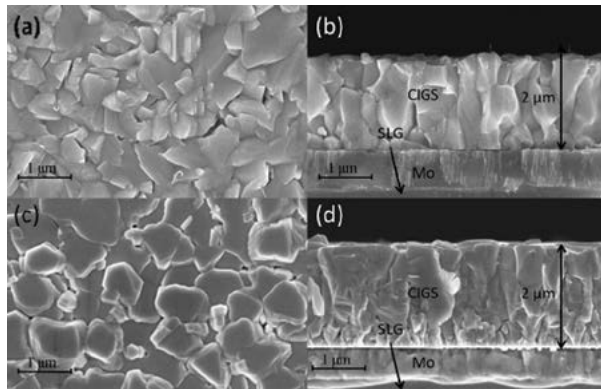


FIGURE 4 SEM images showing a top view (a) and cross section (b) of evaporated CIGS and a top view (c) and cross section (d) of sputtered CIGS.

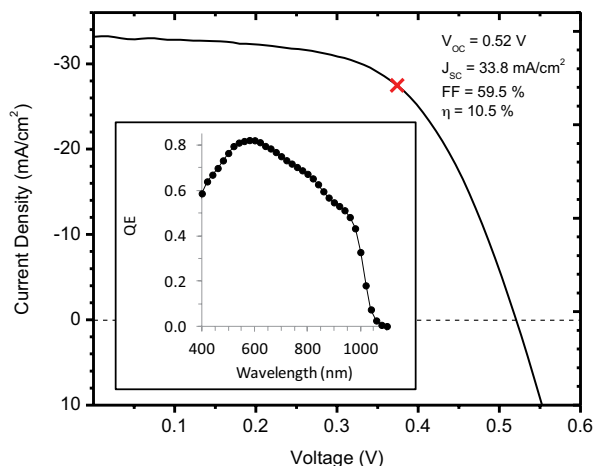


FIGURE 5 Light J - V of a sputtered CIGS device measured under AM1.5 illumination. The red "X" indicates the point of maximum power, and the inset shows measured EQE.

MANUFACTURABILITY AND SCALE-UP

To make a large impact on energy consumption for DoD applications, large areas of PV materials will be needed. Sputtering is a technology that is well suited for scale-up to an industrial process. One factor that is important in this case is material utilization. During sputtering, material is preferentially removed from the target in a characteristic "racetrack" pattern, based on the distribution of the magnetic field. Typically, about 50% of the material is used before the entire thickness

of the target is consumed within a racetrack. In order to assure that unused material can be reclaimed, we performed a series of experiments in which several old targets were recycled into new ones. Figure 6(a) shows a spent target with a characteristic racetrack pattern, while Fig. 6(b) shows a target made of reclaimed material. The performance of the resulting devices was as good as the performance of those made from unused precursors, demonstrating material utilization for the quaternary sputtering process can be very high.

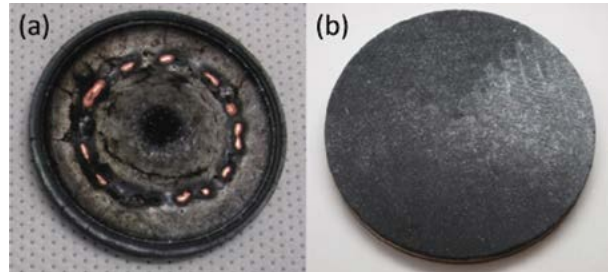


FIGURE 6 A spent target is shown in (a), with a typical racetrack wear pattern visible, while (b) shows a target formed from material recaptured from two spent sputtering targets.

SPUTTERED CIGS ON FLEXIBLE SUBSTRATES

Results for sputtered films on rigid glass substrates have been promising, indicating that the method is viable for scale-up for manufacturing purposes. The ultimate goal, however, is a large-scale process that can be used to make flexible solar cells. Two flexible substrate materials, polyimide and Corning Willow Glass, were evaluated for this purpose. Willow Glass is a flexible glass with a bending radius small enough that it is compatible with roll-to-roll processing. Calculations of module weight were made assuming a module efficiency of 15% for each substrate type, unconcentrated AM1.5G illumination, and substrate thicknesses of 1 mm for the soda lime glass (SLG) and $50 \mu\text{m}$ for each of the thin-film materials.

The weight of each of the thin-film substrates is significantly less than that of the rigid glass substrate, with PI lighter by a factor of more than 30, and Willow Glass lighter by a factor of more than 20. Willow Glass has the advantage that it can withstand temperatures above $600 \text{ }^\circ\text{C}$, making it compatible with the high temperatures preferred in CIGS processing. Devices on polyimide, on the other hand, must be deposited below the optimum deposition temperature of $550 \text{ }^\circ\text{C}$ to prevent degrading the PI. Even though Willow Glass is slightly heavier than PI, the higher processing temperatures may eventually result in better device performance, so NRL is continuing to assess both materials.

To evaluate NRL's technology for use with flexible substrates, the sputtered CIGS process was applied to

make devices on several types of flexible substrates. CIGS was sputtered onto 125 μm thick PI films and onto 100 μm thick sheets of Willow Glass. Figure 7 shows several examples of working flexible sputtered CIGS devices. Figure 7(a) shows devices on a PI substrate. A Willow Glass substrate with a 3 \times 3 array of Mo bottom contacts is shown in Fig. 7(b). The inset shows completed devices on one of the bottom contact pads. A polymer protection tab, visible as an orange band in the images, was used for handling during fabrication.

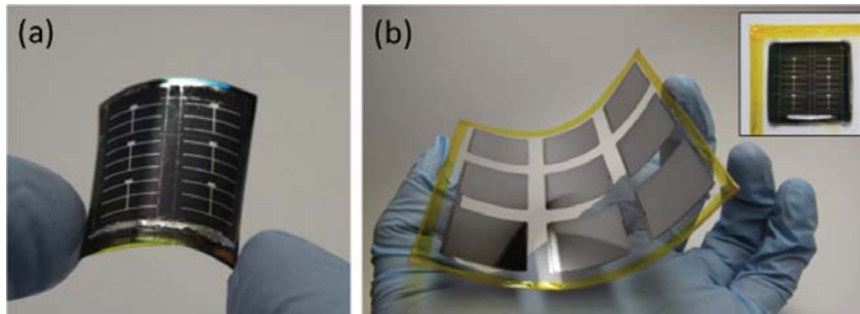


FIGURE 7
Flexible substrates for sputtered CIGS. A PI substrate with completed devices is shown in (a). A Corning Willow Glass substrate with a 3x3 array of Mo bottom contacts is shown in (b). The inset shows completed devices on one of the bottom contact pads.

CONCLUSIONS

Quaternary sputtered CIGS offers a promising pathway to the large-scale manufacturing of flexible thin-film solar cells. Sputtering is a well-established technique for large-scale manufacturing, and NRL's work has demonstrated that it is viable for CIGS-based PVs. With target reclamation, material utilization is quite high, making the technology cost effective as well. The method has been demonstrated to produce working devices on several types of flexible substrates. Moving forward, this technology is viable for scale-up for large-area, roll-to-roll deposition, and has a promising future for DoD applications such as power for unmanned aircraft systems and battery charging in the field.

ACKNOWLEDGMENTS

The authors gratefully acknowledge financial support from the Office of Naval Research and Sunlight Photonics, Inc. They also thank their collaborators in the Solid State Devices Branch: Dr. Sergey Maximenko, who obtained the EQE data, Dr. Maria Gonzalez, Dr. Joe Tischler, and Dr. Robert Walters.

[Sponsored by the NRL Base Program (CNR funded) and Sunlight Photonics, Inc.]

References

- ¹ M. Schwartz, K. Blakeley, and R. O'Rourke, "Department of Defense Energy Initiatives: Background and Issues for Congress," Congressional Research Service, Dec. 10, 2012.
- ² S. Niki, M. Contreras, I. Repins, M. Powalla, K. Kushiya, S. Ishizuka, and K. Matsubara, "CIGS Absorbers and Processes," *Prog. Photovolt. Res. Appl.* **18**, 453–466 (2010).
- ³ J.A. Frantz, R.Y. Bekele, V.Q. Nguyen, J.S. Sanghera, A. Bruce, S.V. Frolov, M. Cyrus, and I.D. Aggarwal, "Cu(In,Ga)Se₂ Thin Films and Devices Sputtered from a Single Target without Additional Selenization," *Thin Solid Films* **519**, 7763–7765 (2011). ♦

We've got you covered, topsides...

The predominant topside (freeboard and superstructure) coating used on U.S. Navy surface ships for the last 50 years has been haze gray silicone alkyds. These coatings are simple, single-component (1K) products that have a limitless pot-life (in a closed can) and will cure in the harsh marine environment. Unfortunately, these “user friendly” silicone alkyd paints have shown to exhibit higher levels of fading, chalking, loss of gloss, and vulnerability to rust-staining than more advanced coating systems that have entered the market over the past decade. As a result of the inherent performance limitations of silicone alkyds, sailors have historically spent a lot of their time repainting or touching-up the topsides of ships. This maintenance painting is a mundane task that can add extra weight to a ship, and if not performed in accordance with requirements, can lead to unsightly peeling of the coating.

So, the challenge faced by the Naval Sea Systems Command (NAVSEA) was to find a commercial, high-performance coating system that could shift the paradigm for the sailor from one of regularly repainting the ships to one of simply cleaning a durable, color-stable haze gray topside coating. Two-component (2K) polysiloxane coatings were identified as offering the best opportunity to shift the paradigm away from having to repeatedly repaint ship topsides. These polysiloxane products were tested on Navy ships beginning in 2005, and their enhanced color-stability, gloss retention, and cleanability versus silicone alkyds have been proven over the past 8 years. Unfortunately, these two-component products are not as “user friendly” as the single-component silicone alkyds, and will not cure properly if inadequately mixed.

NRL chemists have stepped up to the challenge to create a more “user friendly” and high performance polysiloxane topside coating. The newly designed and patented technology is a single-component polysiloxane coating that has demonstrated better color stability, hardness, solvent resistance, and adhesion than silicone alkyds when tested in the laboratory, including greater color stability than two-component polysiloxanes. The coating also has an indefinite pot-life (in a closed can) and is low in volatile organic compounds (VOCs). Preliminary results from small demonstrations aboard several Navy surface ships show that the new coating is outperforming all current qualified coatings with regard to color stability. Thus far, the new, single-component polysiloxane is proving itself as an invaluable tool for reducing the sailor painting workload, while ensuring Navy ships maintain the haze gray color over the longer term.

Single-Component Polysiloxane Coating for Navy Topsides

E. Iezzi, J. Martin, J. Tagert, P. Slebodnick, J. Wegand, and E. Lemieux
Center for Corrosion Science and Engineering

Silicone alkyds have been the Navy's standard haze gray topside coating for nearly 50 years and remain the only single-component paints qualified under military specification MIL-PRF-24635 (Coating System, Weather-Resistant, Exterior Use). Although the predominant coating in the Fleet, silicone alkyd coatings are inherently limited in color and gloss retention, cure time, and exhibit limited cleanability, especially as it relates to rust staining. To address these issues, the Naval Research Laboratory (NRL) has recently designed and patented a novel single-component polysiloxane coating for Navy topsides. When tested in the laboratory, the coating has demonstrated exceptional color stability, hardness, solvent resistance, and adhesion that rivals silicone alkyds, in addition to outperforming the recently qualified two-component polysiloxane topside coatings with respect to color stability. The new coating is currently being demonstrated aboard the USS *Oak Hill* (LSD 51) and USS *Hopper* (DDG 70) surface ships. NAVSEA program sponsors are interested in transitioning the new coating to the Fleet, and NRL is working to obtain all the required performance testing, safety reviews, and chemical registrations required to field the innovative, new technology.

BACKGROUND

The U.S. Navy's predominant haze gray topside coatings are single-component silicone alkyds that are qualified under MIL-PRF-23635¹ for use on the topsides (freeboard and superstructure) of surface ships. These coatings have been in use by the Navy since the early 1960s, and were originally specified under TT-E-490² as semigloss coatings. These coatings have proven over the years to be "user friendly" in that they are single-component paints that have an indefinite pot-life (in a closed can), have been reformulated to maintain compliance with volatile organic compound (VOC) limits, and will cure even under the most adverse conditions. Unfortunately, these user-friendly paints have several inherent limitations, which include color fading, color shifting toward a pinkish hue with low solar absorbance (LSA) variants, chalking, loss of gloss, and limited surface hardness that makes running rust and soot staining extremely difficult to remove. In addition, peeling, cracking, and delamination of cured silicone alkyds can often result due to application over inadequately prepared surfaces. Silicone alkyd coatings have provided the Navy with decades of acceptable performance and repeated product reformulations; however, the current demands for topside coatings on Navy ships mean that evolutions of silicone alkyds have reached their end-point.

Silicone Alkyd Coatings

Silicone alkyd coatings are formulated as single-component (1K) systems (all-in-one can) because they

contain unsaturated fatty acid groups that crosslink in the presence of atmospheric oxygen. The coatings do not begin to cure until they are applied to a surface and the solvent evaporates, thereby possessing essentially a limitless pot-life in a closed can. For Navy ships, silicone alkyd topside coatings are specified as a Haze Gray color (Fed. Std. 26270) with a semigloss finish, are available in a variety of volatile organic compound (VOC) levels (e.g., 340 g/L, 250 g/L), and have a service-life of approximately 6 to 12 months. Ship's Force can often be found applying silicone alkyd coatings via roller or brush for the sake of touch-up and repair during field and depot level maintenance (Fig. 1(a)), yet this mundane and non-war-related task would not be required if silicone alkyd coatings did not easily fade, discolor, peel/delaminate (Fig. 1(b)) or stain within a few months after application. A single application of silicone alkyd is specified at 2 to 5 mils dry film thickness (DFT); however, due to the constant overcoating by sailors, it is not uncommon for surface ships to possess greater than 50 mils of topside coating.

In the late 1990s, the Navy began using silicone alkyd topside coatings with low-solar-absorbing (LSA) pigments, which later became specified in MIL-PRF-24635 as Grades B and C. These pigments are incorporated to reduce the thermal loads on ships and corresponding energy required to cool the interior spaces, which can become uncomfortable for sailors on hot summer days. LSA pigments provide reflectivity of solar energy in the near-infrared (NIR) region (780 to 2500 nm), which is commonly known as the "heat region" of sunlight. Unlike non-LSA silicone alkyds that contain mainly carbon black and white to provide



FIGURE 1
 (a) Roll application of a silicone alkyd topside coating by Ship's Force, and (b) peeling/delamination of a silicone alkyd topside coating on a Navy ship.

the Haze Gray color, LSA versions yield Haze Gray by using a mixture of titanium dioxide (white), red iron oxide, yellow iron oxide, and copper phthalocyanine blue pigments. This mixture provides a reflectivity of approximately 80% in the 780 to 1200 nm range, as opposed to a mere 10% to 20% when formulated with titanium dioxide and carbon black pigments. Unfortunately, after only a short period of external exposure, many of the Grade B and C silicone alkyds change from the required Haze Gray color to a pinkish color (Fig. 2), thus deviating from the Navy's camouflage requirements. This undesirable color change results in topside over-coating by Ship's Force with more LSA silicone alkyd, thus leading to a continuous downward spiral



FIGURE 2
 Pinking of LSA silicone alkyd coating on the USS *San Antonio* (LPD-17).

of painting and pinking that leads to excessive coating thicknesses and additional weight to the ships.

Polysiloxane Coatings

Polysiloxane-based coatings have an inherent durability advantage over traditional organic-based materials due to the presence of silicon-oxygen bonds. The Si-O bond, which has a bond enthalpy of 110 kcal/mol, is stronger than the carbon-hydrogen (99 kcal/mol) and carbon-carbon (83 kcal/mol) bonds found in organic coatings, thereby leading to an increase in thermal stability and resistance to oxidative degradation by sunlight. Silicone alkyd coatings can contain up to 30 weight percent of silicone in the base co-polymer to improve weathering; however, this level of addition is still insufficient to overcome the poor weathering contributions from the unsaturated fatty acids groups.

Two-component (2K) polysiloxane coatings are based on materials that contain both reactive organic groups and moisture-curable alkoxy silanes in the same molecules. These coatings are often referred to as "hybrid cure coatings," where one portion of the coating is crosslinked by the ambient reaction between organic groups, such as amines and epoxies, while the other portion forms a siloxane network via moisture hydrolysis of the alkoxy silane groups and condensation of the resulting silanols. These coatings offer excellent exterior durability, hardness, chemical resistance, and direct-to-metal adhesion; however, they can suffer from photo-oxidation and yellowing due to the presence of amines in the coating. The Navy has recently qualified several commercial two-component (2K) polysiloxane coatings for topside use under MIL-PRF-24635, Type V, and all are outperforming silicon alkyd coatings in the field. Unfortunately, these polysiloxane coatings require the mixing of components before application, which can result in insufficient cure times, reduced hardness, poor adhesion, and poor appearance if Ship's Force and/or contractors do not mix the materials correctly.

Single-component (1K) polysiloxane coatings are typically based on acrylic-silane binders. These binders are manufactured via radical polymerization of gamma-methacryloxypropyltrimethoxysilane with methyl methacrylate, hexyl acrylate or other organic monomers to form linear copolymers with pendant alkoxy silane groups (Fig. 3). The copolymers are high in molecular weight and require significant quantities of solvent(s) to solubilize the large polymer chains, thus making it difficult to generate low VOC coatings. The pendant alkoxy silane groups are the only reactive functionalities on the copolymer, which enables the coating to be cured via moisture hydrolysis and condensation. Single-component coatings based on these binders are available on the commercial market from several manufacturers, although they are not without

their drawbacks. For instance, these coatings are slow to hydrolyze and crosslink (cure) at room temperature when not exposed to high humidity environments, and they display poor chemical resistance when not fully cured due to the low crosslink density within the coating. These issues result because the acrylic-silane copolymers in the coating contain pendent propyltrialkoxysilane groups that are inherently slow to hydrolyze and limited in quantity when compared to non-reactive groups in the copolymer backbone. This contrasts the two-component polysiloxane coatings that contain aminopropyltrialkoxysilanes and are faster to hydrolyze. Acrylic-silane binders often possess glass transition temperatures (T_gs) above room temperature in order to provide fast dry-to-touch times (e.g., 1-3 hours) as the solvent evaporates, although this attribute should not be confused with rapid crosslinking (curing) of the binders.

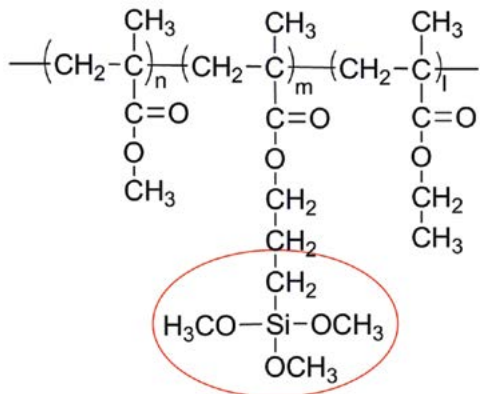


FIGURE 3
General structure of an acrylic-silane with pendent trimethoxysilane group.

A single-component polysiloxane coating that provides excellent exterior durability (color and gloss retention), low VOCs, low toxicity, good chemical resistance and adhesion, moderate cure times over a wide range of humidity, a semigloss finish, and is easy for Ship's Force to apply does not currently exist, and a solution is desperately needed for the touch-up and repair of Navy topside coatings.

Advanced Single-Component Polysiloxane Coating

The Naval Research Laboratory has recently developed a novel moisture-curable polymer for a single-component (1K) polysiloxane topside coating.³ The technology is based on an N-substituted urea framework with terminal alkoxy silane groups (Fig. 4) and addresses the issues of slow cure times, high VOC content, and solvent resistance that are associated with commercial 1K polysiloxane coatings based on

acrylic-silane copolymers. NRL's technology enables the formulation of a low VOC and Hazardous Air Pollutants (HAPS) free coating with excellent exterior durability, surface hardness, and solvent resistance, in addition to good adhesion over bare steel and epoxy primed substrates. The coating can be applied via spray, brush or roll, and most importantly, provides Ship's Force with a system that does not require the mixing of components before application.

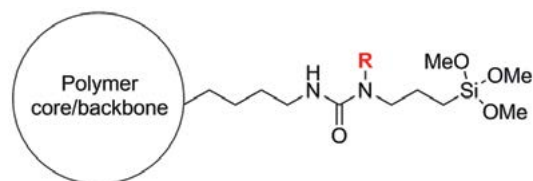


FIGURE 4
A generic structure of NRL's single-component polymer.

The polymer possesses a unique design that enables its terminal alkoxy silane groups to hydrolyze and crosslink faster than the alkoxy silanes found in acrylic-silanes. It is believed that this acceleration is due to the inclusion of specific "R" groups on nitrogen atoms of the urea linkages, which lead to accelerated hydrolysis of the terminal alkoxy silanes. This is currently under investigation at NRL. In addition, because one of the nitrogen atoms in the urea linkages contains a second substituent, the urea groups in the polymer are no longer planar, thereby providing lower intermolecular hydrogen bonding character than would otherwise be found in a traditional urea polymer. This in turn leads to a reduced viscosity for the polysiloxane polymer that requires less solvent to form a usable coating, in addition to providing for a system with greater internal flexibility.

When tested for exterior color stability using accelerated weathering instruments, NRL's 1K LSA polysiloxane outperformed qualified LSA silicone alkyds and 2K LSA polysiloxane topside coatings. As shown in Fig. 5, exposure to artificial sunlight (Xenon-Arc Weatherometer, ASTM G155) for 3000 hours resulted in a color change (ΔE) of only 0.6 for the NRL 1K polysiloxane, whereas the silicone alkyds demonstrated a pronounced color change over time. The 2K polysiloxane coating performed well, and the color change of greater than 1.0 after 3000 hours was only slightly noticeable to the eye. Exposure of the 1K polysiloxane to the more destructive UV-B radiation (ASTM G154, 313 nm bulb) for 3000 hours demonstrated a color change of less than 0.70, whereas the silicone alkyds and 2K polysiloxane began to yellow after only a few hundred hours. It should be noted that a color change of ≤ 1 is undetectable by the human eye.

Table 1 shows a comparison of tack-free times (ASTM D5895), surface hardness (ASTM D4366), and

Color change of LSA coatings after 3000 hours Weatherometer (WOM)

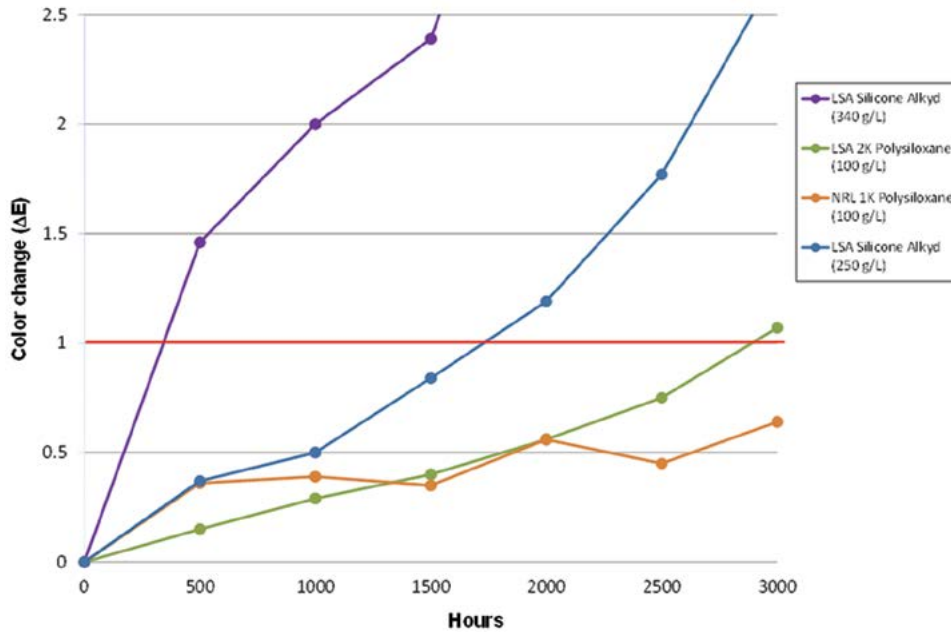


FIGURE 5 Xenon-Arc weathering comparison of NRL’s 1K LSA polysiloxane coating, a Navy qualified 2K LSA polysiloxane coating, and two Navy qualified LSA silicone alkyd coatings.

TABLE 1 — Comparison of coating properties between NRL’s 1K polysiloxane with various amounts of a catalyst, a commercial 1K polysiloxane (acrylic-silane based), and a Navy qualified silicone alkyd.

3 mil (75µm) films @ 71°F, 49% R.H.			
	← properties after 7 days →		
1K Coating	Tack-free times	Hardness- KönigPendulum	MEK Resistance- dbl. rubs
NRL polysiloxane w/ 0.3% cat.	3 hrs.	76 osc.	100+ (no damage)
NRL polysiloxane w/ 0.15% cat.	3-4 hrs.	71 osc.	100+ (no damage)
NRL polysiloxane w/ no cat.	7 hrs.	21 osc.	25 (marred)
Commercial polysiloxane	1 hr.	10 osc.	8 (rubbed through)
Navy Silicone Alkyd	2 hr.	20 osc.	8 (rubbed through)

methyl ethyl ketone (MEK) solvent resistance (ASTM D4752) for NRL’s 1K polysiloxane coating with various amounts of a catalyst, a commercial white 1K polysiloxane (acrylic-silane based), and a Navy qualified silicone alkyd topside coating. All coatings were applied to give 3 mil (75 µm) dry films, and were allowed to cure at ambient conditions for 7 days before being tested. As the table shows, the commercial polysiloxane and silicone alkyd have faster tack-free times than the NRL systems, which are mainly attributed to the copolymers in the coatings having glass transition temperatures (T_gs) above room temperature. However, these commercial systems are extremely slow to crosslink (cure)

when compared to the NRL 1K polysiloxanes, as shown by their low surface hardness and resistance to MEK after 7 days. The NRL 1K coatings with catalysts are significantly harder and more solvent resistant, and even the coating without a catalyst had developed greater solvent resistance within the 7 day period. It is also worth noting that the NRL 1K polysiloxanes will pass a Conical Mandrel Bend (ASTM D522) test without cracking or loss of adhesion.

Several gallons of the NRL 1K polysiloxane were scaled-up by a commercial coating manufacturer, and a small test area (~100 ft²) was used for a topside demonstration aboard the USS *Oak Hill* (LSD-51) in 2011. For

the demonstration, the coating was not color-matched to Haze Gray, and thus has an appearance of a blue-gray color. The coating was inspected after 10 months of active service and remained in excellent condition with a color change (ΔE) of less than 0.25. A Haze Gray (Fed. Std. 26270) colored version was recently roll- and brush-applied by Ship's Force aboard the USS *Hopper* (DDG-70) (Fig. 6), and several additional demonstrations are planned for both Norfolk, VA- and San Diego, CA-based surface ships.



FIGURE 6
Haze Gray version of NRL's 1K polysiloxane topside coating aboard the USS *Hopper* (DDG-70).

The 1K polysiloxane coating is currently being tested and evaluated to MIL-PRF-24635, Type V and VI, Class 2, Grade B specifications under a NAVSEA program, and will transition to the Fleet if proven successful. In addition, the newly developed polymers in the coating must be registered under the EPA's Toxic Substance Control Act (TSCA) before the coating can be utilized in commercial quantities.

SUMMARY

The Naval Research Laboratory has recently developed a novel single-component (1K) polysiloxane coating for the topsides of Navy ships. The coating does not require the mixing of components before application, can be applied direct-to-metal or over an epoxy primer, and outperforms all Qualified Product Database (QPD) silicone alkyds and 2K polysiloxane coatings when tested for color stability in accelerated weathering tests. The technology is designed to give a semigloss finish; is low in VOCs; can be brushed, rolled, or sprayed; and most importantly, provides applicators, such as Ship's Force, with a topcoat that does not require the mixing of components before performing touch-up or repairs to Navy topsides. The coating is currently being demonstrated in small areas on the topsides of active Navy

surface ships while also being tested and evaluated in the laboratory to MIL-PRF-24635 specifications.

ACKNOWLEDGMENTS

The authors would like to acknowledge the support of the Naval Sea Systems Command (NAVSEA) in the development and demonstration of this technology.

[Sponsored by NAVSEA]

References

- ¹ MIL-PRF-24635E, Performance Specification. *Coating Systems, Weather-Resistant, Exterior Use*. September 15, 2009.
- ² G.L. Witucki, "The Evolution of Silicone-Based Technology in Coatings," Dow Corning, 2003; TT-E-490, Federal Specification: *Enamel, Silicone Alkyd Copolymer, Semigloss* (for Exterior and Interior Use), Sept. 25, 1975 [S/S by MIL-PRF-24635].
- ³ E.B. Iezzi, "Single-Component Coatings Having Alkoxysilane-Terminated N-Substituted Urea Resins." U.S. Patent 8,133,964, March 13, 2012.



With Graphene Tunnel Barriers, Resistance Is Not Futile

Graphene, the two-dimensional, hexagonal lattice form of carbon discovered in 2004, has been revealing its unique properties ever since. It can be used as a highly effective atomically thin electrical conductor, but it also exhibits extraordinary out-of-plane resistance and spin transport. Although these properties have not been greatly studied, they might prove just as useful. NRL researchers are testing graphene's applicability as a tunnel barrier for transport perpendicular to the basal plane. With its out-of-plane resistance combined with its low spin-scattering, graphene is poised to become the material of choice in tomorrow's electronic technologies.

Graphene's excellent spin-transport quality is important in two ways: use of it should be able to provide a huge advancement in magnetic random access memory (MRAM) technology, and it should also revolutionize semiconductor spintronics. Today's MRAM devices' chips use magnesium oxide magnetic tunnel barriers on the chips; however, the use of graphene tunnel barriers instead on those chips should reduce resistance significantly, providing faster and smaller non-volatile memory. In semiconductor spintronics applications, graphene will enable a whole new field of electronically reconfigurable logic. Functions that are currently performed in dedicated hardware [Application-specific Integrated Circuits (ASICs)] could be taken over by software-driven reconfigurable logic. The low-resistance graphene provides the ability to change logic gates on a chip on the fly. The result will be more complex computing at a substantially lower power consumption. The potential savings in hardware and energy usage, along with the greatly increased flexibility of the resulting electronics, should provide not only astounding new commercial electronics but, more significantly, great advantage to the soldier in the field.

Graphene as a Tunnel Barrier

O.M.J. van 't Erve, E. Cobas, A.L. Friedman, C.H. Li, J.T. Robinson, and B.T. Jonker
Materials Science and Technology Division

Electrical transport in graphene, a single sheet of carbon atoms in a hexagonal lattice, has quickly become one of the most well-studied topics in materials science and condensed matter physics since initial reports of its discovery in 2004. The discovery stimulated a substantial redirection of international research effort in nanoscience, and ultimately led to the award of the Nobel Prize in physics in 2010.

While these efforts have focused on graphene's extraordinary in-plane charge carrier mobility and conductivity, the out-of-plane charge and spin transport of this remarkable material have not been addressed. Its parent compound, graphite, is known to have a strong conductance anisotropy — the weak interlayer coupling and wave function overlap produce relatively poor conductivity perpendicular to the basal plane. The combination of excellent lateral transport and low out-of-plane conductivity suggests that graphene could uniquely serve as both a low-loss medium for in-plane conduction as well as a tunnel barrier for transport perpendicular to the plane, providing a highly versatile single-material platform for future nanoscale devices. In addition, its low spin-orbit interaction results in low spin scattering, suggesting that graphene may be a key material for spin-based information storage and processing. Intriguingly, ferromagnet-graphene-ferromagnet structures have also been predicted to yield highly efficient spin-filtering properties due to band structure interactions and could find use in a variety of new spin-based technologies.

TECHNOLOGY BACKGROUND

The *International Technology Roadmap for Semiconductors* has identified the electron's spin angular momentum as a potential new state variable for semiconductor device operation for use beyond Moore's Law. Semiconductor spintronics aims to incorporate the electron spin in CMOS-like devices, such as the spin-MOSFET. New paradigms for spin-based devices, such as spin-FETs and reconfigurable logic, have been proposed and modeled. These devices rely on electron spin being injected, transported, manipulated, and detected in a semiconductor channel. These new spin-based technologies promise to combine the advantages of charge-based dynamic memory (speed, solid state) with those of magnetic storage (non-volatility, low power, radiation hardness). For example, spin-torque magnetic random access memory (ST-MRAM) based on magnetic tunnel junctions (MTJs) has made great advances in recent years through a better understanding of the science behind spin transport and manipulation, with the first commercial chips now available.

Future devices based on tunnel barriers will require much improved tunnel barrier materials. An ideal tunnel barrier should exhibit several key material characteristics: uniform, well-controlled thickness, minimal defect/trapped charge density, a low resistance-area product for minimal power consumption,

and compatibility with adjacent materials, ensuring minimal diffusion to/from the surrounding materials at temperatures required for device processing. These requirements have remained beyond the reach of contemporary oxide-based tunnel barriers.

We show here that while graphene exhibits metallic conductivity in-plane, it serves effectively as an insulator for transport perpendicular to the plane, and provide the first demonstration of two potential applications. First we show how a single layer of graphene can be used as an atomically thin tunnel barrier in an MTJ, preserving the spin polarization of the electrons while providing thickness control unattainable with traditional oxide materials. We have measured out-of-plane transport through a single layer of graphene by fabricating metal-graphene-metal junctions using two ferromagnetic (FM) metals, in an MTJ structure.¹ We observe spin-polarized electron tunneling clearly measurable even above room temperature. Secondly, we demonstrate the use of graphene as a tunnel barrier for spin injection into a silicon channel. The spin-injection contact resistances achieved are three orders of magnitude lower than for comparable oxide tunnel barrier contacts and fall within a critical window of values required for practical devices.² These results enable realization of semiconductor spintronic devices such as spin-based transistors, logic, and memory.

GRAPHENE-BASED MAGNETIC TUNNEL JUNCTIONS

Fabrication: Standard microfabrication techniques are used to produce an array of NiFe bottom electrodes on a heavily oxidized silicon wafer. A single sheet of graphene grown by chemical vapor deposition (CVD) is transferred from its original copper foil substrate to the electrode array and patterned using deep-UV photolithography. The graphene's conductive edge states are buried in a layer of SiO₂ and a Co top electrode is deposited (see Fig. 1). This wafer-scale fabrication process was performed at NRL's Nanoscience Institute.

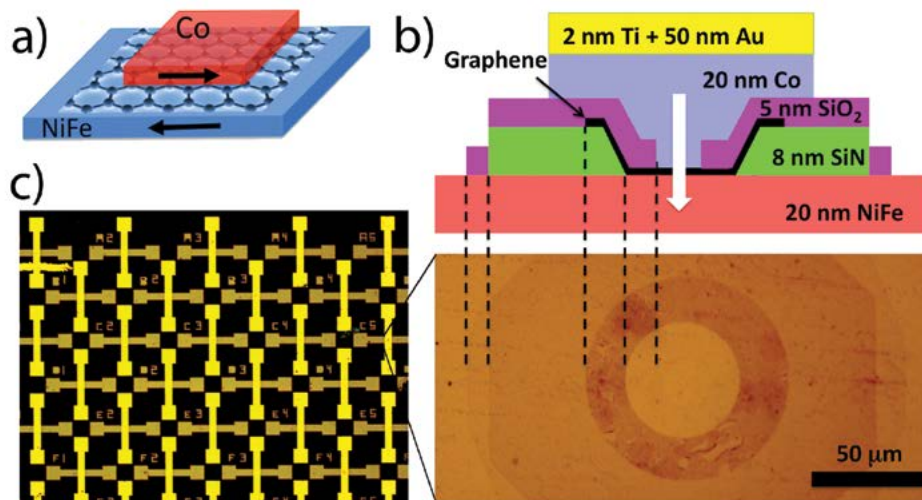


FIGURE 1 Depiction of graphene magnetic tunnel junctions. A conceptual schematic (a), cross-sectional diagram and corresponding top-view micrograph (without top metal), (b) and an optical micrograph of a completed structure (c).

Results: Initial I-V characterization shows a non-Ohmic junction with the increased low-bias resistivity typical of tunnel junctions. The weak temperature dependence of the low-bias resistivity was used to confirm that transport occurs by tunneling. In canonical tunnel junctions, the resistance depends on the ability of electrons from the emitter to tunnel into available states of matching polarization in the collector (see Fig. 2). When the electrodes are oppositely magnetized, the majority-spin density of states in the emitter corresponds to the smaller minority-spin density of states in the collector and vice versa. Consequently, resistance is higher in the antiparallel configuration than in the parallel case, where majority-spin states in the electrodes have the same polarization. As NiFe and Co have different magnetic coercivities, we can align the electrodes parallel or antiparallel by varying an external magnetic field. The relation between junction resistance (tunneling magnetoresistance or TMR) and applied field (Fig.

3) shows the characteristic parallel/antiparallel/parallel switching behavior of an MTJ. At low temperatures and low drive biases, where the physics of tunneling is simplest and most evident, the TMR reaches two percent.

As the bias and temperature increase, the effect is reduced (see Fig. 4). Higher voltages impart electrons with more energy, enabling them to access more empty states in the collector electrode even in the antiparallel case, lowering the resistance. The exact behavior depends on the density of states of the collector electrode, and, thus, on which metal is the collector, producing an asymmetry in the forward vs reverse-bias dependence. Higher temperatures lower the spin-polarization of the

metal surfaces through various mechanisms, similarly reducing the observed effect. We compare these measurements with an established model of temperature-dependent spin tunneling and observe good agreement using accepted parameters for the metals used.

GRAPHENE IN SEMICONDUCTOR SPINTRONIC DEVICES

In semiconductor spintronic devices, spin-polarized electrons are injected into a semiconductor channel, where the spins are transported, manipulated, and finally detected at the collector. Silicon (Si) is an attractive host for such a spin-based technology because of its technological importance as the backbone of modern electronics and because its low atomic mass and crystal inversion symmetry result in very small spin orbit interactions and long spin lifetimes.

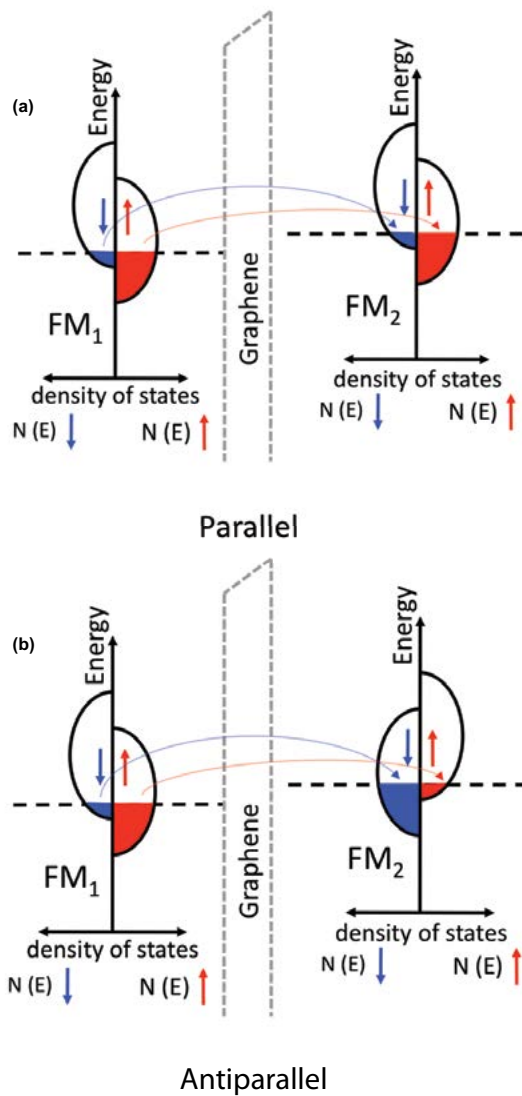


FIGURE 2 Magnetic tunnel barrier conceptual diagram, parallel vs antiparallel.

Ferromagnetic (FM) metals seem like the ideal candidates as contacts for electrical injection and detection of spin currents in the semiconductor channel. Any current in a ferromagnet is naturally spin-polarized at temperatures far above room temperature. However, keeping this spin polarization while the current is transferred from the ferromagnet into silicon is impossible due to the large difference in conductivity. A tunnel barrier between the FM metal and semiconductor was identified as a potential solution and extensive effort has been directed towards developing appropriate tunnel barriers for spin contacts. Most work has focused on either a reverse-biased FM Schottky barrier or an insulating oxide layer such as Al_2O_3 or MgO with a FM metal contact.

Metal Schottky barriers and oxide layers are susceptible to interdiffusion, interface defects, and trapped

charge, which have been shown to compromise spin injection/transport/detection. FM metals readily form silicides even at room temperature, and diffusion of the FM species into the Si creates magnetic scattering sites, limiting spin diffusion lengths and spin lifetimes in the Si. Oxide barriers of atomic thickness contain unavoidable pinhole leaks. The additional thickness needed to avoid pinholes results in contacts with high resistance, increased power consumption, and contact resistances outside the window of resistance-area (RA) products essential for efficient spin injection/detection.

Graphene offers a compelling alternative — a single monolayer provides a much lower RA product than a film of any oxide thick enough to prevent pinholes (~ 1 nm). An FM metal/monolayer graphene contact can serve as a spin-polarized tunnel barrier contact that successfully circumvents the classic metal/semiconductor

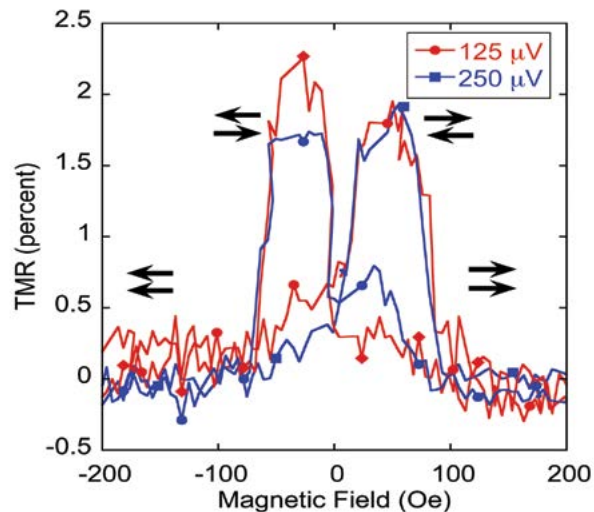


FIGURE 3
TMR of 2% at 0.25 mV.

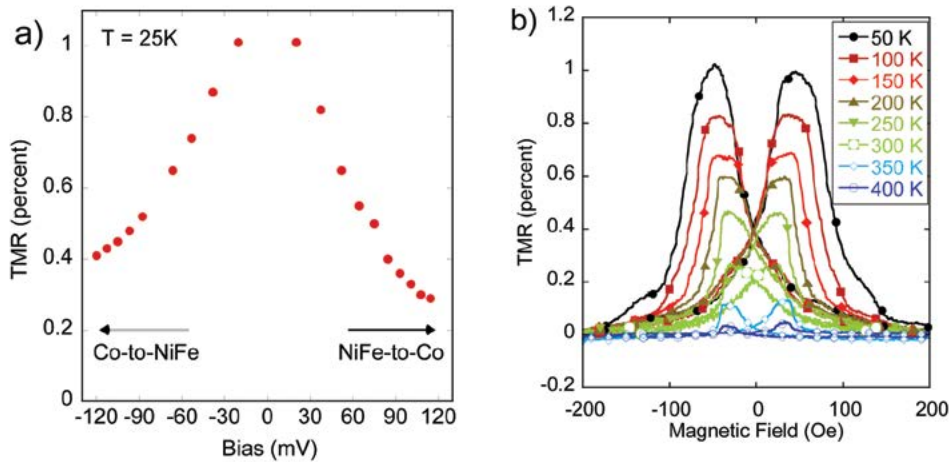


FIGURE 4
(a) TMR(V), (b) TMR(B) at various temperatures.

conductivity mismatch issue for electrical spin injection.

The Devices: Three types of tunnel barriers – SiO₂, Al₂O₃, and graphene — were fabricated on identical Si substrates. Here, 2 nm of SiO₂ was grown on HF etched Si using plasma oxidation to obtain pinhole-free barriers. Al₂O₃ tunnel barriers are routinely used in research grade and commercially available magnetic tunnel junctions. Here, a 1.5-nm-thick Al₂O₃ layer is grown in situ by a two-step natural oxidation process. Finally, graphene was grown by low-pressure CVD within Cu foil “enclosures” and transferred onto hydrogen-passivated n-type silicon. For this study, Si wafers with donor concentrations of 1×10^{19} , 3×10^{19} , and 6×10^{19} were used. The top electrode for all three types of tunnel barriers is sputter-deposited Ni₈₀Fe₂₀. Figure 5 is a schematic of the device used in this study.

The Results: Spin lifetime and spin diffusion lengths are important figures of merit for spin devices. For a practical device, the spin diffusion length ($L_{SD} = (D\tau_s)^{1/2}$) in the semiconductor channel has to be longer than the device dimensions. Hanle spin precession (caused by dephasing of electron spins in an applied magnetic field) measurements are used to determine spin lifetimes and spin diffusion lengths. The top three curves in Fig. 6 are the Hanle measurements of the Al₂O₃, SiO₂, and graphene tunnel barrier samples at room temperature. For all three barriers, a negative magnetoresistance was observed with a Lorentzian line shape caused by field-induced precession, confirming successful spin accumulation in silicon. The bottom two measurements of Fig. 6 are for the NiFe/Si(1×10^{19}) reference sample and a nonmagnetic/graphene/Si(1×10^{19}) control sample, measured at 10K. No magnetic field dependence is observed and none is

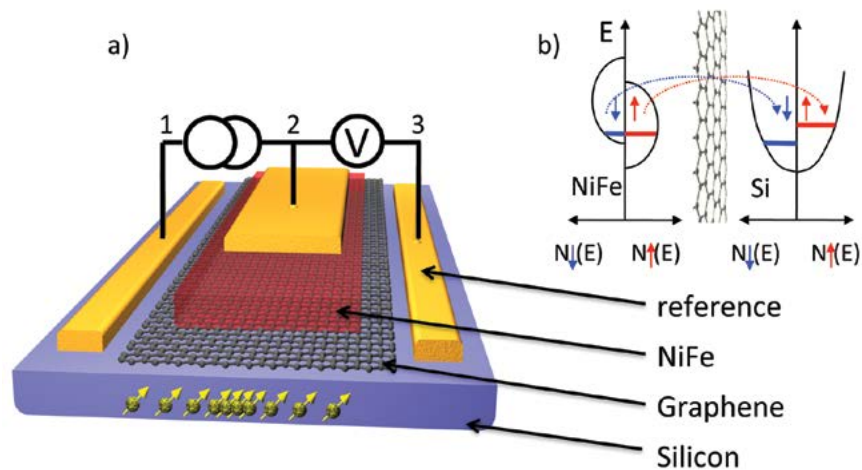


FIGURE 5
Schematic of the samples. (a) Monolayer graphene serves as a tunnel barrier between the FM metal contact and the Si substrate. Contacts 1 and 3 are Ohmic Ti/Au contacts. (b) Schematic illustrating spin injection and spin accumulation.

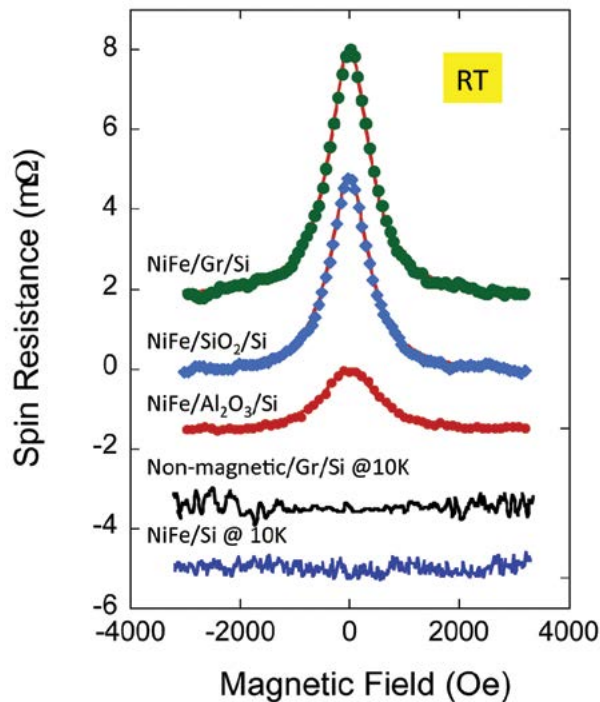


FIGURE 6
Hanle spin precession measurements; graphs are offset for clarity. Room temperature Hanle data for spin injection NiFe/Al₂O₃/Si (3×10^{19}) (red), NiFe/SiO₂/Si (3×10^{19}) (blue) and NiFe/Graphene/Si (1×10^{19}) (green). Also shown are the control samples; nonmagnetic/graphene/Si (1×10^{19}) and NiFe/Si (1×10^{19}) measured at 10 K.

expected. Although NiFe/Si(1×10^{19}) forms a Schottky contact and spin-polarized electrons could, in principle, tunnel across this barrier, silicide formation and diffusion of metallic ions from the NiFe are likely, suppressing spin injection for this contact. The top three Hanle curves can be fit with a Lorentzian lineshape given by $\Delta V_{3T}(B_z) = \Delta V_{3T}(0)/[1 + (\omega_L \tau_s)^2]$, where ω_L

is the Larmor frequency and τ_s is the spin lifetime. Fits to this lineshape (shown in Fig. 6) give a lower bound of $\tau_s \sim 150$ ps for each of the tunnel barrier materials used (graphene, SiO₂, and Al₂O₃), demonstrating that the lifetime measured is not dominated by some characteristic of the tunnel barrier. This is also explicitly demonstrated in Fig. 7, where we plot the spin lifetime

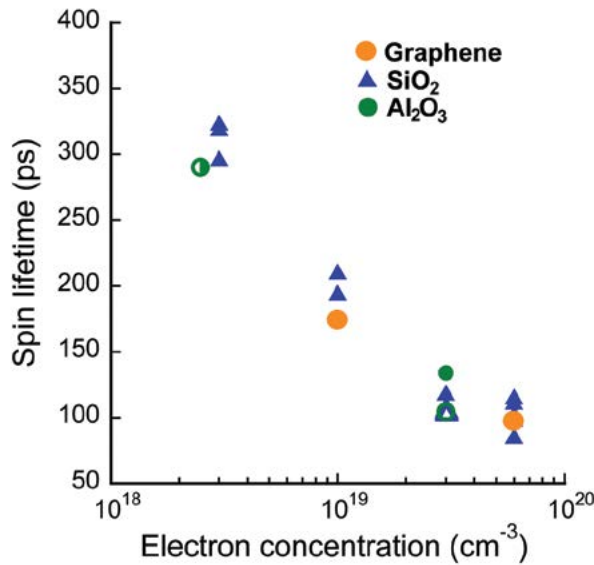


FIGURE 7

Spin lifetimes obtained from three-terminal Hanle measurements at 10 K as a function of the Si electron density for the tunnel barrier materials indicated and different ferromagnetic metal contacts (Fe, CoFe, NiFe). The symbol shape distinguishes the tunnel barrier material: triangles – SiO₂, green circles – Al₂O₃, and orange circles – graphene. Solid symbols correspond to devices with Ni_{0.8}Fe_{0.2} contacts, half-solid symbols to Fe contacts, and open symbols to Co_{0.9}Fe_{0.1} contacts. The spin lifetimes show a pronounced dependence on the Si doping level, and little dependence on the choice of tunnel barrier or magnetic metal.

obtained from three-terminal Hanle data on n-Si as a function of electron density for three different tunnel barrier materials (graphene, Al₂O₃, and SiO₂) and three different magnetic metal contacts (Fe, CoFe, and NiFe). The spin lifetime measured with the three-terminal Hanle geometry shows a clear dependence only on electron density, and the dependence is consistent with literature electron spin resonance data on bulk Si. The spin lifetime is completely independent of the tunnel barrier material or magnetic metal used for the contact. The values for the graphene tunnel barriers fall directly on the curve. These data confirm that the spin accumulation occurs in the Si, and not in the graphene or possible interface trap states.

The magnetic contact's conventional RA product is an important parameter in determining the practical application of a spin-based semiconductor device. Calculations have shown that significant local MR can be achieved only if the contact RA product falls within a range, which depends upon the Si channel conductivity, the spin lifetime, and the contact spacing. The RA products of all tunnel barrier contacts to date have been much larger than required, making such devices unattainable. However, the low RA products provided by the graphene tunnel barriers fall within this window, and enable realization of these and other important spintronic devices. We calculate the range of optimum RA products and the corresponding local MR as a function of the Si electron density using the contact geometry shown as the inset to Fig. 8. The geometric parameters are chosen to be consistent with the node anticipated for Si device technology within the next 5 years. The color code in Fig. 8 identifies the range of useful MR and the corresponding window of contact RA products required.

Tunnel barrier contacts of FM/AIOx and FM/SiO₂ fabricated in our lab on identical substrates have been shown to produce significant spin accumulation in Si, but have RA products that are too high to generate usable local MR. In contrast, using monolayer graphene as the tunnel barrier lowers the RA product by orders of magnitude, and values for the NiFe/graphene contacts on bulk wafers fall well within the range required to generate high local MR. Reducing the RA product

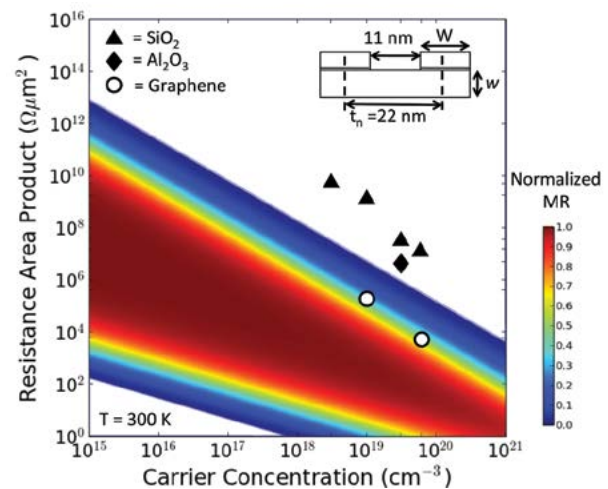


FIGURE 8

Calculation of the local (two terminal) magnetoresistance as a function of the contact's conventional RA product and the Si electron density for the device geometry shown in the inset. The data points are the RA products measured for our FM metal/tunnel barrier/Si contacts using 2-nm SiO₂ (triangles), 1.5-nm AlOx (squares), and monolayer graphene (circles) tunnel barriers prepared from identical Si wafers in our lab. The FM metal/graphene RA products fall within the window of useful MR values. In this figure, W and w both equal 11 nm.

also has a positive effect on the electrical properties of the spin device, as lowering the resistance reduces noise and increases the speed of an electrical circuit.

SUMMARY

This work is the first demonstration of the use of a single layer of graphene as a tunnel barrier. By incorporating a single layer of CVD-grown graphene into an MTJ structure, we've shown that charge and spin transport across the graphene occurs by tunneling and preserves the spin polarization of the tunneling carriers. Using FM-graphene tunnel contacts to inject spin into a silicon channel, we've shown that such contacts achieve dramatically lower resistance than equivalent oxide-based tunnel contacts. These discoveries pave the way for a new generation of spintronic devices using graphene in an unconventional way, but providing unparalleled potential for better than state-of-the-art performance.

ACKNOWLEDGMENTS

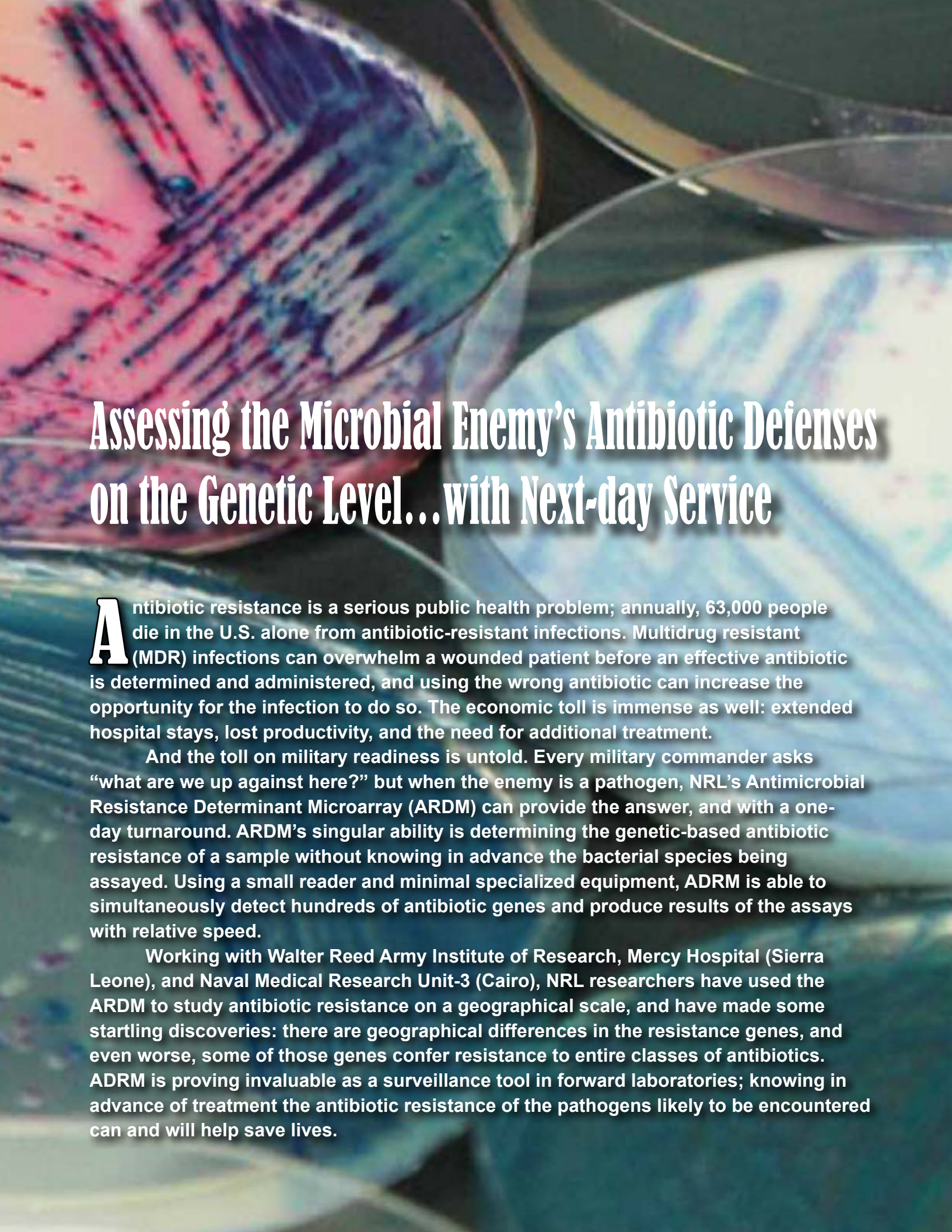
This work was supported by core programs at NRL, and the Office of Naval Research. EC and ALF gratefully acknowledge support through the NRL Karles Fellow program. The authors gratefully acknowledge the use of facilities in the NRL Nanoscience Institute, and thank David Zapotok and Dean St. Amand for continual technical support.

[Sponsored by ONR]

References

- ¹ E. Cobas, A.L. Friedman, O.M.J. van 't Erve, J.T. Robinson, and B.T. Jonker, "Graphene as a Tunnel Barrier: Graphene-Based Magnetic Tunnel Junctions," *Nano Lett.* **12**, 3000 (2012).
- ² O.M.J. van 't Erve, A.L. Friedman, E. Cobas, C.H. Li, J.T. Robinson, and B.T. Jonker, "Low-resistance Spin Injection into Silicon Using Graphene Tunnel Barriers," *Nature Nanotech.* **7**, 737 (2012).



The background of the entire page is a close-up photograph of several petri dishes containing bacterial cultures. The cultures show various patterns of growth, including streaks and colonies, in different colors like pink, purple, and blue. The lighting is dramatic, with strong highlights and deep shadows, giving the scene a scientific and somewhat mysterious feel.

Assessing the Microbial Enemy's Antibiotic Defenses on the Genetic Level...with Next-day Service

Antibiotic resistance is a serious public health problem; annually, 63,000 people die in the U.S. alone from antibiotic-resistant infections. Multidrug resistant (MDR) infections can overwhelm a wounded patient before an effective antibiotic is determined and administered, and using the wrong antibiotic can increase the opportunity for the infection to do so. The economic toll is immense as well: extended hospital stays, lost productivity, and the need for additional treatment.

And the toll on military readiness is untold. Every military commander asks “what are we up against here?” but when the enemy is a pathogen, NRL's Antimicrobial Resistance Determinant Microarray (ARDM) can provide the answer, and with a one-day turnaround. ARDM's singular ability is determining the genetic-based antibiotic resistance of a sample without knowing in advance the bacterial species being assayed. Using a small reader and minimal specialized equipment, ARDM is able to simultaneously detect hundreds of antibiotic genes and produce results of the assays with relative speed.

Working with Walter Reed Army Institute of Research, Mercy Hospital (Sierra Leone), and Naval Medical Research Unit-3 (Cairo), NRL researchers have used the ARDM to study antibiotic resistance on a geographical scale, and have made some startling discoveries: there are geographical differences in the resistance genes, and even worse, some of those genes confer resistance to entire classes of antibiotics. ARDM is proving invaluable as a surveillance tool in forward laboratories; knowing in advance of treatment the antibiotic resistance of the pathogens likely to be encountered can and will help save lives.



Molecular Epidemiology of Global Antimicrobial Resistance

C.R. Taitt, T.A. Leski, and G.J. Vora
Center for Bio/Molecular Science and Engineering

The emergence and spread of antibiotic resistance present a serious challenge to modern day public health. To identify resistance potential in less than a day, we have developed the Antimicrobial Resistance Determinant Microarray (ARDM) to provide DNA-based analysis for over 250 resistance genes, including those for last-resort antibiotics used to treat war trauma-associated infections. The breadth of the ARDM's content has allowed us to detect rare, emerging, or unexpected resistance genes without prior knowledge of bacterial species. A collaborative study with Walter Reed Army Institute of Research, Mercy Hospital (Sierra Leone), and Naval Medical Research Unit-3 (Cairo) showed geographic differences in resistance genes that can be used to track the prevalence and spread of antimicrobial resistance. More concerning was the presence of several genes conferring resistance to entire classes of antibiotics. This information is critical in steering medical personnel towards strategies with the highest chances of success when treating individuals deployed to those regions.

INTRODUCTION

The emergence and spread of antibiotic resistance presents a serious challenge to modern day public health. Resistant organisms are implicated in more than 63,000 deaths in the United States per year, with European Union estimates of economic losses ranging 1.5 billion € per year in lost productivity, additional treatments, and extended hospital stays.¹ Military readiness is also affected by the prevalence of resistant bacterial pathogens. Infectious diarrhea affects between 25% and 80% of deployed personnel at least once during deployment, with drug resistant strains on the rise.² Furthermore, an alarming increase in the number of multidrug resistant (MDR) infections has been noted in military personnel wounded in Operations Iraqi Freedom (OIF), New Dawn (OND), and Enduring Freedom (OEF). Estimates of MDR in non-diarrheal pathogens have exceeded 80% within some military treatment facilities.³

Currently, the standard approach for treating bacterial infections with antibiotic compounds is empirical. If the pathogens causing infection are not sensitive to the applied therapy, the delay in application of an effective treatment may cause the infection to become worse and possibly spread. Moreover, the growth of resistant strains may be encouraged due to decreased competition from sensitive strains, or from the stress-induced exchange/transfer of resistance genes. Thus, it is very important to have a full picture of the antimicrobial resistance status of both clinical isolates and local baseline patterns of resistance to aid medical

personnel in making timely, more effective therapeutic decisions.

Despite these long-standing needs, there does not exist a single comprehensive surveillance tool that can rapidly generate antimicrobial resistance profiles. Standard microbiological methods involving growth in the presence of antibiotics may take several days until results are available. More rapid molecular methods, such as polymerase chain reaction (PCR), are limited by the number of individual or multiplexed reactions that can be performed simultaneously and require a priori knowledge. On the other hand, DNA microarrays, which consist of an array of spatially localized oligonucleotide probes and use nucleic acid hybridization to enable the simultaneous interrogation of hundreds to thousands of genetic elements, provide unprecedented high-throughput analysis capabilities for the detection of antibiotic resistance genes in a single test.

THE ANTIMICROBIAL RESISTANCE DETERMINANT MICROARRAY (ARDM)

Scientists at the Naval Research Laboratory's Center for Bio/Molecular Science and Engineering have developed the ARDM to provide the military's forward laboratories with the capability to detect hundreds of antibiotic resistance genes simultaneously using a small reader and minimal specialized equipment. The ARDM chip has been designed to test four samples for 278 different resistance genes at the same time. Each of the four subarrays on the chip harbors 2,240 different DNA oligonucleotide "capture" probes immobilized on an

array of microelectrodes. Furthermore, each of the 278 resistance genes targeted by the ARDM is represented by 10 unique probes that were designed to hybridize to conserved and nonconserved portions of each targeted gene. In this manner, identical, closely related, and less conserved versions of the resistance determinants can be detected. Genes represented on the ARDM include those conferring resistance to 12 different families of antibiotics and are derived from species most commonly associated with hospital-acquired infections and war wound infections from Iraq and Afghanistan, as well as the most often encountered diarrheal pathogens (Fig. 1). A key advantage of the ARDM's broad coverage is elimination of any need for a priori knowledge of what might be present (which is required for PCR).

breadth of the ARDM's content, allows us to detect rare, unexpected, or emerging resistance genes without knowing or assuming what might be present.

GLOBAL SURVEILLANCE OF ANTIBIOTIC RESISTANCE

We have conducted studies to determine the prevalence and spread of resistance determinants in multiple geographic regions to monitor the global evolution of MDR in militarily relevant pathogens. For this purpose, we have initiated collaborative studies with the Walter Reed Army Institute of Research/Multidrug Resistant Organism Surveillance Network (WRAIR/MRSN), Mercy Hospital (Bo, Sierra Leone), and Naval Medi-

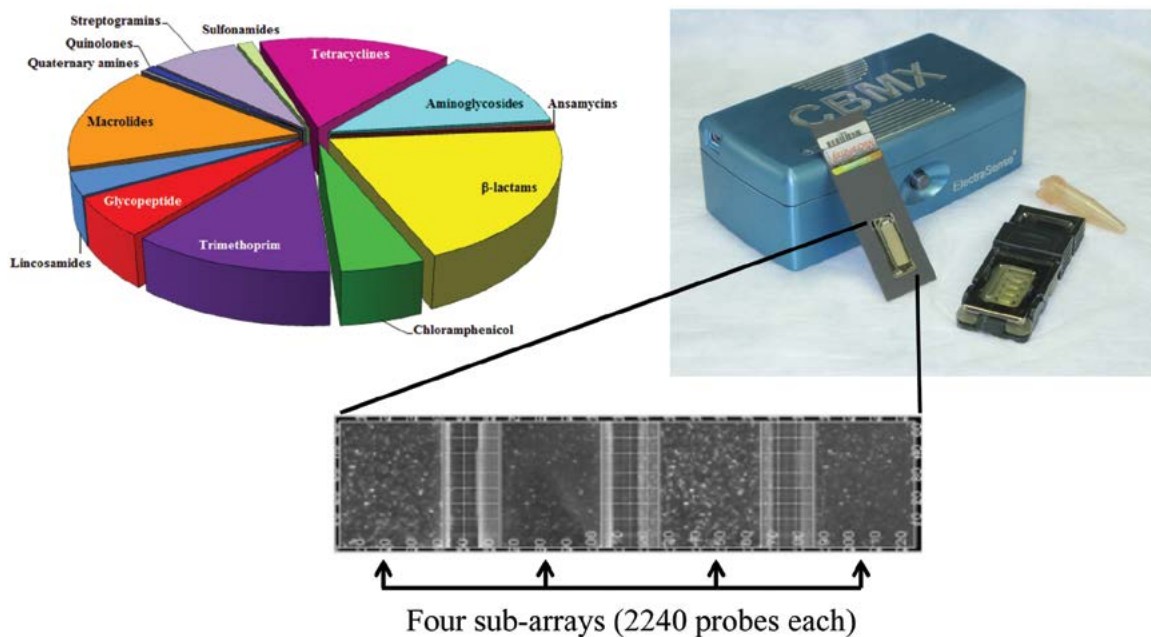


FIGURE 1 Clockwise, from right: ARDM chip with reader in the background; false-color image of the signals from four samples analyzed on the same chip (four subarrays/chip); pie chart of resistance gene content on each subarray [2,240 oligonucleotide probes; shown are different classes of antimicrobial compounds and mechanisms of resistance]. (Photo courtesy of Dr. Joel Golden, NRL)

Extracted DNA samples to be analyzed on the ARDM are processed using an unbiased amplification method, fragmented for efficient hybridization to the microarray probes, and then labeled with a tag that allows the bound DNA to be detected. After hybridization to the microarray, the DNA-DNA hybridization duplexes are detected electrochemically using a small, brick-sized reader that is commercially available. The time-to-result ranges from 11 to 24 hours depending on the length of hybridization, and beyond the small reader, only standard microbiological lab equipment is needed for all processing steps. Furthermore, the unbiased amplification method, combined with the

cal Research Unit-3 (NAMRU-3; Cairo, Egypt). Of the samples obtained from WRAIR/MRSN, approximately 20% were *Acinetobacter* isolates from war wounds. All of the samples collected to date have been selected for their resistance to common antibiotics, and DNA from each sample was extracted, processed, and analyzed on the ARDM to determine its unique genetic profile for antibiotic resistance.

We observed clear differences in resistance determinant profiles when assessing samples taken from different geographic regions (Fig. 2), with each region presenting with a different set of antibiotic classes for which resistance genes were encountered. The most

obvious difference was the broader spectrum of resistance genes from samples collected in Sierra Leone; resistance genes for 11 different classes of antibiotics were observed within this population. Multidrug efflux pumps and determinants directed against glycopeptides such as vancomycin — not detected in the other two populations — were observed in the Sierra Leonean samples. On the other hand, a gene conferring resistance to quinolone antibiotics such as ciprofloxacin was detected in samples from Egypt but not in the other populations. Conversely, a much lower percentage of OIF/OEF samples possessed chloramphenicol resistance determinants, but genes conferring resistance to macrolides, lincosamides, and streptogramins were detected in samples from this region only.

six or more genes conferring aminoglycoside resistance. Importantly, we unexpectedly observed the *armA* gene in one of the WRAIR/MRSN samples; this gene confers resistance to the entire class of aminoglycoside antibiotics and has clear implications when considering chemotherapeutic countermeasures.

The majority of samples from all three populations also carried at least one gene conferring resistance to β -lactam antibiotics but the overall distribution of specific β -lactamase genes varied (Table 1). Due to their cost, broad clinical spectrum, and low toxicity, β -lactams are generally considered as the starting point for treatment of Gram-negative bacterial infections. As expected, the *Acinetobacter* samples from WRAIR/MRSN harbored *Acinetobacter*-specific β -lactamases

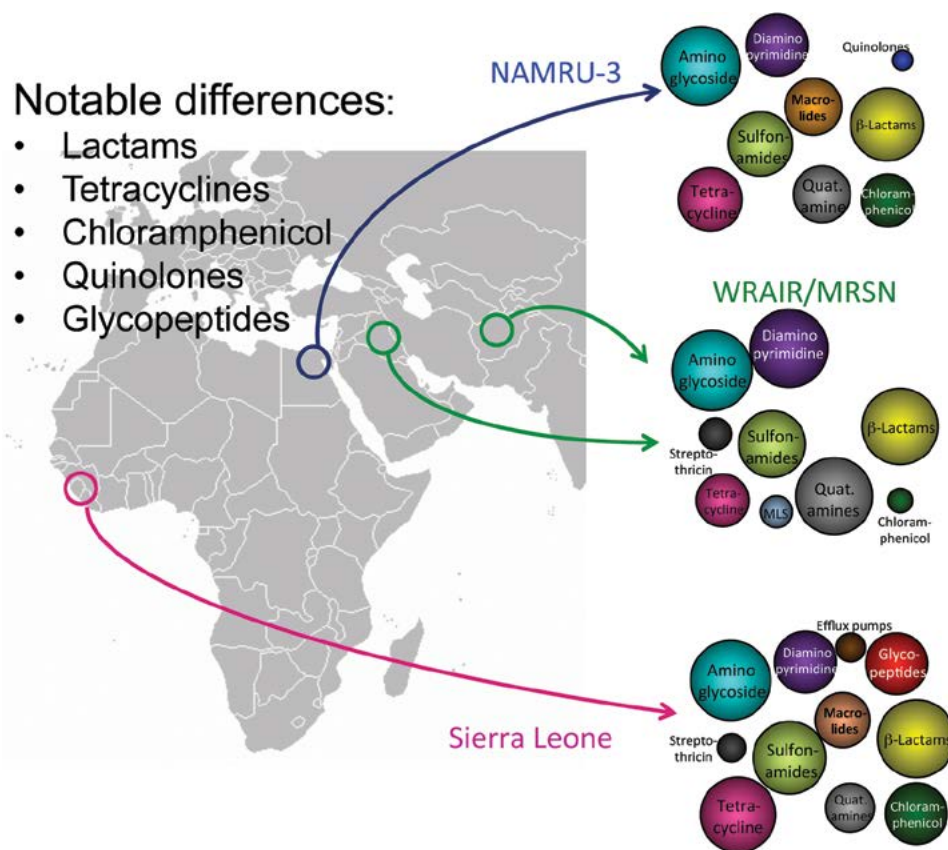


FIGURE 2
Geographic profiles of antibiotic resistance gene content. Bubble size indicates the percentage of samples from each site harboring at least one gene that confers resistance for each class of antimicrobial compound.

Genes directed against aminoglycosides such as gentamicin and amikacin were common throughout the three sample sets tested. At least 80% of all tested samples contained at least one aminoglycoside resistance gene, and over half possessed three or more; moreover, a small number of samples from Sierra Leone and WRAIR/MRSN (approximately 5%) harbored

such as *bla*_{OXA-51} and *bla*_{OXA-23}, which confer resistance to the most potent lactam antibiotics such as imipenem and meropenem. On the other hand, the majority of Egyptian strains possessed genes for extended-spectrum β -lactamases (ESBLs), which hydrolyze all third-generation cephalosporins.⁴ The possession of multiple ESBLs with overlapping specificities made

TABLE 1 — Resistance Determinants Detected in >10% Isolates Tested

<u>WRAIR</u>	<u>NAMRU-3</u>	<u>Sierra Leone</u>
β-lactam resistance determinants		
<i>Acinetobacter</i> -specific carbapenemases: <i>bla</i> _{OXA-51} , <i>bla</i> _{OXA-23}	ESBL families: <i>bla</i> _{TEM} , <i>bla</i> _{OXA-1} , <i>bla</i> _{OXA-9} , <i>bla</i> _{SHV} , <i>bla</i> _{CTX-M-1} , <i>bla</i> _{CTX-M-9}	ESBL family: <i>bla</i> _{TEM}
Aminoglycoside resistance determinants		
<i>aac</i> (C1), <i>aadA1</i> family <i>aadB</i> , <i>aphA1</i> <i>strA</i> , <i>strB</i>	<i>aac</i> (3)-III, <i>aac</i> (6)- <i>ib</i> family <i>aadA1</i> family <i>aadB</i> , <i>aphA1</i> <i>strA</i> , <i>strB</i>	<i>aac</i> (6)- <i>ib</i> family, <i>aadA1</i> family <i>aadB</i> , <i>aphA1</i> <i>strA</i> , <i>strB</i>
Macrolide resistance determinants		
	<i>macA</i> , <i>macB</i> <i>mphA</i> / <i>mphK</i>	<i>macA</i> , <i>macB</i> <i>mphA</i> / <i>mphK</i>
Tetracycline resistance determinants		
<i>tet39</i> , <i>tetA</i> , <i>tetB</i>	<i>tet39</i> , <i>tetA</i> , <i>tetB</i>	<i>tet39</i> , <i>tetA</i> , <i>tetB</i> <i>tetS</i> , <i>tetX</i>
Multidrug resistance efflux pumps		
		<i>vcaM</i>
Chloramphenicol resistance determinants		
	<i>catA1</i> / <i>cat4</i> family	<i>catA1</i> / <i>cat4</i> family
Quarternary ammonium compound resistance determinants		
<i>qacEΔ1</i>	<i>qacEΔ1</i>	<i>qacEΔ1</i>
Sulfonamide resistance determinants		
<i>sulI</i> , <i>sulII</i>	<i>sulI</i> , <i>sulII</i>	<i>sulI</i> , <i>sulII</i>
Trimethoprim resistance determinants		
<i>dfrA1</i> , <i>folA</i>	<i>dfrA1</i> , <i>dfrA14</i> , <i>dfrA17</i>	<i>dfrA1</i> , <i>dfrA14</i> , <i>dfr20</i>

many of these Egyptian isolates virtually untreatable with standard β -lactam antibiotics. A significant number of the isolates from Sierra Leone harbored genes for only one of the ESBLs, *bla*_{TEM}, but were negative for the other ESBLs detected in the Egyptian samples.

The carriage of tetracycline resistance determinants also varied between the three regions. Whereas the Egyptian samples harbored four different genes, those from WRAIR/MRSN were limited to only three of those. Almost 80% of the Sierra Leonean samples harbored tetracycline resistance genes, with over half of them positive for the presence of multiple genes, including two additional determinants. The high prevalence of multiple tetracycline determinants clearly distinguishes this region from the others tested here, as well as other Gram-negative bacterial populations isolated throughout the world.⁵ Perhaps more importantly, the ARDM detected the presence of the *tetX* gene in the Sierra Leonean isolates. The *tetX* gene encodes an enzyme that hydrolyzes all known tetracycline antibiotics, including the most recently approved third-generation glycylycylcline antibiotic, tigecycline. Although the *tetX* gene had previously never been found in any Gram-negative human pathogens, our results confirmed its presence in 21% of the hospital isolates collected from Sierra Leone.⁶ Therefore, its presence in a large number of samples from clinical infections was both surprising and alarming, as it may portend the eventual failure of all tetracycline antibiotics in this region. The ability of the ARDM to detect an unexpected resistance determinant in samples where it otherwise might be missed speaks to the impact of the broad-based surveillance capability enabled by this technology.

DETECTION OF GENETIC ASSEMBLAGES

Bacteria exchange genetic information — including antibiotic resistance genes — through lateral transmission of clusters of genes, or genetic assemblages. The ARDM's broad coverage allowed us to deduce the likely presence of different genetic assemblages by identifying clusters of characteristic resistance genes. Integrons are genetic elements that capture antibiotic resistance gene “cassettes” through site-specific recombination; in this study, we observed assemblages indicative of two types of integrons. Class 1 integrons (markers - *sull*, *qacEΔ1*) were found in approximately half of the samples from Egypt and WRAIR/MRSN, but at a much lower rate amongst the Sierra Leone sample collection. Class 2 integrons (markers - *dfrA1*, *sat2*, *aadA1*), on the other hand, were observed in only approximately 7% of the WRAIR/MRSN samples. Furthermore, genes corresponding to several *Acinetobacter*-specific resistance islands, potential hotspots for the integration of resistance genes, were observed in two of the Egyptian samples (AbaR3 [seven markers] and AbaR6/7 [four

markers]). The presence and types of such genetic assemblages can not only help epidemiologists track the spread of related species, but can indicate the potential efficacy of different antibiotic combination therapies, which are now common practice for the treatment of MDR infections.

SUMMARY

In collaboration with researchers from NAMRU-3, WRAIR/MRSN, and Mercy Hospital, we have tested over 120 MDR bacteria from different geographic regions using NRL's Antimicrobial Resistance Determinant Microarray. In doing so, we identified significant differences in overall patterns of resistance, as well as in the individual genes present within each population. Of particular concern were both the presence of genes responsible for resistance to last-resort antibiotics and co-localization of genes directing resistance to the antibiotics most commonly used in combination therapy. While the ARDM is not intended as a diagnostic test, our studies have demonstrated its utility as a surveillance tool, enabling detection of unexpected resistance determinants (e.g., *tetX*, *armA*) with obvious and high potential impact. The single-test screening and surveillance capabilities that are afforded by the ARDM can lead to more effective therapeutic decisions, decreased use of inappropriate antimicrobials, and early detection of emerging drug-resistant pathogens, thus decreasing the threat of MDR infections to military personnel deployed to these regions. On the merits of these findings, we have expanded our surveillance efforts in the form of ongoing collaborations with Naval Medical Research Unit-2 (NAMRU-2; Phnom Penh, Cambodia), Naval Medical Research Unit-6 (NAMRU-6; Lima, Peru), the Centers for Disease Control and Prevention (CDC; Atlanta, Georgia), the University of Chicago hospital pavilion (Chicago, Illinois) and the Landstuhl Regional Medical Center (Germany).

ACKNOWLEDGMENTS

The authors gratefully acknowledge Dr. David A. Stenger for establishing the necessary infrastructure and overseeing the collaboration with Mercy Hospital in Bo, Sierra Leone, LT Stephen E. Lizewski and CDR Michael G. Stockelman for their technical expertise, and Dr. Joel Golden for the photograph of the ARDM.

[Sponsored by ONR and the Defense Medical Research and Development Program (Intramural Applied Research and Advanced Technology Development Award)]

References

- ¹ World Health Organization. *The Evolving Threat of Antimicrobial Resistance – Options for Action* (2012).
- ² J.W. Sanders, D.W. Isenbarger, S.E. Walz, L.W. Pang, D.A. Scott, C. Tamma, B.A. Oyofe, W.C. Hewitson, J.L. Sanchez, C.

Pitarangsi, P. Echeverria, and D.R. Tribble, "An Observational Clinic-Based Study of Diarrheal Illness in Deployed United States Military Personnel in Thailand: Presentation and Outcome of Campylobacter Infection," *The American Journal of Tropical Medicine and Hygiene* **67**, 533–538 (2002).

³ M.J. Zapor, D. Erwin, G. Erowele, and G. Wortmann, "Emergence of Multidrug Resistance in Bacteria and Impact on Antibiotic Expenditure at a Major Army Medical Center Caring for Soldiers Wounded in Iraq and Afghanistan," *Infect. Control Hosp. Epidemiol.* **29**, 661–663 (2008).

⁴ T. Leski, G. Vora, B. Barrows, G. Pimentel, B. House, M. Nicklasson, M. Wasfy, M. Abdel-Maksoud, and C.R. Taitt, "Molecu-

lar Characterization of Multidrug Resistant Hospital Isolates Using the Antimicrobial Resistance Determinant Microarray," *PloS ONE* **8**(7), e69507.

⁵ M. Tucker, P. Petersen, A. Howe, M. Orłowski, S. Mullen, K. Chan, P. Bradford, and C. Jones, "Occurrence of Tetracycline Resistance Genes among Escherichia Coli Isolates from the Phase 3 Clinical Trials for Tigecycline," *Antimicrob. Agents Chemother.* **51**, 3205–3211 (2007).

⁶ T.A. Leski, U. Bangura, D.H. Jimmy, R. Ansumana, S. Lizewski, D.A. Stenger, C.R. Taitt, and G.J. Vora, "Multidrug-Resistance tet(X)-Containing Hospital Isolates in Sierra Leone," *Int. J. Antimicrob. Agents*, **42**, 83-86 (2013).



NRL Has a Flare for Studying CMEs: Staring into the Sun to See the “Rosetta Stone” of Flux Rope Formation

While there might be “nothing new under the Sun,” observations by NRL scientists in 2012 offered a new understanding of what bursts forth from the Sun.

Coronal mass ejections (CMEs), the massive and explosive releases of plasma and magnetic material from the solar corona, can have tremendous, sometimes devastating effect on satellites, radio communications, and the Earth’s power grids. Their effects on Earth and its near-space environment is called space weather, and accurately predicting that weather could aid in protecting both ground and space-based civilian and military systems. Therefore, learning how CMEs form and what they are made of is critical. Since not all CMEs are created equal, knowledge of their three-dimensional magnetic structure is necessary to determine whether or not a given CME could damage these assets.

An estimated 40 percent, at least, of CMEs contain large-scale, slinky-shaped magnetic fields called flux ropes (FR). For many years, solar physicists hotly debated the question of whether CMEs originate in the lower solar corona from preformed FRs or whether FRs form from the eruption of CMEs. While the existence and formation of FRs had been postulated for many years, the formation of a flux rope was not actually observed until July 19, 2012. This was when the LASCO imager in combination with the AIA instrument aboard the Solar Dynamic Observatory (SDO), viewing the phenomenon at the correct temperature (131 Å), were able to capture the formation of a flux rope and the ensuing CME eruption and thus elucidate the role of preformed flux ropes in large CMEs.

We may never be able to answer the chicken-and-egg problem, but it appears that NRL scientists have made great progress in answering a hotter and maybe more useful question.

The Stuff Coronal Mass Ejections Are Made Of

A. Vourlidas
Space Science Division

Knowledge of the magnetic structure of coronal mass ejections (CMEs) is essential for assessing their damaging effects on satellites and radio communications. In the past year, we made great strides towards uncovering the three-dimensional structure of CMEs thanks to observations from space-borne imagers designed, assembled, and operated in the Space Science Division (SSD). We devised methods to determine whether large, potentially damaging CMEs contain large-scale coiled magnetic fields reminiscent of a slinky toy, called a magnetic flux rope. We found that at least 40% of them do. We have also discovered that the flux rope forms in the low corona (within 50,000 km of the solar surface) just before the eruption of the CME. Our results validate a long-standing theoretical prediction that CMEs are driven by the formation and ejection of flux ropes. This is an important step towards achieving a CME predictive capability for improved Space Situational Awareness.

INTRODUCTION

CMEs are explosive releases of plasma and magnetic field from the solar corona. A typical CME carries away four billion tons of magnetized coronal material at speeds in excess of two million km/hour. The associated kinetic energy of 5×10^{23} joules corresponds to the release of 120,000 gigatons of TNT equivalent, 12 times higher than the energy released during the 2004 Indian Ocean earthquake. However, we have measured events with at least 100× larger energies. CMEs are the manifestations of the largest explosions in our astrophysical neighborhood, and their effects can be sensed at the outer boundaries of the solar system months or even years after they left the Sun.

CMEs have another, more direct effect on our society. The Earth's magnetic field creates the magnetosphere, a cocoon that encircles the planet and protects it, and the nearby space, from high-energy radiation. But CMEs can compress the magnetosphere to such an extent that satellites become exposed to open space and may suffer damage to their electronic systems. On the other hand, the (as yet unknown) magnetic fields within CMEs can interact and even blow a hole in the magnetosphere, allowing the high energy particles entrained in the CME to enter. The glowing lights of the auroras are a beautiful and relatively benign manifestation of this interaction. But the CME collision throws the whole upper atmosphere of the Earth (ionosphere, magnetosphere, and thermosphere) out of balance, causing geomagnetic storms that can result in further damage to satellites and even drive currents on

the ground that may damage power grids and disrupt GPS and communications. Given our society's growing dependence on global communications and networks, both civilian and military authorities place great importance on a reliable assessment of the damaging potential of an Earth-directed CME. But the first step is to understand what CMEs are made of.

FROM LOOPS TO ICE CREAM CONES AND NOW TO CROISSANTS

CMEs are traditionally detected and analyzed in visible light images obtained by coronagraphs, telescopes that feature a disk at the telescope entrance to create an artificial eclipse by blocking the Sun, thus making the extended corona visible. Their emission is caused by the Thomson scattering of photospheric light by the free electrons within the CME and hence it is optically thin and quite weak. Typical CME brightnesses are about 8 to 10 orders of magnitude fainter than the solar disk. Despite centuries of eclipse observations from the ground, CMEs were discovered only in 1971 by SSD researchers¹ using their pioneering coronagraph aboard the OSO-7 satellite. Space-based coronagraphy, a field that is still led by NRL, is today the primary means for the study of CMEs and an indispensable tool for space weather, as the terrestrial effects of CMEs are collectively known.

The typical CME appears in the images as an outward propagating cloud of emission with a well-defined curved front, followed by an area of depressed emission (cavity), and a bright core (Fig. 1). The interpretation

of this appearance led to the first controversy on CME structure. Some researchers suggested that CMEs are essentially two-dimensional objects, coronal loops ejected from the lower corona, while others proposed that CMEs were the projections of three-dimensional bubbles of coronal plasma. The scale tilted towards the “bubble” camp in the mid-1980s when a group of SSD researchers² using another SSD-made coronagraph (Solwind) realized that Earth-directed CMEs appeared as halos encircling the Sun and, hence, had to be projections of 3D objects. The resulting model of CMEs as “ice cream cones” is still in use today.

theories and simulations of CME eruption mechanisms kept coming up with the same result — *the ejected structure is always a flux rope irrespective of the actual eruption mechanism*. While this idea was able to explain the observations of a subset of events, the great majority of CMEs lacked many of the expected characteristics such as filamentary structure or a cavity. Why? Was there a class of non-flux rope ejections that defied our theoretical understanding? The answer could have profound implications for the physics of energy release and came from the observations of the latest SSD-led set of coronagraphs: the Sun-Earth Connection Coronal and

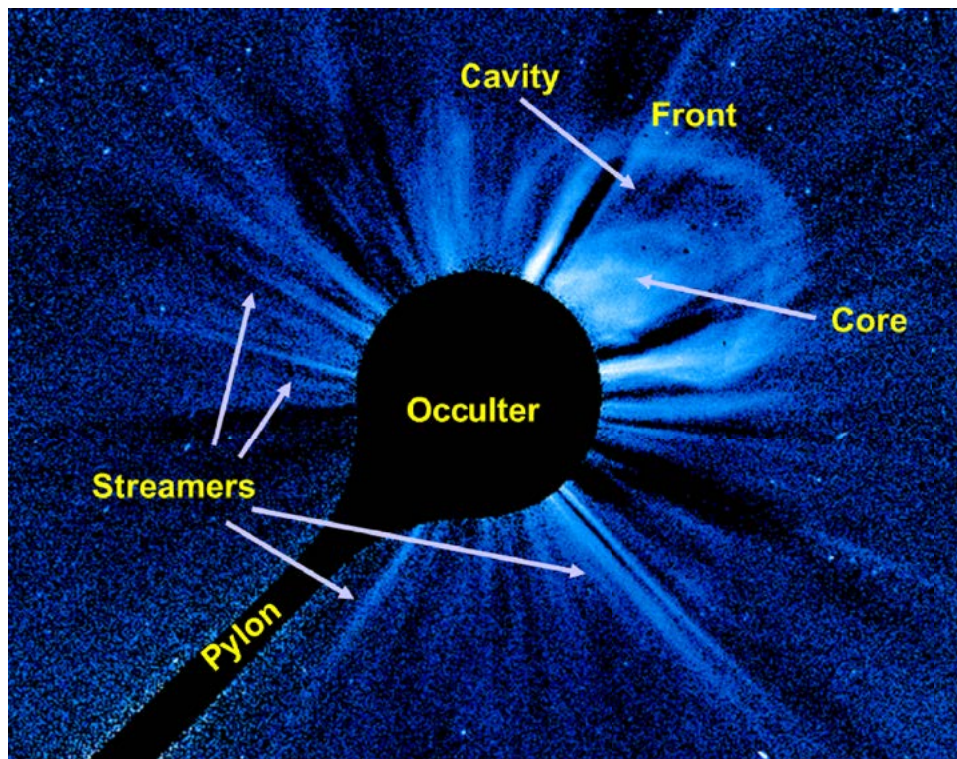


FIGURE 1 A typical CME captured in a LASCO coronagraph image. The occulter is a disk at the entrance of the telescope supported by a pylon. It creates an artificial eclipse by blocking the bright light from the solar disk thus making visible the much fainter corona. The CME consists of a front, cavity, and a core. The streamers are structures of the quiescent background corona.

This “ice cream” model, however, seemed inadequate when the SSD-led Large Angle and Spectrographic Coronagraph (LASCO) experiment aboard the SOHO mission began high resolution observations in the late 1990s. CMEs exhibited lots of fine structure (Fig. 2), incompatible with the simple bubble concept. Again, the breakthrough came from NRL researchers³ who proposed that CMEs can be understood as projections of a 3D structure of helical magnetic fields, a so-called flux rope (FR). The striations inside CMEs were simply the emission from plasma trapped inside the flux rope helical fields. At the same time, however,

Heliospheric Investigation (SECCHI) suite aboard the STEREO mission.

STEREO comprises two spacecraft with identical instrumentation drifting ahead and behind the Earth’s orbit at an annual rate of 22.5°. The simultaneous SECCHI observations of the Sun and its extended corona from two vantage points provides unique 3D information on the CME properties, including their structure. Observations like the ones shown in Fig. 3 and simulations quickly revealed to us⁴ that the lack of flux rope structure was the result of projection effects and not an intrinsic difference among CME events. It allowed

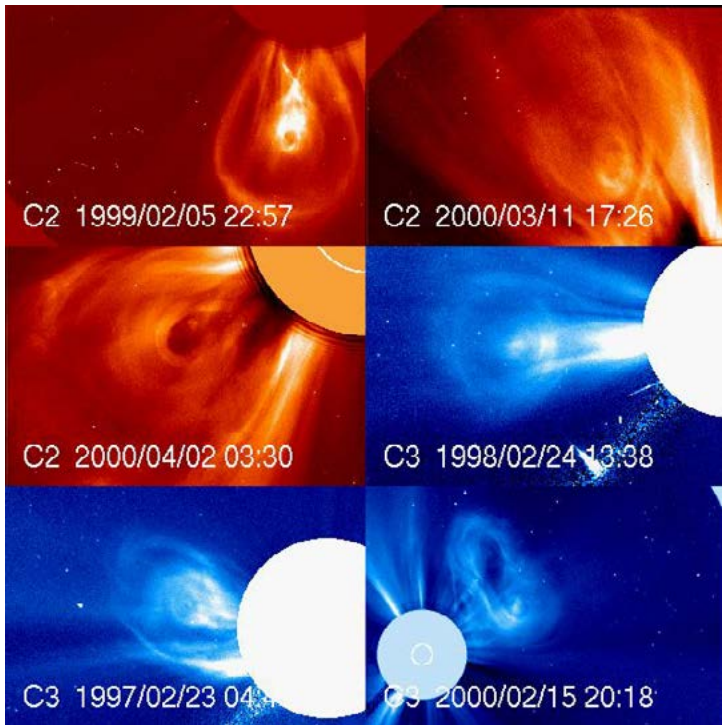


FIGURE 2
 LASCO observations of CMEs with fine-scale internal structure consistent with a magnetic flux rope. The solar disk size is represented by the white circle in some of the images.

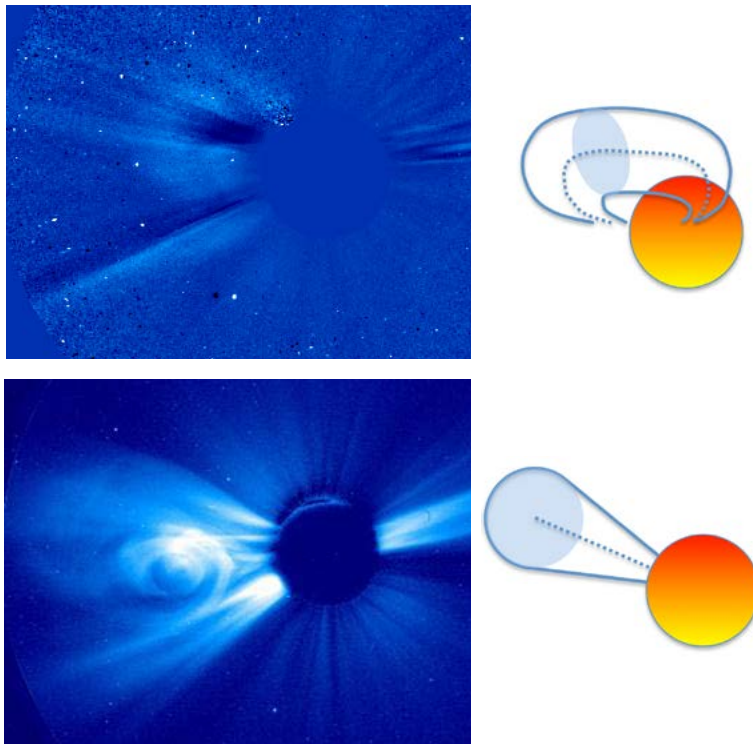


FIGURE 3
 Simultaneous observations of a CME from the SSD-led SECCHI COR2 coronagraphs on the STEREO mission. Top: The CME appears as a faint cloud of emission in COR2-B. Bottom: The same CME at the same time appears as a highly structured flux rope in COR2-A. The angular distance between the two viewpoints is 39°. The figures on the right are cartoon representations of the approximate projection of the event on the sky plane of each instrument.

us to revisit the single-view, but 16-year long, LASCO database and count the appearance of flux rope CMEs during a full solar cycle. Fully 40% of the CME sample (962 out of 2403 events) had unambiguous flux rope structure while another 40% had some hints but the emission was either too faint or the background was too disturbed to make a definitive identification. We were not able to identify any other characteristic CME morphology apart from jets, which also have helical fields but are too small to be geoeffective. The absence of solar cycle dependence in the FR-CME occurrence rate was another indication that we are dealing with an intrinsic property of the eruption rather than the phase of the cycle. The preponderance of FR-CMEs, the lack of another common morphology and absence of solar cycle influence, all point out that the ejection of flux ropes is very likely the only way to produce large scale CMEs.

FLUX ROPE FORMATION AND ERUPTION MECHANISMS

So the eruption theories are correct on what comes out from the solar corona but when does the flux rope form? This question is the heart of another major controversy in solar physics because the answer will determine the dominant physical mechanism behind solar eruptions and consequently how the magnetic energy is released into light, mass motion, and accelerated particles. In a nutshell, if the flux rope is formed before the CME (“preformed”), then most theories propose that the eruption is primarily driven by ideal processes, i.e., plasma instabilities such as kink, and torus instabilities, that act on the large-scale flux rope structure. The spectacular eruptions from polar crown filaments are examples of this mechanism (Fig. 4, left). On the

other hand, if the flux rope forms during the eruption (“on-the-fly”), then the eruption is driven by non-ideal processes such as magnetic reconnection, a topological change in the magnetic connectivity of neighboring field lines, which liberates magnetic energy. Highly impulsive eruptions accompanied by flares are usually put forth as examples of this mechanism (Fig. 4, right). Both types of theories predict that the actual eruption occurs over very short time scales of minutes.

The ideal vs non-ideal debate has been raging on for several years due mostly to the inability of instrumentation to capture the formation of flux ropes and the birth of CMEs in the low corona with sufficient temporal and spatial resolution. Again, SSD researchers and collaborators⁵ have made considerable progress over the last year, thanks to the full 360° coverage of the solar corona achieved by a combination of SSD-led and other space instrumentation.

On July 19, 2012, the corona expelled a large CME in excess of 1000 km/s. A flux rope was clearly detected at its center by the LASCO coronagraph (Fig. 5, top right). Usually, the low corona source is identified in images of highly ionized Fe captured in the extreme ultraviolet (EUV) wavelength of 193 Å (Fe XII) corresponding to plasmas at the average coronal temperature (1.4 million K). In this case, the best viewing was offered by the Atmospheric Imaging Assembly (AIA) EUV imagers on the SDO mission. The 193 Å images showed nothing more than expanding loops, seen many times before in such eruptions. But AIA is equipped with filters at 131 Å (Fe XXI or 10 million K) and 335 Å (Fe XVI or 2.8 million K), among others. When we investigated, we found a flux rope structure hiding in the 131 Å images, completely invisible in the other, cooler wavelengths (Fig. 5, top middle). What is more, that structure was there for at least eight hours

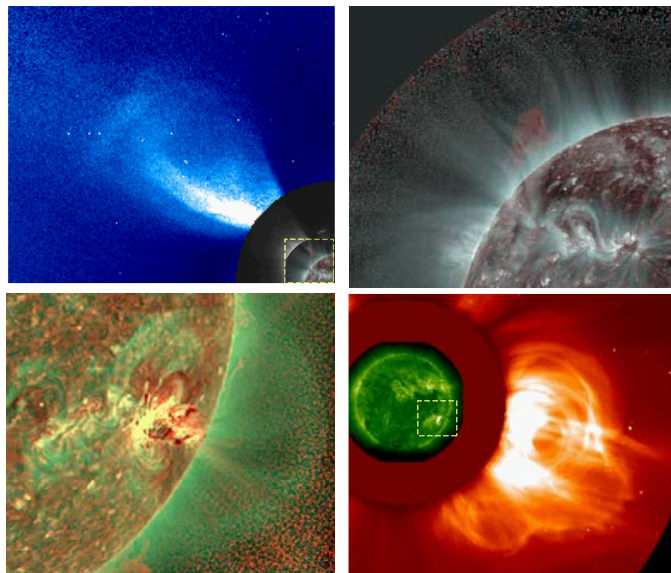


FIGURE 4
 Top left: A flux rope CME morphology caused by the eruption of a polar crown filament. The yellow dashed box marks the source region. Top right: Detail of the source region about 8 hours prior to the eruption. A faint cavity with helical structures is already visible in the EUV images. Red (sliver) show plasma at 80,000 (1.4 million) K. Bottom right: An impulsive CME associated with a large flare and energetic particles above 100 MeV. A flux rope can be discerned at the center of the CME. The yellow dashed box marks the source region. Bottom left: Detail of the source region just half an hour earlier when the eruption became evident. A shock front is visible but there is no clear flux rope in the image. Red (green) show plasma at 80,000 (1.4 million) K.

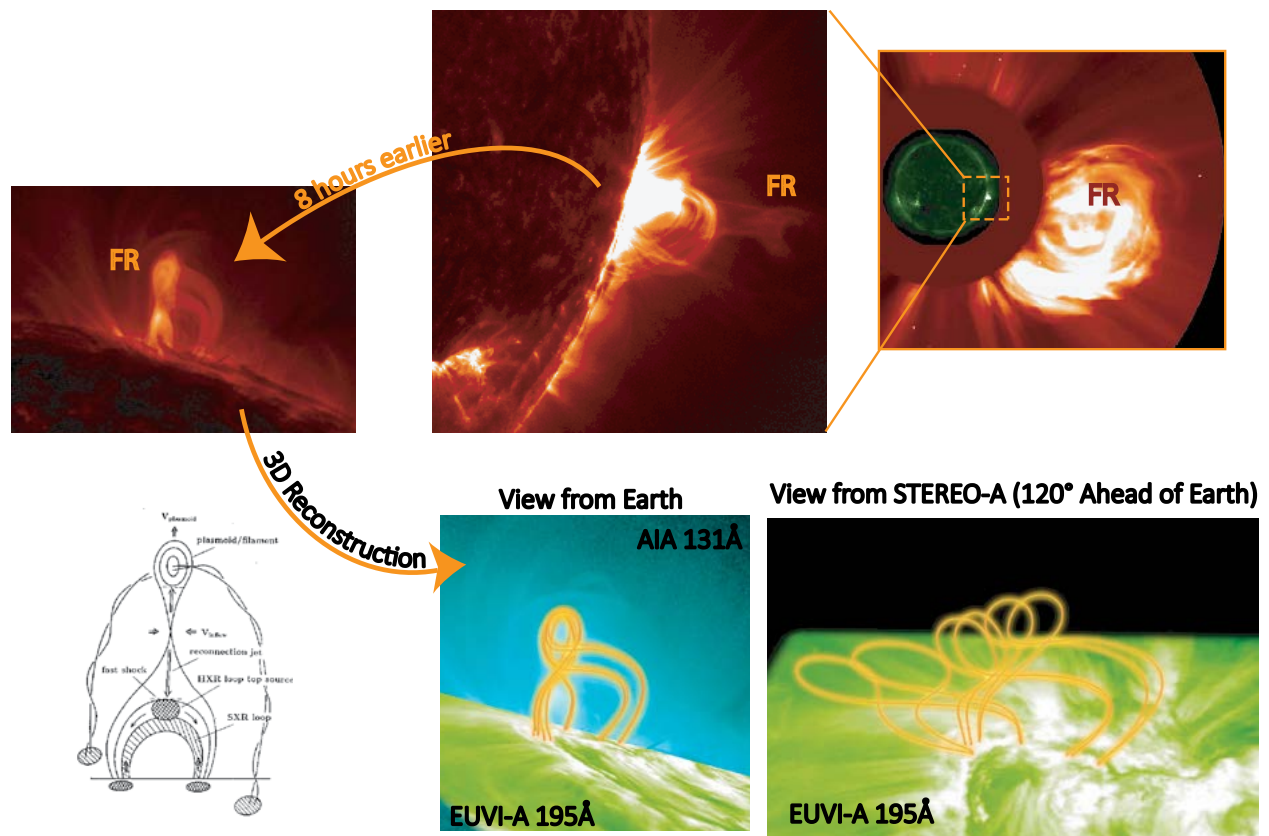


FIGURE 5

The CME-flare event of July 19, 2012. A “Rosetta stone” event that elucidates the role of preformed flux ropes in CME eruptions. The flux rope structure is marked by “FR” in the top three panels. Top right: The LASCO image shows an impulsive CME with flux rope morphology. Top middle: The same flux rope is seen in the low corona at a temperature of ~10 million K. Top left: The same flux rope forms 8 hours prior to the eruption but is observed only at a single EUV wavelength (131 Å or 10 million K), which has been available only since 2010. This observation explains immediately why flux ropes have not been detected directly in the past 16 years of EUV observations...at lower temperatures. Bottom left: Cartoon of the “standard” model of CME-flare eruptions from Shibata et al. (1995). The similarity with the 131 Å above is uncanny. Bottom right panels: Thanks to the SECCHI EUV observations, we can derive the 3D structure of the flux rope. It is a collection of kinked field lines that explains the high temperature and instability of the structure.

before the eruption and looked exactly as theories have predicted since the 1970s (Fig. 5, top and bottom left). It appeared during a flaring episode on July 18. The structure was extremely hot, (around 10 million K) since it was initially visible only in 131 Å. As it cooled down, it progressively appeared in cooler wavelengths (335 Å→94 Å→211 Å→193 Å) while it kept rising slowly at a speed of a few km/s. When we incorporated the SECCHI EUV observations to derive the 3D structure of the flux rope, we found that only a kinked loop morphology was consistent with the observations (Fig. 5, bottom). This event can be thought of as a kind of “Rosetta stone” for solar eruptions. It exhibits three of the expectations of ideally driven eruption theories with exceptionally clear observations: the preformed FR, the kink instability, and the slow rise (drive towards torus instability). Other observers have identified several more events where the FR makes its appearance in a hot channel at various times before the CME.

PUTTING IT ALL TOGETHER

A coherent picture of solar eruptions is emerging. FRs form a few minutes to several hours before the CME, rise through the low corona until they reach a critical height where a plasma instability (most likely the “torus instability”) sets in and, then, they explode outwards carrying with them overlying plasma and magnetic field. This picture does not exclude non-ideal processes. Magnetic reconnection is required to sever the magnetic links between the outgoing structure and the Sun and provides additional energy during the initial acceleration phase. The scenario is applicable to large-scale, structured CMEs as compared to the small “puffs” and cloudlike ejections that occur frequently but never make it beyond 10 solar radii or so. Our findings last year imply that all such CMEs carry flux ropes, whereas the absence of the flux rope from the images is a matter of projection effects.

Besides clearing the debate on the internal structure of CMEs, this scenario is quite attractive for space weather operations. If the flux rope always forms before the CME, we should be in position to track its evolution and eventually predict when the eruption will take place. But first we must detect it. The reason we failed for some many years is because we have been looking at the wrong place...or, more precisely, at the wrong temperature. Our EUV results show that we should be looking both at hotter temperatures (3 to 10 million K) and at many temperatures simultaneously to trace the rise and temperature evolution of this structure.

WHERE DO WE GO FROM HERE?

Now that we are confident about the internal structure of CMEs and can estimate their 3D properties from SECCHI, we are left with one major outstanding piece of their geo-effectiveness puzzle: the strength and orientation of their internal magnetic field. This is, at present, impossible to measure remotely. An interplanetary fleet of in-situ probes distributed along the Sun-Earth line seems highly unlikely given the current fiscal climate. Empirical approaches to estimating the magnetic field with existing data and instrumentation are being developed by NRL researchers and scientists

throughout the world. Their work and the advancement of space weather prediction will benefit greatly from instrumentation optimized by the lessons learned last year: use many EUV wavelengths, look over the limb in the EUV, and cover the low corona to Earth seamlessly. A payload of EUV imagers and visible light coronagraphs at the L5 Lagrangian point will be the perfect fit.

[Sponsored by NASA]

References

- ¹ R. Tousey, "The Solar Corona," *Space Research XIII*, Vol. 2, (Akademic-Verlag, Berlin, 1973), p. 713.
- ² R.A. Howard et al., "The Observation of a Coronal Transient Directed at Earth," *Astroph. J. Lett.* **263**, L101 (1982).
- ³ J. Chen et al., "Evidence of an Erupting Magnetic Flux Rope: LASCO Coronal Mass Ejection of 1997 April 13," *Astroph. J. Lett.* **490**, L191 (1997).
- ⁴ A. Vourlidas et al., "How Many CMEs Have Flux Ropes? Deciphering the Signatures of Shocks, Flux Ropes, and Prominences in Coronagraph Observations of CMEs," *Sol. Phys.* DOI 10.1007/s11207-012-0084-8 (2012).
- ⁵ S. Patsourakos, A. Vourlidas, and G. Stenborg, "Direct Evidence for a Fast Coronal Mass Ejection Driven by the Prior Formation and Subsequent Destabilization of a Magnetic Flux Rope," *Astroph. J.* **764**, 125 (2013).
- ⁶ K. Shibata et al., "Hot-Plasma Ejections Associated with Compact-Loop Solar Flares," *Astroph J. Lett.* **451**, L83 (1995). ♦

Doing the Locomotion...with a Microrobot Powered by a Microbial Fuel Cell

Until they start building tiny fueling stations on Mars, the problem of meeting the low-power generation and distribution requirements of small robotic planetary explorers will loom large. The extended duration required of these missions necessitates bringing their own fuel source, which is no small matter.

But if the proof-of-concept robotic system made by NRL researchers using a microbial fuel cell (MFC) becomes a functioning system, that's how microrobots in tomorrow's planetary missions could be powered. Building on NRL's decade-long experience and large investment in using micro-organisms for power generation and in the area of space robotics, NRL researchers, sponsored by the NASA Innovative and Advanced Concepts (NIAC) program, successfully performed an end-to-end demonstration of an MFC-powered microrobot locomotion system.

LITTLE ROBOTS, BIG CHALLENGES: while the MFC-generated fuel has a very high energy density, available instantaneous power is low compared to that afforded by batteries. This meant devising a multi-tiered approach to powering the onboard electronics while reducing the power requirements of the onboard systems.

Three research areas were simultaneously pursued – low-power robotic locomotion, proving the pure-culture (*Geobacter sulfurreducens*) dual-chamber MFC concept as an effective power source, and developing low-power electronics for vehicle control and energy distribution – with the goal of tying the results of all three subsystems into one working end-to-end system. The successful demonstration, a walking minirobot powered for 13 seconds by an MFC, proved the advancement of all three areas.

That might not seem to be a big deal, but with advancements in all of the technology areas, the potential is vast. It's one small step for a microrobot, but a giant leap for robot-kind.



Low Power Microrobotics Utilizing Biologically Inspired Energy Generation

G.P. Scott, S.P. Arnold, and C.E. Person
Spacecraft Engineering Department

L.M. Tender and K.P. Gregoire
Center for Bio/Molecular Science and Engineering

The Low Power Microrobotics (LPM) project was a multidisciplinary Phase I research effort funded by NASA's Innovative and Advanced Concepts (NIAC) Program to investigate integration of a low-power robotic mobility system with a microbial fuel cell (MFC) power supply. NASA's interest in this topic lies in their goal to create low mass planetary exploration vehicles. In this program, the team successfully performed an end-to-end system demonstration in which an MFC was used to operate a robotic locomotion system.

BACKGROUND

In the past decade, more than \$10M has been invested in the development of MFC research at the NRL focusing on generating power and energy using microorganisms. In addition, nearly \$30M in research funding has been awarded to space robotics research, including the development of space-qualified actuators, mechanisms, and electronics. Considering the extensive research experience in these areas, a team was assembled at the NRL to investigate low-power micro-robotic systems powered by microbial fuel cells (Fig. 1).

The primary investigator (PI) for this program, Dr. Gregory P. Scott, was awarded the NRL's Karles' Fellowship in 2010 to investigate novel space robotics research. Using a portion of this funding, he began investigating technology for maturing small robotic systems, including power generation and distribution. Looking into alternative and innovative technology options for addressing this problem, he turned to MFCs as the primary power generation system owing to their potential to scavenge fuel and oxidants from the environment (Fig. 2). Dr. Leonard Tender, NRL's and the Navy's subject matter expert in MFCs, was brought



FIGURE 1
The Low Power Microrobotics research team, from left to right: Dr. Leonard M. Tender (Code 6930), Dr. Stephen P. Arnold (Code 8242), and Dr. Gregory P. Scott (PI, Code 8231).

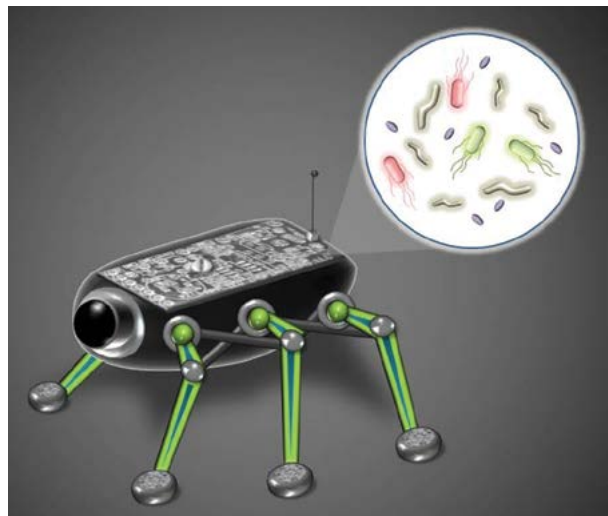


FIGURE 2
The initial concept of the Low Power Microrobotic system, powered by a microbial fuel cell and controlled by a low-power electrical power distribution system. (Credit: K. Reilly, NASA NIAC)

on board to support this aspect of the program. The high energy density of the fuel used in an MFC is one attractive aspect of these systems, yet one significant problem with using an MFC for power generation is their exceptionally low instantaneous power availability compared to batteries. Further discussion with Dr. Stephen Arnold, subject matter expert in spacecraft electronics, led to a consideration of a multitiered approach to powering the onboard electronics, while actively working to reduce the electrical requirements of the onboard components themselves.

Following this initial investigation and using the expertise of this team and others, a research project was awarded by the NASA Innovative and Advanced Concepts Program to investigate low power microrobotic systems using biologically inspired energy generation.

LOW POWER MICROROBOTICS

To achieve the goals set forth in this research project, the project was broken down into three primary research areas:

- low-power mobility systems for robot locomotion on planetary surfaces;
- electronics with low power requirements for core robot control functionality;
- biologically inspired power generation techniques for long duration vehicle lifetime.

The first research area followed the development of the low-power robotic locomotion system. Due to the high power requirements of motors in traditional wheeled/tracked locomotion, nontraditional methodologies were considered to reduce onboard electromechanical hardware for locomotion. Slow-charging spring-loaded hopping locomotion was considered for ground mobility and a gravity-assisted offset “pendulum” system was also investigated. Trade studies and designs were completed, weighing the capability of locomoting a 1-kilogram system while constrained by the power available from the fuel cell and energy storage devices.

The second research area followed the investigation of MFCs. This research area focused on a dual chamber MFC using the microorganism *Geobacter sulfurreducens* as the anode catalyst. This low power generation technology was selected as it would have an exceptionally long lifetime, beneficial for recharging onboard batteries or capacitors for long duration robotic scouting missions. A prototype MFC was fabricated to determine its power density and to demonstrate the ability of an MFC to actuate an electromechanical system. The third research area followed the development of low-power electronics for vehicle control and energy distribution. A power budget was developed based on

power output of the MFC and proposed onboard power storage system based around a small super-capacitor. The output requirements of the locomotion actuators and additional onboard sensor systems that would be required for a robotic system were also baselined. A prototype control board with an energy distribution circuit was built and the power consumption was tested while operating a microrobotic system.

Although all three research areas were conducted independently, they were all directly interrelated and relied on constant design iterations and constant collaboration in order to ensure the systems could converge into a demonstrable proof of concept.

EXPERIMENTAL RESULTS

Through the work performed on this study, the technology readiness level of each system was advanced, allowing for an increased understanding of how these systems operate independently, as well as how they could interact together. Experiments showed that the dual-chamber MFC used in this research can produce an effective amount of power (~2 mW at 0.3 V) that could be harnessed by an energy harvesting circuit. Low-power electronics were tuned to charge a supercapacitor and eventually discharge the stored energy to activate an electromechanical system. Two distinct low-power mobility actuators were designed for operation in different environmental conditions, and sized to appropriately be actuated by this system.

In the final experiment, a benthic microbial fuel cell (BMFC) was used as the microbial fuel cell power source operating in a benthic mesocosm (Fig. 3) in



FIGURE 3
Sediment-based microbial fuel cell in the Laboratory for Autonomous Systems Research.

the littoral facility of the Laboratory for Autonomous Systems Research (LASR). The BMFC was used instead of the dual-chamber MFC tested earlier in this project due to the inoculation cycle not being ready for use at the time of the final experiment. Although the BMFC

is significantly larger and sits on the sediment/water (benthic interface) at the bottom of marine environments and generates power using microbes naturally residing in marine sediment, the available power was nearly identical to that of the dual-chamber MFC. With an electrical output of 9 mA at 0.35 V, the BMFC was able to charge a 280 mF 3.6 V supercapacitor through the energy harvesting circuit in less than 2 hours. The charged supercapacitor was then discharged to operate the 3 V motor in a small walking robot for 13 seconds. This demonstrated the effective usage of a microbial fuel cell to locomote a robotic system using low-power electronics and an effective power management system (Figs. 4 and 5).

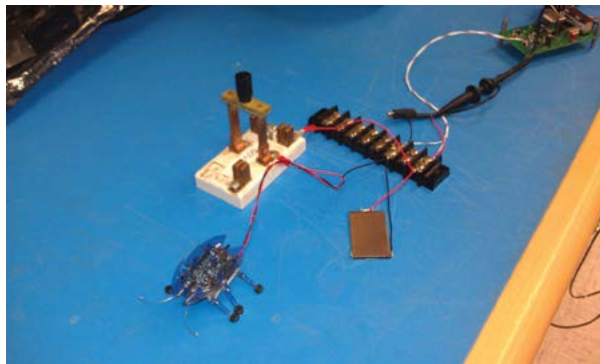


FIGURE 4
The test bench setup for the end-to-end test, including (from left to right) the robotic locomotion system, control switch, supercapacitor, wiring block, and energy harvesting circuit (oscilloscope not shown).

The Low Power Microrobotics project accomplished the following specific successes:

1. Further application and advancement of a dual-chamber, pure-culture microbial fuel cell;
2. Development of an electrical storage and distribution subsystem at low power;
3. Design of efficient mechanisms to be powered from a biological source;
4. Proving the proposed concept through an end-to-end test of the microbial fuel cell to power an electromechanical output system.

With further advances in each technology (such as improving the efficiency of the cathode reaction of the low-volume microbial fuel cell or improving electromechanical efficiency for locomotion systems), a future application of these interdisciplinary areas could include a low-power microrobotic system for low-gravity environments using a microbial fuel cell to generate electricity.

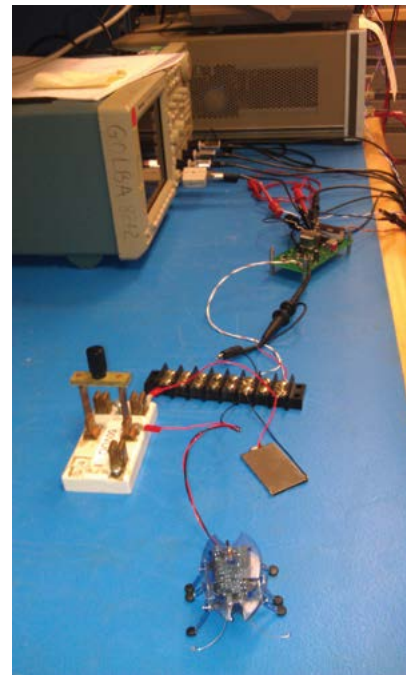


FIGURE 5
The test bench setup for the end-to-end test, including (from bottom to top) the robotic locomotion system, supercapacitor, control switch, energy harvesting circuit, and oscilloscope.

ACKNOWLEDGMENTS

The PI was selected as a NASA Innovative Advanced Concepts Fellow to perform Phase I research on this topic and thanks the NASA Innovative Advanced Concepts Program within the Office of the Chief Technologist for funding this research and helping to extend the state of the art in three key research areas to support low power microrobotics.

[Sponsored by NASA NIAC]





128 Controlling Sonar Clutter via Higher-Order Statistics

130 Transition and Optimization of a Fast Broadband Pulse Propagation Algorithm for Fleet Use

132 Range-Dependent Seismo-Acoustics

Controlling Sonar Clutter via Higher-Order Statistics

R.C. Gauss and J.M. Fialkowski
Acoustics Division

Introduction: Active antisubmarine warfare sonar systems use acoustic sources and receivers coupled with signal processing to detect and classify undersea targets. The sources transmit broadband signals that propagate into, and interact with, the waveguide. The backscattered energy is received on high-resolution arrays and correlated (“match filtered”) with the transmitted signal, permitting a high degree of temporal and spatial localization in the search for potential targets. However, the limiting influence of clutter has long been recognized, with echoes from complex bathymetry, fish schools, and anthropogenic objects such as wrecks, capable of creating false targets that can both mask real targets and overload the sonar operator with false alarms.¹

To help reduce the false alarm rate, a variety of signal-processing strategies have been employed in analyzing the received data time series. In particular, statistical methods which provide measures of echo time-series characteristics, such as its spatial extent, rise time, and highlight structure, help to distinguish between real and false targets. NRL has been investigating higher-order statistical methods that allow extraction of even more information about the echoes, which in turn provide more reliable and robust clutter control.

Statistical Clutter Modeling: At the heart of statistical clutter modeling is a probability density function (PDF) of the matched-filter time series. Within each analysis window, the normalized time series data are histogrammed according to amplitude level. Clutter is defined as target-like echoes that result in false alarms (threshold exceedances) at the detector stage of the data processing. While background noise typically generates Rayleigh PDFs, clutter generates non-Rayleigh PDFs (Fig. 1(a)), which result in an increased probability of false alarm (PFA). Accordingly, from a sonar-performance perspective, characterizing and controlling the tails of these data distributions is paramount. While many PDFs have been explored over the years, very few have a physical basis. NRL has recently developed the physics-based Poisson-Rayleigh (P-R) PDF that models data amplitudes as a joint process arising from two statistically independent mechanisms, namely returns from a continuous background and a set of acoustically strong discrete scatterers.² Its key parameters are α , which represents the effective number of discrete scatterers, and ρ_D^2 , their relative strength.

Higher-order statistics (HOS) refer to functions involving the third or higher sample moments; for example, skewness and kurtosis are respectively the 3rd and 4th normalized moments. One way to assess a PDF model’s generality or narrowness in representing higher-order moments and matching data is to examine how it depends on skewness γ_3 and kurtosis γ_4 , as they represent scale-invariant measures of departure from normality: skewness represents PDF asymmetry and kurtosis PDF shape. By its capability to represent a much wider range of (γ_3, γ_4) values (Fig. 1(b)), the multiparameter P-R model has a clear advantage in describing data distributions (Fig. 1(a)) over conventional single-parameter models (such as the lognormal). Another advantage of the P-R model is that its parameters can be efficiently estimated from the data via the 2nd, 4th, and 6th moment equations of the P-R distribution.

Clutter Control: NRL has developed a sonar clutter-control method based on the P-R PDF model that leverages the P-R parameters’ relatability to scatterer attributes (density, spatial dispersion, and relative strength).³ The model parameters are first estimated from data prior to thresholding within analysis windows of fixed time duration (range extent). Next, these quantities are mapped to range-bearing or latitude-longitude cells to form distributions of parameter values associated with echo returns on a sonar display. Classification features are then derived from parameter distribution statistics associated with each data cell. Lastly, the relative values of these features are used to classify echo returns based on scatterer characteristics, thereby providing a physical basis for distinguishing real from false targets.

Results: The clutter-control method has been demonstrated using broadband data collected with coherent sources and towed horizontal receiver arrays in both a geologically complex environment, the Malta Plateau (south of Sicily) during the Boundary 2004 (B2004) experiment (Fig. 2(a)), and a biologically complex Gulf of Maine environment during a 2011 experiment (GOM2011). During B2004, additional sources of echoes were of anthropogenic origin (an offshore oil platform, a water-column-spanning pipe used to moor its tending tanker, and a passive reflector). Due to their spatial compactness in range, the pipe and passive reflector serve as surrogate target objects.

Figures 2 and 3 demonstrate on real-world data the potential of our clutter classification technique for improved rejection of clutter relative to target-like objects. Figure 2 shows how application of our method effectively eliminates the pervasive bottom clutter associated with the Ragusa ridge (Fig. 2(b)), while

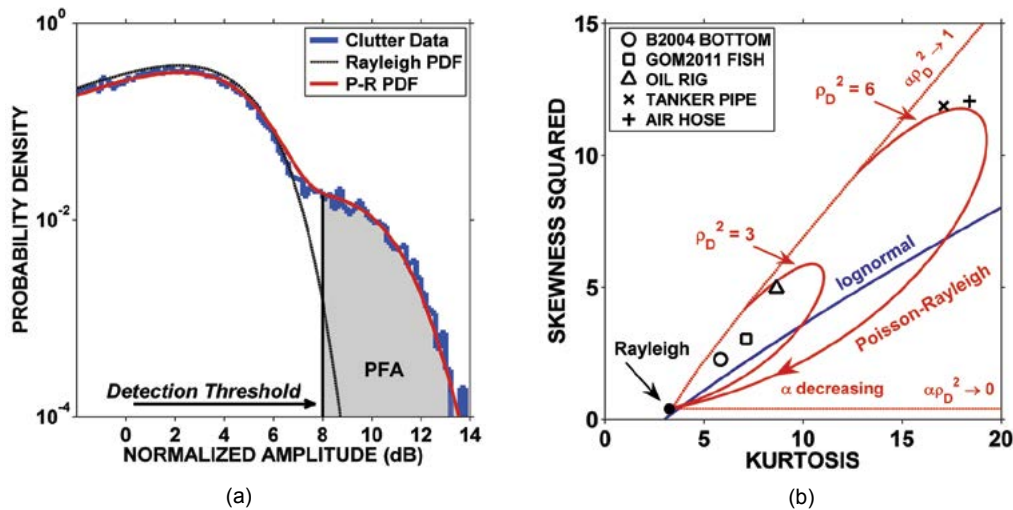


FIGURE 1
 (a) PDF of sonar data, and (b) distribution of data and model values in the (γ_4, γ_3^2) plane.

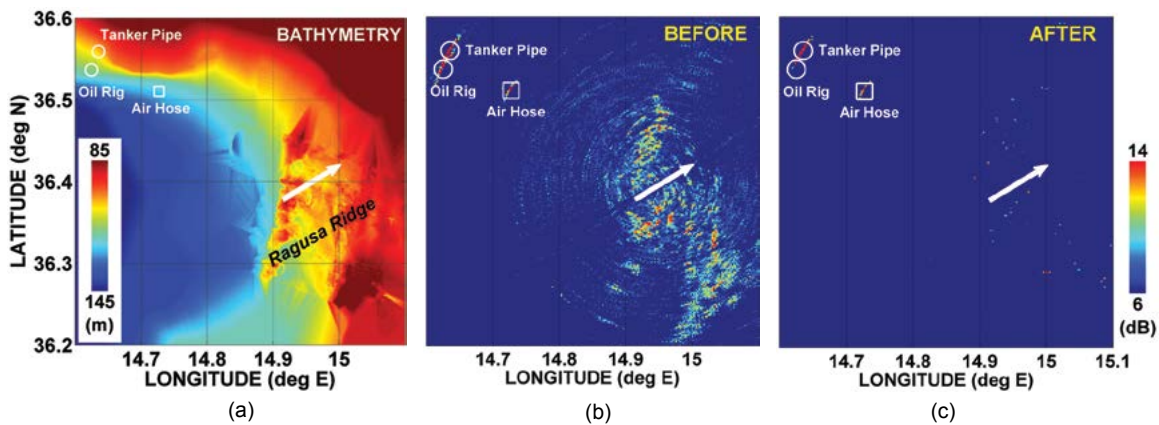


FIGURE 2
 (a) Malta Plateau bathymetry and active sonar track (white arrow), (b) georeferenced clutter and target-like echoes, and (c) reduction in clutter after applying our classification method.

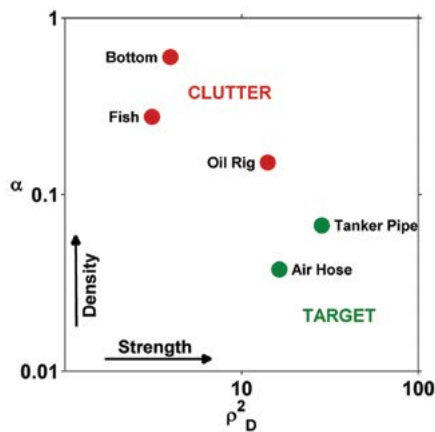


FIGURE 3
 Classification of echoes by their derived P-R parameter values.

retaining echoes from the more target-like objects (Fig. 2(c)). Figure 3 further shows how our P-R parameter

estimates can separate different classes of echoes. Significantly, the data results additionally suggest that in contrast to current methods, this new moment-based technique can provide feature information that is largely independent of an echo's signal-to-noise ratio (SNR) — this could allow lowering the detection threshold, and so enhance detection of low-SNR targets.³ Assessing the general utility of this method and optimizing performance in terms of environmental and system variables remains the focus of current work.

[Sponsored by the NRL Base Program (CNR funded)]

References

- ¹ R.C. Gauss, "Characterizing and Controlling Reverberation and Clutter," Ch. 12 in *Important Elements in: Geoacoustic Inversion, Signal Processing, and Reverberation in Underwater Acoustics*, ed. A. Tolstoy (Research Signpost, India, 2008), pp. 327–370.
- ² J.M. Fialkowski, R.C. Gauss, and D.M. Drumheller, "Measurements and Modeling of Low-Frequency Near-Surface Scattering Statistics," *IEEE J. Ocean. Eng.* **29**, 197–214 (2004).

Transition and Optimization of a Fast Broadband Pulse Propagation Algorithm for Fleet Use

R.A. Zingarelli
Acoustics Division

Introduction: An algorithm to minimize the number of frequency-domain model runs needed for Fourier synthesis of broadband time-domain pulses, developed earlier under NRL 6.2 Base Funding,¹ has been transitioned to Fleet use as part of the Navy Standard Parabolic Equation model (NSPE)² package. The method is based on observed regularities in acoustic phase and magnitude variation with frequency, in single-frequency model results. These regularities allow many of the model runs, which would normally be required by the Nyquist sampling condition, to be omitted and later filled in through phase and magnitude interpolation. In transitioning this algorithm to automated operational use, further optimizations were combined and exploited to give even greater computational efficiencies. In operational applications, this method allows a roughly 20-fold speedup over conventional Fourier synthesis techniques, while remaining robust enough for Fleet use. In a limited number of benchmark test cases, up to 650-fold speedups have been achieved.

Method: Fourier synthesis of time-domain (TD) results from a set of single-frequency results of continuous-wave (CW) modeling is a standard numerical analysis technique.³ Parabolic equation (PE) based CW acoustic models, such as the NSPE, generate complex output field values at each computational grid point. Examination of complex PE results at a single receiver location show that the phase and magnitude vary with significant regularity, as shown in Fig. 4. The phase varies almost linearly with frequency, wrapping back whenever its usual $-\pi$ to π bounds are exceeded, while the magnitude is a smoothly varying simple curve. Using the average slope near the center frequency of the TD pulse being propagated, the phases can be unwrapped. Intermediate phase and magnitude values can then be linearly interpolated, either to reduce the frequency spacing and thus increase the time window duration, or — as done here — to provide a frequency skipping optimization to eliminate a large number of CW model runs.

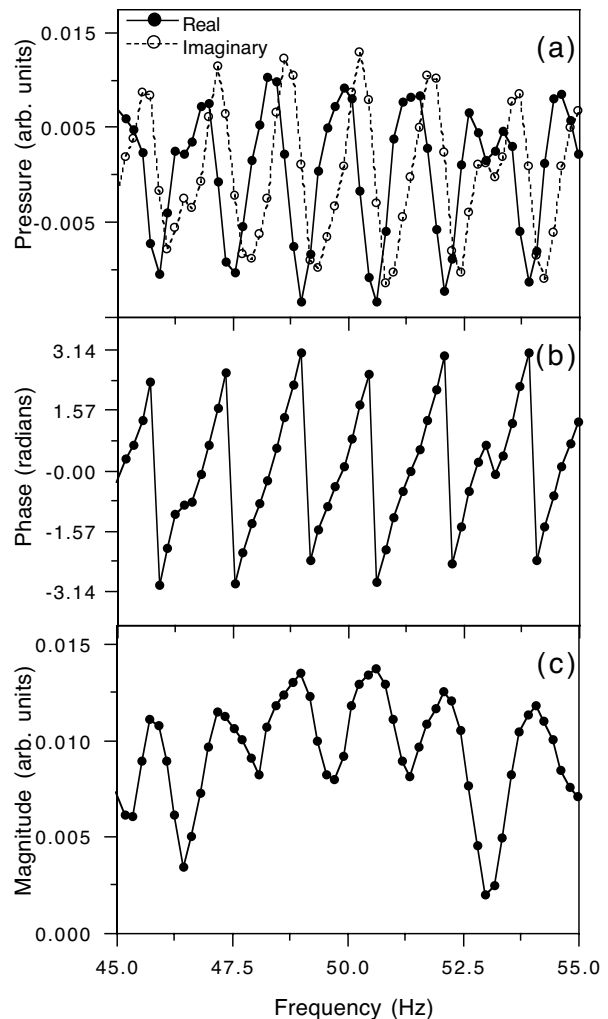


FIGURE 4 Complex field values for the example described in the text, (a) from NSPE, decomposed into (b) phase, and (c) magnitude components as a function of frequency at a receiver location. Circles indicate frequencies at which PE model was run. For clarity, only a small portion of the entire frequency range is shown. The actual frequency band spanned from 23 to 76 Hz, with zero padding out to 95 Hz. Note the wrapped linear behavior of the phase and the relatively smooth behavior of the magnitude, making both of these functions amenable to linear interpolation for intermediate values.

Example: In this case, an omnidirectional source emitting a Gaussian pulse 10 Hz wide centered on 50 Hz is used in a seamount environment with a sandy bottom. A field plot at the center frequency is shown in Fig. 5. The source is at 91 m depth, while the receiver is at 100 m on the right edge of the plot.

Time domain results are shown in Fig. 6 for (a) the real sound pressure and (b) the replica correlator output. The reference solution made with tight NSPE gridding and no frequency skipping is shown in blue, while the operational-grade solution is shown in black. Runtimes were 500.4 and 18.45 s, respectively, a 27-fold speed increase. Disabling the frequency skipping

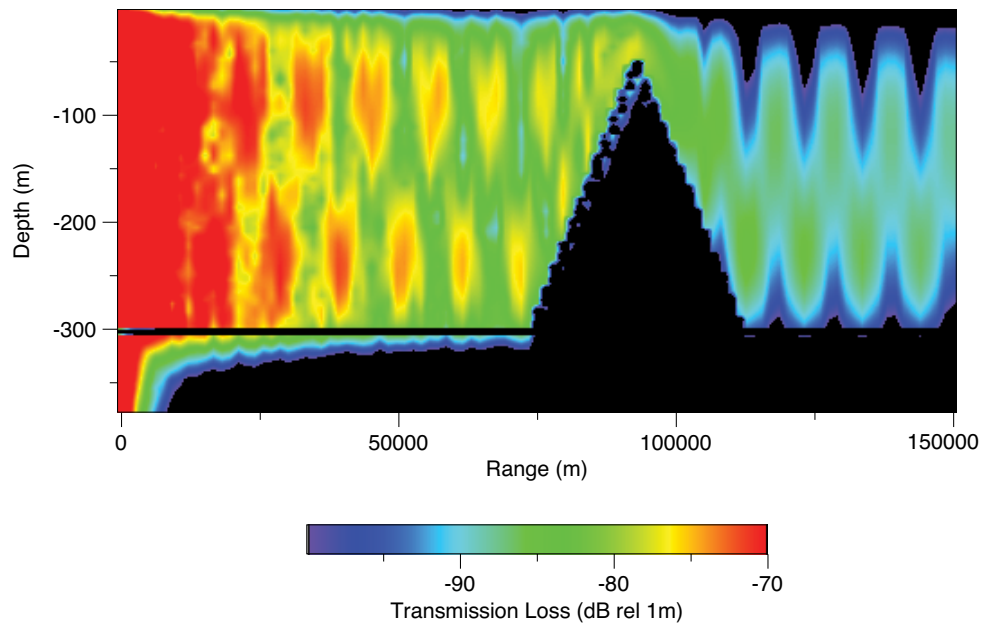


FIGURE 5 Full-field transmission loss plot at the Gaussian pulse center frequency for the example described in the text. A large seamant between 75 and 115 km is evident. The source location is at the left axis, at 91 m depth. The receiver is located on the right edge of the plot at 100 m depth.

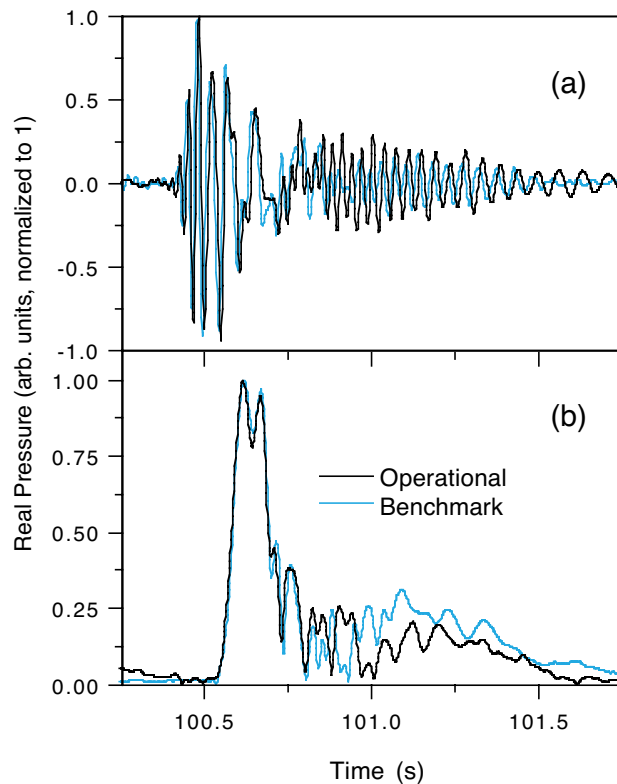


FIGURE 6 Time series results from the example described in the text, for the (a) real pressure and (b) replica correlator output. Results from operational grid and frequency interpolation settings are shown in black, while settings from research-grade settings are shown in cyan.

algorithm while retaining all other frequency-space optimizations and operational grid spacing gave a 45.86 s runtime, 2.5 times slower than the nonskipping version. For all PE grid settings and frequency skip factors used in these test runs, the pulse arrival times and transmission loss were in agreement at 100.6 s and 98 dB, respectively.

Summary: An algorithm to minimize the number of frequency-domain PE calculations required for Fourier synthesis of broadband time-domain pulses has been presented. An example in a challenging range-dependent seamount environment has been presented, with a 2.5-fold speedup over conventional optimizations demonstrated for full pulse waveform output, and a 24-fold speedup demonstrated when only arrival time and transmission loss are required. The software package is being readied for final delivery to the Navy for inclusion in the Ocean and Atmospheric Master Library.

[Sponsored by the NRL Base Program (CNR funded)]

References

- ¹R.A. Zingarelli, S.A. Chin-Bing, and M.D. Collins, "Optimizations for Fourier Synthesized Time Domain Pulse Propagation Calculations," Proceedings of the OCEANS 2009 MTS/IEEE Conference and Exhibition, Biloxi, MS, Oct. 26–29, 2009, pp. 2179–2183.
- ²R.A. Zingarelli and D.B. King, "RAM to Navy Standard Parabolic Equation: Transition from Research to Fleet Acoustic Model," 2003 NRL Review (Naval Research Laboratory, Washington, DC, 2003), pp. 212–214.
- ³W.H. Press et al., *Numerical Recipes, The Art of Scientific Computing (FORTRAN Version)* (Cambridge University Press, New York, 1989), pp. 381–429.



Range-Dependent Seismo-Acoustics

M.D. Collins
Acoustics Division

Introduction: Problems of interest in ocean acoustics typically involve grids that are much larger than a wavelength in both depth and range (horizontal distance), interaction with a seafloor that supports compressional (longitudinal) and shear (transverse) waves, and range dependence in the medium. It is usually not practical to directly solve the elliptic wave equation that governs such problems, which may often be solved routinely and accurately by reducing to a parabolic wave equation.¹ The key assumption in the derivation of a parabolic approximation is that outgoing energy dominates energy that is backscattered in the horizontal direction. In a stratified medium, arbitrarily accurate solutions may be obtained by using an appropriately

designed parabolic approximation. When the medium is range dependent, it is necessary to include a correction to guarantee that energy is conserved. This issue was unresolved for many years for the seismo-acoustic case involving a sloping fluid–solid interface at the seafloor. Appearing in Fig. 7 is a range-dependent problem involving an interface wave propagating along a sloping seafloor.

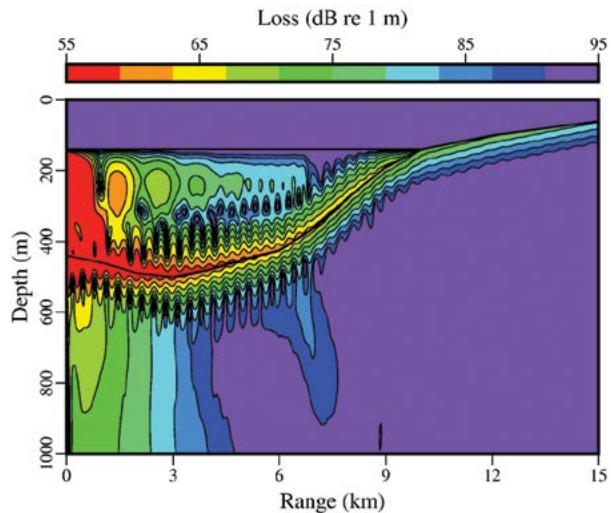


FIGURE 7

Seismo-acoustic propagation in an ocean environment with an upward sloping seafloor. A 5 Hz acoustic source is in the water column to the left, where the ocean depth is 320 m. After initially increasing, the ocean depth decreases all the way to the beach at a range of 10 km, and the slope continues beyond the shoreline. Energy concentrated near the seafloor corresponds to a Scholte wave, which becomes a Rayleigh wave beyond the shoreline. The ocean waveguide also supports a water-borne mode that transmits into the elastic sediment as a beam near a range of 7 km.

Single-Scattering Correction: The accuracy of the parabolic equation method was confirmed for range-independent acoustics problems in the late 1980s. Around the same time, it came to light that sloping interfaces and other types of range dependence may give rise to significant errors and even cause stability problems. In the implementations that were in use at the time, range dependence was handled with the naïve approach of approximating the medium in terms of a series of range-independent regions and conserving the dependent variable across the vertical interfaces between regions. For the purely acoustic case, effective corrections were developed within a few years using the concepts of energy conservation and single scattering. The seismic and seismo-acoustic cases proved to be much more challenging. A useful single-scattering correction was developed for the seismic case,² but it requires iterations that adversely affect efficiency and may not converge.

Improving the single-scattering correction for the seismic case so that iterations are no longer required led to a single-scattering correction for the seismo-acoustic case that has provided promising results.³ Since the elliptic wave equation has two range derivatives and the parabolic wave equation only has one range derivative, it is not possible to impose all of the conditions across vertical interfaces on solutions of the parabolic wave equation. For the acoustic case, effective results have been obtained by conserving quantities that guarantee that energy is conserved or to solve a single-scattering problem and discard the backscattered field (the latter approach may require iterations).

In the improved single-scattering solution for the seismic case, the transmitted field across a vertical interface consists of an average of two terms. One of the terms corresponds to conserving normal displacement and tangential stress. The other term corresponds to conserving tangential displacement and normal stress. The solution of the elliptic wave equation would be required to conserve all four quantities, but only two of them may be conserved in the solution of the parabolic wave equation. The improved single-scattering solution conserves these quantities in a mean sense; the transmitted field is the average of two fields that each correspond to conserving only two of the quantities. The simple physical interpretation of the improved single-scattering correction for the seismic case facilitated its extension to the seismo-acoustic case.³

Navy Standard Model: The earliest parabolic wave equations were based on crude approximations of the square root of a differential operator. The accuracy of this approach was suspect prior to the introduction of improved approximations based on rational functions. The next key step in the development of this approach was to incorporate the range numerics into the rational approximations; the parabolic wave equation is solved formally in terms of an exponential of the square root of an operator, which is then approximated in terms of a rational approximation.¹ This approach provides significant gains in efficiency and led to a major upgrade in the Navy Standard Model for ocean acoustic propagation. The Navy Standard Model does not currently account for shear waves, but it is anticipated that future versions will account for shear waves and handle them accurately using a single-scattering correction.

[Sponsored by the NRL Base Program (CNR funded)]

References

- ¹ M.D. Collins, "A Split-Step Padé Solution for the Parabolic Equation Method," *J. Acoust. Soc. Am.* **93**, 1736–1742 (1993).
- ² E.T. Küsel, W.L. Siegmann, and M.D. Collins, "A Single-Scattering Correction for Large Contrasts in Elastic Layers," *J. Acoust. Soc. Am.* **121**, 808–813 (2007).
- ³ M.D. Collins, "A Single-Scattering Correction for the Seismo-Acoustic Parabolic Equation," *J. Acoust. Soc. Am.* **131**, 2638–2642 (2012). ♦

Atmospheric Science and Technology

136 High-Altitude Flight Control of a Micro Air Vehicle Using Only Two Sensors

138 The Navy Global Environmental Model

140 Long-Range, Low-Frequency, Atmospheric Sound Propagation Physics

143 Smart Voyage Planning — Saving Fuel by Using Environmental Forecasts to Aid in Ship Routing

High-Altitude Flight Control of a Micro Air Vehicle Using Only Two Sensors

A. Kahn and D. Edwards
Tactical Electronic Warfare Division

Purpose: The Vehicle Research Section of the Naval Research Laboratory's Tactical Electronic Warfare Division designed an experiment to evaluate whether a small, low-cost, expendable air vehicle could be released from high altitude and fly autonomously to a preprogrammed location on the ground. Such a technology could emplace ground/ocean sensors, insert last-mile network connectivity nodes, or deliver critical medical drugs to difficult-to-access areas.

Design Considerations: A key element of the experiment was to keep the overall manufacturing cost of the vehicle to a minimum. Two unique design elements help achieve this goal. First, vehicle manufacturing and assembly are simplified by the dual use of the autopilot electronics circuit card also as the air vehicle's structure and wing. The highly automated PC board fabrication process simultaneously produces the major airframe components. Second, hardware cost and complexity are kept to a minimum by utilizing only two sensors, a rate gyroscope and GPS receiver, for navigation and flight control of the vehicle.

The Vehicle Design: CICADA (Close-In Covert Autonomous Disposable Aircraft) is the result of this design effort, shown in Fig. 1. The air vehicle is a glider, with simple flight controls on the wing to control pitch and roll. The CICADA design has a wingspan of 36 cm, length of 20 cm, and mass of 226 g. The vehicle electronics are powered by small cellphone-like lithium batteries and an internal heater keeps these battery cells warm in the extreme cold present at altitudes in excess of 9000 m. All the electronics are also encased in

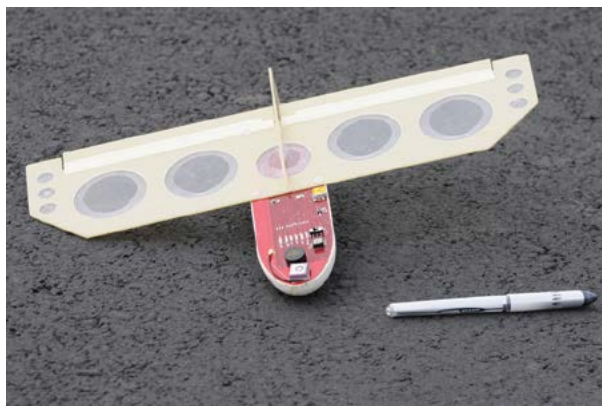


FIGURE 1
CICADA air vehicle.

polyurethane foam to provide thermal insulation and to protect against condensation.

Flight Control: Navigation and control for the CICADA uses only two simple sensors: a roll-rate gyroscope and a GPS receiver. The navigation system estimates the roll attitude and vertical descent rate of the vehicle. Roll attitude is estimated by using the rate of change of the ground track from the GPS and the roll-rate signal from the gyroscope. Vertical descent rate is estimated using GPS altitude measurement along with an a priori measurement of the vehicle's lift-to-drag ratio. These two estimated states provide the necessary measurements to control the roll and pitch attitude of the vehicle using traditional linear proportional-integral-derivative controllers.

Guidance of the CICADA is broken into two flight modes. First, the vehicle flies in a straight line toward the preprogrammed landing location. Once the vehicle is sufficiently close to the target location, the guidance system then directs the vehicle to orbit around the landing location until impact with the ground.

Results: Flight tests were performed at the Army's Yuma Proving Ground by mounting two CICADA air vehicles to the wings of a mother-ship unmanned air vehicle. The assembly was then flown to high altitude using a weather balloon, as seen in Fig. 2. At high altitude, the mother-ship was released from the balloon and flew about halfway toward the desired target location. Then, the CICADA vehicles were released from the mother-ship for final ingress to the target landing location. The flight path from one CICADA is shown in Fig. 3, illustrating the precision control of this small air vehicle. Fourteen high-altitude flights showed that the CICADA could repeatedly land within 5 m of the preprogrammed location. These results proved the robustness of this minimal, yet capable vehicle and control system.

Conclusions: This experiment demonstrated that a small, low-cost, expendable vehicle can be launched from high altitudes and precisely land at a preprogrammed location. This work provides the ability to emplace such items as ground/ocean sensors, deliver critical medical drugs, or insert last-mile network connectivity nodes into difficult-to-access locations. The unique design of the air vehicle allows for highly automated manufacturing methods to be used, thereby keeping per-unit costs low, without sacrificing the precision needed by tomorrow's Navy.



FIGURE 2
High-altitude weather balloon lifting mother-ship UAV with two CICADA vehicles attached.

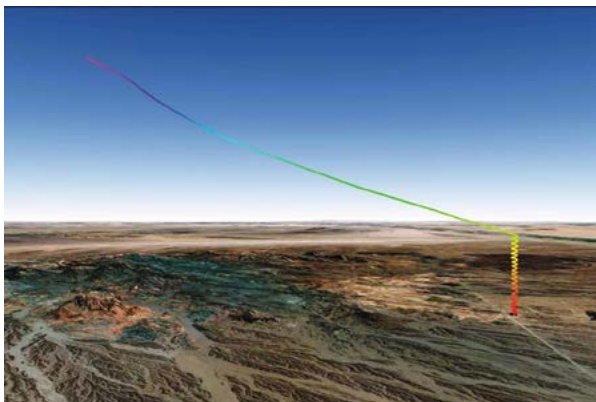


FIGURE 3
Flight path of the CICADA vehicle.

References

- ¹A. Kahn and D. Edwards, "Navigation, Guidance and Control for the CICADA Expendable Micro Air Vehicle," AIAA Guidance, Navigation, and Control Conference, Aug. 2012, Minneapolis, MN, doi:10.2514/6.2012-4536.
- ²D. Edwards and A. Kahn, "Design Evolution of a High Packing Density Micro Air Vehicle for Local-Area Seeding," AIAA At-

mospheric Flight Mechanics Conference, Aug. 2012, Minneapolis, MN, doi:10.2514/6.2012-4735.



The Navy Global Environmental Model

T. Hogan,¹ M. Peng,¹ N. Baker,¹ C. Reynolds,¹ B. Ruston,¹ M. Liu,¹ J. Ridout,¹ S. Eckermann,² J. Moskaitis,¹ T. Whitcomb,¹ K. Viner,¹ J. McLay,¹ P. Pauley,¹ L. Xu,¹ R. Langland,¹ M. Flatau,¹ J. McCormack,² and S. Chang¹

¹*Marine Meteorology Division*

²*Space Science Division*

A New Global Model: The Navy Global Environmental Model (NAVGE M) is the U.S. Navy's new high-resolution global weather prediction system, replacing the existing Navy Operational Global Atmospheric Prediction System (NOGAPS), which was introduced in 1982. Development of NAVGE M was sponsored by the Office of Naval Research (ONR) and OPNAV N2/N6E (Oceanographer of the Navy). NAVGE M represents a significant NRL milestone in numerical weather prediction (NWP) system development by introducing a semi-Lagrangian/semi-implicit (SL/SI) dynamical core together with advanced moisture and ozone physical parameterization schemes. The new SL/SI dynamic core allows for much higher model resolutions without the need for small time steps. This capability has permitted NAVGE M's initial operational transition to have both higher horizontal and higher vertical resolutions than NOGAPS (50 vertical levels in place of NOGAPS's 42 levels and an increase of horizontal resolution from 42 km to 37 km); to include cloud liquid water, cloud ice water, and ozone as fully predicted constituents; to contain new moisture, solar radiation, and longwave radiation parameterizations; to contain significant upgrades to the data assimilation component; and to complete the 180 h forecast in the allotted operation window.

NAVGE M Advancements: Critical to NAVGE M's success is the new SL/SI dynamical core. The SL method is to find the trajectory of the fluid motion that starts at the previous time step and ends up at the NAVGE M grid point location.¹ The SL integration removes the Courant-Friedrichs-Lewy (CFL) limitation of NOGAPS for conventional fixed point integration of the dynamical equations; however, high-speed gravity waves associated with high-frequency fluctuations in the wind divergence remain. This is mitigated by incorporating an SI method into the SL integration, where the terms responsible for the gravity waves are identified and treated in an implicit manner, thereby slowing down the fastest gravity waves. The combined SL/SI schemes have enabled NAVGE M to run with a time step that is three times faster than NOGAPS. With the addition of cloud liquid water and cloud ice water advection, NRL has developed a new two-species microphysics cloud water parameterization based on

the work of Zhao.² Convective clouds are allowed to evaporate at a finite rate that varies with cloud cover, providing for a more realistic representation of convective processes. This feature is enhanced by detraining cloud condensate between the lifting condensation level and the level of free convection in the NAVGE M modified versions of the Simplified Arakawa-Schubert and National Centers for Environmental Prediction (NCEP) Global Forecast System (GFS) shallow convection schemes.

Another significant improvement in NAVGE M is the addition of the Rapid Radiative Transfer Model for General Circulation Models (RRTMG) parameterizations for solar and longwave radiation, developed by Atmospheric and Environmental Research (AER, Lexington, MA).³ RRTMG includes significantly more radiation frequency bands in the solar and longwave spectra than the previous NOGAPS radiation parameterizations and incorporates additional molecular absorbers and emitters. A unique feature of the RRTMG is the use of a Monte Carlo technique to compute the subgrid cloud variability and the vertical cloud overlap.

Satellite radiance observations typically account for more than 65% of the total assimilated observations in NAVGE M. The data assimilation component that brings these observations into NAVGE M is the NRL Atmospheric Variational Data Assimilation System – Accelerated Representer (NAVDAS-AR), which has been operational in NOGAPS since 2009.⁴ The NOGAPS radiance bias correction method has been replaced in NAVGE M with a variational bias correction approach, which estimates the bias predictors simultaneously with the atmospheric analysis during each data assimilation cycle.⁵ This way, the bias corrections are constrained by other observations, the NWP model, and the analysis procedure itself.

Accuracy and Forecast Skill: Verification of NAVGE M's accuracy shows significant improvements over NOGAPS. Figures 4 and 5 show the northern hemisphere 1000 hPa geopotential height anomaly correlations (AC) for summer 2012 and fall/winter 2012/2013, respectively. The AC, a fundamental metric used by all major NWP centers, is the normalized correlation of the forecast and analysis differences with climatology, with 1.0 being a perfect forecast. The NAVGE M 120 h near-surface forecasts show a 6 h improvement over the NOGAPS forecasts for this same parameter. Tropical cyclone (TC) track forecasts are of vital importance to the safety of U.S. Navy ships, aircraft, and personnel. Figure 6 shows the TC track error comparison in nautical miles (nmi) for summer/fall 2012. The NAVGE M 120 h TC track error is 30 nmi less than that in NOGAPS, approximately a 12 h improvement. Synoptic evaluations of daily weather maps show reduced

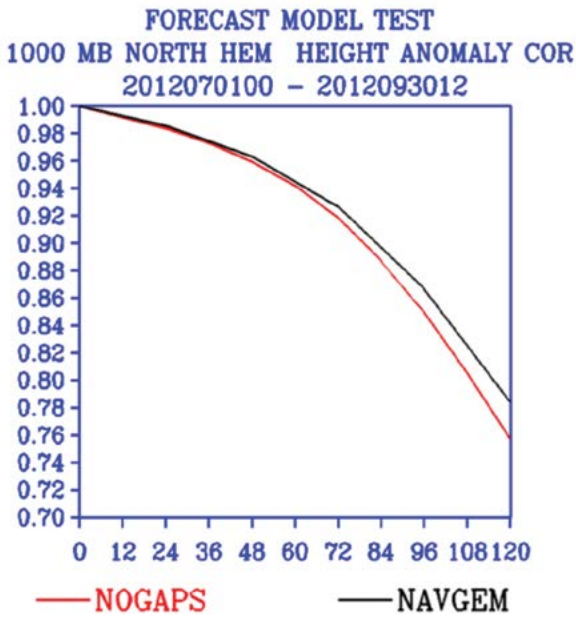


FIGURE 4
The 1000 hPa height anomaly correlations scores for NOGAPS and NAVGEM for the forecast period of July 1, 2012, to September 30, 2012.

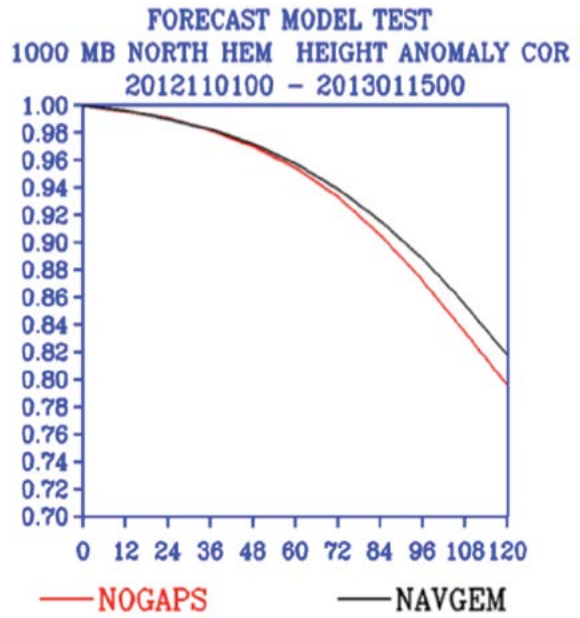


FIGURE 5
The 1000 hPa height anomaly correlations scores for NOGAPS and NAVGEM for the forecast period of November 1, 2012, to January 15, 2013.

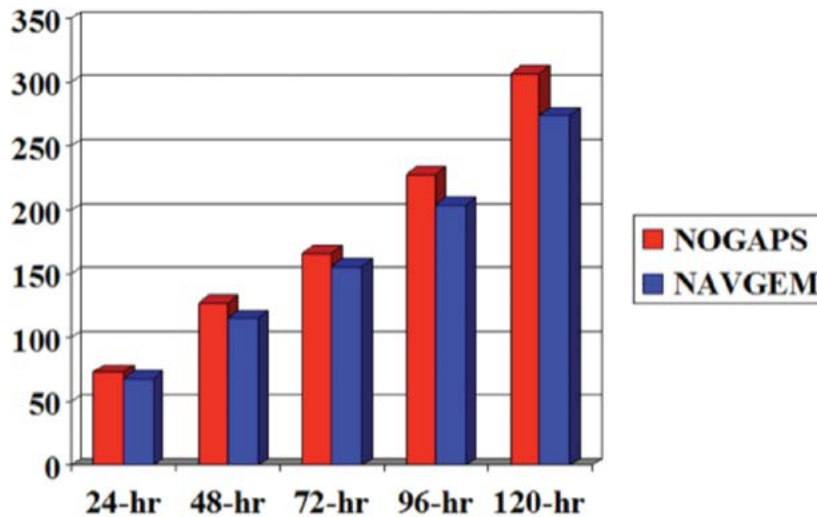


FIGURE 6
The tropical cyclone track errors in nautical miles for NOGAPS and NAVGEM for the period of July 1, 2012, to October 31, 2012. At 120 h there were 132 tropical storms that verified.

surface pressure errors with NAVGEM, particularly for maritime lows that impact the safety of ships at sea. In addition, the mid-level troughs associated with frontal systems were more realistic (deeper and faster moving) in NAVGEM than in NOGAPS.

An official operational test (OPTTEST) of NAVGEM versus NOGAPS was conducted by Fleet Numerical Meteorology and Oceanography Center (FNMOC) for the period of November 6, 2012, to December 18,

2012, with a statistical evaluation based on FNMOC's standard global scorecard. This scorecard evaluates the comparative skill of the models based on AC, mean and root mean square errors of 16 different fields and observation types, including TC tracks, 10 m winds at buoy sites, 1000 hPa and 500 hPa AC, and winds and temperatures at radiosonde locations, assigning a weighted positive score to the model with statistically significant better forecasts. Improvements in all

categories would yield a skill score of +24. NAVGEM scored a +14, the highest score ever obtained for a global model transition at FNMOC. Historically, global model improvements resulted in a skill improvement of +2. NRL will continue to upgrade NAVGEM with planned transitions to higher vertical and horizontal resolutions, a more computationally efficient dynamical core, further improvements to the data assimilation system, more advanced physical parameterizations, and the assimilation of data from recently launched satellite sensors.

[Sponsored by SPAWAR PMW-120]

References

- ¹ H. Ritchie, "Application of the Semi-Lagrangian Method to a Multilevel Spectral Primitive-Equations Model," *Q. J. R. Meteorol. Soc.* **117**, 91–106 (1991).
- ² Q.Y. Zhao and F.H. Carr, "A Prognostic Cloud Scheme for Operational NWP Models," *Mon. Wea. Rev.* **125**, 1931–1953 (1997).
- ³ R. Pincus, H.W. Barker, and J.-J. Morcrette, "A Fast, Flexible, Approximate Technique for Computing Radiative Transfer in Inhomogeneous Clouds," *J. Geophys. Res.* **108**(D13), 4376 (2003); doi:10.1029/2002JD003322.
- ⁴ B.S. Chua, L. Xu, T. Rosmond, and E.D. Zaron, "Preconditioning Representer-based Variational Data Assimilation Systems: Application to NAVDAS-AR," in *Data Assimilation for Atmospheric, Oceanic and Hydrologic Applications*, eds. S.K. Park and L. Xu, pp. 307–320 (Springer-Verlag, 2009).
- ⁵ D.P. Dee, "Variational Bias Correction of Radiance Data in the ECMWF System," in Proceedings of the ECMWF Workshop on Assimilation of High Spectral Resolution Sounders in NWP, 28 June–1 July 2004, Reading, UK, pp. 97–112 (2004); available at <http://www.ecmwf.int/publications/library/do/references/list/17444>.



Long-Range, Low-Frequency, Atmospheric Sound Propagation Physics

D.P. Drob¹ and M.A. Hedlin²

¹ *Space Science Division*

² *Scripps Institution of Oceanography, University of California*

Introduction: Subaudible low frequency atmospheric sound in the 0.02 to 10 Hz frequency band, also known as infrasound, is continually produced around the globe by a variety of natural and manmade sources. Much like seismic signals, infrasound provides a means to detect, locate, and characterize explosions and other high-energy events. Infrasound can propagate for thousands of kilometers in atmospheric waveguides because the acoustic attenuation at these frequencies is weak. First used to detect approaching aircraft and artillery batteries during World War I, today's infrasound moni-

toring applications range from the supplementation of civilian natural-hazard warning systems to a component of the International Monitoring System (IMS) of the Comprehensive Nuclear Test Ban Treaty Organization (CTBTO).^{1,2}

To accurately detect, locate, and characterize unknown infrasound events of interest over regional and long-range distances, detailed knowledge the atmosphere, often to very high altitudes, is required. One of the challenges of infrasound monitoring is that the atmosphere is constantly changing. Infrasound signal propagation characteristics thus vary widely with geographic location, propagation direction, time-of-day, and day-of-year.¹ Through research in remote sensing, acoustic wave propagation, atmospheric modeling, and other fields, the Naval Research Laboratory (NRL) has developed the means to account for this variability and compute time-dependent infrasound propagation characteristics in near real time. Figure 7 shows a local atmospheric profile from the hybrid Ground to Space (G2S) atmosphere specification technique developed at NRL (left panel) along with the resulting computed infrasound signal propagation characteristics (right panels). Research into the effects of subgrid-scale atmospheric irregularities has also further increased the fidelity of infrasound propagation calculations.

Making Sense of Infrasound Network Observables: The locations and status of the permanent infrasound arrays in the CTBTO's infrasound monitoring network — which complements the IMS seismic and radionuclide ground-based nuclear explosion monitoring networks — are shown in Fig. 8(a). Each IMS infrasound array is comprised of several distributed high-gain pressure sensors spaced approximately 750 m apart. For each infrasound array in the network, automated signal processing algorithms continuously compute the observed line of bearing (incoming signal direction), coherency measures, amplitude, and frequency content of any detected infrasound signals. This information is then combined with the infrasound detections from other infrasound stations via standard seismic network data processing techniques in order to identify potential events of interest. The automated event bulletins generated by the systems are then reviewed by human analysis in conjunction with the data from the other monitoring technologies to identify any potential Comprehensive Nuclear Test Ban Treaty violations. Individual single-element broadband seismic sensors are also capable of detecting the infrasound that propagates through the atmospheric waveguides. Shown in Fig. 8(b) is the National Science Foundation EarthScope Transportable Array seismic network that has provided data for NRL's basic research in infrasound propagation physics.

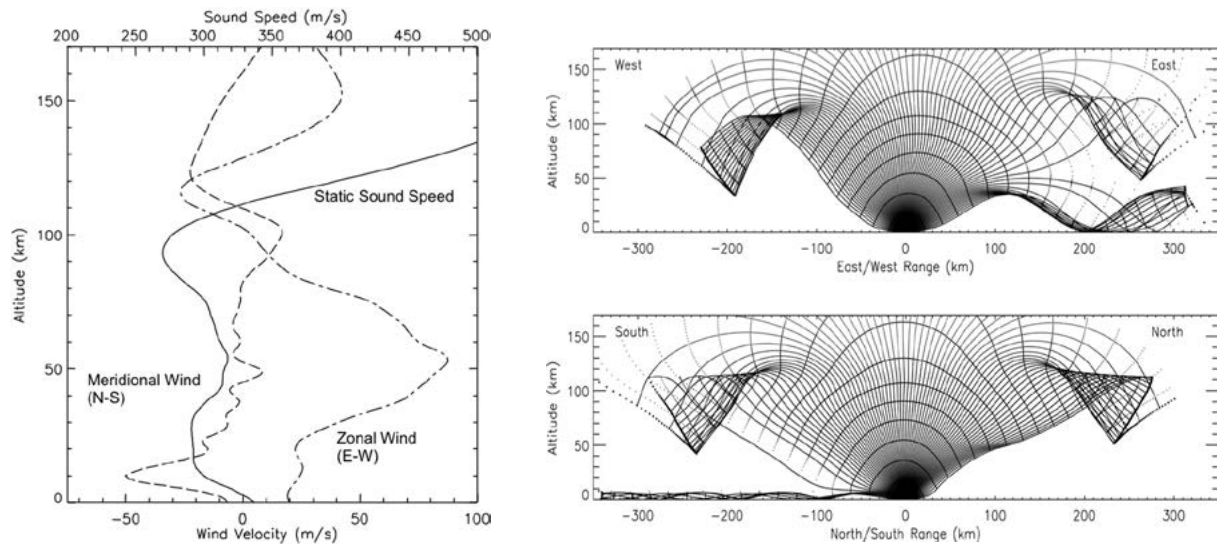


FIGURE 7 Left panel: The atmospheric zonal wind velocity (dash-dotted line), meridional wind velocity (dashed line) and sound speed (solid line) profiles at 45°S, 260°E on June 17, 2001 at 0600 UTC. Right panel: A 1000 s infrasound ray-tracing simulation performed in the east/west (top) and north/south (bottom) planes. The location and evolution of the composite wave front(s) are shown at 5 min intervals.

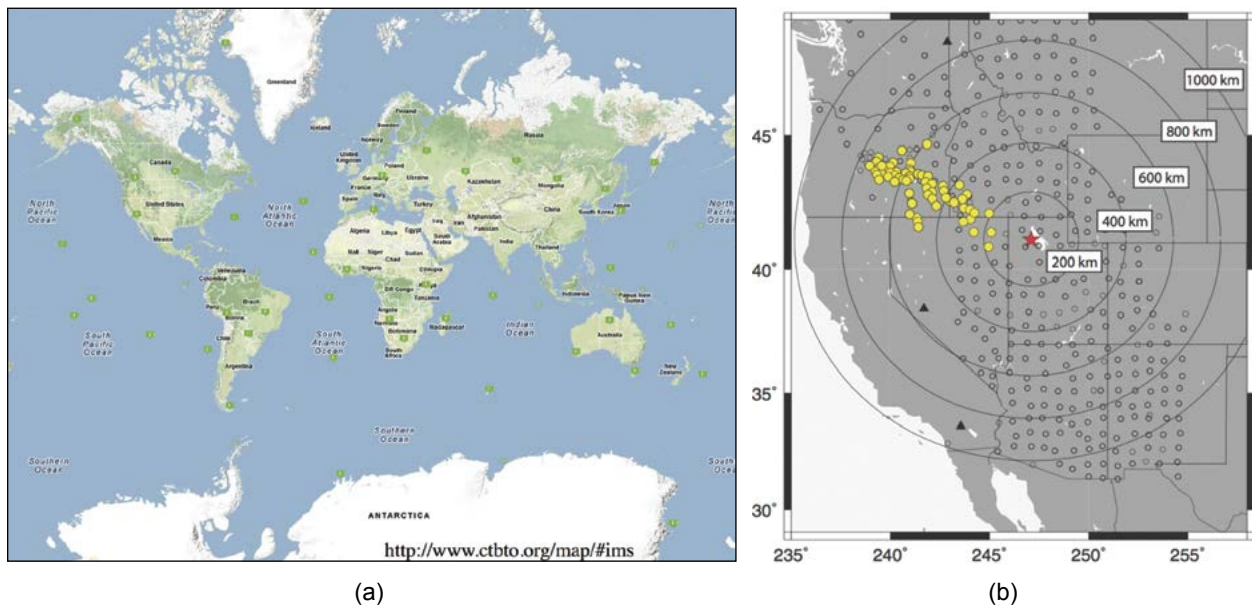


FIGURE 8 (a) Location of the 60 infrasound stations (green squares) in the Comprehensive Nuclear Test Ban Treaty Organization (CTBTO) International Monitoring System (IMS). (b) The National Science Foundation EarthScope Transportable Array (TA) comprises 400 broadband seismic stations (empty circles) installed on a Cartesian grid spanning 2,000,000 km². Through individual station redeployments, the TA network is gradually moving to the east coast. Also shown is the dense, permanent, 73-station, High Lava Plains Broadband Seismic Experiment network (yellow circles). Three permanent infrasound arrays are also shown (black triangles). The location of the Utah Test and Training Range (UTTR) is indicated (red star).

The ground-based infrasound monitoring technologies developed at NRL provide global ground-to-space specification of the atmosphere along with the supporting acoustic propagation codes needed to calculate infrasound propagation characteristics in near real time. These characteristics can then be used in network

processing algorithms to lower system false alarm rates, increase network detection thresholds, and reduce source location uncertainties. These gains are achieved by accounting for several factors in near real time: how infrasound signals travel at different velocities in the various waveguides (e.g., upwind versus downwind); to

what extent observed back azimuths deviate from the true great circle path back to a source as the result of cross-track wind effects; and how specific atmosphere waveguides might vary with range.

Atmospheric Wave–Wave Interactions: In addition to the need to account for the time-dependent macroscopic behavior of the atmosphere in propagation calculations, the importance of also accounting for unresolved small-scale atmospheric buoyancy fluctuations (known as atmospheric gravity waves) was recently recognized. The presence of these waves explains frequently observed infrasound signals in the classical near-field shadow zones, as well as how quickly infrasound signals lose their coherency over regional distances. Much like turbulence, the atmosphere’s internal gravity waves arise from wind flow over mountains, cumulus convection, and large-scale atmospheric instabilities. The intermediate and small-scale part of the internal gravity wave spectrum cannot be deterministically resolved by today’s operational meteorological systems. Therefore, just as subgrid-scale turbulence is parameterized in aerodynamic drag calculations, internal gravity wave interactions can be treated in a similar way for infrasound propagation calculations. A stochastic internal gravity wave model suitable for infrasound propagation modeling calculations was developed at NRL in partnership with the Scripps Institution of Oceanography, Raytheon BBN Technologies, and Computational Physics Incorporated.³ Adapted from the gravity wave parameterizations used within numerical weather prediction and climate general circulation models, the resulting NRL stochastic wave model is fully three-dimensional, time dependent, and physically self-consistent with the observed atmospheric background state.

To validate the updated propagation physics model, it was used to predict waveforms and signal travel times for over 100 seismic stations within the EarthScope seismic network. These stations routinely detected solid rocket body destruction events (typically >15 ton TNT equivalent) that occurred at the Utah Test and Training Range (UTTR) during summer months as part of the Strategic Arms Reduction Treaty (START) protocol. Figure 9 shows the predicted and observed results for a UTTR event on June 16, 2008. Included for comparison (in green) are the classical deterministic ray trace results through the unperturbed G2S atmospheric specifications. The model calculations (red) explain the detection of signals in the classical near-field shadow zone (a.k.a. the classical zone of silence), as well as traditionally anomalous early arrivals at greater distances. The regions of the Transportable Array record section where wave–wave interactions are predicted to fill in classical shadow zones, as well as extend the band

heads of secondary acoustic arrivals, are highlighted by the blue ovals. The purple oval highlights the regions where elevated evanescent arrivals (the traditionally anomalous second bounce range early arrivals) are also successfully predicted. The statistical scatter in the ensemble calculations also closely matches the observed waveform signal durations.

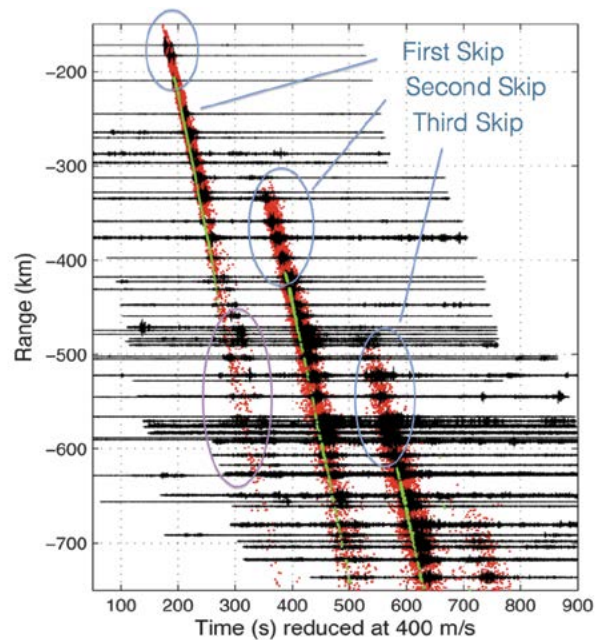


FIGURE 9 A comparison of classical acoustic travel-time predictions (green) and the new NRL stochastic ensemble ray trace predictions (red) against observed infrasound waveforms (black) by the network shown in Fig. 2(b) for a UTTR event on June 16, 2008. The observed waveforms are shifted in time with range by an average group velocity of 400 m/s. The ovals indicate regions of differences between classical ray theory and the observations, which can now be reconciled by accounting for internal atmospheric gravity fluctuations.

Summary: Infrasound research has burgeoned in conjunction with the increased sophistication of available atmospheric specifications and acoustic propagation modeling codes developed by NRL. The fidelity of information such as source location, origin time, and event classification that can be derived on the basis of infrasound network data alone (i.e., without being supplemented with seismic network data or eyewitness accounts) depends to a great extent on the state and knowledge of the atmosphere along the entire acoustic propagation path. As the result of our research, scientific knowledge of how computed range–bearing solutions and other infrasound propagation characteristics are affected by the spatiotemporal variability of the atmosphere has improved measurably. The new knowledge will lead to improvements in infrasound network detection performance metrics, minimum detection

thresholds, automatic detection algorithm false alarm rates, and event bulletin source location accuracy.

[Sponsored by ONR, Department of Energy National Nuclear Security Administration, and U.S. Army Space Missile Defense Command]

References

- ¹ D.P. Drob, M. Garcés, M. Hedlin, and N. Brachet, "The Temporal Morphology of Infrasound Propagation," *Pure Appl. Geophys.* **167**, 437–453 (2010); doi:10.1007/s00024-010-0080-6.
- ² D. Drob, J. Picone, and M. Garcés, "Global Morphology of Infrasound Propagation," *J. Geophys. Res.* **108**, 4680 (2003); doi:10.1029/2002JD003307.
- ³ D.P. Drob, D. Broutman, M.A. Hedlin, N.W. Winslow, and R.G. Gibson, "A Method for Specifying Atmospheric Gravity-Wave Fields for Long-Range Infrasound Propagation Calculations," *J. Geophys. Res.*, in press, doi:10.1029/2012JD018077.



Smart Voyage Planning — Saving Fuel by Using Environmental Forecasts to Aid in Ship Routing

J. Cook and J. Hansen
Marine Meteorology Division

Introduction: The Department of Defense (DoD) is responsible for nearly 2% of the petroleum consumption in the United States. The Navy consumes approximately 25% of the DoD portion, roughly 28.5M barrels (bbls) in FY2008, and maritime operations represent about 50% of the Navy total.¹ With energy consumption and costs increasing in a climate of resource conservation, energy independence, and fiscal responsibility, the Chief of Naval Operations (CNO) established Task Force Energy with these objectives: raise visibility and awareness of energy as a strategic resource; optimize energy considerations in budgeting and acquisition; and recommend Navy-wide energy conservation, environmental stewardship, and alternative energy strategies.

In response to the CNO, the Secretary of the Navy developed focused energy goals of sailing the "Great Green Fleet" by 2016 with a demonstration in 2012, and reducing nontactical petroleum use by 50% by 2020.

As part of the Naval Sea Systems Command (NAVSEA) Energy Office program, the NRL Marine Meteorology Division (MMD) worked with Itri Corp. in coordination with DRS Defense Solutions, LLC, to address these energy goals by developing the Smart Voyage Planning Decision Aid (SVPDA). SVPDA is a software application used to optimize ship transit routing for fuel savings. The software incorporates ship hull, mechanical, and electrical (HM&E) models

combined with a sophisticated treatment of real-time environmental forecast data to produce route guidance that optimizes fuel efficiency while ensuring ship safety. SVPDA was demonstrated during the Rim of the Pacific 2012 exercise, with fuel efficient route guidance provided from a prototype system at NRL MMD to USS *Princeton* (CG 59) via Fleet Weather Center San Diego (FWC-SD).

Methodology: The Navy has devoted considerable effort to develop the operational global ensemble forecast system consisting of the Navy Operational Global Atmospheric Prediction System (NOGAPS), WAVE WATCH III (WW3), and the global Navy Coastal Ocean Model (NCOM) systems. (NOGAPS was used in development and has since transitioned to NAVGEM – see pages 138 to 140.) Ensembles refer to a collection of numerical model forecast runs from the same start time, with each run (or "member") having a slightly different, but realistic (within the bounds of expected uncertainty) set of initial conditions. The result is a suite of forecasts spanning the range of possible future states. Ensembles have the potential to improve forecasting over deterministic systems (a single forecast run) through improvements in data assimilation and with their additional information about the expected distribution of forecast environmental parameters. Recently, NRL MMD worked with Itri Corp. to develop the Ensemble Forecast Application System (EFAS) to provide a framework to easily utilize ensemble data and perform automated post-processing to improve the forecast statistics. Post-processing refers to the practice of correcting model output based on the historical performance of the forecast system.

EFAS is configurable, not model specific, and produces a consensus based on bias correction (removal of systematic error) over a 30-day period that conveys deterministic-like values (for ease of interfacing with applications expecting deterministic data) and confidence in the consensus within a user-defined tolerance of forecast error. EFAS outputs were interfaced to the Ship Tracking and Routing System (STARS) to provide improved guidance for ship routes as part of SVPDA. Experiments with EFAS showed that a hybrid combination of raw ensemble average and bias-corrected ensemble average provided the optimum set of environmental parameters for STARS. These parameters are shown in red in Table 1.

During RIMPAC 2012, NRL MMD, Itri Corp., and DRS worked with FWC-SD and USS *Princeton* and USS *Chafee* (DDG 90) to demonstrate SVPDA. FWC-SD watch standers initiated route requests after entering the ship's Movement Report (MOVEREP) information into the operational Joint METOC Viewer (JMV) software. JMV produced a SVPDA request, which was e-mailed to NRL MMD for servicing. NRL MMD used

Table 1 — Environmental Data Products from EFAS

Parameter	Post-Processed Data from EFAS			
10 meter – U west wind component	16 member NOGAPS forecast	Raw Ensemble Average	Bias Corrected Ensemble Average	Wind Speed Confidence
10 meter – V south wind component	16 member NOGAPS forecast	Raw Ensemble Average	Bias Corrected Ensemble Average	
Sea height (wind wave)	16 member WW3 forecast	Raw Ensemble Average	Bias Corrected Ensemble Average	Sea Height Confidence
Sea period (wind wave)	16 member WW3 forecast	Raw Ensemble Average	Bias Corrected Ensemble Average	
Sea direction (wind wave)	16 member WW3 forecast	Raw Ensemble Average	Bias Corrected Ensemble Average	
Swell height	16 member WW3 forecast	Raw Ensemble Average	Bias Corrected Ensemble Average	
Swell period	16 member WW3 forecast	Raw Ensemble Average	Bias Corrected Ensemble Average	
Swell direction	16 member WW3 forecast	Raw Ensemble Average	Bias Corrected Ensemble Average	
Surface currents – U east component	<i>NCOM deterministic forecasts used (ensembles were not available)</i>			
Surface currents – V north component	<i>NCOM deterministic forecasts used (ensembles were not available)</i>			

the EFAS output and JMV ship request file to execute a version of STARS modified by DRS to incorporate the ship HM&E models. The STARS output routes were then plotted using Google Earth Geospatial Information Services (GIS) software for quality control and e-mailed back to FWC-SD for consideration by the Ship Routing Officer for forwarding to the ship. Aboard ship, the route recommendations were entered into the Electronic Chart Display and Information System – Navy (ECDIS-N) for navigation and display. Figure 10 shows the sequence of events and data flow.

Engineering, navigation, and environmental logs taken by USS *Princeton* throughout the voyage from Pearl Harbor to San Diego are being used to assess the SVPDA fuel savings effectiveness for the AEGIS Cruisers. Data for assessment will also be collected from additional surface Navy and Military Sealift Command ships that will be issued SVPDA routes in the future. The recorded environment will be compared to the “perfect forecast” created from the retroactively determined best estimate of the environmental conditions along the voyage and to the ensemble weather forecast valid at that time that was used for the recommended SVPDA route. The impact of any variations between the observed values and those used for the recommended route will be assessed. Engineering plant settings and ship speed throughout the voyage will be reconciled. The following will be addressed:

- Fuel savings projections versus measured;

- The fuel burned for the route followed will be compared to the predicted fuel consumed for the SVPDA-recommended route and for the minimum-distance great circle route (with the same start and destination and the same arrival time);
- Ship HM&E model calibration; and
- Individual leg fuel consumptions down to the component level will be compared for the route USS *Princeton* followed and an equivalent SVPDA route generated using the actual route that USS *Princeton* followed and the observed weather during its voyage to determine the validity of the ship HM&E model and identify possible improvements.

As shown in Fig. 11, ship fuel consumption rate increases rapidly with ship speed, approximately 1% to 4% per knot at moderate speeds and about 9% per knot at high speeds. Thus, optimizing the ship speed profile during transit can yield significant fuel savings. Figure 12 shows the impact of the environment, with ship fuel consumption increasing significantly with moderate waves, wind, and currents. At constant speed, fuel consumption in sea state 4 increases by approximately 10% over the calm water value. According to modeling estimates, using SVPDA-optimized transit routing — optimizing the ship route together with the speed profile to avoid adverse environmental conditions — can save approximately 4% in annual fuel costs.

Figure 13 shows an example SVPDA route recommendation for a ship traveling from Guam to Sydney

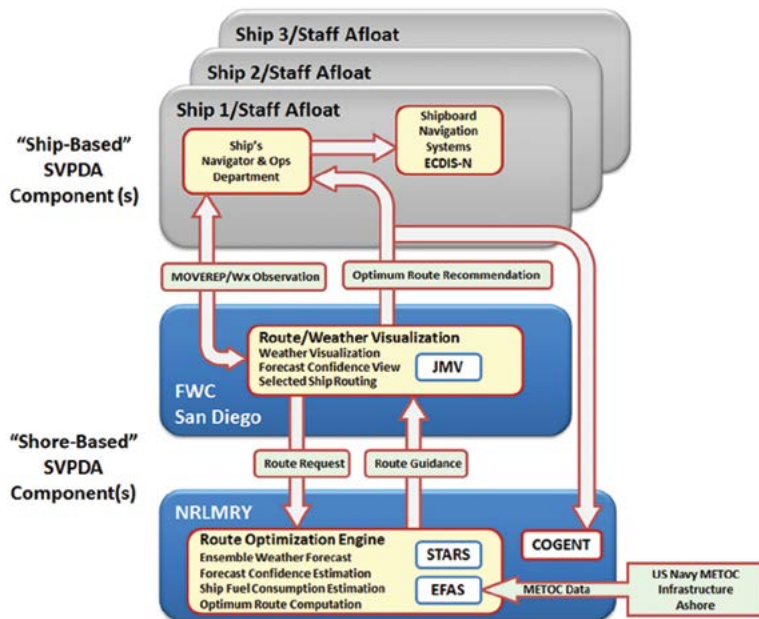


FIGURE 10
 Notional components of SVPDA exercised during RIMPAC 2012 showing shore-based EFAS and STARS components at NRL MMD in Monterey and FWC-SD and shipboard components on USS *Princeton* and USS *Chafee*. The COGENT component was not exercised.

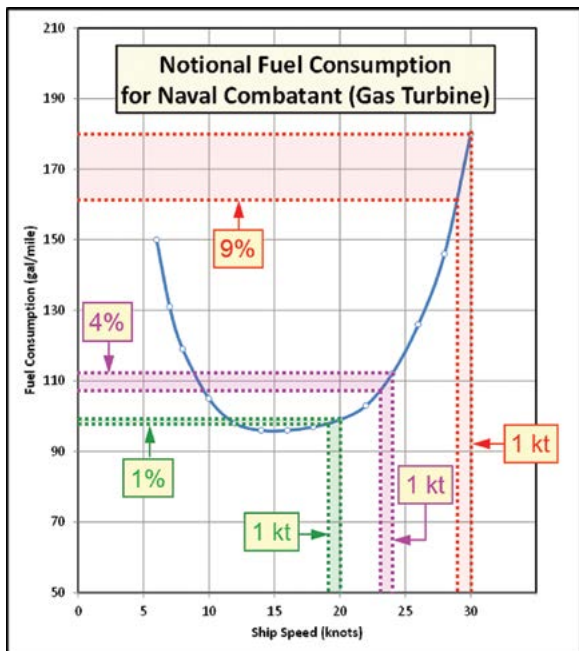


FIGURE 11
 Fuel consumption sensitivity to ship speed in calm water.

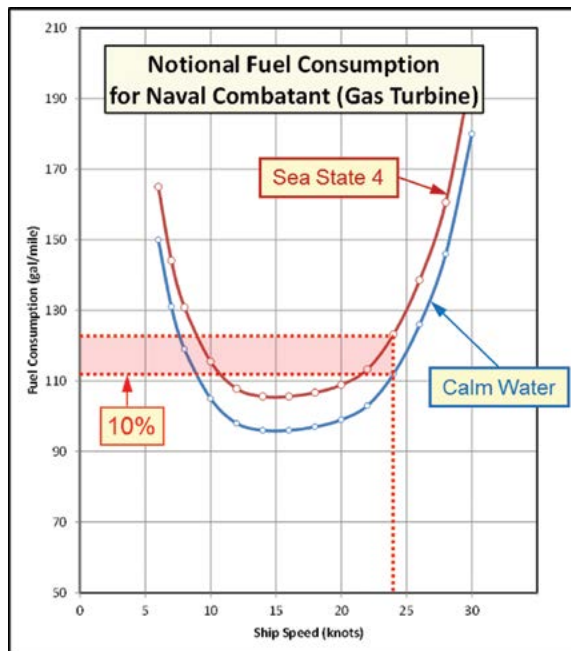


FIGURE 12
 Fuel consumption sensitivity to environment with calm water vs sea state 4.

(red line). The great circle route (green line) serves as a baseline for fuel usage comparison. SVPDA selected the route with the minimum overall cost (in gallons of fuel expended) that arrives on time while not exceeding weather-related ship safety limits. The SVPDA route exploits information in the forecasts of adverse weather and the ship's most efficient speed to save 4.5% of fuel expended (savings over 16,500 gal) in spite of a longer distance traveled (3029 nmi vs 3595 nmi); the arrival times are the same.

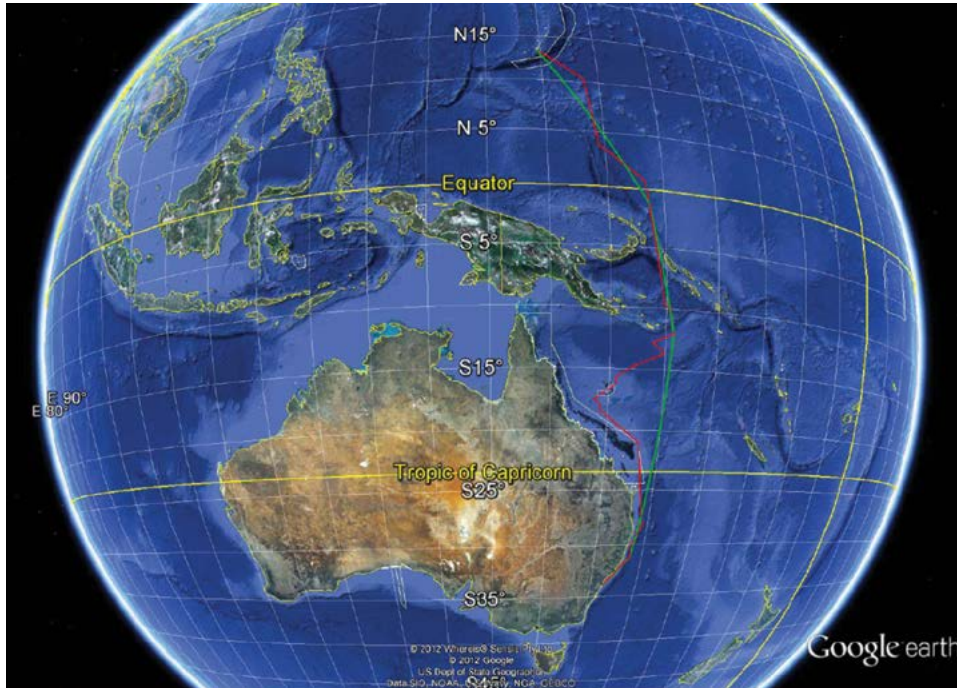


FIGURE 13
SVPDA-recommended minimum fuel route (red line) compared to great circle route baseline (green line) from Guam to Sydney.

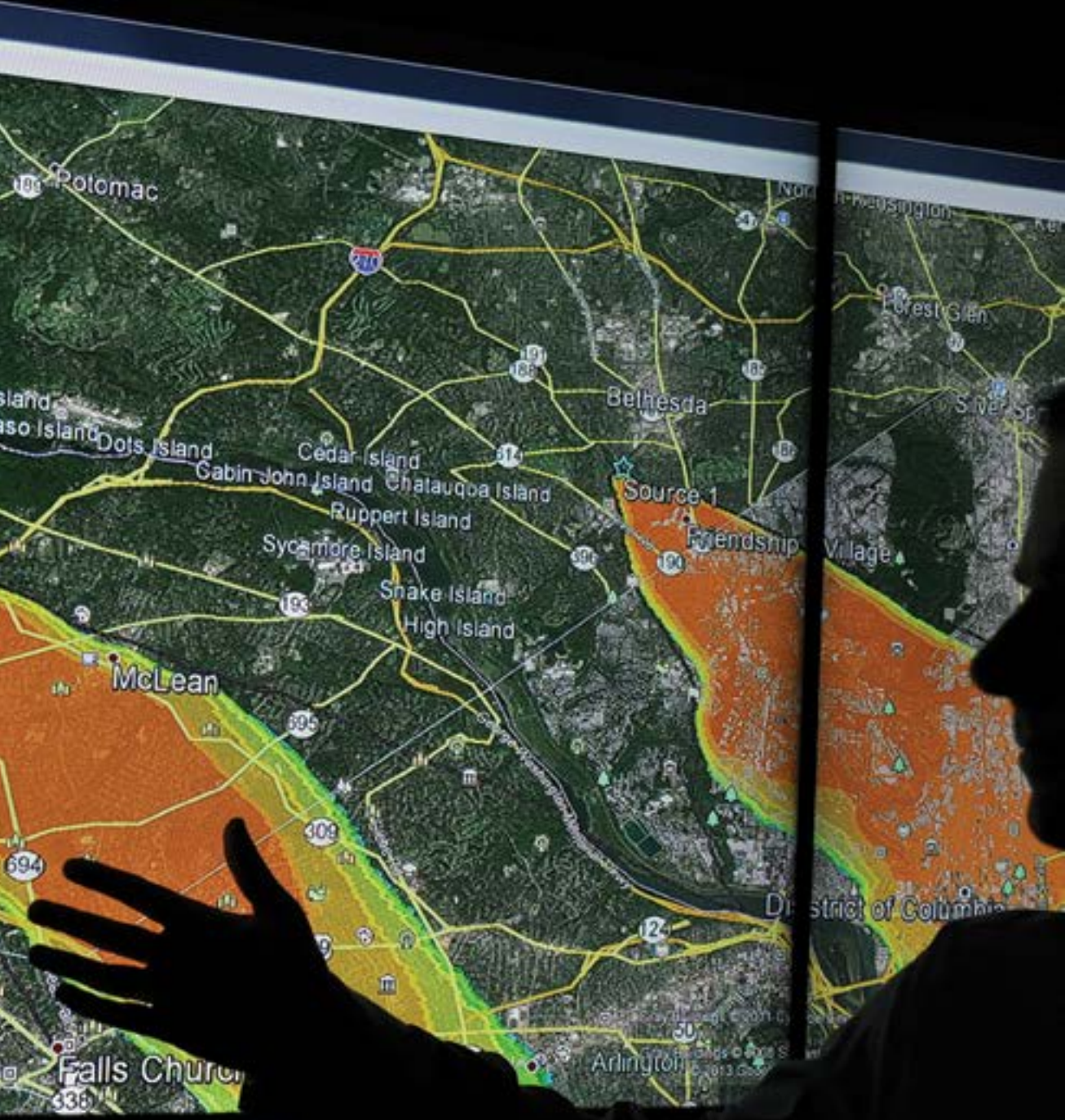
Conclusions: SVPDA is a technology that blends a unique, sophisticated treatment of environmental ensemble forecast data with ship HM&E models to provide ship transit recommendations optimized for fuel efficiency and ship safety. SVPDA may be used ashore for ship scheduling with a focus on minimizing fuel usage and it may be enhanced to include environmental mission impact parameters to help improve mission effectiveness and to maximize ship hull life expectancy.

[Sponsored by NAVSEA]

Reference

¹RADM P. Cullom, Navy Task Force Energy Briefing, Director of Fleet Readiness, OPNAV N43 (2010).





Chemical/Biochemical Research

148 Barnacle Adhesion Two-Step

150 Pulsed Electron Beam Driven Chemistry

Barnacle Adhesion Two-Step

K.J. Wahl,¹ C.M. Spillmann,² D.E. Barlow,¹ R.K. Everett,³ B. Orihuela,⁴ D. Rittschof,⁴ and D.K. Burden⁵

¹Chemistry Division

²Center for Bio/Molecular Science and Engineering

³Materials Science and Technology Division

⁴Duke University Marine Laboratory

⁵NRL/NRC Postdoctoral Research Associate

Prologue: Hard foulers such as barnacles compromise Navy ship hulls and other underwater surfaces, significantly increasing drag and fuel consumption of deployed ships. Increased maintenance of coatings and components due to fouling, as well as pressure to develop less toxic paints and surface treatments, motivates research into how foulers adhere in order to inform future coating development and antifouling strategies. Barnacles are among the most pervasive foulers, curing their insoluble adhesive underwater. The details of the curing process remain elusive due to the inherent challenge of the “buried” bonding interface underneath the barnacle.

NRL has established a multidisciplinary research team combining expertise in chemistry, biology, and materials science to study barnacle glue under living barnacles. The research team has discovered barnacle adhesion involves sequential secretions under the organism’s expanding periphery. Barnacles repeat this cycle throughout their lives, constantly adhering to the substrate as they expand to cover new territory. The team devised a way to reattach adult barnacles to clean,

petitive, timed movements or music’s adagio and allegro tempos, barnacle adhesion is accomplished sequentially: first by understated movement, then followed by a burst of activity. The majority of the growth (the big step or adagio-like movement) accomplishes half the adhesion, while a faster event (a short, quick step or allegro movement) quickly doubles the adhesive strength.

Step One — Adagio: Watching barnacles grow, like watching paint dry (or literally glue curing), is a slow process. Barnacles grow radially about one to two microns per hour, creating a set of rings that resemble the growth rings seen on a tree stump. For perspective, it would take a barnacle 30 to 60 hours to grow a ring as wide as a single strand of human hair. To speed things up, the team uses young barnacles and time-lapse photography under a microscope to watch the barnacles grow and develop their adhesive interfaces.

The barnacle grows larger by nearly continuously expanding and lengthening the side shell plates to create more volume inside the shell for the barnacle body and a larger diameter at the base where it adheres. While the process of advancing the perimeter is slow, the barnacle periodically develops some interesting features at the interface. During the slower, “adagio” growth, new capillary structures appear, extending ductwork and output ports that drain into the interface (Fig. 1, top). In young, fast growing barnacles, this repetitive process occurs every three days. However, the barnacle spends most of that time advancing the side plates, while the capillary ductwork appears well behind the leading edge of growth and becomes visible over a period of less than an hour.

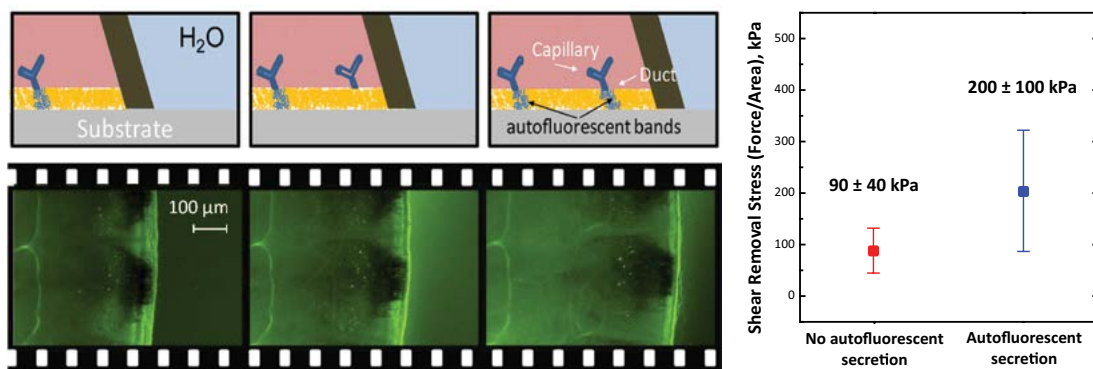


FIGURE 1

Cartoon depicting expansion of barnacle as viewed from the side (upper panels, left) and as viewed from below an actual barnacle through glass with UV illumination (lower panels, left). The base expands, and subsequently a new set of capillaries forms, secreting an autofluorescent fluid into the interface. Barnacles (*Balanus amphitrite*) removed from substrates before (right, red data) and after (right, blue data) the autofluorescent secretion show marked differences in the removal stress, which is nearly doubled after the capillary autofluorescence appears.

transparent substrates to monitor adhesion strength throughout the cycle. Watching the process from underneath, the team found that barnacle adhesion is a sequential, two-step process. Not unlike a dance’s re-

Step Two — Allegro: It has long been recognized that the capillary ductwork and the glands from which they originate play a key role in barnacle adhesion. The team was able to follow the development and secre-

tory activity of the capillaries using time-lapse, high-resolution optical microscopy under ultraviolet (UV) or “black light” illumination. The growing edge of the barnacle is semitransparent, and many of the structures within the barnacle light up under UV illumination in a process called autofluorescence. The capillaries are particularly bright (Fig. 1), and time-lapse photography reveals that these capillaries secrete an autofluorescent material over a short window of time (hours) at the end of the long adhesion cycle (days). Adhesion was measured before new capillary structures were visible, and doubled after the autofluorescence was detected. This experiment demonstrated that the second, quick step, identifiable by its bright autofluorescence, has a surprisingly powerful impact on adhesion (Fig. 1).¹

Finale: The experiments include novel approaches to reveal the detailed structure and chemistry of the interface components associated with increased adhesion,^{1,2} as shown in Fig. 2. The structures and chemistries involved in the interface building process are related to molting in invertebrates — the process by which barnacles, crabs, lobsters, and all other crustaceans shed their exoskeletons to enlarge their protective shells. In barnacles, part of this process occurs

underneath the shell where the barnacle adheres; this material cannot be discarded as in the normal molting process and thus is unique to barnacles. This work adds for the first time an analysis showing how multiple secretions, separated temporally and spatially underneath the living barnacle, combine to increase tenacity of barnacles to marine surfaces. Much work remains to identify the composition of these fluids and the chemistries involved. However, the results to date point to the importance of determining how growth and development impact adhesion in these pervasive foulers, as well as assist in guiding development of more effective, nontoxic surface treatments to prevent barnacle fouling.

[Sponsored by the NRL Base Program (CNR funded) and ONR]

References

- ¹ D.K. Burden, D.E. Barlow, C.M. Spillmann, B. Orihuela, D. Rittschof, R.K. Everett, and K.J. Wahl, “Barnacle *Balanus Amphitrite* Adheres by a Stepwise Cementing Process,” *Langmuir* **28**, 13364-13372 (2012).
- ² D.E. Barlow and K.J. Wahl, “Optical Spectroscopy of Marine Bioadhesive Interfaces,” *Annual Reviews of Analytical Chemistry* **5**, 229-251 (2012).

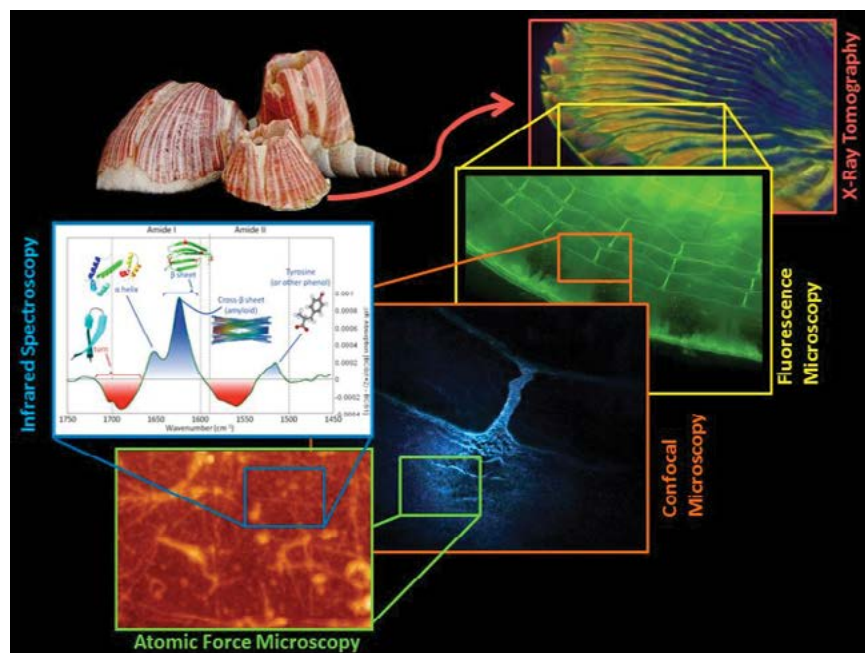


FIGURE 2

We use a multiscale, multiwavelength approach to determine how barnacles adhere to surfaces and the structures and chemistries responsible for adhesion. The structure of a barnacle shell (upper left) is examined by computer-aided X-ray tomography (CAT scan) (upper right). Barnacle growth and adhesion proceeds by expansion of the base and secretion of multiple fluids, a fraction coming from micron-scale capillary structures that form periodically underneath the barnacle. Fluid from the capillary structures autofluoresces (central images) and contains nanoscale fibrillar structures (lower left). Chemical analysis (middle left) reveals features consistent with fibrillar proteins and aromatic (carbon-ring structured) molecules.

Pulsed Electron Beam Driven Chemistry

J.D. Sethian,¹ M. Wolford,¹ M. Myers,¹ and F. Hegeler²

¹Plasma Physics Division

²Commonwealth Technology, Inc.

The Concept: We are studying the use of high energy pulsed electron beams to efficiently drive chemical processes. Practical applications include pollution control and the synthesis of fuels. The latter, if successful, could help meet both Navy and civilian energy needs, as it might lead to an efficient means to provide liquid fuels for existing Navy ships and aircraft as well as civilian transportation systems. At the most fundamental level, chemical processes require breaking apart the chain of one or more types of molecules and then allowing the constituents to recombine to another. Most chemical reactions require external energy, usually in the form of heat. When carried out in practice, this leads to large systems requiring high temperatures and pressures, and sometimes catalysts. A more efficient means of breaking chemical bonds is to deposit the energy with an energetic particle, such as an electron beam.¹ This is called electron beam radiolysis.

Advantages of a Pulsed Beam: Almost all chemical synthesis involves multiple steps. The initial bond-breaking takes only a few tens of nanoseconds (10 billionths of a second), whereas the subsequent recombination takes much longer. Thus, it is desirable to have the electron beam “on” long enough to break the bonds, but then “off” so as not to interfere with the recombination. Since one wants to break as many

bonds as possible, this calls for a high power, very short duration, electron beam. To be practical, the system must be capable of efficiently running at several pulses per second for long periods of time.

NRL Pulsed Electron Beam Science and Technology: The NRL Plasma Physics Division is developing the science and technology needed for just such a system. The NRL Electra facility (Fig. 3) generates a 500 kV, 100 kA, 100 ns, repetitively pulsed (5 Hz) electron beam and deposits its energy into a gas.² The peak power is 5×10^{10} (50 billion) Watts. Electra was originally developed to pump a krypton fluoride laser for inertial fusion energy. Our research has led to a system that operates at 5 Hz for several hours with a projected efficiency (wall plug to electron beam energy deposited into the gas) of greater than 60%. The present duration limit is due to the high voltage “spark gap” switches in the electron beam power supply. Just like their more common automotive spark plug cousins, these switches erode in time, leading to erratic performance. However, we have recently developed a prototype, all solid-state, pulsed power system that has run continuously for 11 million pulses at 10 Hz (319 hours). The individual components have been tested to at least 300 million pulses.

Conversion of Natural Gas and CO₂ to Liquid Fuels and Basis for Syngas: In one experiment, we irradiated a mixture of 10% CH₄ and 90% CO₂ with 500 electron beam pulses. The deposition per pulse was 0.08 J/cc. The gas constituents were measured before and after exposure using a residual gas analyzer (RGA). As shown in Fig. 4, we converted some of the carbon dioxide, a greenhouse gas, into hydrogen and CO, the basis of Syngas, and methanol, a cleaner burning liquid fuel.

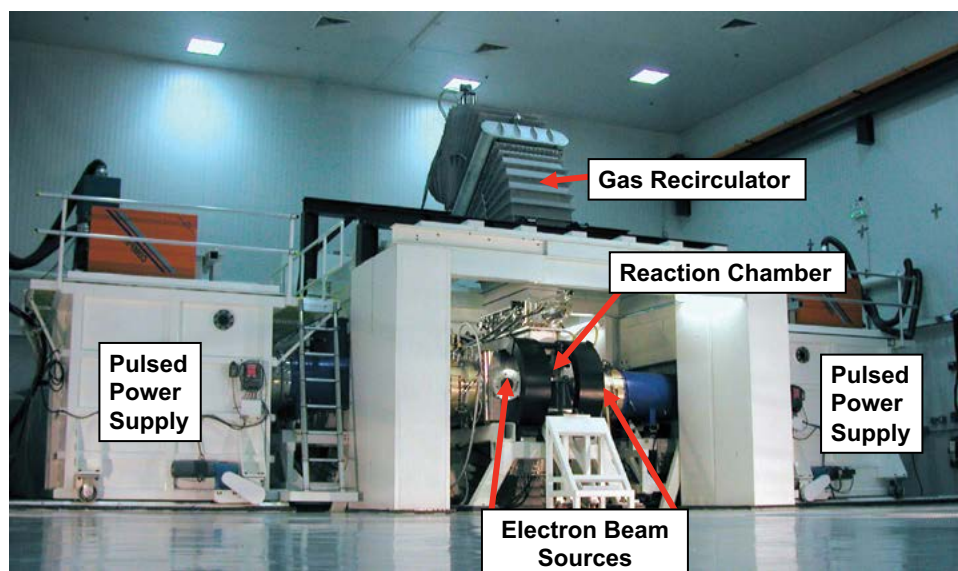


FIGURE 3
The NRL Electra Electron Beam Facility.

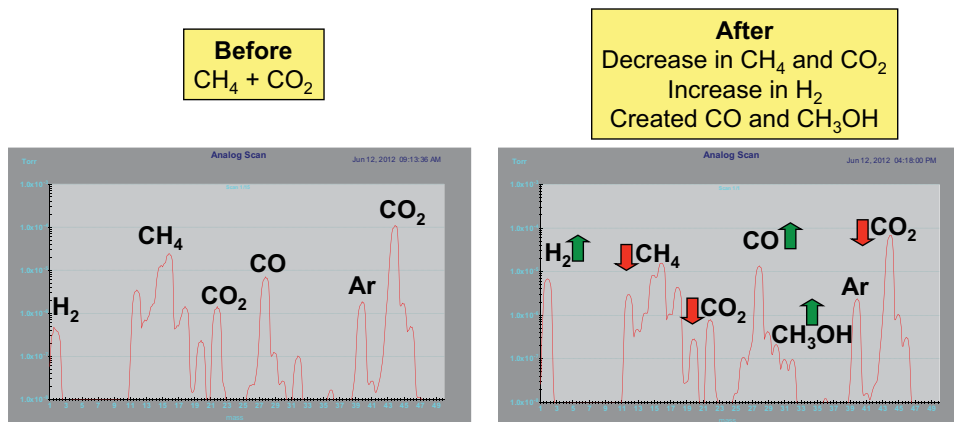


FIGURE 4 Residual gas analyzer of chamber constituents. Left, before; right, after. The data shows a conversion of a mixture of 10% natural gas CH_4 and 90% CO_2 to hydrogen and CO (Syngas), and methanol (CH_3OH).

Conversion of NO_x from a Coal Power Plant

Exhaust to Nitrogen and Oxygen: We have also shown that the electron beam can efficiently convert NO_x to nitrogen and oxygen. NO_x (mainly NO and NO_2) is a major source of acid rain and is found in the exhaust of any hydrocarbon-based power plant, be it fired by coal, oil, or even natural gas. Our experimental results are shown in Table 1.

TABLE 1 — Conversion Results

Initial NO_x (ppm)	Final NO_x (ppm)	Removal efficiency	Electron beam deposition (J/cc)
500	9.91	98%	.084

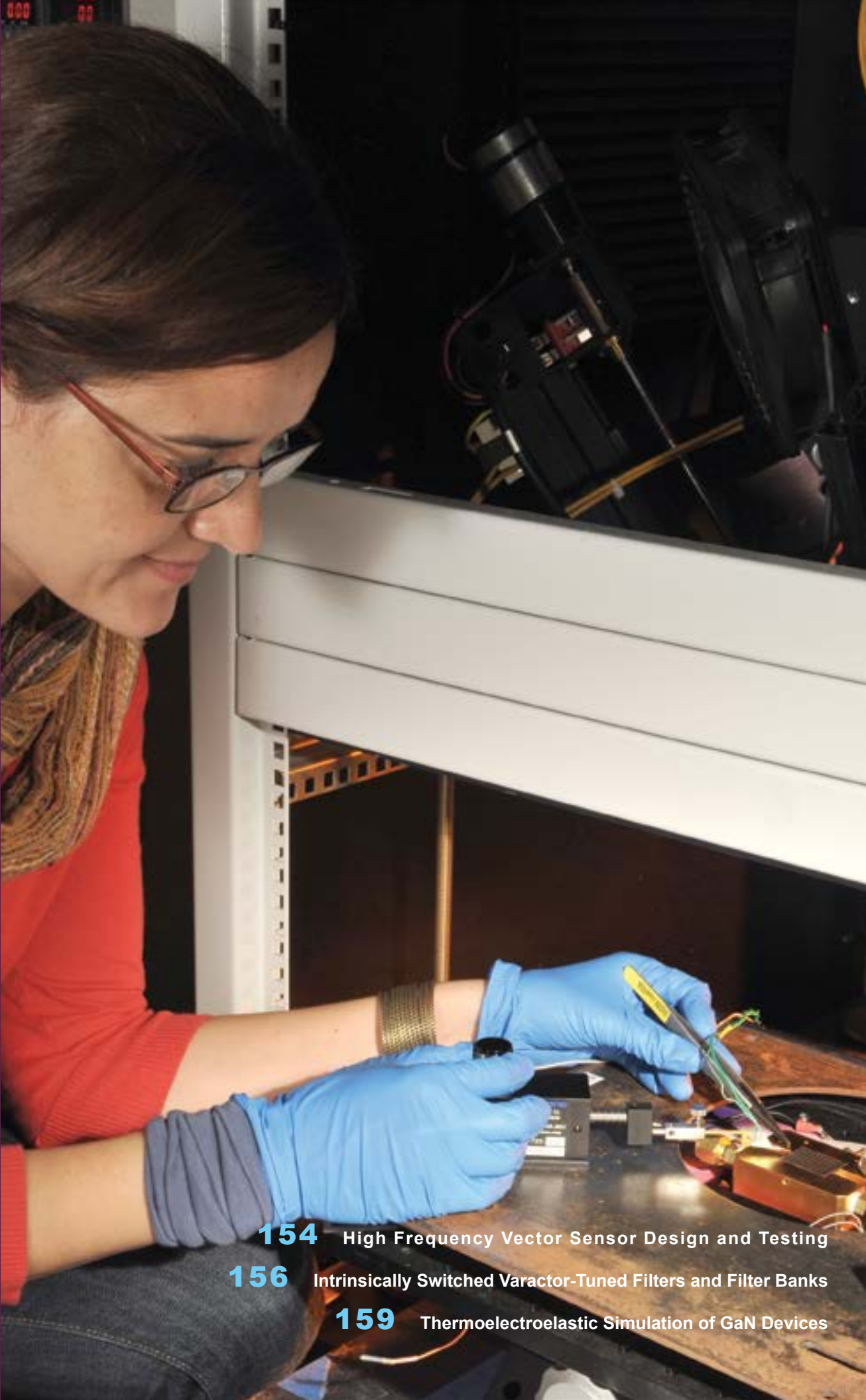
The electron beam converted 98% of the NO_x to nitrogen and oxygen. The remaining concentration is below the current EPA requirements for power plant emissions.

Summary: There are many more applications for chemical reactions induced by pulsed electron beams. All would be optimized by a better understanding of the fundamental e-beam physics and chemistry. We are just starting to scratch the surface of this scientifically rich and diverse field.

[Sponsored by the NRL Base Program (CNR funded)]

References

1. R.A. Lee, "Febetron Radiolysis of CO_2 in the Presence of Oxygen and Carbon Monoxide," *Radiation Research* 77(2), 233–241 (1979).
2. J.D. Sethian et al., "ELECTRA: A Repetitively Pulsed, Electron Beam Pumped KrF Laser to Develop the Technologies for Fusion Energy," *Special Issue of the Proceedings of the IEEE on Pulse Power: Technology and Applications, Proc. IEEE* 92, 1043 (2004).



Electronics and Electromagnetics

154 High Frequency Vector Sensor Design and Testing

156 Intrinsically Switched Varactor-Tuned Filters and Filter Banks

159 Thermoelastic Simulation of GaN Devices

High Frequency Vector Sensor Design and Testing

W.W. Lee, M. Parent, and G. San Antonio
Radar Division

Introduction: An electromagnetic vector sensor (EMVS) is a complex antenna; it measures the three orthogonal components of the electric field in addition to the three components of the magnetic field at a single point.^{1,2} It is sensitive to both the direction-of-arrival and polarization of incoming electromagnetic waves. While the use of traditional antennas and antenna arrays for direction-of-arrival estimation/beamforming is well understood, the EMVS provides new potential applications and fresh challenges. The design and construction of a structurally sound EMVS for high-frequency (HF) skywave applications opens the door to further explore ionospheric and signal processing possibilities utilizing the additional information provided by the EMVS antennas.

Relevance: Ground-based radar systems that survey vast areas and operate over large distances are tasked to detect small targets thousands of kilometers away. Radio waves tend to travel in straight lines, limiting detection to objects above the horizon, due to the curvature of the Earth. Over-the-horizon radar systems use radio signals that are transmitted skyward and refracted toward the ground by the ionosphere to get energy to and from targets beyond the horizon.

The ionosphere is a dynamic channel and thus target geolocation and detection is subject to precise characterization of the propagated HF signals. The development and understanding of advanced HF antennas are essential in accurately understanding the state of the ionospheric channel path and its effect on radio frequency (RF) signal refraction and subsequent changes in polarization. To this end, the Radar Division at the Naval Research Laboratory has built and experimentally tested a novel EMVS design for use in the HF band (3 to 30 MHz).

Construction: EMVS antennas provide more information than traditional whip antennas. A single vertical monopole antenna has an azimuthally equal omnidirectional radiation pattern with a minimum at its zenith. The Radar Division–designed EMVS consists of three orthogonally oriented electrically short dipoles and three electrically small orthogonal loop elements (Fig. 1). The EMVS uses active electronic circuits to force the unbalanced coax transmission line to properly feed the balanced loops and dipoles. As such, a power source is required to operate the EMVS. The loop electronic components are independently housed at the

base of each orthogonal loop while electronics for all dipoles are housed in a sphere at the co-located center of the EMVS.

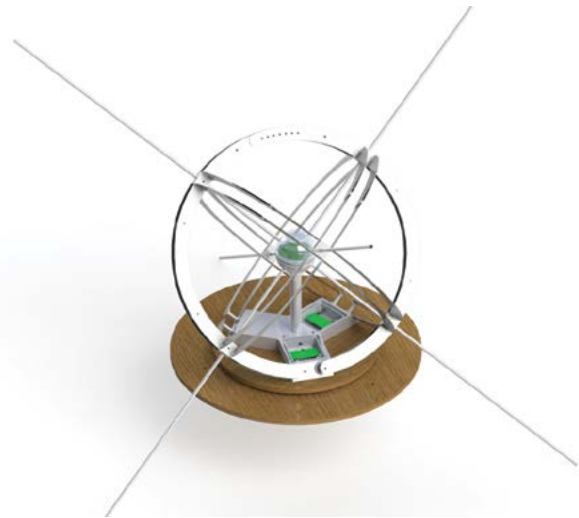


FIGURE 1

The electromagnetic vector sensor consists of three loops and three dipoles. Antenna electronics are shown in green. An “active balun” is housed at the base of each loop, while circuitries for the dipoles are housed together in the center sphere. The loops are 3 ft in diameter while the dipole elements are 8 ft from end to end.

A single EMVS can be considered to be composed of six independent antennas. The three loop components are used primarily to sense magnetic fields while the three dipoles act like traditional short dipole antennas and primarily sense the electrical fields. Careful consideration in the design is given to the structural stability, isolation, and symmetry of the sensor. A twin loop antenna design is adopted so that at joints where two twin loop antennas intersect, a dipole antenna can be inserted between with an insulated nylon block. In addition, the twin loop design widens the bandwidth response from the loop elements. This provides support for the loop intersection joint as well as durability for the dipole. Nylon construction components are used to minimize coupling effects between the antenna elements. Experimental measurements show the components to be sufficiently decoupled for purposes of directional wave analysis in spite of their relatively close electrical spacing.

The orthogonal sets of loop and dipole antennas are initially oriented with dipole elements directed along the x-y-z axes of the Cartesian coordinate system. This is then rotated along the z and y axes to create a symmetric response (with respect to the ground) from individual field sensing components due to ground interaction and reduce the signal processing requirements.

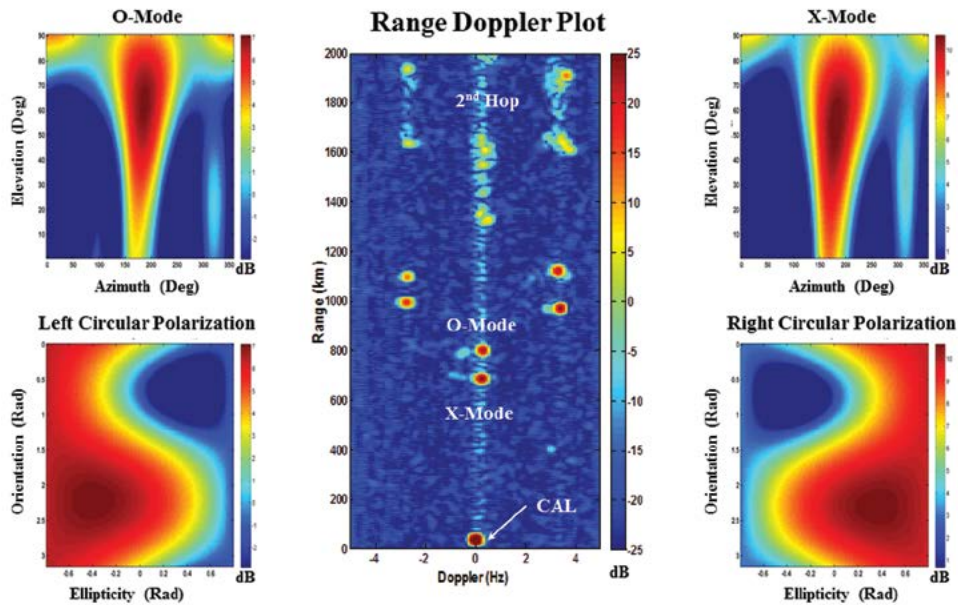


FIGURE 2 Experimental results demonstrate direction-of-arrival and polarization estimation by EMVS. Range Doppler plot (center) shows range separation of ordinary (O) and extraordinary (X) modes at each of three different sites offset in Doppler. The azimuth and elevation are estimated and plotted for the select ordinary and extraordinary modes (top left and top right, respectively). Polarization ellipticity and orientation angles are also estimated and plotted showing accurate left-hand circular and right-hand circular states for the select ordinary and extraordinary modes (bottom left and bottom right, respectively).

Processing: Field testing of the EMVS was conducted to verify the operational sensing capabilities of the EMVS antenna design (see Figs. 2 and 3). The bistatic transmit and receive setup is adopted with known linear frequency modulated chirp waveforms in order to collect single-hop ionospheric radar data. A local source at the receive site transmitting synchronized waveforms is used for calibration. The dataset is collected for a frequency at which the ionosphere supports two propagating modes that are distinguished by different refracted ionospheric heights.

The received electromagnetic signal can be modeled as having independent delay, spatial, and polarization components. Delay characteristics are often used to identify range and Doppler. Spatial components enable azimuthal and elevation signal direction-of-arrival estimation. The polarization component provides a means of measuring the orientation of the electric field vector, which for skywave signals means an added ability to separate ordinary and extraordinary propagating modes and mitigate Faraday fading effects.

Raw IQ (in-phase/quadrature) data is first range- and Doppler-processed at each channel. The local source signal is selected from the range-Doppler surface for calibration of the collected dwell. Due to different reflected ionospheric heights, the signal path delay resultant from differing propagation path distances produces a unique scenario whereby the ordinary or



FIGURE 3 Fielded EMVS setup on 5 ft tall stand with battery to power antenna "active balun" on ground plane at base.

extraordinary mode signals appear range separated. This is particularly useful for validation of EMVS polarization identification.

Selecting a skywave signal of interest, the polarization state is held constant while a coarse estimate of the azimuth and elevation for the signal is calculated.³ Approximate polarization ellipticity and orientation angles are then obtained by holding the spatial components constant and utilizing the coarse azimuth and elevation estimate. This process is performed once more for refined azimuth and elevation estimates.

Summary: In the preliminary datasets, target polarization aspect changes as well as temporal and spatial ionospheric dynamics are observed. The experimental results demonstrate angle-of-arrival and validate polarization estimation capability for ionospherically propagated HF signals. The structural stability of the EMVS has enabled data collections in a variety of environments including sun, rain, snow, and ice. Studies on the EMVS for accuracy of direction-of-arrival estimation and for improved noise mitigation techniques are ongoing.

[Sponsored by the Intelligence Advanced Research Projects Activity (IARPA)]

References

- ¹ A. Nehorai and E. Paldi, "Vector Sensor Processing for Electromagnetic Source Localization," Conference Record of the 25th Asilomar Conference on Signals, Systems and Computers, Pacific Grove, CA, 1991, pp. 566–572.
- ² A. Nehorai, K. Ho, and B.T.G. Tan, "Minimum-Noise-Variance Beamformer with an Electromagnetic Vector Sensor," *IEEE Trans. Sig. Proc.* **47**(3), 601–618 (1999).
- ³ W. Lee, M. Parent, and G. San Antonio, "EMVS Design and Characteristics," 2012 Allerton Antenna Applications Symposium.



Intrinsically Switched Varactor-Tuned Filters and Filter Banks

A.C. Guyette
Electronics Science and Technology Division

Introduction: Tunable filters are essential to the realization of frequency-agile microwave systems. They are particularly useful in receiver applications because they can be reconfigured to adapt to a changing electromagnetic environment, capturing signals of interest while blocking unwanted interferers. There is a need for both high-performance tunable *bandpass* and *bandstop* filters, depending on the configuration and the specific requirements of the system.¹

When designing a tunable filter, there are several performance trade-offs to be considered. For example, as the tuning range of a tunable filter is widened, it becomes increasingly difficult to maintain a good filter response across the entire tuning range. As the tuning range is increased, the tuning elements are necessarily coupled more tightly to the resonators, and so their loss has greater effect on the overall resonator unloaded Q (Q_u). Poor resonator Q_u results in a degradation of filter selectivity, as well as increased passband insertion loss in the case of bandpass filters and decreased stopband rejection in the case of bandstop filters.

In an attempt to extend the tuning range of tunable filters without degrading performance, switched-bank tunable filter configurations are often used. Switched tunable bandpass filter banks (Fig. 4(a)) and switched tunable bandstop filter banks (Fig. 5(a)) are comprised of a number of tunable filters with tuning ranges corresponding to bands within the desired full tuning range. To select the appropriate filter, RF switches are placed at the input and output in the bandpass bank, and before and after every filter in the bandstop bank. The result is superior performance, in terms of either total tuning range or passband insertion loss, to that which is possible with a single tunable filter. The switches themselves, however, add significant passband insertion loss, which tends to increase as the number of filters in the bank increases; this significantly diminishes or eliminates the insertion loss improvement provided by reducing the tuning range of each of the individual constituent filters. In addition, the switches increase the size, weight, power consumption, and control complexity, and they can degrade the linearity of the filter bank. NRL has developed a solution to this problem in the form of intrinsically switched tunable filters, wherein the switching function is performed by the filters themselves, thereby completely eliminating the need for switches in filter banks (Fig. 4(b) and Fig. 5(b)) and in other applications where a switchable filter is needed.

Intrinsically switched tunable filters² are tunable filters that are switched on and off using the same tuning elements that tune their center frequencies and/or bandwidths. In its "off" state, an ideal intrinsically switched bandpass filter rejects signals of all frequencies, and an ideal intrinsically switched bandstop filter passes signals of all frequencies. This is achieved by using the capacitive tuning elements (varactors) to control the voltage and current distributions in the resonators such that the electric and magnetic interresonator coupling coefficients are equal and opposite, resulting in zero net coupling. Intrinsically switched bandstop filters can be realized with bandstop sections consisting of two transmission paths, where the bandstop response is suppressed with constructive interference.

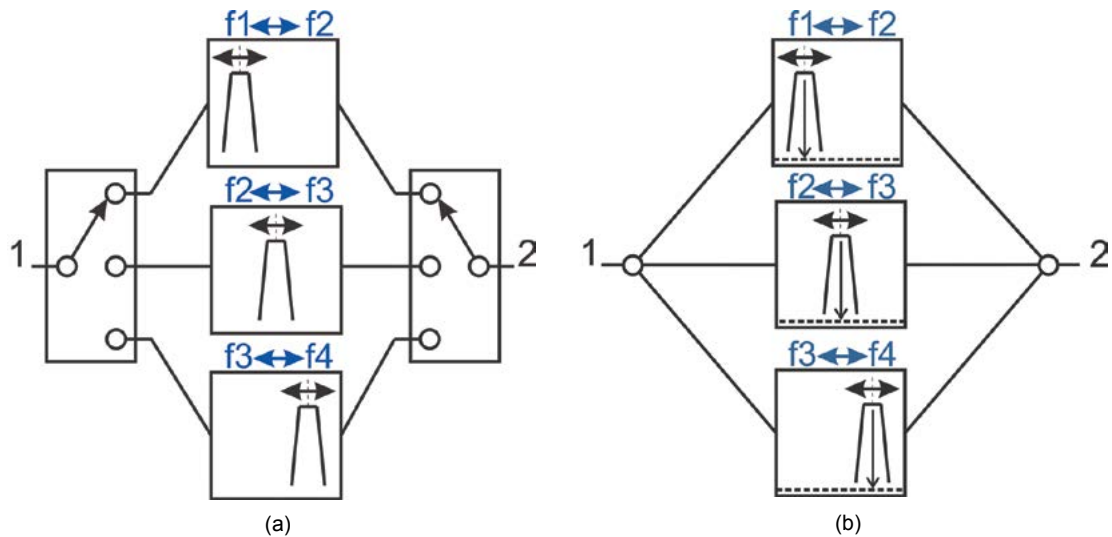


FIGURE 4 (a) Conventional switched tunable bandpass filter bank. (b) Switchless tunable bandpass filter bank using intrinsically switched tunable bandpass filters.

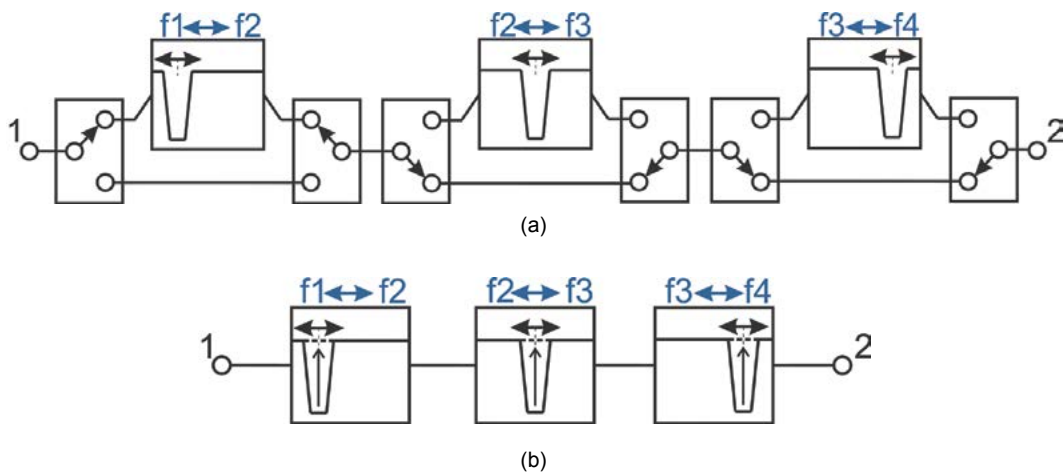


FIGURE 5 (a) Conventional switched tunable bandstop filter bank. (b) Switchless tunable bandstop filter bank using intrinsically switched tunable bandstop filters.

Intrinsically Switched Tunable Bandstop Filters:

A second-order intrinsically switched notch filter prototype is shown in Fig. 6(a). It consists of two intrinsically switched bandstop sections in cascade, with a small amount of coupling introduced between the two resonators, which has the effect of significantly increasing the notch depth by adding a small amount of destructive interference.³ Design and simulation were conducted using a combination of circuit and electromagnetic simulation software. The substrate is Rogers Duroid RO4003 and the varactors are commercially available hyper-abrupt varactors. Shown in Fig. 6(b) and Fig. 6(c) are the simulated and measured results. In the intrinsic-off state measurement, the resonators

are tuned to 725 MHz but the bandstop response is completely suppressed.

Intrinsically Switched Tunable Bandpass Filter Bank:

An intrinsically switched tunable bandpass filter bank microstrip prototype was designed, built, and tested to demonstrate the feasibility of an intrinsically switched filter bank. The prototype (Fig. 7(a)) is comprised of three third-order intrinsically switched bandpass filters (filters A, B, and C) coupled to short-circuit-terminated transmission-line manifolds at the input and output. The substrate is Rogers Duroid RO4003 and the varactors are commercially available hyper-abrupt varactors. Only five unique control volt-

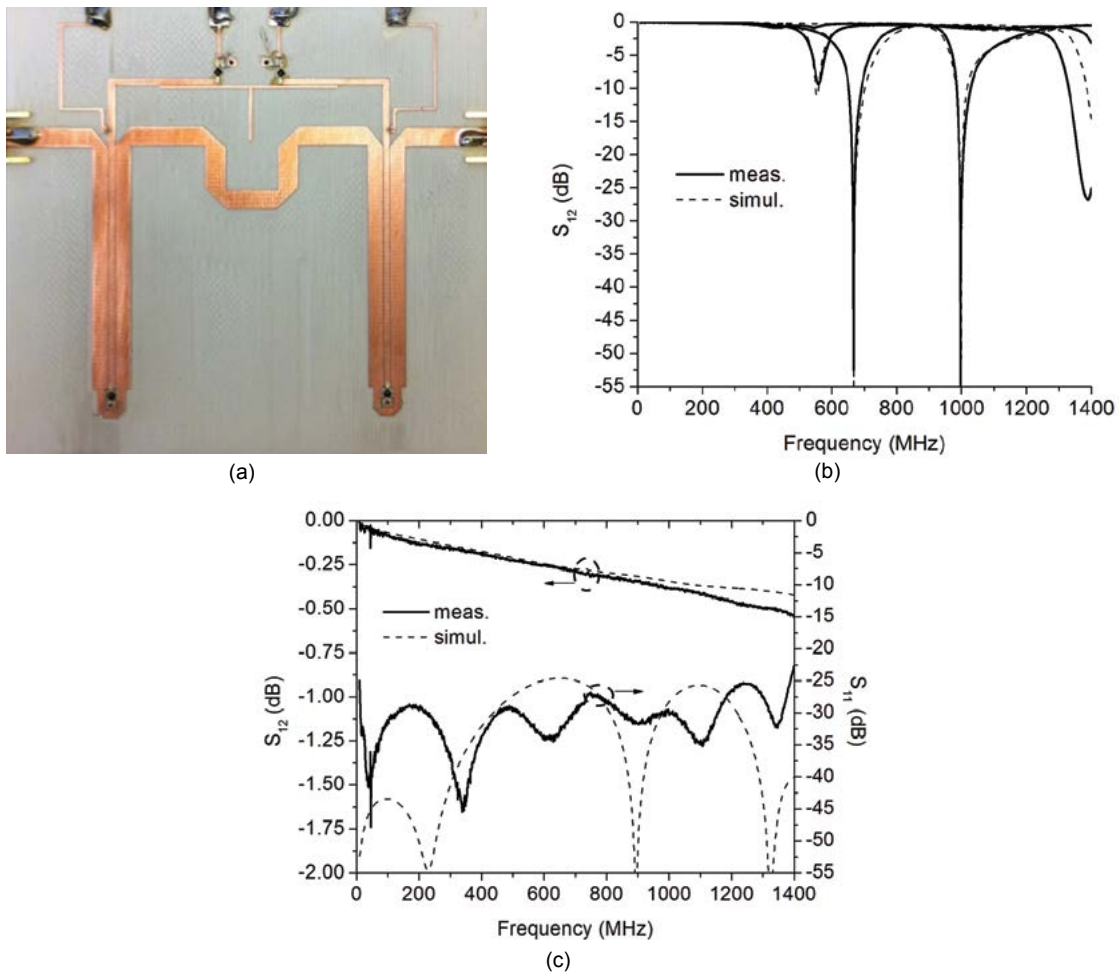


FIGURE 6 Intrinsic switched tunable notch filter prototype: (a) fabricated circuit (overall dimension 8.6 cm × 8.1 cm), (b) center frequency tuning, and (c) intrinsic off state. S_{11} = reflection, S_{12} = transmission.

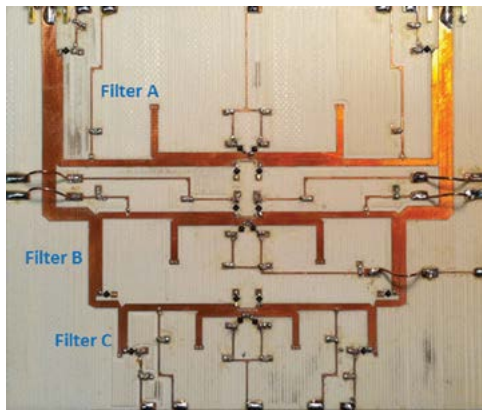
ages are needed for standard operation. The passband bandwidth is a constant 50 MHz, with more than 40 dB of isolation between filters. Shown in Fig. 7(b) are measurements showing the full composite tuning range, and shown in Fig. 7(c) are simulated and measured results with all three filters on simultaneously. The intrinsically switched bank approach removes the switch-loss-imposed upper limit to the number of filters that can be used; so realizing low-loss tunable filter banks comprised of large numbers of low-loss narrow-tuning-range filters becomes a problem of manifold design rather than the much more difficult problem of realizing low-loss high-throw or cascaded switches.

Summary: NRL has developed a new class of reconfigurable RF device called intrinsically switched tunable filters. It is expected that intrinsically switched tunable filters and filter banks will play an important role in the realization of future high-performance microwave systems.

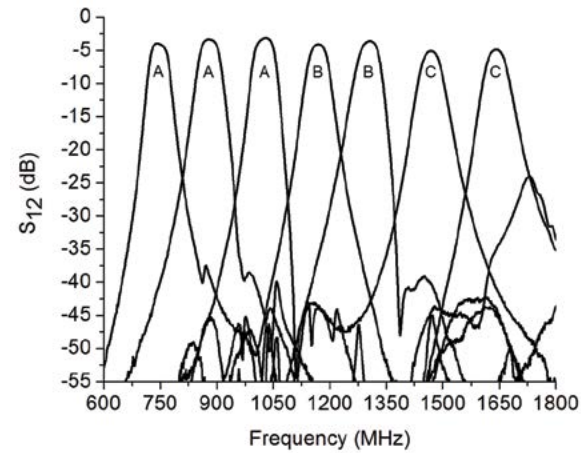
[Sponsored by ONR]

References

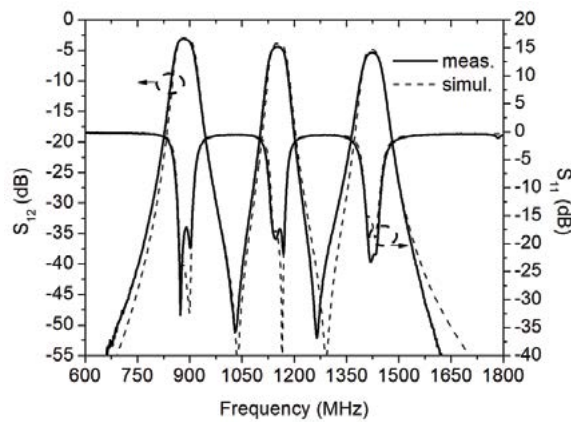
- ¹ P. Wong and I. Hunter, "Electronically Tunable Filters," *IEEE Microwave Magazine* **10**, 46–54 (2009).
- ² A.C. Guyette, "Intrinsically Switched Varactor-Tuned Filters and Filter Banks," *IEEE Trans. Microwave Theory Tech.* **4**, 1044–1056 (2012).
- ³ D.R. Jachowski, "Compact, Frequency-Agile, Absorptive Bandstop Filters," 2005 *IEEE MTT-S International Microwave Symposium Digest*, pp. 513–516, June 2005.



(a)



(b)



(c)

FIGURE 7

Intrinsically switched tunable bandpass filter bank prototype: (a) fabricated circuit, (b) measured full tuning range, (c) all filters on simultaneously. S_{11} = reflection, S_{12} = transmission.

Thermoelectroelastic Simulation of GaN Devices

M.G. Ancona,¹ S.C. Binari,² and D.J. Meyer¹

¹Electronics Science and Technology Division

²Electronics Science and Technology Division, retired

Introduction: Because of the large bandgap and high electrical conductivity of the semiconductor GaN, electronic devices based on this material are playing an increasingly indispensable role in Navy applications in RF electronics, power electronics, and solid-state lighting. To understand the operation, performance, and reliability of these devices, it is crucial that one take into account GaN's electroelastic and thermoelastic properties, its strong spontaneous polarization, its built-in strains, and the coupling of these phenomena to the electron transport. From a theoretical perspective, all these interactions are well understood, but heretofore

they had been studied in detail only in simplified one-dimensional cases, and not in realistic device geometries. The work reviewed here^{1,2} developed a numerical simulation code that solves the complete thermoelectromechanical equations in multi-dimensions and thereby allows a variety of important GaN devices to be fully analyzed for the first time. Especially relevant application areas include the design of scaled GaN transistors for high frequency operation and the physics of their failure. Through such uses, this advanced simulator is likely to impact Navy-relevant applications such as solid-state radar and electric ship power distribution, as well as the larger GaN research and development community.

Theory and Numerics: GaN and its alloys with indium and aluminum are unique among the technologically important semiconductors in being strongly piezoelectric. As a result, full quantitative analyses of electronic devices made of these materials must include

the mechanical degrees of freedom. That GaN applications often involve high temperatures means thermal coupling should be modeled also. And since all device situations are inhomogeneous, usually in 2D but sometimes 3D, a multidimensional capability is essential. To incorporate all this physics in a tractable fashion, a continuum approach was used in which the system is described by five coupled partial differential equations plus five crucial constitutive equations and a consistent set of boundary conditions. The solutions consist of the electric potential, the electron density and current, the stress/strain, and the temperature as functions of position and time.

The governing equations are solved in geometries and with material properties set by the particular device being modeled. In our work we have focused on high electron mobility transistor (HEMT) structures of varying geometries. The equations are programmed and solved for both DC and small-signal AC conditions within COMSOL's general finite-element program.³ Finally, the run-time of the simulations was greatly improved by exploiting the 2D nature of the devices of most interest and by solving the electron transport equations (which require a fine mesh) only in small "device regions" near the contacts.

Application – RF Devices: The simulated current–voltage (I – V) curves for a standard GaN HEMT are plotted in Fig. 8(a) and they look very much like those measured experimentally (e.g., in Ref. 4). Using the ability of numerical simulation to look inside a working device, we plot in Figs. 8(b–d) solution profiles under ON-state conditions. Of note is the fact that the peak mechanical stresses, while quite high (~ 3.5 GPa), are well below the yield strengths of these materials.

Application – Transistor Reliability: GaN HEMTs are known to fail by apparently mechanical means, with grooves, pits, and cracks often appearing during accelerated life testing.⁵ An intriguing hypothesis about these failures is that they are triggered by piezoelectric stress,⁵ and to investigate this we examine solutions under high-power conditions with drain voltage $V_D = 20$ V and gate voltage $V_G = 0$. The simulated channel temperature (Fig. 9(a)) is very high (~ 400 °C), and this would surely accelerate any degradation processes. The electric field (Fig. 9(b)) is also quite high at the drain corner of the channel and this would undoubtedly lead to significant electron injection. But the mechanical stresses (Fig. 9(b)) do seem not especially elevated (< 5 GPa), and half of the peak stress comes not from the piezoelectric contribution but from thermal stresses.

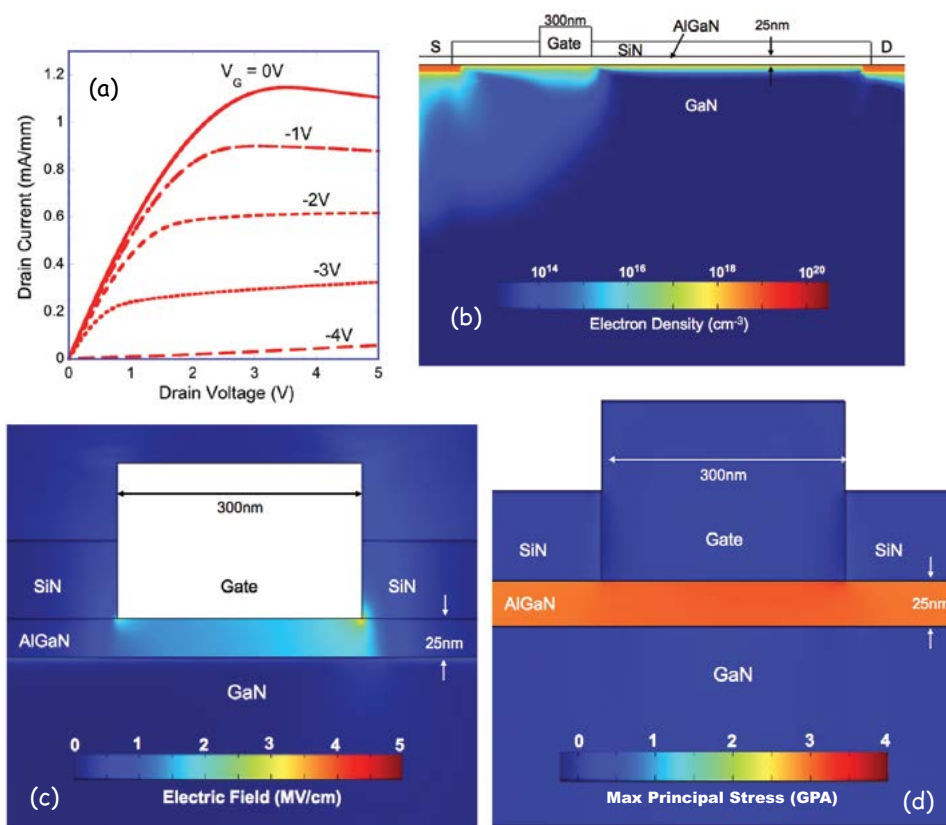


FIGURE 8 Simulated (a) I – V curves for a standard GaN HEMT, and plots of its (b) electron density, (c) electric field, and (d) principal stress in the ON-state ($V_G = 0$ V, $V_D = 5$ V).

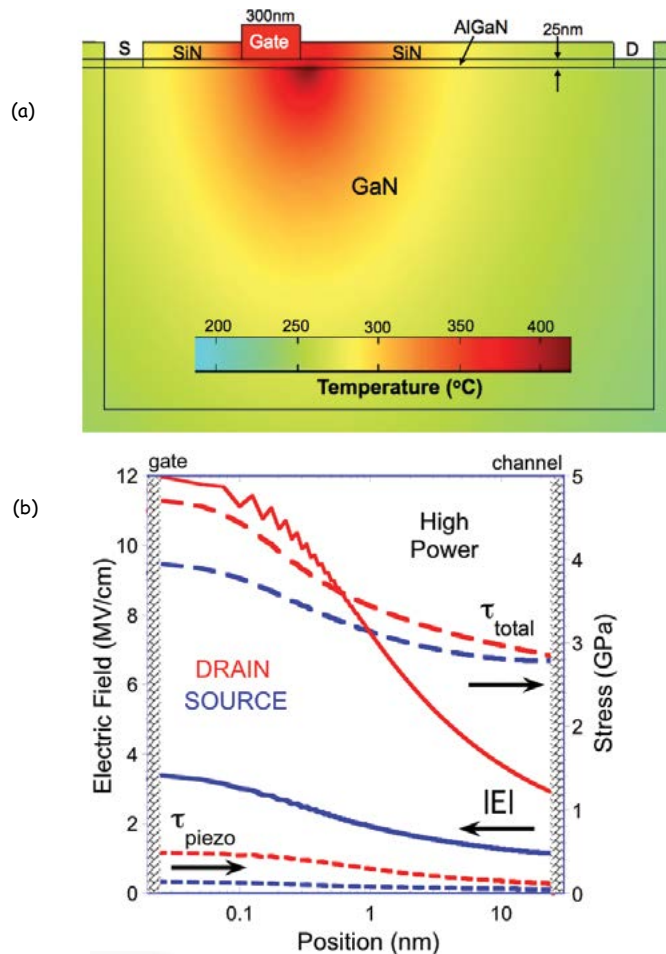


FIGURE 9 Simulated (a) temperature field and (b) electric field, piezoelectric stress, and total stress profiles across the AlGaN at the source/drain-side corners of the gate under high-power conditions.

A further set of simulations looked at the stress-concentrating effect of a crack (Fig. 10(a)), the effects of the crack's radius of curvature and depth on the stress concentration (Fig. 10(b)), and the impact that a crack can have on the drain characteristics (Fig. 10(c)).

Application – Transistor Scaling: To reach higher frequencies, a variety of scaled HEMT designs are being investigated with gate lengths below 100 nm. Of particular interest are the stresses introduced by gate structures and by regrown InGaN/InN source/drain contacts.⁶ Modeling is especially valuable for the scaled devices because as the geometrical size is reduced, the strain fields become increasingly multidimensional and the inhomogeneous mechanics plays an ever larger role in setting important device parameters such as the threshold voltage.

Summary: A numerical simulation code was developed that solves the complete thermoelectromechanical

equations describing piezoelectric semiconductors in multi-dimensions.^{1,2} The code was applied to variety of important GaN devices, and for the first time allows for their full analysis.

[Sponsored by ONR]

References

- ¹ M.G. Ancona, S.C. Binari, and D.J. Meyer, "Fully Coupled Thermoelectromechanical Analysis of GaN High Electron Mobility Transistor Degradation," *J. Appl. Phys.* **111**, 074504 (2012).
- ² M.G. Ancona, "Fully Coupled Thermoelectroelastic Simulations of GaN Devices," 2012 IEEE International Electron Devices Meeting, San Francisco, CA; doi:10.1109/IEDM.2012.6479037.
- ³ www.comsol.com.
- ⁴ S.C. Binari, K. Ikossi, J.A. Roussos, W. Kruppa, D. Park, H.B. Dietrich, D.D. Koleske, A.E. Wickenden, and R.L. Henry, "Trapping Effects and Microwave Power Performance in Al-GaN/GaN HEMTs," *IEEE Trans. Electron. Devices* **48**(3), 465–471 (2001).
- ⁵ U. Chowdhury, J.L. Jimenez, C. Lee, E. Beam, P. Saunier, T. Balistreri, S.-Y. Park, T. Lee, J. Wang, M.J. Kim, J. Joh, and J.A. del Alamo, "TEM Observation of Crack- and Pit-Shaped Defects in Electrically Degraded GaN HEMTs," *IEEE Electron. Device Lett.*

29(10), 1098–1100 (2008).

⁶ U. Singiseti, M.H. Wong, S. Dasgupta, Nidhi, B. Swenson, B.J. Thibeault, J.S. Speck, and U.K. Mishra, “Enhancement-Mode N-Polar GaN MISFETs With Self-Aligned Source/Drain Regrowth,” *IEEE Electron Device Lett.* **32**(2), 137–139 (2011).

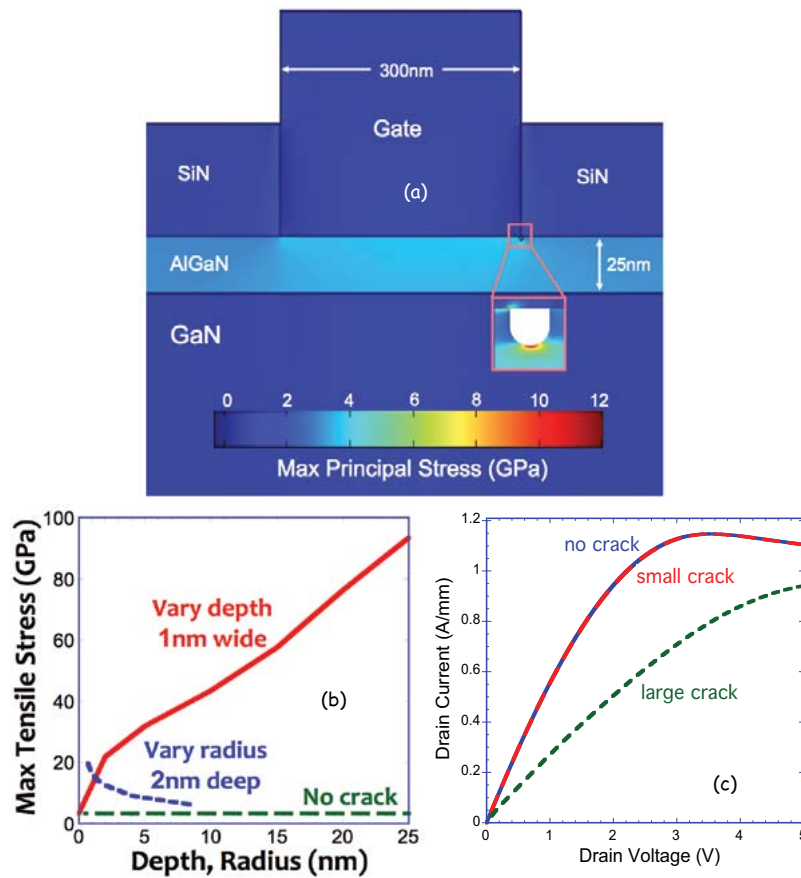
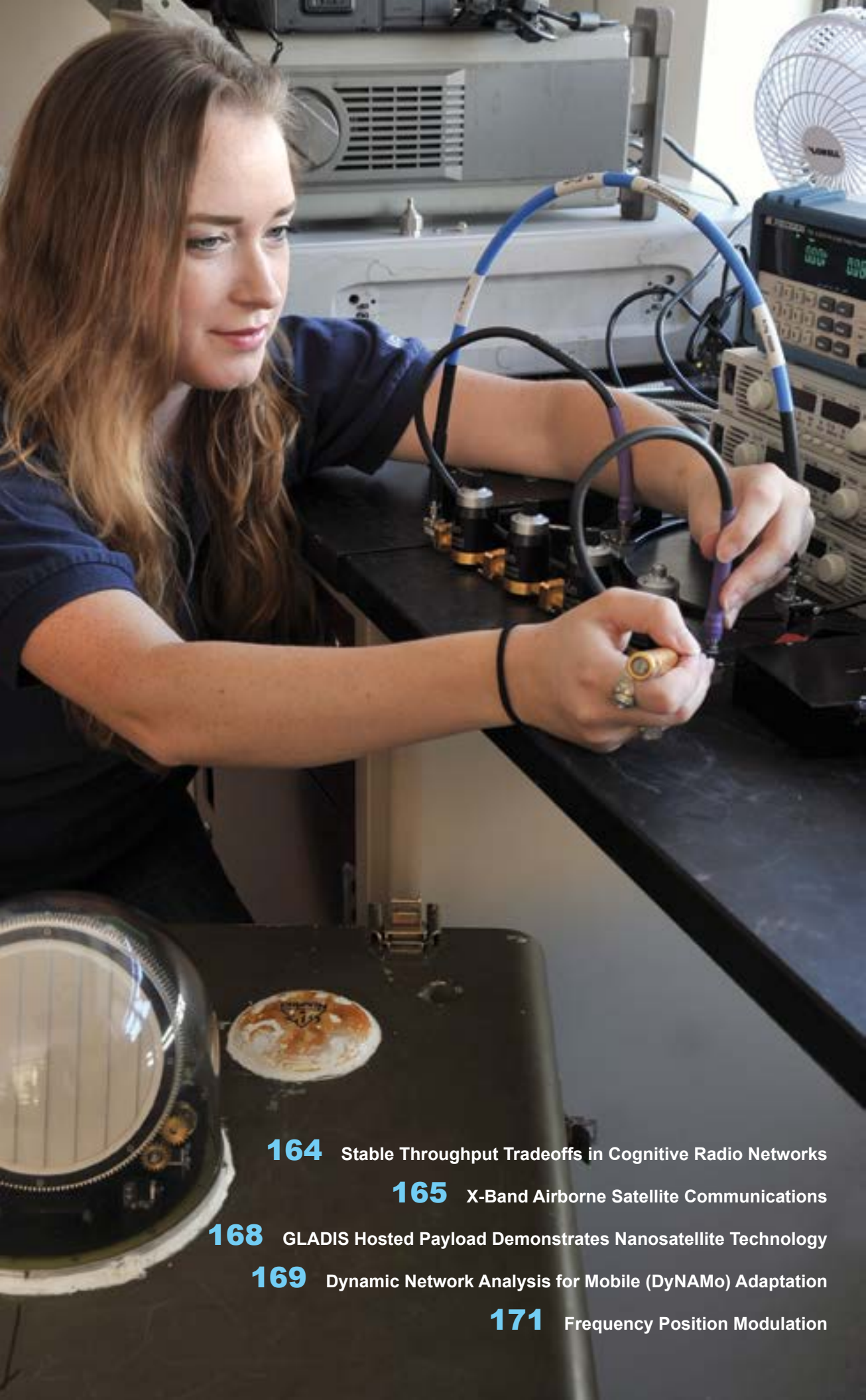


FIGURE 10

Simulations of a damaged AlGaIn/GaN HEMT with a “crack” at the drain-side corner of the gate and showing (a) the stress concentration effect, the dependence of the peak stress on (b) the radius of curvature and depth of the crack, and (c) the effect of small and large cracks on the drain characteristics.





164 Stable Throughput Tradeoffs in Cognitive Radio Networks

165 X-Band Airborne Satellite Communications

168 GLADIS Hosted Payload Demonstrates Nanosatellite Technology

169 Dynamic Network Analysis for Mobile (DyNAMo) Adaptation

171 Frequency Position Modulation

Information Technology and Communications

Stable Throughput Tradeoffs in Cognitive Radio Networks

S. Kompella,¹ G.D. Nguyen,¹ J.E. Wieselthier,² and A. Ephremides³

¹Information Technology Division

²Wieselthier Research

³University of Maryland

Introduction: This work introduces a highly innovative approach for the operation of cognitive radio networks that is suitable for tactical wireless environments and provides a rigorous analysis of tradeoffs in network throughput that enables improved system performance. Cognitive wireless network technology, which integrates adaptive algorithms, dynamic spectrum access, and channel sensing, has the potential to provide significant gains in communication capability to warfighters. To achieve the needed performance improvements and avoid disruptions, cognitive radios offer tremendous opportunities for adaptation. Systems will have the capability to sense the conditions of their local operating environment and then dynamically adapt their data rate, modulation, coding, transmit power, and frequency, as needed, to changes in propagation, signal fading, multipath, or friendly/unfriendly interference.

Although there has been considerable research and development in the area of cognitive radios in recent years, few studies have addressed the challenges of forming cognitive radio networks. Consequently, issues associated with cognitive tactical wireless networks have scarcely been addressed. The present work addresses fundamental issues in cognitive shared channels where the users have different priority levels, a situation that is commonly seen in tactical edge networks. This work is being carried out as part of the Office of the Secretary of Defense (OSD) Networked Communications Capabilities Program (NCCP), and is in line with the Navy/Marine Corps evolving strategic plan and priorities.

System Model and Analysis: In the prevailing paradigm of operation for cognitive radios, “secondary” (lower priority) users are required to sense idle periods during which the “primary” (higher priority) users are not transmitting, and transmit their own data during such idle periods, so as to not cause interference to primary users. Furthermore, the secondary users are required to cease transmission when a primary user is detected in a channel.

The present work departs from this standard model by permitting secondary users to use transmission policies that exploit the multireception capabilities of modern receivers, thereby allowing secondary users to transmit concurrently with primary users (with a transmission probability p), a crucial capability for future

tactical networks. In the simplest (noncooperative) mode of operation, the secondary users’ performance is optimized by choosing the appropriate value of p . An enhanced cooperative mode of operation is then developed in which secondary users can serve as relays for unsuccessful packets transmitted by primary users (see Fig. 1). In this cooperative mode, a tradeoff arises when the secondary node is activated along with the primary so that both transmissions may be successful, but with a lower probability, compared with the case of the secondary node staying idle when the primary user transmits.

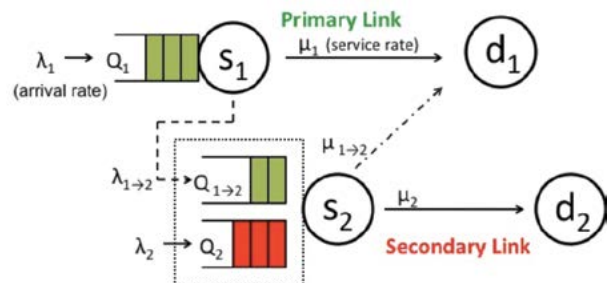


FIGURE 1

Cognitive radio network model. s_1 = primary user; s_2 = secondary user; d_1 = primary destination; d_2 = secondary destination; λ = arrival rate; Q = queue length; μ = service rate.

The computation of the stable throughput region of a network with one primary user and one secondary user (i.e., the set of input data rates that can be supported by the primary and secondary user, while maintaining finite queues) is an intractable problem because it is characterized by interacting packet queues. This work, therefore, uses the queueing-theoretic notion of “stochastic dominance” to construct a “dominant system” in which the queues do not interact with each other, and whose stability region inner-bounds that of the original system. It is shown that the dominant system and the original system behave identically at the boundary of the stability region. Therefore, the dominant system, whose analysis is tractable, is used to determine the stability region of the original (intractable) system.

Results: The ensuing analysis^{1,2} shows that the appropriate behavior of secondary users (secondary cooperation) not only provides improved service for the secondary users, but actually provides better performance for the primary user than that which would be achieved even if no secondary users were competing for channel access, as can be observed in Fig. 2. This key insight has far-reaching implications in tactical and commercial environments alike. Furthermore, analyzing the impact of the knowledge of secondary users’ channel state information³ (queue states, channel conditions, etc.) on the stable throughput region illustrates

that such knowledge benefits the entire network in terms of improved throughput region, much more than cooperation alone.

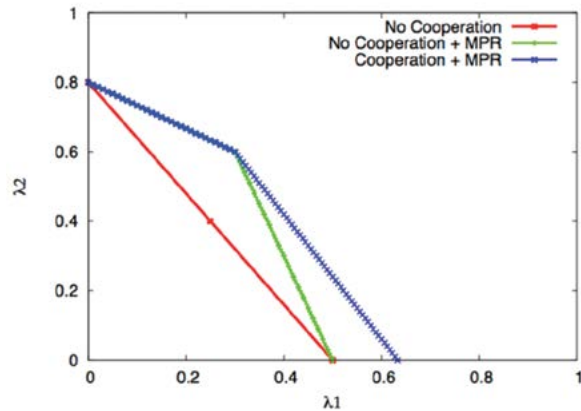


FIGURE 2 Comparison of the stability regions of the noncooperation and the cooperation schemes (MPR = multipacket reception).

Summary: The main contributions of this work are the development of a cooperative cognitive radio networking technique that provides improved performance for both the primary and secondary user, and the development of a rigorous mathematical model that enables the evaluation of performance tradeoffs that will lead to the improved performance of realistic tactical communication networks.

[Sponsored by the NRL Base Program (CNR funded)]

References

- ¹ S. Kompella, G.D. Nguyen, J.E. Wieselthier, and A. Ephremides, "Stable Throughput Tradeoffs in Cognitive Shared Channels with Cooperative Relaying," in *2011 Proceedings IEEE INFOCOM* (IEEE, Piscataway, NJ, 2011), pp. 1961–1969.
- ² S. Kompella, G.D. Nguyen, C. Kam, J.E. Wieselthier, and A. Ephremides, "Cooperation in Cognitive Underlay Networks: Stable Throughput Tradeoffs," under review, *IEEE/ACM Transactions on Networking*.
- ³ S. Kompella, G.D. Nguyen, J.E. Wieselthier, and A. Ephremides, "Impact of Channel State Information on the Stability of Cognitive Shared Channels," in *2012 Proceedings IEEE INFOCOM* (IEEE, Piscataway, NJ, 2012), pp. 3021–3025.

X-Band Airborne Satellite Communications

T.R. Husson and M.A. Rupar
Information Technology Division

Introduction: The Department of Defense is increasingly reliant upon airborne sensors to provide battlespace information. This means there is a greater

need for sending large amounts of data from these airborne platforms in real time to analysts on the ground. Since the ground stations are often beyond line-of-sight to the aircraft, the use of satellite communications provides the best solution.

L-band (1.5 to 1.6 GHz) commercial satellite communications systems for aircraft have been in use for a long time. However, the data bandwidth provided by these systems is not nearly enough to accommodate the current broadband sensors. The latest airborne L-band system from Inmarsat (SwiftBroadband) provides a maximum data rate of 432 kbps, which is insufficient for streaming video and other high-bandwidth sensors. X-band (8 GHz) provides the required bandwidth for these applications, and spectrum is available on military satellites and from a limited number of satellite providers.

This article describes the testing of an airborne X-band satellite communications system. Bandwidths of 10 MHz from the air to a small (2.4 m) ground station antenna were demonstrated. Figure 3 shows the communications architecture. The testing was conducted in the vicinity of Hagerstown, Maryland.

Communications System: The airborne system consisted of a tracking antenna, satellite modem, voice-over-IP (VoIP) adapter, laptop computer, and a spectrum analyzer (for RF measurements). The test aircraft was a Beechcraft King Air A2000. The EMS AS-X Wavestorm airborne antenna system provided 27 to 28 dB of gain (equivalent to a 0.4 m dish antenna). The antenna system was able to track the satellite throughout the aircraft maneuvers using an integrated attitude and heading reference system (AHRS) and global positioning system (GPS) receiver.

Two different satellite modems were tested. Both the Paradise Quantum 20 and the Newtec EL470 used standard DVB-S2 waveforms and error coding and had the capability to log lock status, signal level, and Eb/No (signal quality).

The ground station was set up at the Intelsat Mountainside Teleport in Hagerstown. The antenna was a GATR 2.4 m portable X-band antenna. The antenna included an integrated block downconverter and low-noise amplifier for the receive signal, and an integrated block upconverter and power amplifier for the transmit signal. Other equipment at the ground station mirrored the equipment on the aircraft with two different satellite modems, a laptop computer, and a spectrum analyzer.

Test Setup: Two different geostationary satellites were used during the testing to provide different pointing angles. Identical bandwidth channels were used on both satellites. The XTAR-LANT satellite is located at 30° W which required pointing angles of 120.1°

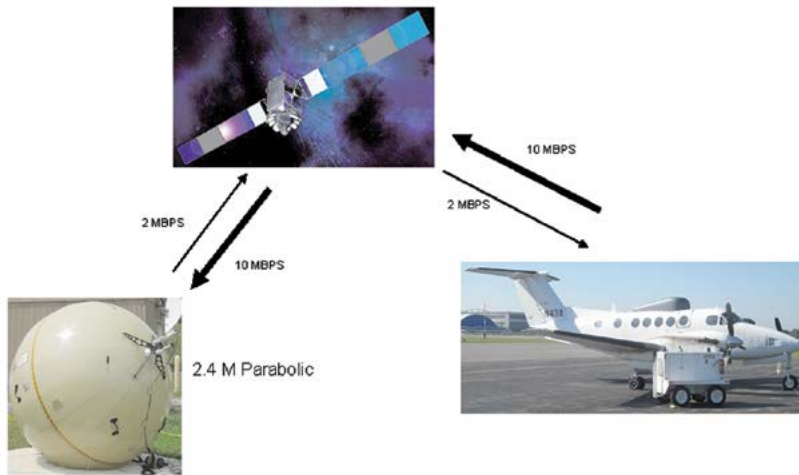


FIGURE 3
Communications architecture for X-band airborne satellite communications testing.

azimuth and 23.3° elevation from Hagerstown. The SKYNET 5C satellite is located at 18° W and required pointing angles of 110.2° azimuth and 14.4° elevation.

A number of applications were used for testing the satellite links (both air-to-ground and ground-to-air). The NRL Multi-Generator (MGEN)¹ was used to test the capacity of the communications links. The software was used both during straight and level flight and during aircraft maneuvers. Transfer of large data files was tested using the open-source FileZilla² server and client software. Streaming of video was tested using the VLC Media Player.³ Real-time data chat was tested using the VSee⁴ collaboration tool, and, remote desktop control was implemented using the TightVNC⁵ software package.

Test Results: Identical channels on both satellites were used with a 10 MHz link from the aircraft and a 2 MHz link to the aircraft. Figure 4 shows the 10 MHz air-to-ground carrier and the 2 MHz ground-to-air carrier as recorded at the ground station. Both satellites provided equivalent performance through the various tests.

Modem logs were recorded both on the ground and in the aircraft during all test flights. The primary parameter of interest from the logs was Eb/No (energy per bit to noise power spectral density ratio). This figure of merit indicates the quality of the signal and is related to the received bit error rate. Figure 5 shows a typical Eb/No plot from the modem on the aircraft.

Both satellite modems were configured for QPSK modulation with half rate forward error correction (FEC) coding. This configuration provides 10 Mbps data transfer across the 10 MHz air-to-ground link. The ability to sustain these data rates was tested and verified using the NRL MGEN software. Figure 6 is a plot from MGEN that shows a sustained 9 Mbps transfer rate from the aircraft. Simultaneously with this sustained transfer rate, a data chat and a VoIP voice call were also in progress. The dropouts on the plot are due to antenna blockage on the aircraft during maneuvers. However, the plot shows the data transfer rate fully restored as soon as the aircraft antenna was able to reacquire lock on the satellite.

The Newtec EL470 satellite modem had an adaptive coding and modulation (ACM) option. The ACM allowed the modem to adapt its data transfer rate and FEC

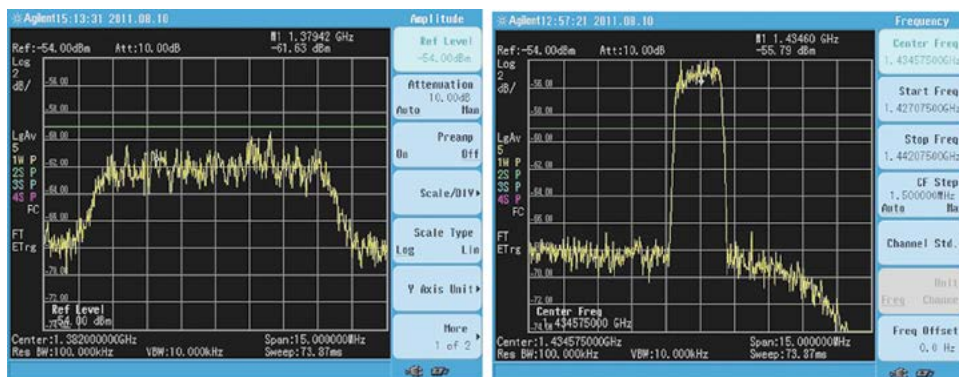


FIGURE 4
Forward and return carrier signals from the satellite.

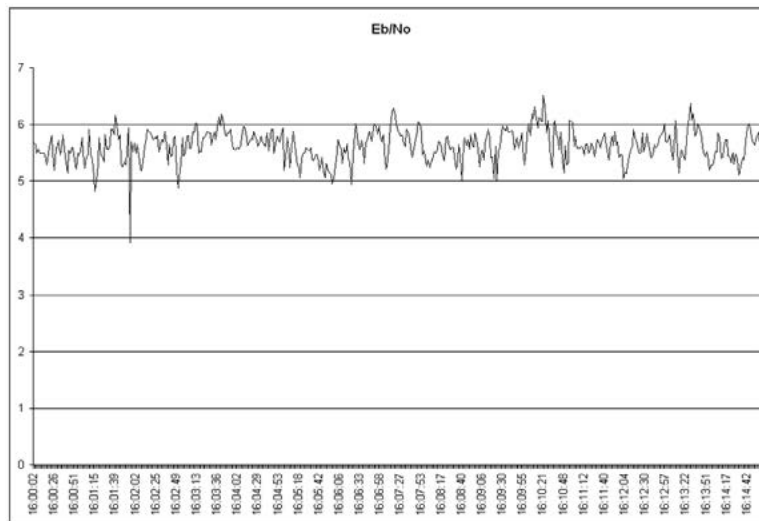


FIGURE 5
Typical Eb/No plot from the aircraft modem.

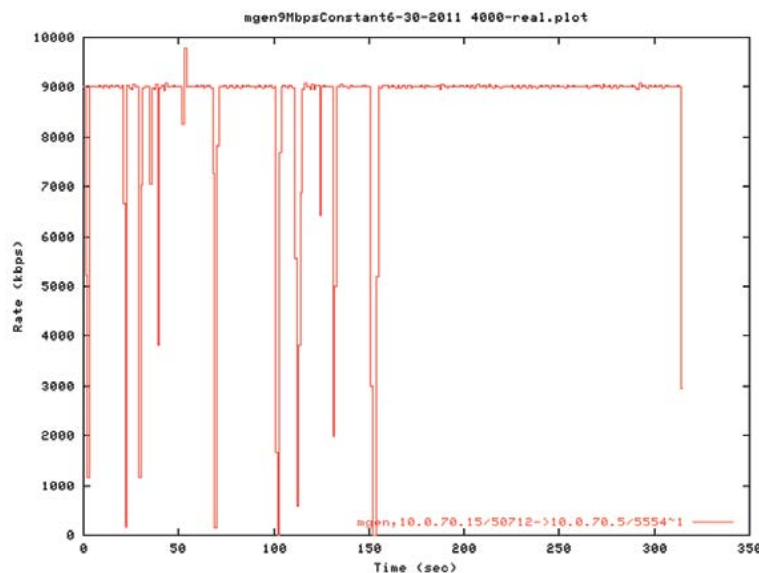


FIGURE 6
MGEN plot of sustained air-to-ground data transfer rate.

coding based on the received signal quality (Eb/No) to make optimal use of the channel. Using the Newtec modem with ACM the aircraft was able to transfer data at rates up to 16 Mbps as measured by the MGEN software.

In addition to the throughput testing using the MGEN software, other data transfer applications were tested. Large file transfers using file transfer protocol (FTP) were initiated in both directions and results showed transfer rates that matched those recorded by the MGEN tests. Multicast streaming video was sent from the aircraft to the ground station during flight. There were brief interruptions of the stream due to antenna blockage during aircraft maneuvers, but the

stream was quickly restored when the antenna reacquired lock on the satellite.

VoIP voice calls and real-time data chat applications were used simultaneously during all the higher data rate tests, allowing close coordination between the operators on the aircraft and at the ground station.

Also demonstrated during the tests was the ability of the ground station operator to remotely control the laptop computer on the aircraft using the TightVNC software.

Summary: During a series of flight tests, the ability to maintain a consistent 10 Mbps/2 Mbps link between the airborne terminal and a ground station using a 2.4

m antenna was demonstrated. The airborne antenna demonstrated the ability to track two different satellites including one at a low elevation angle (14.4°). Two different satellite modems were successfully tested at these data rates. Using the ACM on the Newtec modem, a higher data rate was achieved.

The availability of X-band spectrum on several different satellites provides the DoD with the flexibility to deploy various airborne sensors and send high-bandwidth data in real time to ground-based analysts.

[Sponsored by Cold Regions Research and Engineering Laboratory, U.S. Army Corps of Engineers]

References

¹ <http://cs.itd.nrl.navy.mil/work/mgen/>

² <http://filezilla-project.org/>

³ <http://www.videolan.org/vlc/>

⁴ <http://vsee.com/>

⁵ <http://www.tightvnc.com/>

GLADIS Hosted Payload Demonstrates Nanosatellite Technology

J. Middour,¹ I. Galysh,¹ K. Clark,¹ T. Rodillos,¹ M. Haffner,¹ C. Belmonte,¹ R. Baummer,¹ J. Graham,² and J. Tugman³

¹*Space Systems Development Department*

²*Three Lions Consulting, LLC*

³*JTM & Associates, Inc.*

Overview: NRL's Space Systems Development Department completed development and testing of a hosted payload system intended to demonstrate key technologies for very small satellites. So-called "nano" satellites, typically less than 10 kg, are of interest for their potential to fulfill certain scientific and military missions at greatly reduced cost for manufacture and launch to orbit. The Global Awareness Data-Extraction International Satellite hosted payload, GLADIS for short, was conceived, designed, and built by the Space Systems Development Department (Fig. 7). It is due to be launched to the International Space Station in 2013 for a one-year, in-orbit evaluation of a two-way UHF communications capability using specially developed structures, electronics, and antennas.

History: The GLADIS hosted payload stemmed from a concept for a space-based infrastructure comprised of many small satellites providing a communications backbone to control and manage autonomous, distributed, unattended sensors and unmanned vehicles which are increasingly employed to monitor the unwired regions of the Earth for improved scien-

tific, environmental, safety, and security awareness.¹ As envisioned, a GLADIS constellation would employ a network of simple ground terminals, up to 30 nanosatellites, and an efficient command and control service to extract the maximum communications capacity from many small and low-power satellites. As built, the GLADIS hosted payload will prove key technological elements required for the full constellation, including small satellite structural and power systems, low-power electronics, and very small antenna arrays suited for space communications. The demonstration will also test an enterprise command and control system along with very small, low-power, satellite-to-ground communications terminals.



FIGURE 7
The NRL GLADIS team with the flight payload.

Key Development Attributes: The GLADIS Data Extraction payload evolved from the Ocean Data Telemetry Microsatellite Link (ODTML) experiments flown and tested sequentially on TacSat-3, STPSat-2, and TacSat-4. The Data-X transmitter/receiver operates around 401 MHz to provide two-way data relay from ocean and terrestrial sensors to users via Internet connection. The UHF frequency is suitable for low power and is also good for foliage penetration. The Data-X payload transmits queries to small, low-power communication terminals attached to unattended sensors and receives sensor-collected data in reply at digital bit rates of 2400 to 9600 bits per second. The payload enables data exfiltration and infiltration to remote sensors of any kind, such as ocean sensors, unattended ground sensors, or portable radios. Two-way communication allows acknowledgments and error correction. The data handling architecture can accommodate thousands of sensors such that tasking can be performed autonomously and data disseminated using the Internet. The UHF ground terminals are low cost, have a simple antenna that does not require pointing, and their sleep

mode saves power. Both ground and space segments are customizable via reprogrammable software, including while on orbit.

The GLADIS transceiver uses an antenna, Data-X receiver, Data-X transmitter, field programmable gate array (FPGA), and a general purpose processor (GPP) to perform its data relay mission. The antenna is circularly polarized with four quarter wavelength monopoles phased 90° apart and tilted away from each other. A plastic ring around the bottom of the payload electrically insulates the antenna ground plane, achieving an enhanced beam pattern for ground coverage.² The Data-X receiver filters, amplifies, digitizes the received signal, and feeds it to the FPGA for digital signal processing to demodulate the uplink. The demodulated bit stream goes to the GPP for message decoding and high-level protocol implementation. The GPP also provides sensor handshake and interrogation bit streams back to the FPGA. The FPGA implements a binary-phase-shift-keyed control signal to the Data-X transmitter for modulation. The transmitter uses a digital-to-analog converter for modulation, along with a frequency mixer and amplifiers to transmit the UHF handshake and interrogation signals to the ground terminals on the sensors.

The GLADIS communications architecture is made up of the enterprise server, the Satellite Operations Center, the operating system, and ground-space comms terminals. “End-to-end” system tests are planned for FY2014.



FIGURE 8
The GLADIS payload attached to STP-H4 in launch configuration.

Summary: The GLADIS hosted payload received funding from the Office of Naval Research, the Department of Homeland Security, and the Department of Defense Space Test Program (STP). It will be shipped to Japan to be loaded aboard a Japanese Space Agency rocket for launch to the International Space Station in

2013. The mission, known as STP-Houston 4 (STP-H4; see Fig. 8), includes GLADIS and two other NRL science payloads: the Small Wind and Temperature Spectrometer (SWATS) and the Miniature Array of Radiation Sensors (MARS), both designed and built by the NRL Space Science Division.

NRL scientists and engineers will use the results of the GLADIS hosted payload demonstration of key technologies for very small satellites to improve the capacity of future satellites while controlling cost and increasing access to space.

[Sponsored by ONR]

References

- ¹J. Middour, J. Mittleman, J. Tugman, J. Graham, S. Thonnard, and F. Hellrich, “Concept for an International Small Satellite Constellation to Monitor Unattended Ground Sensors,” presented at CANEUS 2009, NASA Ames Research Center, Moffett Field, CA, March 2009.
- ²W. Lippincott, “Development of a Deployable UHF Crossed Dipole Antenna Suitable for Nano Satellites,” presented at the ACES Applied Computational Electromagnetics Society 27th International Review of Progress in Applied Computational Electromagnetics, Williamsburg, VA, March 2011.

Dynamic Network Analysis for Mobile (DyNAMo) Adaptation

J. Macker, J. Dean, and D. Claypool
Information Technology Division

Overview: In the Dynamic Network Analysis for Mobile (DyNAMo) adaptation project, NRL’s Protocol Engineering and Advanced Networking Section is conducting research to address novel network design and analysis challenges involving significant mobility, autonomy, and disruptive dynamics. Figure 9 is an overview of the approach and goals of this research.

Commensurate with NRL’s leadership in developing a next generation of mobile network modeling capabilities is our goal of developing new approaches for analyzing dynamic networks to enable further improvements in protocol design, analysis, and adaptation for mobile, autonomous communication networks.

Measurement Tools and Methods: By leveraging high-fidelity mobile network modeling components we have developed, it is possible to examine dynamic communication networks with novel and repeatable methods that reflect real-world deployment conditions. These high-fidelity models and mobile network scenario tools produce dynamic metadata that is stored and manipulated using a network graph language (e.g., graphML). In this way, researchers can capture the state

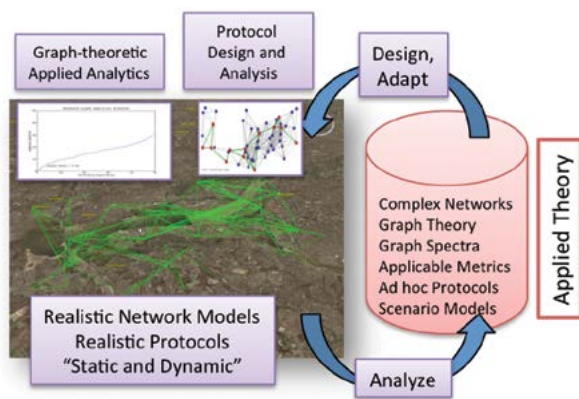


FIGURE 9
Overview of DyNAMo process and goals.

conditions of dynamic autonomous networks under study and perform scenario-driven design and analysis in a repeatable fashion. Dynamic topological metadata examples include metrics related to distributed protocol organization (e.g., algorithm decision state) and environmental state variables (e.g., stochastic node and edge conditions). Recently, this dynamic modeling capability has been applied to studying two specific autonomous networking problems: (1) self-organizing structural stability and (2) temporal detection and tracking of dynamic network structures.

Improving the Stability of Self-Organizing Networks: By applying DyNAMo models, we have achieved temporal stability improvements to distributed connected dominating set (CDS) algorithms. These algorithms are typically used for structural control and efficient data distribution within autonomous mobile networks, such as mobile ad hoc networking technical standards. Such distributed algorithms compute topologically connected control structures within dynamic network topologies, but at present, standard algorithms experience high degrees of membership reelection changes. While such algorithms are needed and beneficial, the topological churn caused by continual reelection has been shown to be significantly problematic in disruptive deployment scenarios such as hybrid airborne-surface communication networks and urban environments. Using DyNAMo techniques and related modeling workflows, we developed both an analytical approach and a recent solution for a well-known distributed algorithm that provides up to 30% to 40% stability improvements under dynamic wireless network conditions. Figure 10 provides an example of such an improvement within a 600-second modeled mobile scenario; stability gains are achieved without additional redundancy in the topological structure, thus improving the performance of related network protocols without sacrificing additional precious wireless bandwidth. We are presently examining the

measurable performance improvements to distributed operations and upper layer applications once increased stability is realized through methods we have developed as discussed in Ref. 1.

Analyzing Evolving Structures in Dynamic Networks: Many networks of interest, including communication and information networks, often naturally evolve or divide into communities or nodal structures over time. This division or evolution can be intentional or may be caused by many factors across layers of a networking architecture, including clustered or constrained motion, physics and environmental effects, and organizational or informational relationships that evolve over time. By identifying the relative strengths and weaknesses of existing network structures, pinpointing critical network locations, and classifying the evolution of clustered relationships, we can better address future dynamic network planning and adaptation challenges, including defense of networks and robust adaptation in disruptive environments.

We have taken a multidisciplinary approach of applying machine learning methods and recent advances in spectral graph theory to both detecting and tracking clusters within autonomous networks over time. Figure 11 depicts the results from autopartitioning and tracking network clusters using graph spectral eigen-decomposition through a 10-minute, 90-node network deployed in a maritime-modeled scenario. The lower graph in Fig. 11 also provides an example of research improvements to dynamic autopartitioning and shows that we can in practice do better than known eigen-based spectral gap techniques.²

The following summarizes recent accomplishments of this work.

- (1) We have applied spectral analysis to mobile network traces to detect, stabilize, and track structural community decomposition.
- (2) We have determined the size of partitions over time using eigendecomposition data along with a usable partition quality metric for dynamic analysis and adaptation purposes.

Future Work: This work demonstrates the use of high-fidelity mobile network modeling and associated analytics to detect and research dynamic network conditions and protocols to improve an understanding of performance in the research, planning, and deployment stages. Future work will address additional challenges of real-time analysis and adaptation of complex, autonomous networks based upon associated applied analytics.

[Sponsored by the NRL Base Program (CNR funded)]

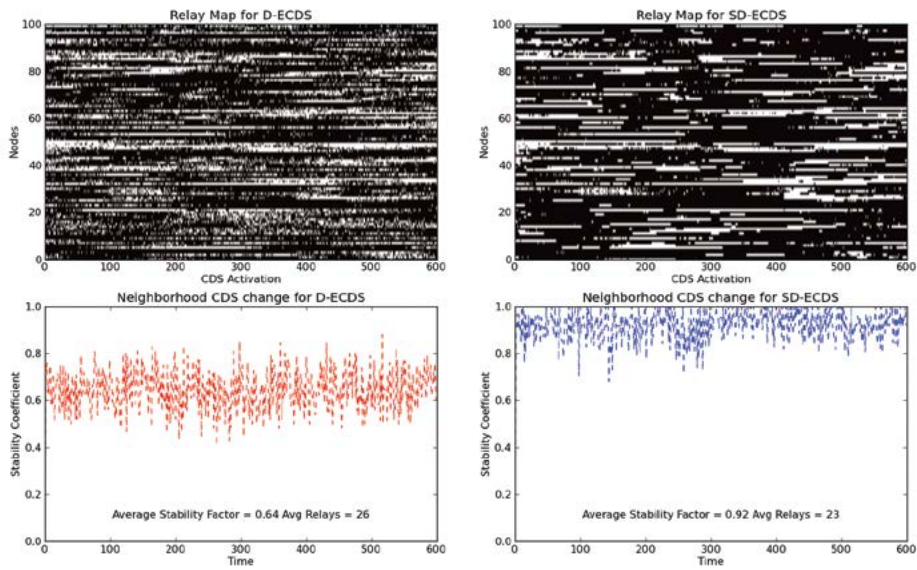


FIGURE 10
Graph of CDS stability improvement results using DyNAMo evolving graph models.

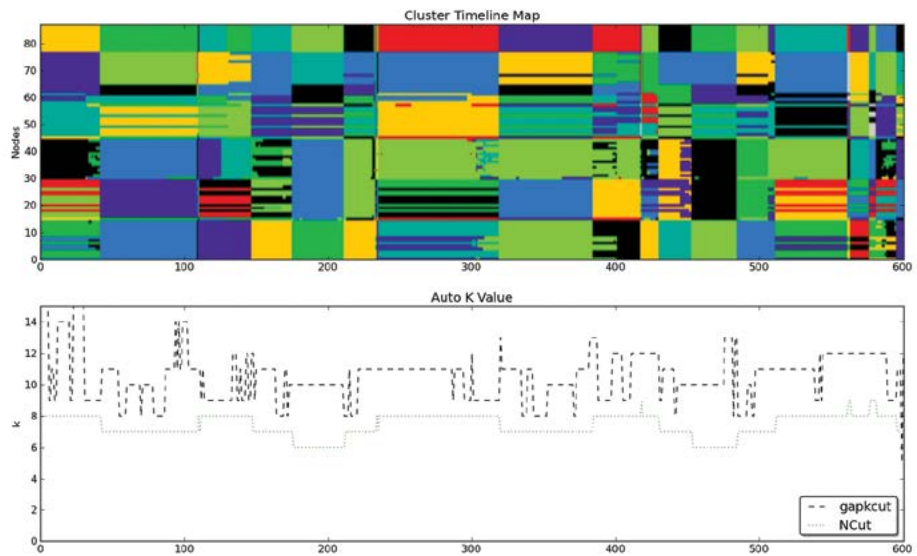


FIGURE 11
Color map illustrating dynamic cluster detection and tracking.

References

¹J.P. Macker, B. Adamson, and D.J. Claypool, “Temporal Stability for Dynamic Network Relay Sets,” in Proceedings MILCOM 2012, Orlando, FL, Oct. 29–Nov. 1, 2012; doi:10.1109/MILCOM.2012.6415615.
²J.P. Macker and D.J. Claypool, “Dynamic Communities in Evolving Network Graphs,” in Proceedings MILCOM 2012, Orlando, FL, Oct. 29–Nov. 1, 2012; doi:10.1109/MILCOM.2012.6415614.

Frequency Position Modulation

J. Goodman, C. Bertoncini, B. Nousain, and G. Cowart
Tactical Electronic Warfare Division

Introduction: NRL has developed a novel, high data, low probability of intercept (LPI) and low probability of detection (LPD) waveform called Frequency Position Modulation (FPM). Each symbol in an FPM waveform is represented by multiple tones that are

spread over an extremely wide instantaneous bandwidth (IBW). Wideband operation enables FPM to achieve higher data rates than conventional LPI/LPD communications without as significant a sacrifice in processing gain. FPM processing is novel in two key respects. The first is that multiple local oscillators (LOs) are simultaneously used at the receiver in the downconversion process to collapse a wideband spectrum into a much narrower one. This enables a single receiver to digitize a wider bandwidth at its input than is normally possible using standard Nyquist sampling. Second, nonlinearities generated by the power amplifier (PA) in the transmitter — which are typically unwanted artifacts — are exploited by FPM demodulation on receive to reduce the symbol error rate (SER). We compare the SER vs signal-to-noise ratio (SNR) of FPM against a common LPI/LPD waveform, direct sequence-code division multiple access (DS-CDMA), and demonstrate nearly an order of magnitude improvement in performance.

FPM Constellation and Symbol Transmission:

Each symbol in an FPM waveform¹ is composed of a discrete set of N_{pos} tones. Each of the N_{pos} tones is spread far apart in frequency to mitigate fading and interference. The tones are positioned in frequency such that when they are mixed with multiple LOs on receive, the symbols collapse into a narrower bandwidth, enabling the use of an undersampling analog-to-digital converter (ADC).

A simple procedure for choosing the frequency locations of the symbols is illustrated in Fig. 12, where each colored group corresponds to a contiguous set of baseband frequencies. From each group, a single tone is selected to generate an FPM symbol. In Fig 12, with $N_{pos} = 4$, the LO and frequency support of the colored groups are selected so that the symbols collapse into a narrower band than the one in which they were transmitted.

To calculate the exact frequencies, we need to define the number of samples per symbol, N_{smp} . The choice of N_{smp} is a trade of data rate against processing gain, e.g., the more samples per symbol, the higher the processing, but the lower the data rate. In each colored group there are M frequencies and the number of symbols that share a common frequency component is represented by q ; we represent the FPM constellation as $M_{q,N_{pos}}$. The selection of q is a tradeoff between SER and data rate; two different values are compared in the results section.

At baseband the tones are shaped to promote or suppress nonlinearities generated by the PA.² The nonlinearities that are promoted appear as additional tones, so they increase the Hamming distance and therefore decrease SER for a fixed SNR. A block diagram of the

transmitter is illustrated on the left-hand side of Fig. 13. FPM symbol integrity is not adversely affected by driving the PA into saturation to generate nonlinearities enabling power efficient operation.

FPM Demodulation: The received signal is passed through a fixed comb filter after the low-noise amplifier (LNA) to isolate the $N_{pos} \times M$ frequency locations in the spectrum where the symbols have support, as illustrated on the right-hand side of Fig. 13. The symbols may in fact be spread out over many GHz of instantaneous bandwidth. Therefore, to recover the symbols using a single receiver, $N_{pos}/2$ LOs are added together to mix the incoming signal down to baseband. This process is illustrated in Fig. 14 for the case in which $N_{smp} = 2048$, $N_{pos} = 4$, and $M = 64$, effectively collapsing the spectrum into one-quarter the original bandwidth. Unlike compressed sensing,³ collapsing the wideband spectrum into a narrower one does not suffer from noise folding and loss of SNR.

Demodulation takes place in the frequency domain using a fast Fourier transform (FFT) matched filter. Maximum likelihood (ML) or maximum *a posteriori* (MAP) demodulation techniques are then used to recover symbols embedded in noise and subject to Rayleigh fading. To supplement these techniques, we also developed a statistical demodulator based on a Hamming distance metric for the case when FPM operates in a spectrally crowded environment and is subject to unexpected interference. In this case, with sufficient SNR, the nonlinearities offer a distinct advantage by increasing the Hamming distance. For example, the minimum Hamming distance of a $64_{2,4}$ -ary constellation increased from 3 to 8 when nonlinearities were exploited, albeit the inherently lower SNR of the distortions prevented their complete exploitation. The performance of each of these techniques is presented in the next section.

Results: The efficacy of FPM was tested by running Monte Carlo simulations of a communications system using $64_{1,4}$ - and $64_{2,4}$ -ary FPM and comparing its SER performance against that of DS-CDMA with BPSK modulation and ML demodulation. The results of this comparison are plotted in Fig. 15. Each of the waveforms was subject to additive white Gaussian noise and Rayleigh fading, as well as random narrowband interference. DS-CDMA and $64_{2,4}$ -ary FPM were parameterized to maintain identical data rates to one another for the performance comparison, while $64_{1,4}$ -ary operated at half the data rate.

When FPM was not subject to interference (SIR = ∞ , $E(N_s) = N_s = 0$), FPM ML demodulation outperformed DS-CDMA. When interference was present, FPM with statistical demodulation using a Hamming

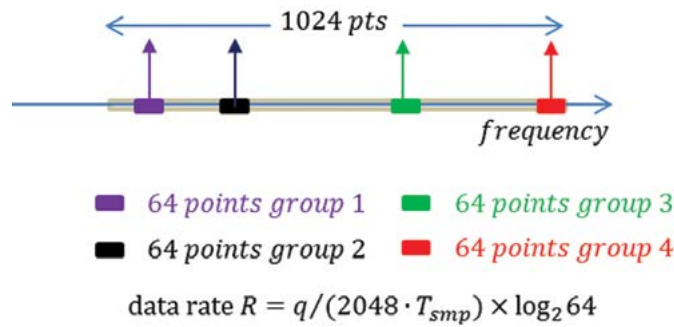


FIGURE 12
 An example FPM $64_{q,4}$ -ary constellation, where $N_{smp} = 2048$, $N_{pos} = 4$, $M = 64$, and the up-arrows represent the location of a transmitted symbol. The 1024 points correspond to the positive frequencies in the 2048-point discrete spectrum, and T_{smp} is the inverse of the sample rate of the analog-to-digital converter.

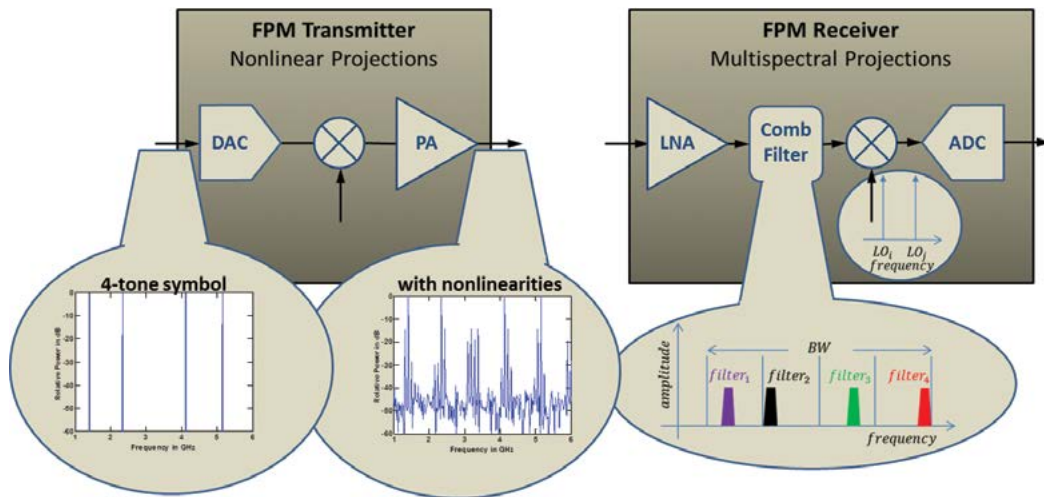


FIGURE 13
 The analog transmit and receive processing chain in FPM. The colored filters represent the comb filter pass-band of the FPM receiver.

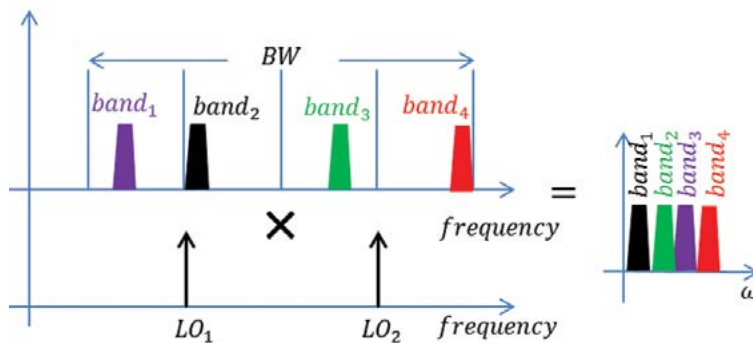


FIGURE 14
 The placement of the LOs with respect to the $N_{pos} = 4$ contiguous bands where FPM symbols have support enable collapsing a wideband spectrum into a narrower one — in the case above at zero-IF prior to digitization — without a loss of information.

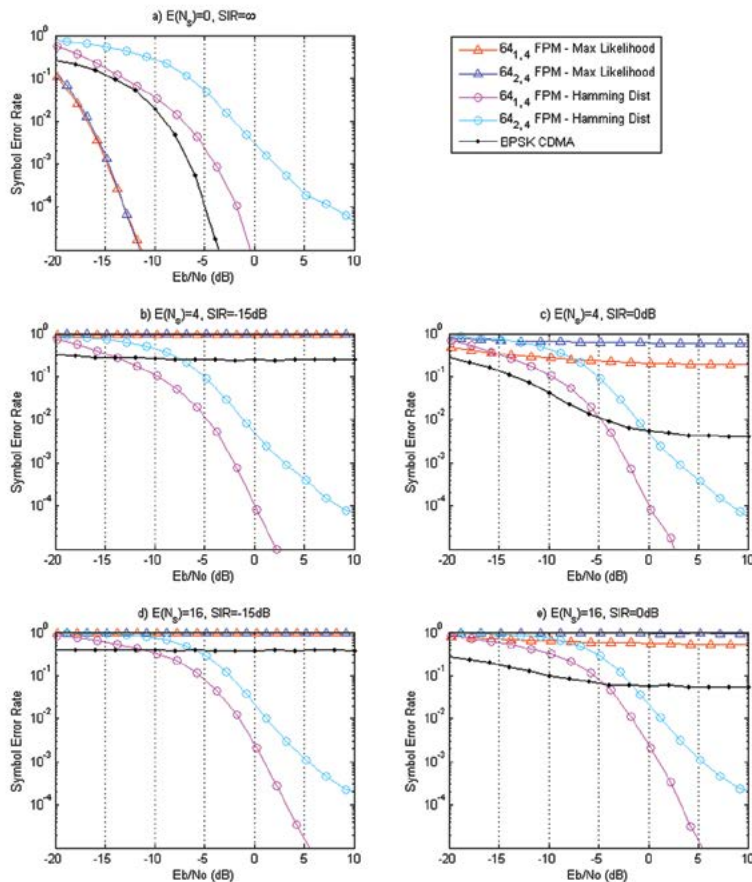


FIGURE 15

The SER performance of FPM vs DS-CDMA. $E(N_s)$ corresponds to the average number of narrowband interference sources present on each Monte Carlo run. SIR is the average signal-to-interference ratio and E_b/N_0 is the ratio of bit energy to noise spectral density.

distance metric significantly outperformed DS-CDMA, which was disproportionately affected by interference due to its wide IBW. Finally, for the same fixed data rate, the processing gain of FPM was roughly an order of magnitude higher than that of DS-CDMA, and this is reflected in the improved SER performance of FPM.

Conclusion: As demonstrated in Fig. 15, FPM is capable of operating in dense interference environments where conventional LPI/LPD communications fail. FPM analog processing used distortions generated by the PA on transmit and wideband undersampling on receive to simultaneously increase both processing gain and data rate. FPM benefits the Navy by providing a robust LPI/LPD communications waveform that can operate in interference-laden environments to ensure high-priority information reaches its intended destination.

[Sponsored by the NRL Base Program (CNR funded)]

References

- ¹ J. Goodman, C. Bertocini, M. Moore, B. Nousain, and G. Cowart, "Frequency Position Modulation Using Multi-Spectral Projections," *Proc. SPIE* **8514**, 85140C (2012).
- ² M. Herman, B. Miller, and J. Goodman, "The Cube Coefficient Subspace Architecture for Nonlinear Digital Predistortion," in *Conference Record of the 42nd Asilomar Conference on Signals, Systems and Computers*, pp. 1857–1861 (IEEE, 2008).
- ³ J. Goodman, K. Forsythe, and B. Miller, "Efficient Reconstruction of Block-Sparse Signals," in *2011 IEEE Statistical Signal Processing Workshop*, pp. 629–632 (IEEE, 2011).

Materials Science and Technology

176 The Physics of the Unconfined Deflagration-to-Detonation Transition

178 Failure of Classical Elasticity

180 Synfuel from Seawater

181 Relationship of Grain Boundary Microchemistry to Stress Corrosion Susceptibility in Aircraft Aluminum Alloys

183 A New Annealing Technique: Multicycle Rapid Thermal Annealing (MRTA)

The Physics of the Unconfined Deflagration-to-Detonation Transition

A.Y. Poludnenko,¹ V.N. Gamezo,¹ and E.S. Oran²

¹Laboratories for Computational Physics and Fluid Dynamics

²Materials Science and Component Technology Directorate

Introduction: Since the discovery of the detonation phenomenon in the late 19th Century, the question of the physical processes that produce these supersonic reaction waves has been at the forefront of combustion science. Due to the extremely large destructive potential of detonations, understanding the mechanisms of their formation so as to prevent them is crucial for the safety of fuel storage facilities, chemical plants, and the like. On the other hand, the ability to initiate detonations in a controlled and efficient manner promises to revolutionize energy-generation and propulsion systems for the Navy through the introduction of detonation-based engines.

Detonations are also studied for the key role they play in a very different type of explosion, those occurring on astronomical scales and known as Type Ia supernovae (SNIa). These are thermonuclear incinerations of compact, white dwarf stars comprised primarily of carbon and oxygen. While the precise mechanism of SNIa is still uncertain, virtually all observationally viable explosion scenarios today involve the formation of a detonation during the later stages of the explosion.

The unifying aspect of all such systems is that burning typically starts as a highly subsonic flame. In order for a detonation to appear, some mechanism must increase pressure dramatically and produce strong shocks. Both experimental and numerical studies over the past several decades have shown that expansion of hot gases in semiconfined systems, e.g., in channels or pipes, can produce fast supersonic flows capable of generating shocks. In the interior of a star or a fuel-vapor cloud, however, there are no walls to confine the flow or to create boundary layers that can generate turbulence and accelerate burning. Is the formation of a detonation from a subsonic flame, known as the deflagration-to-detonation transition (DDT), even possible in such unconfined systems? What mechanisms could produce the pressure increase necessary for DDT?

Modeling Unconfined DDT: In order for pressure to rise in the system, burning needs to accelerate to speeds that are a significant fraction of the speed of sound. Laminar chemical and thermonuclear flames are typically much slower than that. In unconfined systems, the agent capable of providing necessary acceleration is turbulence, which stretches and wrinkles the flame, thus

increasing its surface area and the effective burning rate. Typically, this turbulence is the result of the explosion itself. For instance, in SNIa, hot, light, burning products rising through the interior of a star result in the Rayleigh–Taylor instability, which produces strong turbulence.

Modern computational resources do not allow us to study the entire explosion self-consistently in a numerical simulation, since it would require resolving both the smallest scales of burning, namely, the flame thickness, as well as the largest scales, on which turbulence is generated. These scales are typically separated by many orders of magnitude over the range from millimeters to hundreds of meters on Earth or thousands of kilometers in SNIa.

We, therefore, adopted a different approach, in which only a small section of a much larger turbulent flame is modeled in a simulation.^{1,2} Homogeneous, isotropic turbulence is steadily driven in a long rectangular domain. This reproduces the effect of the turbulent cascade from much larger scales, which are not included in the calculations. To maximize the range of scales that can be resolved, we use simplified single-reaction chemical kinetics, which is calibrated to represent H₂–air or CH₄–air mixtures. This also allows for the comparison with the experiments.

Interaction of fast turbulence with the flame leads to the development of the highly complex structure shown in Fig. 1. A systematic survey of a large parameter space of turbulent intensities and system sizes demonstrated that, in sufficiently large systems, such fast turbulent flames are susceptible to the spontaneous development of a detonation.³ This process does not require any confining effect of walls or the presence of external boundaries or obstacles. It is an inherent property of turbulent reacting flows not present in their nonreacting counterparts.

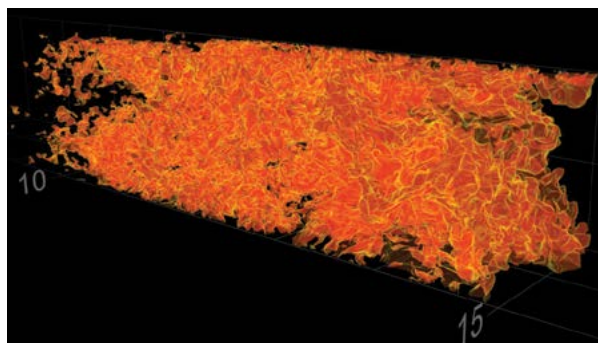


FIGURE 1

Complex structure of the turbulent chemical flame in a stoichiometric methane–air mixture. Uniform computational grid has dimensions $1.33 \times 1.33 \times 42.5$ cm and resolution of ~ 50 μm . Shown is the isosurface of the fuel mass fraction corresponding to peak reaction rate. In this simulation, burning is fully resolved on all scales. Image rendering by the Department of Defense HPCMP Data Analysis and Assessment Center.

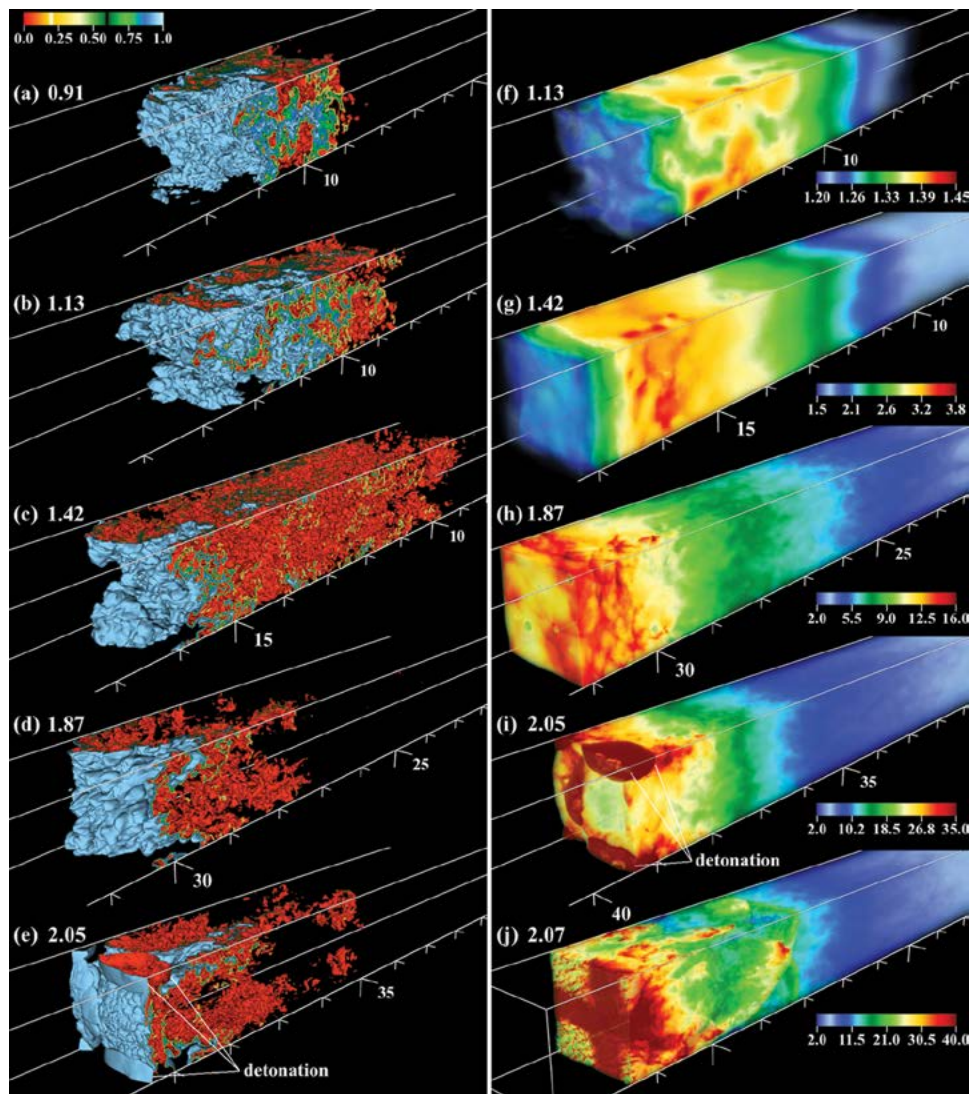


FIGURE 2 Structure of the turbulent flame and the corresponding pressure distribution during DDT in a stoichiometric CH_4 -air mixture. (a) – (e): isovolume of the fuel mass fraction. (f) – (j): volume rendering of pressure normalized by the initial pressure in the domain (note a different colormap range in each panel). Horizontal axis scale gives the distance from the right boundary of the domain in centimeters. The time from the start of the simulation is indicated in each panel in units of the large-scale turbulent eddy turnover time. Note that panels (b)-(f), (c)-(g), (d)-(h), (e)-(i) correspond to the same time instants.

Illustration of DDT is given in Fig. 2. When the turbulent flame speed crosses a certain threshold, pressure begins to rise in the flow. This compresses and heats fuel, thereby further accelerating burning, which causes pressure to grow even more rapidly. As a result, a catastrophic runaway process is initiated leading to the formation of strong shock waves and, ultimately, to the detonation ignition.³ The threshold burning velocity is known as the speed of the Chapman–Jouguet (CJ) deflagration. This is the theoretical maximum speed at which stable flame propagation is possible. Typical laminar chemical and thermonuclear flames have much lower burning velocities. Our simulations show,

however, that turbulent flames can become sufficiently fast to exceed the CJ deflagration threshold. When they do, DDT occurs.³

Summary and Future Directions: Numerical simulations discussed here present the first self-consistent demonstration of spontaneous DDT in unconfined systems. A survey of different reactive mixtures and turbulent conditions showed that the obtained DDT criterion based on the CJ deflagration speed indeed very accurately predicts the onset of DDT.³

Large-scale simulations of combustion systems, such as SNIa or industrial explosions, however, can-

not resolve all scales of burning and, thus, must be supplemented with subgrid-scale models, which specify the local turbulent flame speed based on the resolved turbulent conditions. Existing subgrid-scale models do not account for unsteady phenomena such as DDT. Therefore, the next step in this work involves the incorporation of the CJ-based DDT criterion into the subgrid-scale models for the turbulent flame speed, suitable for use in large-scale simulations.

A preliminary subgrid-scale model developed for SNIa predicts that DDT will occur in these systems at densities $\sim 10^7$ g/cm³. Occurrence of DDT at this density was previously empirically shown to give the best agreement with the observations, which demonstrates the viability of the emerging understanding of the unconfined DDT in realistic combustion systems.

[Sponsored by AFOSR and the NRL Base Program (CNR funded)]

References

- ¹ A.Y. Poludnenko and E.S. Oran, "The Interaction of High-Speed Turbulence with Flames: Global Properties and Internal Flame Structure," *Combustion and Flame* **157**, 995 (2010).
- ² A.Y. Poludnenko and E.S. Oran, "The Interaction of High-Speed Turbulence with Flames: Turbulent Flame Speed," *Combustion and Flame* **158**, 301 (2011).
- ³ A.Y. Poludnenko, T.A. Gardiner, and E.S. Oran, "Spontaneous Transition of Turbulent Flames to Detonations in Unconfined Media," *Physical Review Letters* **107**, 054501 (2011).



Failure of Classical Elasticity

C.M. Roland, J. Roh, and P. Mott
Chemistry Division

Introduction: Determining the mechanical properties of very hard materials, such as diamond or beryllium, can be challenging. Usually, measurements of the sound velocity or Brillouin scattering are used to quantify certain elastic properties. Since there are only two unique constants for an isotropic material, the elastic constants of interest can then be calculated using the equations of "classical elasticity" (i.e., linear elasticity theory). Of course, the accuracy of such determinations depends on the validity of the classical equations.

An important elastic constant is Poisson's ratio, ν , defined as the negative ratio of the lateral strain ϵ_{22} to the longitudinal strain ϵ_{11} . Poisson's ratio can be used to determine the limits of applicability of the classical theory. From the equation relating ν to the bulk, B , and shear, G , moduli,

$$G = B \frac{3(1-2\nu)}{2(1+\nu)}, \quad (1)$$

and the equilibrium requirement that B and G are both greater than zero, the bounds on Poisson's ratio for an isotropic material are obtained:

$$-1 < \nu < 1/2. \quad (2)$$

These well-known limits can be found in engineering texts dating from the 19th century.¹ (Sometimes a less than or equal sign is given erroneously for the upper bound in Eq. (2).²)

Deriving the limits for ν based on B and G is the obvious approach, since these moduli describe the respective changes in a body's size and shape. However, there is neither mathematical nor physical justification for choosing B and G over other pairs of elastic constants. Recently we showed³ that expressions derived for ν in terms of Young's modulus, the longitudinal modulus, the biaxial modulus, etc. lead to a different lower limit on ν than Eq. (2). From our analysis we concluded that classical elasticity can only be applied to materials for which

$$1/5 \leq \nu < 1/2. \quad (3)$$

Since all elastic constants are equally valid, the most restrictive bounds are the correct ones, since they are consistent with any less restrictive limits. Equation (3) also has the appealing feature that it coheres with the range of ν observed for more than 99% of materials. However, it is the few substances for which $\nu < 1/5$ that are of particular interest, because those are the cases for which the (inapplicable) classical elasticity equations are usually employed.

Results: Although the mathematics leading to Eq. (3) is straightforward, ideas long venerated are difficult to overturn. Remarkably, the classical bounds (Eq. (2)) have never been subjected to experimental verification. Thus, we carried out experiments⁴ to validate our finding that classical elasticity fails whenever $\nu < 1/5$. Four samples were prepared (Table 1): a polyurethane foam (PU1) and a solid elastomer (polyisoprene), which had respective values of Poisson's ratio at each extreme of the range in Eq. (3), and two foams (PU2 and PU3) for which $\nu < 0$. These two auxetic samples enable testing of our prediction that classical elasticity fails for $\nu < 1/5$ (Fig. 3).

For each sample, ν , G , and Young's modulus, E , were measured at a strain rate of 0.002 s⁻¹, which is sufficiently slow to yield elastic (mechanical equilibrium) values. The Poisson's ratio of the samples was also calculated using the equation from classical elasticity:

$$\nu_{calc} = \frac{E}{2G} - 1. \quad (4)$$

The calculated and experimental values of ν are compared in Fig. 4; the results extrapolated to zero strain

TABLE 1 — Poisson's Ratios

	polyisoprene	PU1	PU2	PU3
$\nu_{calc} \gamma = 0$	0.499 ± 0.014	0.206 ± 0.012	-0.590 ± 0.020	-0.608 ± 0.023
ν_{exp}	0.496 ± 0.006	0.204 ± 0.006	-0.699 ± 0.008	-0.650 ± 0.015

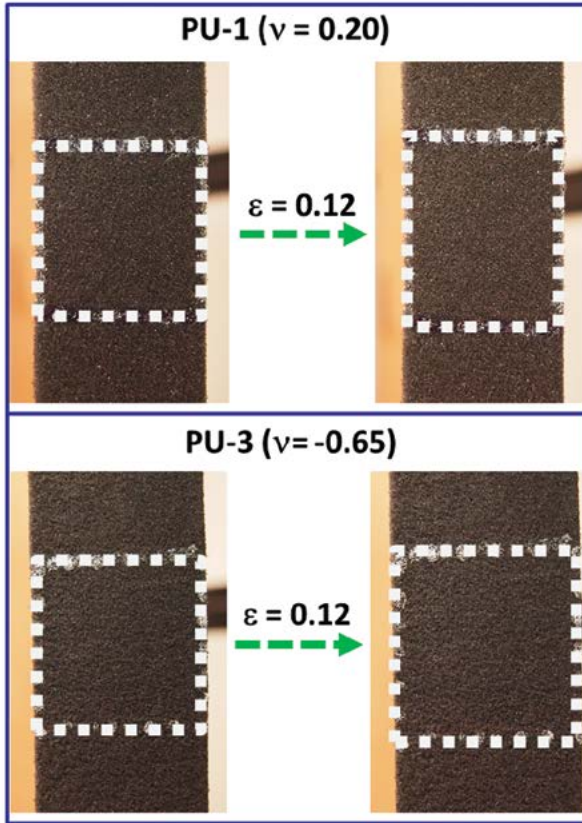


FIGURE 3

Photographs of polyurethane foams; the square markers represent fiducial marks used to calculate strains. Top: Conventional foam exhibiting lateral contraction upon stretching, in accord with a positive Poisson's ratio. Bottom: Auxetic foam, in which de-buckling of the cell structures compensates for the material contraction, yielding lateral expansion upon axial stretching.

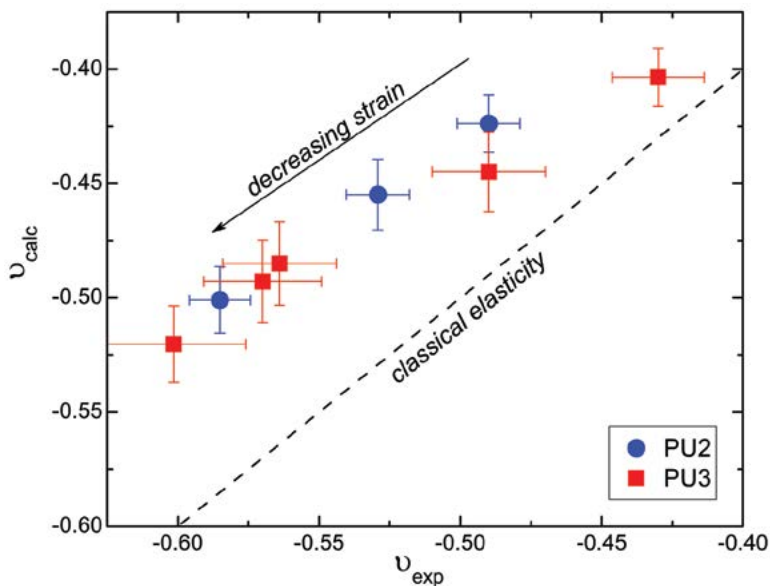


FIGURE 4

The values of Poisson's ratio calculated using Eq. (4) versus the measured ν for the auxetic foams. Extrapolation to zero strain does not yield convergence.

are listed in Table 1. For the two materials with $\nu \geq 0.2$, Eq. (4) is accurate. However, for the two materials with $\nu < 1/5$ (within the traditional limits of Eq. (2), but beyond the more restrictive range), the calculated values ν are significantly larger than the measured values. Thus, Eq. (4) of classical elasticity fails when $\nu < 1/5$.

Summary: A recent derivation³ of the bounds on Poisson's ratio, ν , for linearly elastic materials showed that the equations of classical elasticity are invalid for ν less than 1/5; that is, the lower bound for the classical theory is not -1 , as commonly assumed. To verify this analysis, Poisson's ratio was measured for four materials. Two of these comply with the stricter limits for Poisson's ratio, and their calculated and measured values of ν were in agreement. However, for the two isotropic, auxetic foams, having ν outside the lower bound of Eq. (3), the values calculated using classical elasticity were significantly different than the measured ν . These results⁴ corroborate our determination of the correct limits on ν for the classical theory to be applicable.

The significance of this work is that the small number of materials having $\nu < 0.2$ tend to be very hard, which makes direct measurement of Poisson's ratio and other elastic constants difficult and associated with large error. It is for this reason that recourse is made to the equations of classical elasticity. Unfortunately, this is the situation, as shown herein, for which the classical equations are invalid.

Acknowledgments: We thank C.B. Giller for experimental assistance.

[Sponsored by the NRL Base Program (CNR funded)]

References

- ¹ A.E.H. Love, *A Treatise on the Mathematical Theory of Elasticity*, Vol. 1 (Cambridge University Press, 1892).
- ² P.H. Mott, J.R. Dorgan, and C.M. Roland, "The Bulk Modulus and Poisson's Ratio of 'Incompressible' Materials," *J. Sound Vibration* **312**, 572–575 (2008).
- ³ P.H. Mott and C.M. Roland, "Limits to Poisson's Ratio in Isotropic Materials," *Physical Review B* **80**, 132104 (2009).
- ⁴ J.H. Roh, C.B. Giller, P.H. Mott, and C.M. Roland, "Failure of Classical Elasticity in Auxetic Foams," *AIP Advances*, submitted (2013).

Synfuel from Seawater

H.D. Willauer,¹ D.M. Drab,² F. DiMascio,³ D.R. Hardy,⁴ R. Ananth,⁵ and F.W. Williams⁵

¹Materials Science and Technology Division

²National Research Council Postdoctoral Associate

³Office of Naval Research

⁴Nova Research, Inc.

⁵Chemistry Division

Introduction: NRL is developing and demonstrating technologies that recover carbon dioxide (CO₂) and produce hydrogen (H₂) from seawater. These feedstocks are combined in an NRL gas-to-liquid (GTL) process to produce hydrocarbons, which can be used to produce fuel at sea.

Synthesizing drop-in replacements for petroleum-derived fuel in-theater is a "game-changing" proposition for the Navy. Refueling U.S. military vessels with petroleum-derived fuel, at sea and underway, is a costly endeavor in terms of logistical tails, time, and decreased operational flexibility. In addition, refueling vessels at sea is risky, as ships must remain in close proximity and match course and speed for hours. Producing fuel at sea, from the sea, reduces these vulnerabilities and reduces dependence on fossil fuels. From an environmental perspective, this combination of integrated processes could be considered CO₂ neutral: the carbon dioxide produced from combustion of the synthetic fuel is returned to the atmosphere where it re-equilibrates with the ocean to complete the natural carbon cycle.

Carbon Capture: Using a novel electrochemical acidification cell developed at NRL, up to 92% of both dissolved and bound CO₂ can be removed from seawater. The concentration of carbon dioxide in seawater is 140 times greater than that in air, yet harvesting large quantities of CO₂ rapidly and efficiently from seawater had not been demonstrated prior to the recently announced, patented NRL process.¹ In addition to recovering CO₂, the cell simultaneously produces H₂ gas at the cathode as a byproduct. NRL and partners have developed a carbon capture skid, shown in Fig. 5, that demonstrates the continuous and efficient production of CO₂ and H₂ from seawater. The process of both recovering CO₂ and concurrently producing H₂ gas eliminates the need for additional large and expensive electrolysis units. The process efficiency, H₂ production, and ability to process the seawater without the need for additional chemicals or pollutants have made this technology far superior to membrane and anion exchange processes previously developed and tested by NRL for use at sea.

Synfuel Production: Achieving high catalytic conversion efficiencies and selectivities of CO_2 and H_2 to a jet fuel fraction is a key scientific challenge which NRL continues to study at the basic science level.² NRL has made significant advances in the development of a two-step GTL process to convert CO_2 and H_2 from seawater to a fuel-like fraction of C_9 – C_{16} molecules. In the first step (Fig. 6), an iron-based catalyst has been developed that can achieve CO_2 conversion levels up to 60% and decrease unwanted methane production from 97% to 23% in favor of longer-chain unsaturated hydrocarbons (olefins). In the second step, by a second solid acid catalyst reaction, these olefins can be oligomerized (a chemical process that converts monomers, molecules of low molecular weight, to a compound of higher molecular weight by a finite degree of polymerization) into liquid containing hydrocarbon molecules in the C_9 – C_{16} range, suitable for conversion to jet fuel.² NRL operates a laboratory-scale fixed-bed catalytic reactor system, and the outputs of this prototype unit have confirmed the presence of the C_9 – C_{16} molecules in the liquid fuel.



FIGURE 5
NRL electrochemical acidification carbon capture skid. The acidification cell is mounted onto a portable skid along with a reverse osmosis unit, power supply, pump, carbon dioxide recovery system, and hydrogen stripper to form a carbon capture system (dimensions 63 in. × 36 in. × 60 in.).

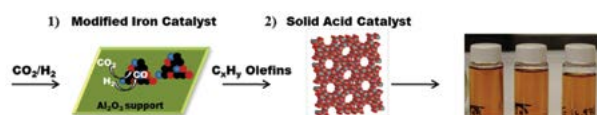


FIGURE 6
NRL liquid hydrocarbons synthesized from carbon dioxide and hydrogen.

The Future of Synfuel at Sea: We are now set to transition the NRL two-step GTL process into commercial modular reactor systems of the type being designed for other offshore and remote synthetic

hydrocarbon fuel synthesis from syngas. The new challenge is to continue optimizing the chemistry of the two-step approach in a commercial system, so that this data can provide the basis for future modular pilot- and commercial-scale processes.

[Sponsored by the NRL Base Program (CNR funded)]

References

- H.D. Willauer, F. DiMascio, D.R. Hardy, M.K. Lewis, and F.W. Williams, "Development of an Electrochemical Acidification Cell for the Recovery of CO_2 and H_2 from Seawater II. Evaluation of the Cell by Natural Seawater," *I&EC Res.* **51**(34), 11254-11260 (2012).
- D.M. Drab, H.D. Willauer, M.T. Olsen, R. Ananth, G.W. Mushrush, J.W. Baldwin, D.R. Hardy, and F.W. Williams, "Hydrocarbon Synthesis from Carbon Dioxide and Hydrogen: A Two-step Process," *Energy Fuels*, DOI: 10.1021/ef4011115 (2013).

Relationship of Grain Boundary Microchemistry to Stress Corrosion Susceptibility in Aircraft Aluminum Alloys

R. Goswami, P.S. Pao, and R.L. Holtz
Materials Science and Technology Division

Introduction: Aluminum 7000 series alloys are used extensively for military and civilian aircraft structural components. However, stress corrosion cracking (SCC) of the higher strength tempers in salt spray/salt fog environments continues to be a problem with these alloys, particularly with respect to maintenance costs. In salt water environments, SCC susceptibility is the result of anodic dissolution of grain boundary precipitates. Certain aging, or precipitation hardening, treatments can improve the resistance to SCC of the 7000 aluminum alloys, and increasing the copper content of the alloy can reduce the dissolution rate of the grain boundary precipitates in corrosive environments. To better understand this behavior and the factors that control SCC, NRL has undertaken a systematic investigation of the effects of aging/hardening treatments and Cu content on the microchemistry and microstructure of grain boundary precipitates of 7075Al alloy.

Grain Boundary Precipitate Structure and Microchemistry: The microstructure evolution of grain boundary precipitates as a function of aging is demonstrated by Fig. 7. Table 2 defines the aging treatments. In naturally aged (NA) condition (Fig. 7(a,b)), grain boundaries are observed to be decorated by nanocrystalline precipitates 5 to 10 nm in size. Extremely fine precipitates (Fig. 7(b,c)), mostly Zn-rich GP zones, can be observed within the grain. At peak-aged (PA)

condition, the precipitates at grain boundaries are much coarser, 50 to 100 nm (Fig. 7(d)). Upon further aging (over-aged condition, OA), the size and spacing of the precipitates (Fig. 7(e)) increase to some extent as compared to the peak-aged condition. Transmission electron microscope (TEM) studies showed that the grain boundary precipitates are η phase ($MgZn_2$) containing considerable amounts of Cu.

TABLE 2 — Aging Treatment Definitions

Aging Designation	Alloy Hardening Treatment
Naturally aged	Allowed to harden at room temperature
Peak-aged (T651 condition)	Reheated to an intermediate temperature
Over-aged (T73 condition)	Reheated to a higher temperature beyond peak strength

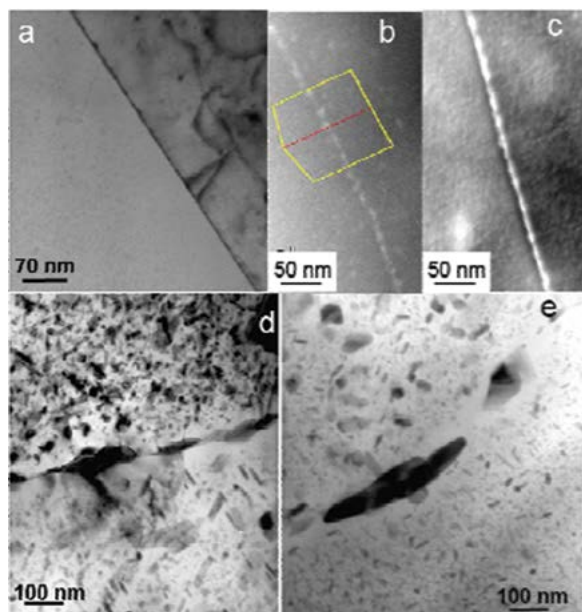


FIGURE 7 Microstructure of grain boundary precipitates in samples with different aging treatments. (a) Bright-field TEM image showing grain boundary precipitates in the naturally aged condition. (b) HAADF image of the naturally aged condition. (c) HAADF image of a sample aged at 120 °C for 12 h (less aging than peak-aged). (d) Bright-field TEM image at peak-aged condition. (e) Bright-field TEM image at over-aged condition.

Figure 8(a) shows grain boundary precipitates in a peak-aged sample. Figure 8(b) is a high-resolution TEM (HRTEM) image of one such grain boundary precipitate close to the [0001] zone. The fast Fourier transform (FFT) obtained from this precipitate showed {10-10} type spots with d-spacing ~ 4.5 Å. Composition maps of Mg, Al, Cu, and Zn and corresponding high-angle annular dark field (HAADF) images were obtained for the different aging conditions; those of the peak-aged condition are shown in Fig. 8(c,d). The composition of precipitate as a function of aging is given in Fig. 9(a), showing a significant increase in Cu content with aging; the Zn decreases considerably and the Mg increases by a small amount (compared to the naturally aged condition). At peak-aged condition, the average content of Mg, Cu, and Zn is 45.18, 15.08, and

39.73 at.%, respectively, and at over-aged condition, the average content of Mg, Cu, and Zn is 40.0, 20.00, and 40.00 at.%, respectively.¹ The precipitate stoichiometry is close to $Mg(Cu_xZn_{1-x})_2$.

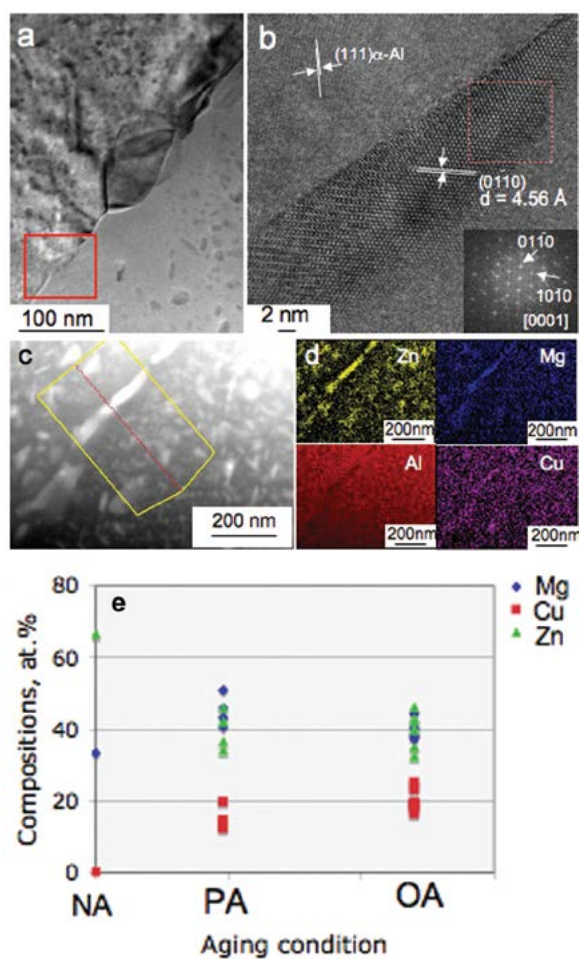


FIGURE 8 (a) Bright-field TEM image at peak-aged condition showing a grain boundary with several precipitates. (b) HRTEM image of one such precipitate showing the crystal structure of the precipitate conforms to hexagonal $MgZn_2$. (c) HAADF image of a grain boundary precipitate in a peak-aged sample. (d) Elemental maps of Mg, Al, Cu, and Zn. (e) The average composition of Zn, Mg, and Cu of the grain boundary precipitate as a function of aging conditions: naturally aged (NA), peak-aged (PA), and over-aged (OA).

Grain Boundary Precipitate Dissolution Behavior: To study the dissolution behavior of the η phase, TEM samples were immersed for 180 to 300 seconds in a brine solution containing 3.5% NaCl at room temperature; subsequent TEM observations were then carried out. For the naturally aged samples, it was observed that grain boundaries were completely dissolved after 300 seconds in the salt water (see Fig. 9(a,b)). However, in peak-aged samples, the precipitates at the grain boundary did not dissolve completely for the same immersion duration (Fig. 9(c)). Our compositional analyses showed that the Cu content of the η phase in the peak-aged condition is 15 at.%, considerably higher than in the naturally aged condition, where it is negligible. The dissolution rate can be directly correlated with the electrochemical potential of the $\text{Mg}(\text{Cu}_x\text{Zn}_{1-x})_2$ compound, which has been observed to increase with an increase in Cu content. This increase in electrochemical potential decreases the driving force for anodic dissolution with respect to the matrix with aging, which suggests the rate of dissolution decreases with the increase in Cu content.

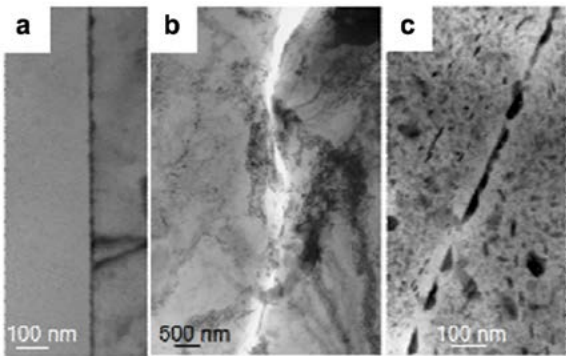


FIGURE 9
(a) Typical grain boundary precipitates in the naturally aged condition before immersion in salt water. (b) Grain boundaries showing the complete dissolution of precipitates in a naturally aged sample after 300 seconds exposure to salt water. (c) Grain boundary in a peak-aged sample showing the precipitates after 300 seconds exposure to salt water.

Significance: An increase in Cu content of the grain boundary precipitates in 7075 alloy was observed for peak-aged and over-aged conditions, relative to the naturally aged condition, in which the Cu content is negligible. The observed increase in Cu content of the precipitates with aging correlates with the increasing resistance to intergranular stress corrosion cracking. The electrochemical potential of the intermetallic $\text{Mg}(\text{Cu}_x\text{Zn}_{1-x})_2$ compound increases with the increase in Cu content. This decreases the driving force for anodic dissolution with respect to the matrix, particularly for the over-aged condition, in which the Cu level is highest. As the dissolution rate decreases with increas-

ing Cu content, the alloy becomes less susceptible to SCC. This result is significant to the Navy in that it demonstrates that Cu enrichment of grain boundary precipitates increases the resistance to crack growth in salt water environments.

[Sponsored by ONR]

Reference

¹ R. Goswami, S. Lynch, N.J.H. Holroyd, S.P. Knight, and R.L. Holtz, "Evolution of Grain Boundary Precipitates in Al 7075 Upon Aging and Correlation with Stress Corrosion Cracking Behavior," *Metallurgical and Materials Transactions 44A*, 1268–1278 (2012), doi:10.1007/s11661-012-1413-0.

A New Annealing Technique: Multicycle Rapid Thermal Annealing (MRTA)

B.N. Feigelson, T.J. Anderson, J.A. Freitas, J.K. Hite, C.R. Eddy, Jr., and F.J. Kub
Electronics Science and Technology Division

Problem: Ion implantation is required for selective-area doping of gallium nitride (GaN) to enable advanced high-power devices.¹ Therefore, post-implant damage removal and impurity activation are critical steps to achieve high quality GaN crystals with high mobility and high dopant activation. To date, there has been no reliable method for annealing Mg-implanted p-GaN to result in adequate Mg electrical activation. The main hurdle for the annealing is the dissociation of GaN at temperatures above 850 °C at atmospheric pressure. Equilibrium nitrogen pressure above GaN increases quickly with temperature, and exceeds 0.1 MPa (1 bar) at 850 °C (only one-third of the melting point). At the same time, it is known that estimated annealing temperature required for sufficient diffusion is about two-thirds of the melting point of the material, and for GaN it is about 1400 to 1500 °C.²

Solution: Annealing at high N_2 pressure (HP) allows the heating of GaN to high temperatures for a long time without GaN dissociation, but the use of very high gas pressures (>2.0 GPa) requires unique HP equipment and time-consuming procedures to load samples and to apply high N_2 pressure. This makes HP annealing too expensive for industry and difficult to scale up to larger wafer sizes. Rapid thermal annealing (RTA) with a protective cap is an attractive alternative for GaN annealing in terms of achievable temperatures and costs, but no electrical activation of Mg after the implantation in GaN without co-doping with other

ions has been shown yet.³ One probable reason for these unsuccessful attempts is the short duration of the GaN annealing at high temperatures. A new technique is required to enable a long-duration annealing at high temperatures without GaN decomposition.

The proposed and developed technique is described as follows. First, consider the case in which a GaN layer with a protective cap is annealed for a very short time at a temperature far above GaN thermodynamic stability. With a careful choice of the cap material and heating duration, it is possible to avoid decomposition of the GaN under the cap. After cooling the sample, the same heating procedure can be repeated without deteriorating the GaN. Following this logic, it should be possible to anneal GaN many times while maintaining the stability of the surface if the heating time above the stability range is sufficiently short and the cap is sufficiently robust. Finally, if this process is repeated without cooling to room temperature, instead just cooling to a temperature where GaN returns to thermodynamic stability, it is possible to rapidly cycle this annealing procedure. In such a process, the material is exposed to high temperature above GaN thermodynamic stability for a long time by accumulating the time of each repetitive cycle, but the stability is maintained due to the extremely short heating duration of each single cycle. Such a process has been developed at NRL, and is described as multicycle rapid thermal annealing (MRTA).⁴

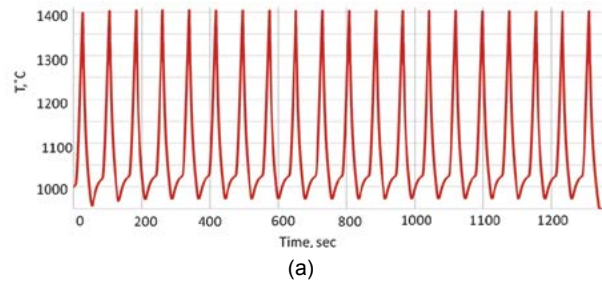
Experimental Details and Results: The GaN films used in the study were grown in a Thomas Swan metal organic chemical vapor deposition (MOCVD) reactor on sapphire substrates. The samples consisted of a 25 nm thick, low-temperature (700 °C) aluminum nitride (AlN) buffer layer, a 2 μm thick, unintentionally doped GaN layer (1030 °C), followed by a thin AlN capping layer. The AlN cap was 4 nm thick, grown at 1000 °C, which was intended to protect the GaN surface during annealing. A single growth run was used to deposit all three layers.

Implantation of only Mg ions was performed to validate the new annealing technique itself. The Mg implant profile was calculated using TRIM implant simulation software.

All annealing experiments were conducted in a chamber with a nitrogen overpressure of 2.0 MPa. A radio-frequency (RF) generator with a graphite susceptor is used for heating. Prior to MRTA, the samples were conventionally annealed in the same chamber for 1 h at 950 to 1050 °C. A typical MRTA schedule is shown in Fig. 10.

The evident advantage of MRTA is clearly shown in the micrographs of Fig. 11. The sample did not show signs of surface degradation after one cycle of the rapid annealing when total heating time between 1300 and

1400 °C was less than 23 s (Fig. 11(a)), but drops of Ga, as a result of GaN dissociation, were seen on the surface of the sample when this time exceeded 31 s (Fig. 11(b)). However, the surface of the sample maintained continuity, i.e., no cracking or GaN decomposition, after MRTA of 40 cycles with the cumulative time between 1300 and 1400 °C totaling 5 min 34 s (Fig. 11(c)).



Run	Accumulated time			Cycles
	From	To	Time	
	T ₁ °C	T ₂ °C	min:sec	
CZ108	1300	1405	3:05	20
CZ113	1300	1410	2:59	20
CZ114	1300	1415	5:34	40

(b)

FIGURE 10

(a) Typical MRTA schedule; (b) MRTA accumulates large total time at high temperature and maintains the stability of the material due to the short duration of each single cycle.

Electrical measurements were performed to look for evidence of Mg activation. It was found that an undoped and unimplanted reference sample was highly resistive (500 MΩ/□), while there was a few orders of magnitude decrease in sheet resistance measured by the transmission line method (TLM) in the implanted and MRTA annealed samples. Hall measurements confirmed the sheet resistance value, and for the first time verified p-type conductivity in Mg-implanted GaN (Fig. 12).

Summary: A new annealing technique, designated multicycle rapid thermal annealing, or MRTA, has been developed to enable annealing of GaN layers. The technique has been proven by the demonstration of electrically active acceptors after Mg implantation in GaN, and for the first time, p-type conductivity in Mg-implanted samples without co-doping enhancement has been observed. Annealing of other nonstable materials may also benefit by applying the MRTA method.

[Sponsored by the NRL Base Program (CNR funded)]

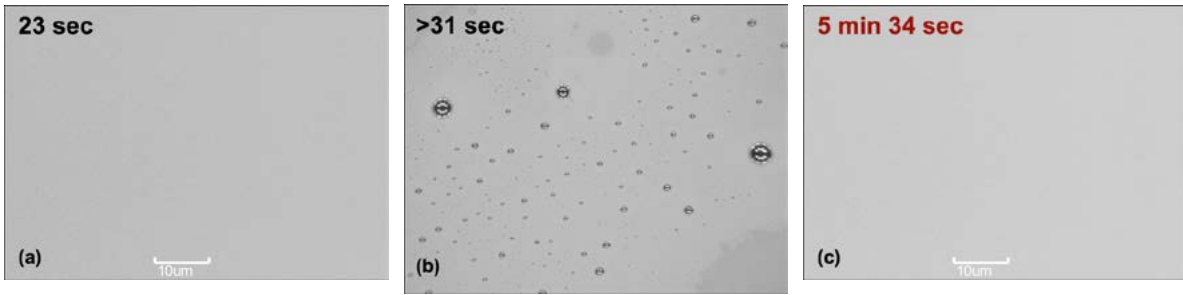
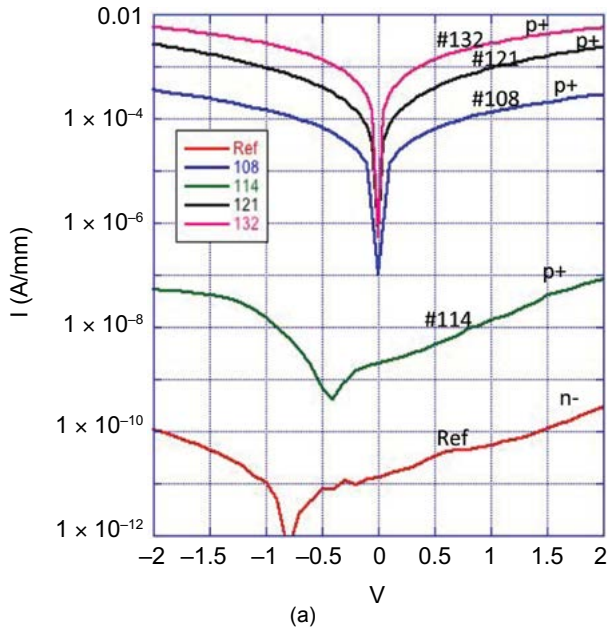


FIGURE 11
Optical micrographs of the annealed samples: (a) one cycle with 23 s total heating time between 1300 and 1400 °C; (b) one cycle with 45 s total heating time between 1300 and 1400 °C; (c) MRTA 40 cycles with 5 min 34 s total cumulative heating time between 1300 and 1400 °C.



(a)

Sample #	R_{SH} $k\Omega/\square$	μ $cm^2/V\cdot s$	N_A (cm^{-3})	Activation %
108	42.6	5	8.4×10^{17}	1.4
114	4850	1	3.7×10^{15}	<0.1
121	5.38	20	1.7×10^{18}	8.2
132	2.69	40	1.7×10^{18}	8.2

(b)

FIGURE 12
(a) I–V curves for a reference sample (as-grown GaN sample, which is unintentionally doped and exhibits n-type conductivity) and Mg-implanted MRTA annealed samples; (b) sheet resistance (R_{SH}), mobility (μ), concentration of noncompensated acceptors (N_A), and activation % of all annealed samples.

References

- ¹ K.T. Liu, S.J. Chang, S. Wu, and Y. Horikoshi, “Crystal Polarity Effects on Magnesium Implantation into GaN Layer,” *Japanese Journal of Applied Physics* **49**(7), 071001 (2010).
- ² S.J. Pearton, “Ion Implantation in Group III Nitrides,” in *Comprehensive Semiconductor Science and Technology*, Vol. 4, pp. 25–43 (Elsevier, Amsterdam, 2011).

- ³ K.T. Liu, Y.K. Su, S.J. Chang, and Y. Horikoshi, “Magnesium/nitrogen and Beryllium/nitrogen Coimplantation into GaN,” *Journal of Applied Physics* **98**(7), 073702 (2005).
- ⁴ B.N. Feigelson, T.J. Anderson, M. Abraham, J.A. Freitas, J.K. Hite, C.R. Eddy, and F.J. Kub, “Multicycle Rapid Thermal Annealing Technique and its Application for the Electrical Activation of Mg Implanted in GaN,” *Journal of Crystal Growth* **350**, 21–26 (2012).

(a)





Nanoscience Technology

188 Measuring Protein Secretions from Individual Live Cells

190 A Micromechanical Analogue to Optical Lasers

Measuring Protein Secretions from Individual Live Cells

M.P. Raphael,¹ J.A. Christodoulides,¹ J.B. Delehanty,² J.P. Long,³ P.E. Pehrsson,³ and J.M. Byers¹

¹Materials Science and Technology Division

²Center for Bio/Molecular Science and Engineering

³Chemistry Division

Introduction: Wounded warriors recovering from blast injuries face wound healing challenges rarely encountered within the civilian population. The need to reconstruct an individual's muscle, skin, or bone on a massive scale has pushed the boundaries of our understanding of the biological signaling that underlies the healing process. Even the healing of a simple cut is an incredibly complex endeavor. The surrounding cells must reconstruct layers of skin, which contain numerous components such as pores and nerve endings, while simultaneously protecting against infection. While it is generally known that this reconstruction process is orchestrated by the cellular secretion of proteins as signaling molecules, very little is understood about how cells organize these secretions in space and time.

This gap in our understanding has its origins in the dominant technique for detecting cell secretions, which is based upon fluorescent labeling. The introduction of these labels necessarily halts or ends an experiment; therefore, the labels are introduced only after a cell has been secreting for hours or days. Using such techniques, any variations in cellular secretions that are on the order of minutes or seconds cannot be detected, leaving an incomplete picture of how cells regulate their secretions throughout the wound healing process. To address this roadblock, we have developed a label-free technique based upon nanoplasmonic imaging that enables the measurement of individual cell secretions with time resolutions below one second. Using this technique, we have captured real-time measurements of antibody secretions from individual hybridoma cells.

Nanoplasmonic Sensors: Arrays of gold nanostructures are fabricated on glass coverslips by electron-beam lithography using NRL's state-of-the-art facilities at the Institute for Nanoscience. The bases of the nanostructures are circular in cross section with diameters of 70 ± 5 nm and heights of 75 ± 2 nm (Fig. 1(a) inset). Each square array typically consists of 400 nanostructures with a spacing of 400 nm between nanostructures. The gold nanostructures are functionalized with a peptide sequence called c-myc, which has a particularly high binding affinity for the antibodies secreted by the hybridoma cells. Nanoplasmonic biosensing is founded upon the fact that the plasmonic resonance of the gold nanostructures exhibits both a red shift and

an increase in scattering intensity when the binding of proteins such as antibodies creates small perturbations in the local index of refraction (Fig. 1(b)).¹ When imaged on a CCD camera, these spectroscopic signatures are manifested as an increase in the brightness of the nanostructures and can be quantified in terms of the local concentration of secreted protein.²

The processed chips are loaded onto an inverted microscope that is enclosed within an environmental chamber designed for live cell studies (Fig. 1(a)). The cells are introduced microfluidically and settle about the arrays (Fig. 1(d)). In addition to monitoring the nanoplasmonic sensors for cell secretions, the design also incorporates a mode from transmitted light illumination for visualizing the cells (Fig. 2(a)) and a fluorescence mode for imaging intracellular fluorescent labels (Fig. 2(c)).

Single Cell Secretions: The real-time measurements on live cells enabled us to observe sudden bursts of antibody secretions as they diffused outwardly from the cell (Fig. 2(b)). The bursts were highly concentrated and corresponded with cell contractions that lasted only about a minute. The size and the slope of the signal were greatest at the array nearest the cell and decreased with increasing distance between cell and array, consistent with a pulsed wave of antibodies originating at the cell and diffusing outward. We also have observed a wide range of continuous secretion rates (Fig. 3(a)), raising the intriguing possibility of linking these secretion rates with the internal state of the cell. From the continuous secretion measurements, we determined the local concentration of antibodies at the sensing arrays closest to the cell (Fig. 3(b)) and from the bursts, we estimated the diffusion constant of the secreted antibodies through the media.

Looking Ahead: The technique presented here describes a methodology for quantitative single cell secretion measurements with unprecedented spatial and temporal resolution and is applicable to almost any cell type. This technique promises to be an enabling technology, providing new insights into how cells signal and coordinate with one another to heal wounds.

[Sponsored by the NRL Institute for Nanoscience]

References

- ¹ M.P. Raphael et al., "A New Methodology for Quantitative LSPR Biosensing and Imaging," *Anal. Chem.* **84**, 1367–1373 (2012).
- ² M.P. Raphael et al., "Quantitative LSPR Imaging for Biosensing with Single Nanostructure Resolution," *Biophys. J.* **104**, 30–36 (2013).

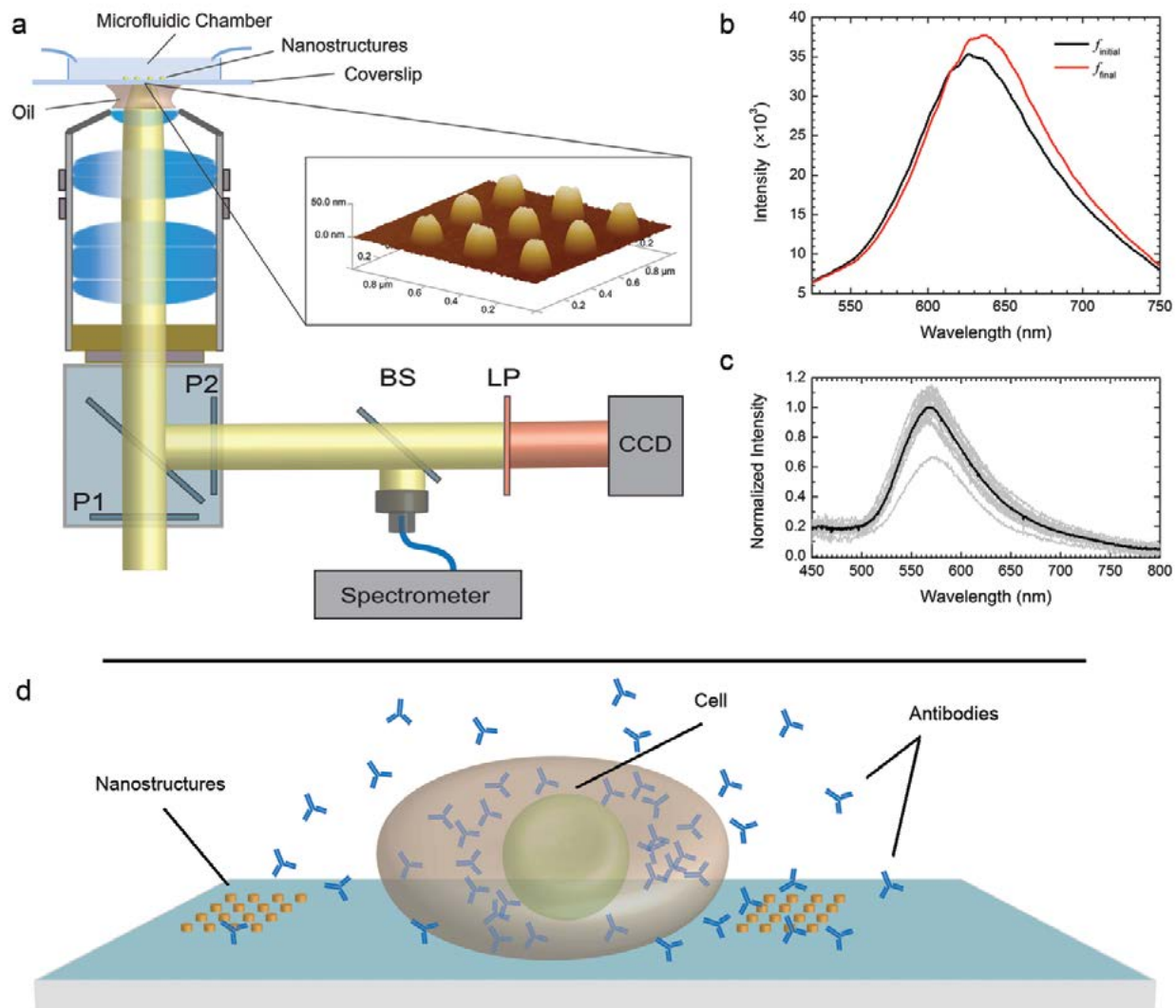


FIGURE 1

(a) Imaging and spectroscopy setup in which P1 and P2 are crossed polarizers, BS is a 50/50 beam splitter, and LP is a long pass filter. The inset shows an atomic force microscope (AFM) scan of a typical array. (b) Two spectra from a specific-binding study in which 200 nM of anti-c-myc was introduced over the c-myc functionalized array. The $f_{initial}$ spectrum (black) was taken before the anti-c-myc was introduced and the f_{final} spectrum (red) after one hour of exposure. (c) Normalized spectra from 18 individual nanostructures taken in air on a separate dark-field microspectroscopy setup. Individual spectra are superposed (gray curves) and compared to the ensemble average (black curve). (d) Illustration of an antibody-secreting cell in registry with nanoplasmonic arrays.

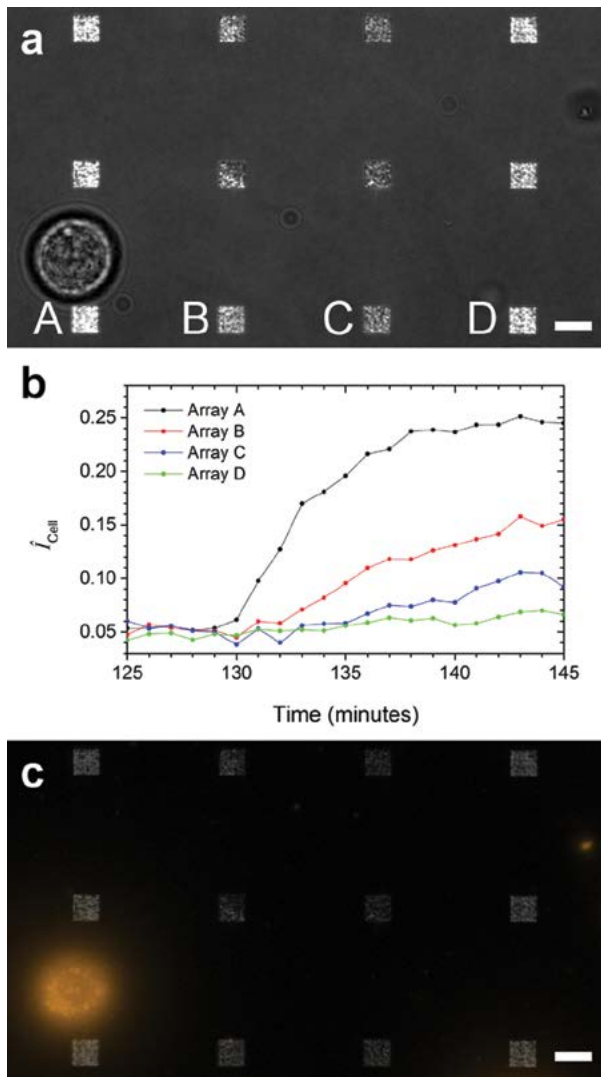


FIGURE 2
 Secretion burst from a single cell (a) Overlay of transmitted light and LSPR images highlights the location of the cell relative to 12 arrays. (b) Normalized LSPR image intensity of four arrays (A-D). The distances from the center of the cell to the center of each array were 15.4 μm , 39.2 μm , 72.2 μm , and 106 μm for Arrays A, B, C and D, respectively. (c) Overlay of LSPR and false-color fluorescence images exposing fluorescently labeled portions of the cell membrane. Scale bar: 10 μm .

A Micromechanical Analogue to Optical Lasers

M.W. Pruessner,¹ J.B. Khurgin,² T.H. Stievater,¹ and W.S. Rabinovich¹

¹Optical Sciences Division

²Johns Hopkins University

Introduction: The force exerted by light is small and generally insignificant. However, optical forces can

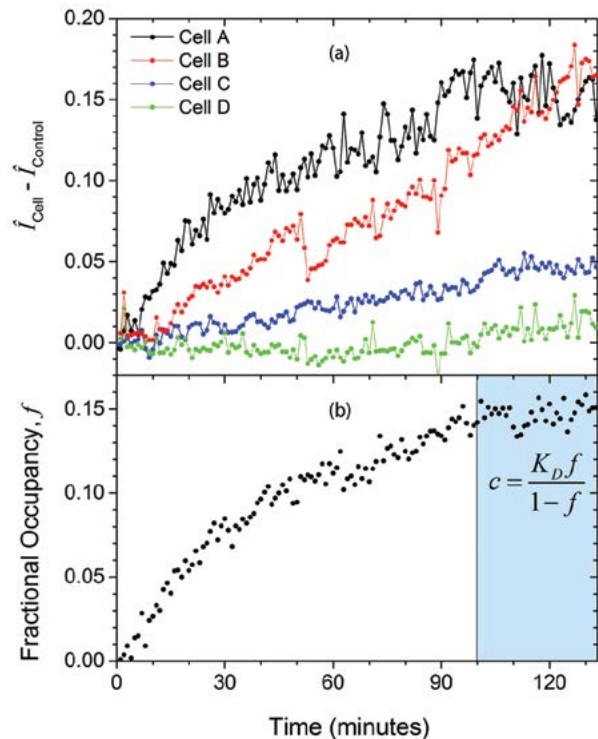


FIGURE 3
 (a) Comparison of the time-dependent secretions from four cells, all of which were within 15 μm of an array. The normalized LSPR image intensity of the array (\hat{I}_{cell}) minus the normalized intensity of a control array ($\hat{I}_{control}$) is plotted versus time. (b) The fractional occupancy, f , of the closest array to the cell as determined from the LSPR spectra which was collected simultaneously with the LSPR imagery. A concentration of $c = 312 \pm 53$ pM was calculated using the data in the highlighted region at which f was constant with time. K_D is the equilibrium dissociation constant.

have a profound influence on micro/nanomechanical devices. Cavity optomechanics¹ is an exciting multidisciplinary field that exploits these forces by enhancing light-matter interactions via feedback. Here, we report a new approach for exploiting optomechanical forces in a silicon chip-scale integrated device.² We measure a characteristic threshold beyond which the structure's mechanical resonance linewidth collapses and the oscillation amplitude increases sharply — in effect an optically driven mechanical oscillator that displays a striking resemblance to a mechanical “laser”.³ Our structure enables narrow mechanical linewidth micro-

oscillators for applications such as sensing and communications in tomorrow's Navy.

Chip-Scale Micro-Optomechanical Structure:

The device features a silicon waveguide optical microcavity coupled to a microbridge mechanical oscillator, as shown in Fig. 4.² Our unique approach allows independent control of the optical and mechanical parameters, enabling simplified device design. The silicon-based architecture implies the potential for dense chip-scale integration with the capability for mass fabrication in existing silicon foundries.

The optical cavity consists of two grating mirrors. One mirror is fixed while the other is attached to a suspended microbridge mechanical resonator (Fig. 4). As the microbridge oscillates, the mirror is displaced and tunes the optical cavity response (Fig. 4(b)). In other words, the mechanical structure acts on the opti-

Continuous-wave (CW) laser light is focused onto the device's input waveguide (P_{IN} in Fig. 4(b)) and the optomechanical response is measured at the output (P_{OUT}). The oscillator's motion tunes the cavity by changing its length, which in turn changes the optical wavelength at which the cavity is resonant. The optical power in this cavity depends on whether the input laser beam's wavelength is resonant or not, so that any mechanical displacement modulates P_{OUT} . Therefore, the time-varying component of P_{OUT} is a direct measure of the oscillator response.

We determine the mechanical oscillator spectrum for two different laser wavelengths, leaving all other measurement conditions the same. For one wavelength, the mechanical oscillation exhibits a narrow linewidth and large amplitude (red line in Fig. 5), while for another wavelength, the oscillation frequency is shifted and appears strongly damped with a broadened line-

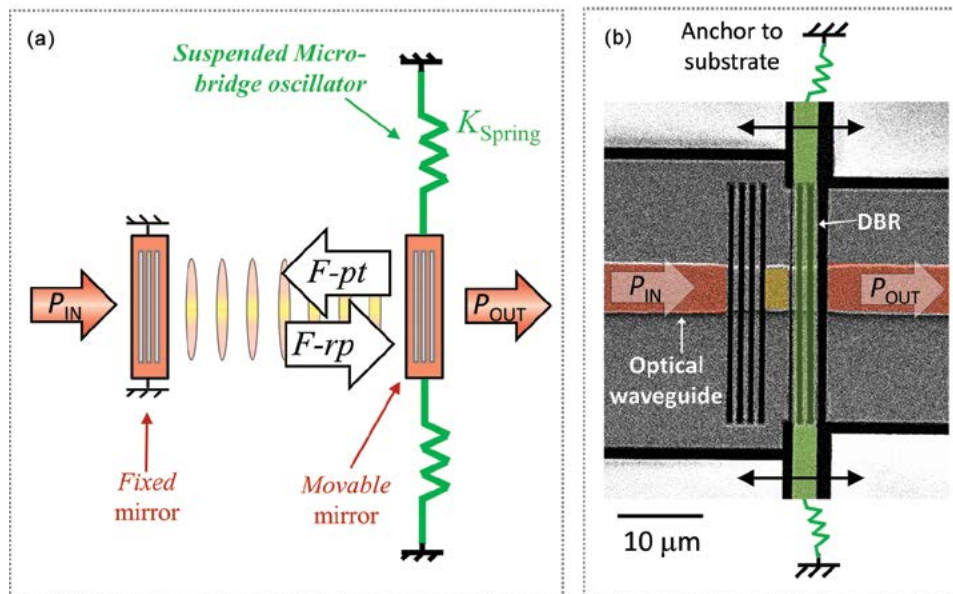


FIGURE 4 (a) Optomechanical device schematic showing an optical cavity consisting of two mirrors (red) and a mechanical oscillator (green). The photothermal ($F-pt$) and radiation pressure ($F-rp$) forces are indicated; (b) scanning electron microscope image of a device fabricated in the NRL Institute for Nanoscience clean room. (DBR = distributed Bragg reflector)

cal structure. Although less intuitive, the optical cavity also affects the mechanical response (“backaction”). Light in the cavity exerts a force on the microbridge, as indicated by $F-pt$ (photothermal force) and $F-rp$ (radiation pressure force) in Fig. 4(a). Therefore, the optical structure also acts on the mechanical structure. This mutual interaction implies a feedback mechanism that we exploit in our measurements.

Mechanical Analog to Optical Laser: The sample is placed in a vacuum cell to minimize air damping.

width (blue line). An analysis shows that the behavior can be explained by feedback optical forces that either amplify or dampen the oscillator's motion,² consistent with observations by other researchers.¹ In particular, we note that the optical forces in Fig. 4(a) act in opposing directions and with vastly different timescales.² The slow photothermal force (microsecond time constant) is responsible for the amplification/damping, while the fast radiation pressure force (picosecond) dominates the frequency tuning. The measurements in Fig. 5 show the profound influence of small optical forces

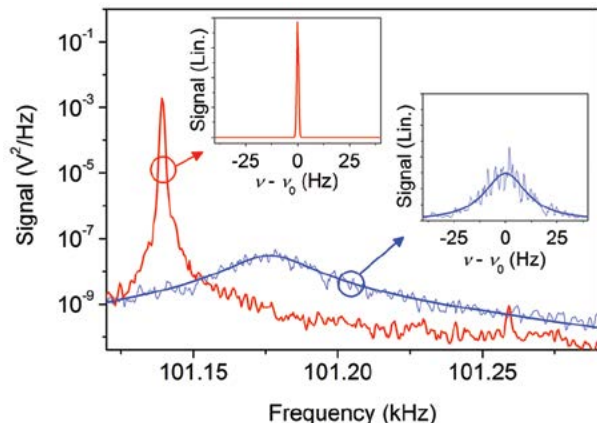


FIGURE 5 Mechanical resonant spectra measured at two different laser wavelengths.² Photothermal (*F-pt*, shown in red) and radiation pressure (*F-rp*, shown in blue) forces change the mechanical oscillators' linewidth, frequency, and vibration amplitude.

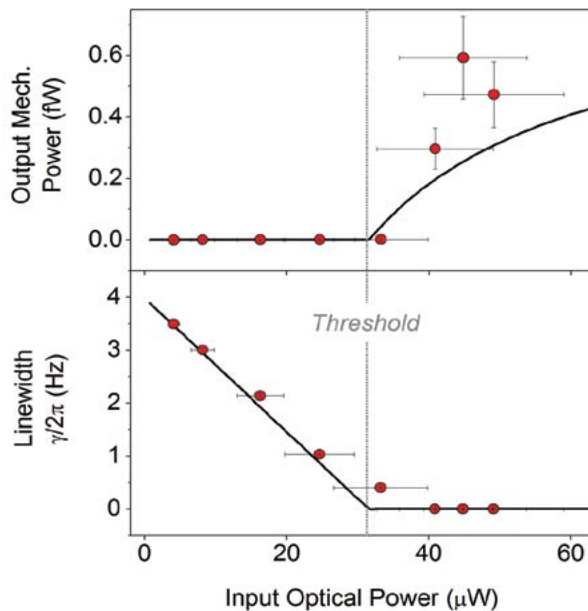


FIGURE 6 Output mechanical power (obtained from the oscillation amplitude) and corresponding linewidth, both measured as a function of input optical power (points: experiment; lines: theory).³

(pico-Newton-level) on micromechanical structures (nanogram-level mass).

Next, we focus on photothermal amplification forces (red line in Fig. 5) by leaving the wavelength and other parameters fixed. We measure the oscillator's vibration amplitude and linewidth as a function of laser power (P_{IN}). The measurements show a strong similarity to the response of an optical laser that is "pumped" with increasing power: (a) a linear decrease in the linewidth, (b) a threshold condition beyond which the linewidth "collapses" (essentially a zero linewidth), and (c) a strong linear increase in oscillation amplitude (mechanical power) beyond threshold (Fig. 6).

Given the similar response between our micromechanical "laser" and a standard optical laser, we develop an optomechanical rate equation theory in analogy to the laser rate equations.³ The theoretical device response shows good agreement with experiments in terms of the mechanical oscillator's output power and linewidth (Fig. 6). Although other groups¹ previously demonstrated a linewidth narrowing as in Fig. 5, our theory is the first to describe this self-oscillation in terms of rate equations with a direct comparison to experiments that clearly exhibit the key characteristics of a laser, namely a threshold condition and linewidth collapse.

Future Directions: Beyond fundamental research our device enables a variety of new sensor applications. First, our approach drives a mechanical resonator to self-oscillation using a single low-power CW laser. Second, the mechanical resonance is monitored using this same laser signal, which has now been modulated by the oscillator motion. Third, the linewidth collapse implies a strong increase in effective $Q_{\text{Mechanical}}$ giving enhanced sensitivity to external perturbations. For example, a chemical sensor may be realized by monitoring the absorption of analytes, which leads to changes in the oscillator mass and frequency. Other future Navy applications include inertial and magnetic field sensors.

Acknowledgments: The authors thank the NRL Institute for Nanoscience staff for clean room access and fabrication assistance. NRL Optical Sciences Division developed the device concept, performed all experiments, and carried out finite element modeling. Johns Hopkins University developed the optomechanical laser rate equation theory and performed calculations.

[Sponsored by the NRL Base Program (ONR) and by ASEE through a Summer Faculty Fellowship]

References

- ¹ T.J. Kippenberg and K.J. Vahala, "Cavity Opto-Mechanics," *Opt. Express* **15**(25), 17172–17205 (2007).
- ² M.W. Pruessner, T.H. Stievater, J.B. Khurgin, and W.S. Rabinovich, "Integrated Waveguide-DBR Microcavity Opto-Mechanical System," *Opt. Express* **19**(22), 21904–21918 (2011).
- ³ J.B. Khurgin, M.W. Pruessner, T.H. Stievater, and W.S. Rabinovich, "Laser-Rate-Equation Description of Opto-Mechanical Oscillators," *Phys. Rev. Lett.* **108**, 223904 (2012).

196

A Target Depth Classification Method for Autonomous Passive Acoustic Surveillance Systems in Littorals

199

Maximizing Effectiveness of Autonomous Underwater Vehicles

201

WAVEWATCH III® Transition to Naval Operations

194

Turbulence Production by Nonbreaking Waves

Turbulence Production by Nonbreaking Waves

I. Savelyev,¹ E. Maxeiner,² and D. Chalikov^{3,4}

¹*Remote Sensing Division*

²*National Research Council Postdoctoral Associate*

³*Swinburne University of Technology, Melbourne, Australia*

⁴*P.P. Shirshov Institute of Oceanology, St. Petersburg, Russia*

Introduction: Historically, the parameterization of turbulence production in the upper ocean has relied primarily on the assumptions of near-wall turbulence theory, in which the wind-generated surface friction velocity acts as a moving boundary. In more complete parameterizations, an additional term is added in the top few meters to account for the dissipation of breaking surface waves. These two mechanisms are responsible for the bulk of the produced turbulence. However, there exists a distinct third mechanism, first described by Phillips,¹ in which turbulence is produced due to turbulence interaction with nonbreaking waves. For decades, the contribution of this mechanism was considered relatively small and was therefore largely neglected in practical applications. However, recent studies suggest otherwise. For example, Ardhuin and Jenkins² demonstrated that long swell waves propagating across the Pacific Ocean dissipate a significant portion of their energy due to wave–turbulence interaction. These findings motivated the present work, in which a series of laboratory and numerical investigations were conducted to explore this phenomenon. Quantitative results of this study provide a validation source and enable improvements of wave dissipation parameterization, which is needed for accurate marine weather and wave forecasting.

Laboratory Experiments: Experiments were conducted in the Free Surface Hydrodynamics Laboratory wave tank (see Fig. 1) at the Naval Research Laboratory in Washington, DC. Starting with quiescent water conditions, nonbreaking waves of small to moderate steepness were generated via sinusoidal motions of the wave paddle. The test area was located ~3.6 m away from the wave maker; test time started upon arrival of first waves and ended before reflected waves from the back wall arrived in the test area.

A priori, near-surface turbulent velocity fluctuations in question were expected to be much smaller than wave orbital velocities, thus falling below detection limits of conventional flow velocimetry techniques. For this reason, a specialized thermal-marking velocimetry (TMV) technique was developed within this study. TMV works by using actively heated points on the water

surface as tracers to visualize and quantify the surface flow. Unlike other floating tracers, thermal markers have the advantage of being minimally invasive to the flow, as well as easily identifiable, renewable, and configurable. Thermal markers were created using a 10-watt CO₂ laser (SYNRAD 48-1) with ~10.6 μm wavelength, which cannot propagate through water and therefore is dissipated into heat at the surface. A motorized mirror, capable of changing its orientation over 1000 times per second, laid down a desired pattern of thermal markers by controlling the direction of the laser beam. A midwave infrared camera (FLIR SC6000) was used to observe water surface temperature and trace movements of thermal markers. An example of an infrared image is shown in Fig. 2, in which vertical dotted lines (initially straight) represent thermal markers, gradually displaced and deformed by the flow. An image-processing algorithm based on a weighted centroid principle was used to analyze pairs of such images and determine marker velocities with a very high accuracy of ±0.8 mm/s, sufficient to detect desired turbulent motion.

Numerical Model: The calculations were made with a large eddy simulation (LES) model of 3D non-potential (vortical) motion to represent the turbulence, coupled with a fully nonlinear 2D model of surface waves. Initial conditions were assigned as a train of four harmonic waves using small amplitude theory. Initial turbulence was introduced as a field of random velocities satisfying the continuity equation. Total initial turbulent energy was set equal to 0.001 of the total wave energy. Since the energy of vortical motion is much smaller than the energy of the waves, the back transfer of energy to waves and attenuation of waves due to dissipation were neglected. Using the periodic boundary condition, waves were allowed to propagate for the duration of up to 10 wave periods.

Results: In both numerical and laboratory simulations, the turbulent kinetic energy (TKE) was found to grow in time, due to the wave–turbulence interaction. The growth of horizontal components of TKE, i.e., u_x^2 and u_y^2 , observed in the wave tank is shown in Fig. 3. Interestingly, the cross-tank y velocity component was found to be more energetic than the x component. A numerical result of TKE dependence on wave phase is shown in Fig. 4. This result demonstrates that the turbulence is most energetic near wave crests, but quickly decays toward troughs. It also confirms y component dominance over x . The reason for this anisotropic behavior can be related to dark and bright bands seen in Fig. 2. These bands correspond to cool skin temperature fluctuations known to be disrupted by near-surface vortex pairs elongated in the streamwise direction.

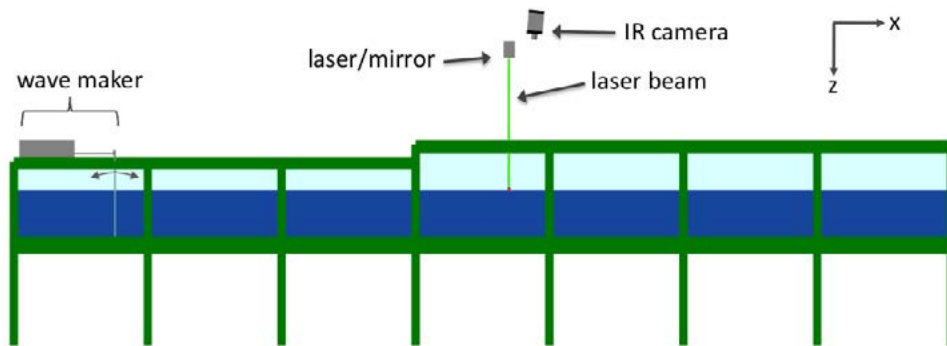


FIGURE 1
Schematic illustration of wave tank and experimental setup. Tank dimensions are 8.5 m long by 2.3 m wide with 0.75 to 0.9 m high transparent sidewalls. The test area is located 3.6 m from the wave maker and 4.0 m from the back wall.

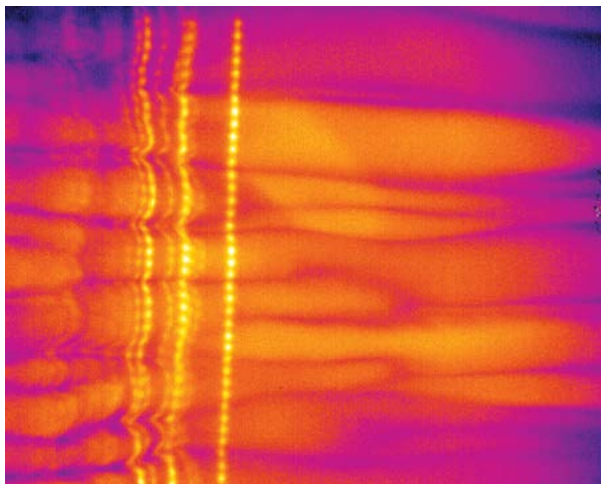


FIGURE 2
An example of a raw 25 × 31 cm infrared image of the water surface with observed thermal streaks. Waves are propagating from right to left. Image brightness represents water temperature, ranging within ~1 °C. Vertical bright dotted lines are thermal markers, and horizontal streaks correspond to elongated near-surface eddies. The oldest thermal markers are located on the left and the most recent ones are on the right.

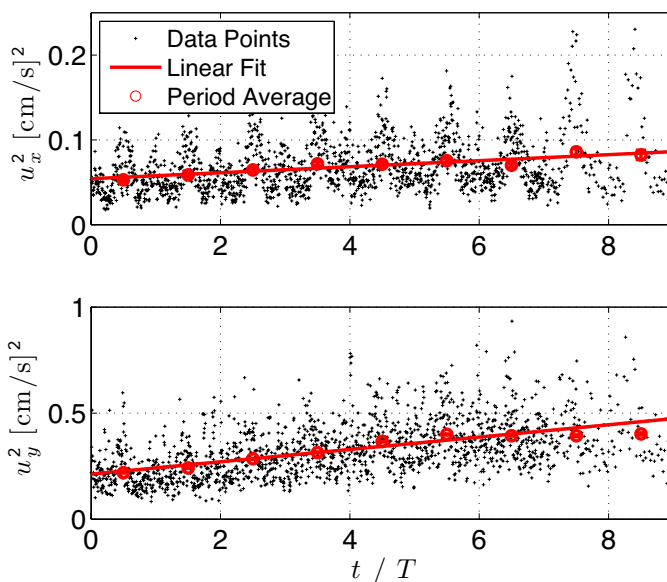


FIGURE 3
Turbulent components of the surface velocities u_x^2 and u_y^2 are shown as functions of time normalized by wave period t/T for the entire data set. Each point is a bin average over 50 realizations, the solid line is a linear fit through all realizations, and circles are averages over each wave period.

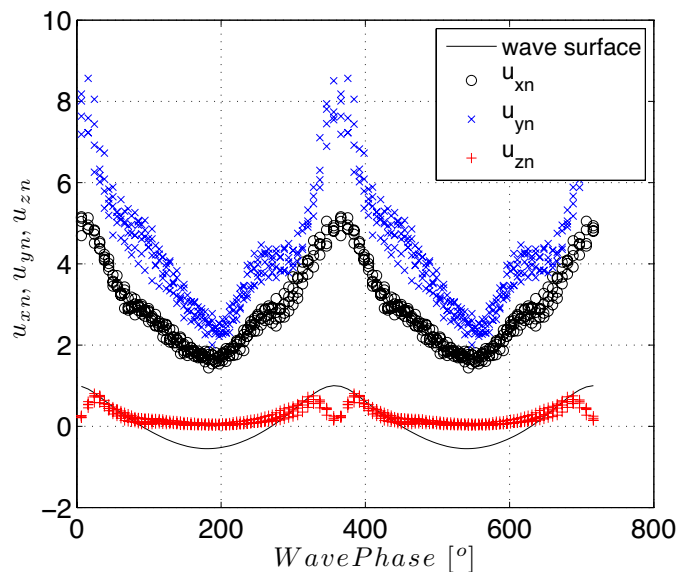


FIGURE 4
Numerical simulation of normalized turbulent velocities, shown as functions of wave phase. Solid line corresponds to the normalized wave-shape, with wave steepness at $ak = 0.167$.

Such circulation patterns are expected to favor velocities in y direction over x . More details on this study can be found in Savelyev et al.³

Acknowledgments: Numerical simulations were contributed by Dmitry Chalikov.

[Sponsored by the NRL Base Program (CNR funded)]

References

- ¹ O. Phillips, "A Note on the Turbulence Generated by Gravity Waves," *J. Geophys. Res.* **66**(9), 2889–2893 (1961).
- ² F. Ardhuin and A. Jenkins, "On the Interaction of Surface Waves and Upper Ocean Turbulence," *J. Phys. Oceanogr.* **36**, 551–557 (2006).
- ³ I.B. Savelyev, E. Maxeiner, and D. Chalikov, "Turbulence Production by Nonbreaking Waves: Laboratory and Numerical Simulations," *J. Geophys. Res.* **117**, C00J13 (2012).



A Target Depth Classification Method for Autonomous Passive Acoustic Surveillance Systems in Littorals

A. Turgut and L.T. Fialkowski
Acoustics Division

Introduction: A robust depth-discrimination method is being developed for passive target classification that provides an autonomous, pervasive, and persistent surveillance capability to the Navy. The new method, appropriate for littoral environments, is based on waveguide invariant theory that requires minimal environmental information and determines if a distant sound source is near the surface or submerged. A two-class discrimination problem is solved using measured acoustic intensity interference patterns; the method

is suitable for existing passive surveillance systems such as horizontal hydrophone arrays or distributed networks of acoustic sensors. The method was successfully validated in a Littoral Depth Discrimination Experiment (LIDDEX12), where shallow and deep sound sources were towed simultaneously and Expendable Mobile ASW Training Targets (EMATTs) were used. Potential applications of the new method are the identification of submarine surges from ports and force protection in ports and harbors.

Autonomous Passive Acoustic Surveillance: Current approaches for depth discrimination in littorals are based on extensions of matched-field processing to more robust methods, such as acoustic mode scintillation¹ and acoustic mode filtering.² These methods rely on environmental inputs and vertical receiver arrays, neither of which are practical nor considered for surveillance systems. Littoral environments are spatially, temporally, and seasonally dynamic; surveillance applications require robustness to these variations in order to achieve a sufficient level of autonomy. The NRL Acoustics Division is developing and validating different waveguide-invariant-based methods that are suitable for littoral environments. These methods show great potential for passively depth-discriminating quiet submerged targets over wide littoral areas. Field experiments will be used to validate the methods for extreme littoral environmental conditions: summer and winter. This article describes experimental validation of one method and discusses its potential use for autonomous passive acoustic surveillance systems.^{3,4}

LIDDEX12 Summer Experiment: The objective of the LIDDEX12 experiment was to validate waveguide-invariant-based depth-discrimination algorithms for

passive sonar in shallow water in a summer environment. The experiment took place August 24 through 31, 2012, on the New Jersey Shelf, where available broadband noise from surface ships of opportunity and controlled acoustic sources were recorded on several experimentally deployed receiver arrays (Fig. 5): a bottom-moored 64-element L-shape (horizontal and vertical) receiver array, four Environmental Acoustic Receiver Systems (EARS), and several sonobuoys. To validate target depth classification algorithms, coherent acoustic data (300 to 1200 Hz) from shallow- and deep-towed sources, as well as acoustic data from quiet EMATTs, were used. Additionally, oceanographic data were collected using Conductivity, Temperature, and Depth (CTD) casts, thermistor arrays, and towed CTDs. The high-quality acoustic measurements, along with the time-coincident oceanographic measurements, will be used to demonstrate the robustness of waveguide-invariant-based passive target classification in complex shallow-water environments.

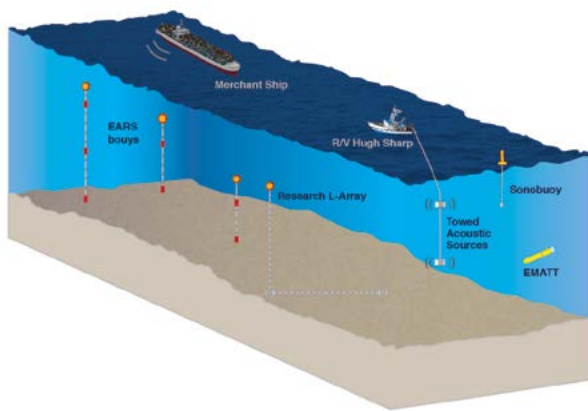


FIGURE 5
LIDDEX12 used a bottom-moored combined horizontal and vertical array, bottom-moored vertical arrays, as well as sonobuoys to record acoustic transmissions from two low-level controlled sources at variable depths, EMATTs, and surface ships-of-opportunity.

The ocean thermocline is a transition layer between the warmer surface water (mixed layer) and the cooler deeper water, and is present in littorals from early spring to late fall. The presence of the ocean thermocline provides an opportunity for passive depth classification through the waveguide parameter, β . Figures 6(a) and 6(b) show measured broadband striations from the controlled sources that were towed at a deep depth (below the thermocline) and at a shallow depth (above the thermocline). The slope of the striations is different for each of these sources, and is related to the depth diversity of the waveguide invariant. For comparison, Fig. 6(c) shows measured broadband striations from the tow ship, the R/V *Sharp*. Note

that the slope of the striations from the R/V *Sharp* is similar to the slope of the striations from the shallow source. The broadband striation patterns of each source are analyzed to provide an estimate of the waveguide invariant parameter, β , through the application of a Hough transform. The result is a waveguide parameter distribution function, shown in Fig. 6(d). The estimate of the waveguide invariant distribution for the shallow source is the red curve, while the estimate for the deep source is the black curve. One example classification implementation of these waveguide distribution estimates is the use of a receiver operating characteristic (ROC) curve, as seen in Fig. 6(e). In this case, the ROC curve is a parametric plot of correct classification probability (P_{cc}) versus false classification probability (P_{fc}), and is generated from the probability density estimates in Fig. 6(d). The classifier ROC curve is obtained as a cumulative distribution by varying the threshold over the expected range of possible β values. An ROC curve that follows the left then top border of the ROC space is indicative of an accurate metric, while an ROC curve that is close to a 45° diagonal is considered an inaccurate metric. The ROC curve in Fig. 6(e) shows that the waveguide invariant distribution is an appropriate method for accurate depth classification in the littoral environment tested. Further validation studies are being performed using broadband noise data measured during LIDDEX12, and verified to originate from merchant ships identified by Automatic Identification System (AIS) contacts. Figure 7(a) shows broadband striations originating from a merchant ship, measured on a bottom-moored hydrophone. Figure 7(b) shows the corresponding waveguide parameter distribution function, calculated by the application of a Hough transform and incorporation of the ship navigation data from AIS. The resulting waveguide parameter distribution for this distant ship is consistent with that of the shallow source in Fig. 6(d) (red line).

Summary: Waveguide-invariant-based methods are being developed at NRL that use a minimal amount of environmental information that is readily available from archival data: the water depth and the depth of the ocean thermocline. One waveguide invariant depth classification method has been validated with a single sensor placed below the ocean thermocline. Analysis of horizontal array data is under way to validate this method for depth classification of ultraquiet targets that cannot be achieved with a single phone. The newly developed methods will be further validated using acoustic data from existing surveillance systems.

[Sponsored by the NRL Base Program (CNR funded)]

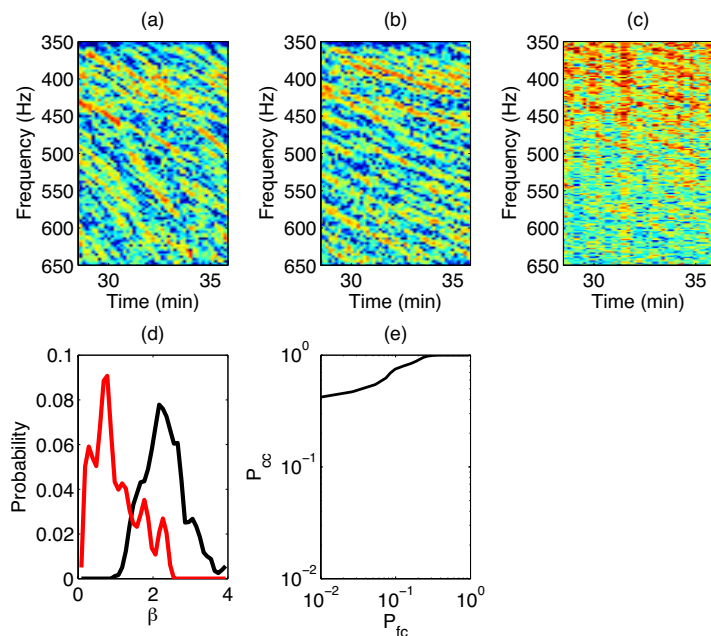


FIGURE 6
 Top row: measured broadband striations from (a) deep source, towed below the thermocline, (b) shallow source, towed above the thermocline, and (c) R/V *Sharp*, the tow ship (also above the thermocline). Bottom row: (d) waveguide parameter distributions for a shallow source (red) and deep source (black), and (e) the ROC curve based on the two distributions.

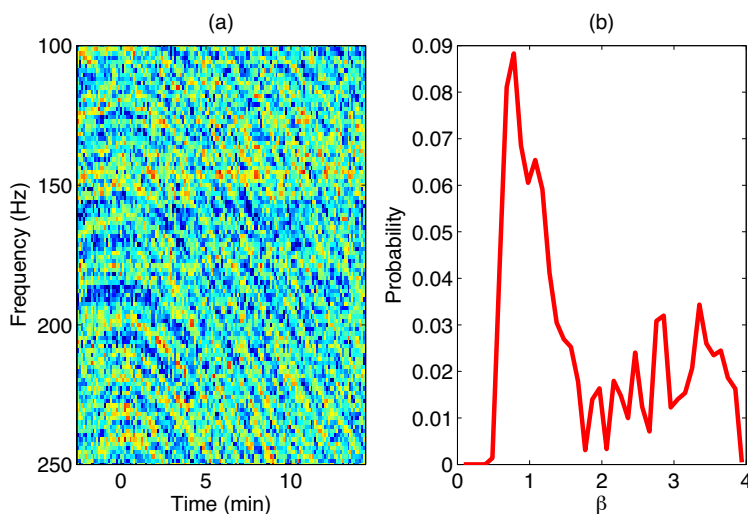


FIGURE 7
 (a) Measured broadband striations from a merchant ship and (b) corresponding waveguide parameter distribution function.

References

- ¹ V.E. Premus, "Modal Scintillation Index: A Physics Based Statistic for Acoustic Source Discrimination," *J. Acoust. Soc. Am.* **105**(4), 2170–2180 (1999).
² V.E. Premus, J. Ward, and C.D. Richmond, "Mode Filtering Approaches to Acoustic Source Depth Discrimination," Conference Record of the Thirty-Eighth Asilomar Conference on Signals, Systems and Computers, Nov. 7–10, 2004, Vol. 2, pp. 1415–1420 (IEEE, 2004).

- ³ A. Turgut and L.T. Fialkowski, "Depth Discrimination Using Waveguide Invariance," *J. Acoust. Soc. Am.* **132**(3), Pt. 2, 2054 (2012).
⁴ A. Turgut and L.T. Fialkowski, "Method and Apparatus for Depth Classification in Shallow Water," Naval Research Laboratory Patent Disclosure, 2012.



Maximizing Effectiveness of Autonomous Underwater Vehicles

L.F. Smedstad,¹ C.N. Barron,¹ K.D. Heaney,²

G. Peggion,³ and E.M. Coelho³

¹*Oceanography Division*

²*Ocean Acoustical Services and Instrumentation Systems, Inc. (OASIS)*

³*University of New Orleans*

Introduction: Ocean gliders and other unmanned underwater vehicles play an increasingly important role for the U.S. Navy as a source of targeted environmental measurements. Glider pilots adjust navigation instructions for each platform in response to changing array distribution and local ocean conditions. Automated guidance for glider missions enables more effective use of growing numbers of ocean gliders without overtaxing limited human resources. NRL-developed systems to optimize glider placement and sampling direction initiated under the Office of Naval Research (ONR) Glider Observation Strategies (GOST) project have been transitioned to the Naval Oceanographic Office (NAVOCEANO). GOST is an autonomous system that develops preferred deployment and navigation plans for glider networks. GOST uses a genetic algorithm (GA)¹ that sorts through potential waypoints to identify glider paths that achieve optimal coverage. Under this approach, the relative merits of alternate pathsets are calculated using mission-appropriate cost functions that combine geographic coverage, forecast uncertainty, and environmental variability. Feedback from GOST-directed gliders into ocean models demonstrated improved ocean forecast skill in two NATO exercises, REP10 and Proud Manta 11. NAVOCEANO will conduct operational tests of the GOST system during the Navy's Trident Warrior 13 exercise.

Application of a Genetic Algorithm to Oceanography: GOST begins with the fundamental postulate that some sets of glider trajectories will be more useful than others. Once the relative merit of a potential set of observations can be quantified, a search algorithm can be implemented to isolate a preferred set. GOST communicates these preferences using cost functions that assign a value based on the time, location, and collective coverage of the glider array. Integrating the vector sum of the velocity and ocean currents reveals the series of observations that could be obtained by a glider. Included in GOST is the Environmental Measurements Path Planner (EMPath) software that contains the GA. Promoting a "survival of the fittest" approach, a randomized set of individuals and a specified number of reproductions (mating of successful individuals) creates generations of a solution. Each individual represents

a different time/space transect pattern for multiple gliders, or sensor laydown, and the natural selection process deems which is best adapted for the mission criteria. EMPath outputs include a morphology figure to provide the user a visual level of confidence in the paths. The morphology computation is an estimate of the shape of the cost function that the genetic algorithm is using to optimize sensor locations. The preferred set of trajectories is communicable to the glider pilots as a set of waypoints and tolerances.

Benefit to Ocean Models and Tactical Decision Aids: The effectiveness of GOST guidance has been demonstrated in virtual and live glider exercises in which glider measurements are assimilated as vertical profile data to influence ocean forecasts. Coverage missions include time scales from days to weeks. A set of idealized Observation System Simulation Experiments (OSSEs) form the basis for the GOST 1.0 validation testing.² Acoustic products such as sonic layer depth (SLD) created from Relocatable Circulation Prediction System Navy Coastal Ocean Model (RELO NCOM) outputs are analyzed with and without glider assimilation. An assimilative RELO NCOM run designated as the true ocean state has relatively shallow SLD (Fig. 8(a)), while a nonassimilative version with overly deep SLD is the forecast that badly needs correcting (Fig. 8(b)). Using cost functions based on RELO NCOM forecast fields, GOST determines preferred trajectories for six simulated gliders that sample the true ocean. Assimilation of the glider profiles produces the beginnings of a clear correction (Fig. 8(c)) in the target area SLD forecast.

GOST-determined sampling in two NATO exercises has demonstrated the impact of glider observations on target-area forecasts. In the Marine Rapid Environmental Assessment (REP10) exercise off La Spezia, Italy, in August, 2010, the effectiveness of a single GOST-directed glider, known as Laura, relative to an alternative fixed survey with other sensors³ reduced the maximum and mean root mean square (rms) errors relative to independent observation and more accurately located a cyclonic eddy on the western edge of the target area (Fig. 9). A similar exercise off the east coast of Sicily (Proud Manta 11) showed the effectiveness of GOST guidance for a pair of gliders. The glider sampling identified a previously undetected cold-core ring that significantly modified sound speed and acoustic transmission across the target area (Fig. 10).

Future Work: Additional work has begun on expanding the usefulness of a system of gliders with the Navy goals of tactical operations, sustained coverage, and feature definition in mind. All three of these have been present in some capacity on the NATO exercises. However, more automation and management of glider

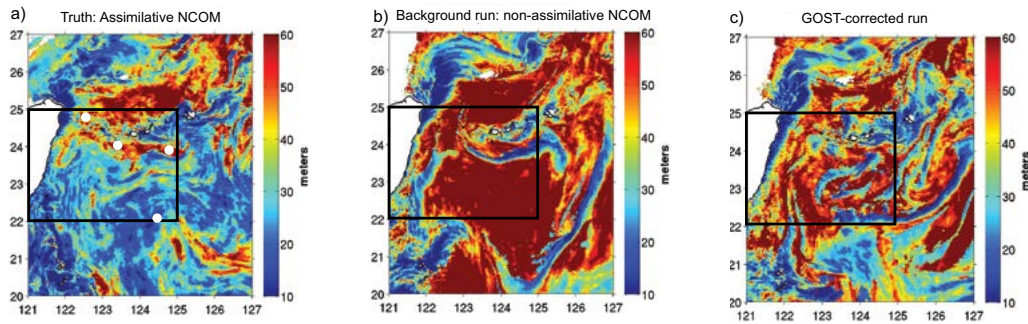


FIGURE 8

Sonic layer depth (SLD) has large differences between the case (a) assimilative run taken to represent the true ocean and the case (b) nonassimilative background run. GOST simulates glider observations (a; white circles) of the true ocean. When these are assimilated, the GOST-corrected forecast case (c) moves from deep background SLD (red) to the shallower SLDs (blue) found in the truth ocean, enabling more accurate predictions of upper-ocean acoustic transmission in the target area box.

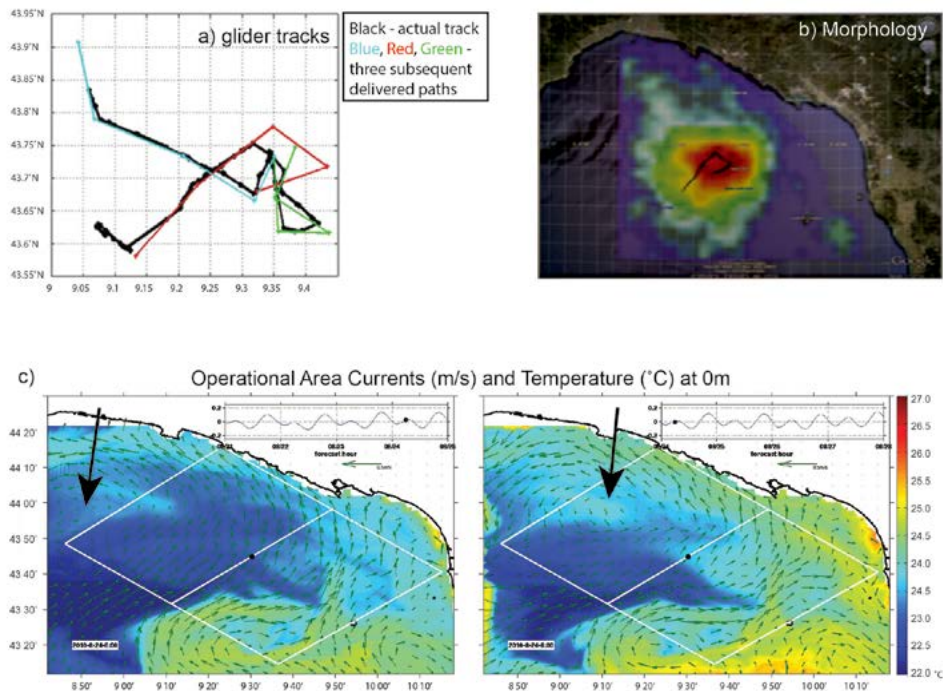


FIGURE 9

The feedback between gliders and models is shown from REP10 results. (a) Forecast target waypoints for glider Laura were delivered every 48 hours. The actual trajectory of Laura over the week is shown in black. The gliders were able to follow suggested paths (b) based on the cost function morphology as projected in Google™ Earth. (c) Assimilating glider data improved the forecast location of an eddy (arrows) in the model between a 78-hour forecast and a 6-hour forecast.

data is required. Additional testing of newer capabilities with EMPATH can be conducted, such as roping off areas to protect gliders from entering naturally or politically hostile areas by geographic exclusion zones or other water space limitations. New options are in development to extend forecast horizons and facilitate glider rendezvous to reduce recovery time and cost at mission end. Optimized use of the expanding glider fleet is only possible with such systems to simplify control and management of these resources.

Acknowledgments: The authors wish to thank Peter Spence and David Sitton of Qinetiq North America for support in development of model inputs for EMPATH testing, Jan Dastugue of NRL for graphics support, Robert Helber of NRL for acoustical analysis routines, Clark Rowley of NRL for RELO NCOM development, and Richard Campbell of OASIS for EMPATH support.

[Sponsored by ONR]

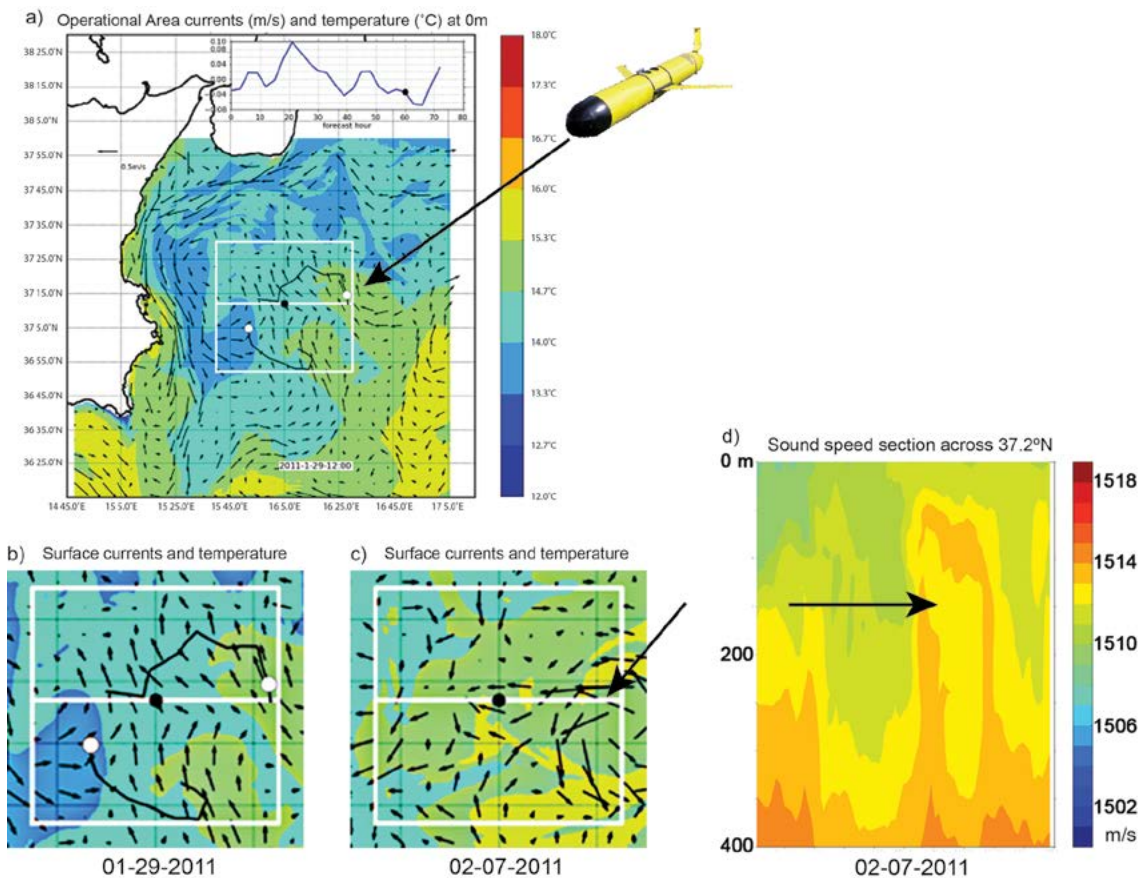


FIGURE 10
 Example of feature definition mission: Surface currents and temperature before (a,b) and after (c,d) assimilation of observations from GOST-directed gliders during the NATO exercise Proud Manta in 2011 off the east cost of Sicily. The gliders identified a cold-core ring (arrows) that significantly modifies currents (c) and sound speed (d) in the operational area.

References

- ¹ K.D. Heaney, G. Gawarkiewicz, T.F. Duda, and P.F.J. Lermusiaux, "Nonlinear Optimization of Autonomous Undersea Vehicle Sampling Strategies for Oceanographic Data-Assimilation," *Journal of Field Robotics* **24**, 437–448 (2007).
- ² L.F. Smedstad, K.D. Heaney, G. Peggion, C.N. Barron, and E. Coelho, "Validation Test Report for a Genetic Algorithm in the Glider Observation Strategies (GOST 1.0) Project: Sensitivity Studies," NRL/MR/7320--12-9361, Naval Research Laboratory, Stennis Space Center, MS, 2012.
- ³ A. Alvarez and B. Mourre, "Oceanographic Field Estimates from Remote Sensing and Glider Fleets," *J. Atmos. Oceanic Technol.* **29**, 1657–1662 (2012).



WAVEWATCH III® Transition to Naval Operations

J.D. Dykes and W.E. Rogers
Oceanography Division

Supporting the Mission: Knowledge of the sea state and thus predictions of wave conditions in real

time are important for naval operations. Two operational centers provide such support. Fleet Numerical Meteorology and Oceanography Center (FNMOC) in Monterey, California, produces and delivers wave forecasts covering large spatial scales and long time scales — for example, global 120-hour forecast fields of significant wave height — to support general operations. The Naval Oceanographic Office (NAVOCEANO) at Stennis Space Center, Mississippi, provides small-scale wave forecasts covering shorter intervals to support specific missions involving littoral waters and surf zones.

The Naval Research Laboratory (NRL) at Stennis Space Center has been the primary transition partner with NAVOCEANO and FNMOC for enabling technologies in wave forecasting for small and large scales. Now, in cooperation with the National Centers for Environmental Prediction (NOAA/NCEP), the latest version (v. 4.10) of the WAVEWATCH III® (WW3) wave model is being transitioned to NAVOCEANO and FNMOC, with additional updates coming later in 2013.

As part of this transition, NRL has developed and tested a system that uses the multi-grid implementation of WAVEWATCH III® at NAVOCEANO as an improvement to the current systems in place; NAVOCEANO runs a set of large-scale domains around the world to provide wave energy boundary conditions to smaller scale regional wave models. In addition, NRL is providing upgrades to the system to include curvilinear gridded domains, e.g., to cover the Arctic Ocean.

Multi-grid Model: WAVEWATCH III®^{1,2} is a third-generation wave model developed at NOAA/NCEP that incorporates sophisticated features not available in predecessors, such as modular Fortran90 and highly scalable parallel programming, dynamic time-stepping, third-order propagation schemes, irregular grids, triangular grids, and two-way communication between domains. The model solves the random phase spectral action density balance equation for wavenumber-direction spectra. Being a phase-averaged model, there is an implied assumption that properties of the forcing, as well as the wave field itself, differ on space and time scales that are much larger than individual waves.

During the past five years, WW3 has evolved such that it can now be regarded as a community model, though primary responsibility and authority for the code is still with NOAA/NCEP, and is freely available as Version 3. The development code currently designated as Version 4 is being used to update systems operational in the U.S. Navy. For wind input, wave breaking, and swell dissipation source functions, the physics package of Ardhuin et al.³ will be used.

The multi-grid (or mosaic grid) feature of WW3 allows for the two-way communication of energy across domain boundaries. Traditionally, as it is with older versions of WW3, a low-resolution host model passes wave energy through the boundary to high-resolution nest domains and whatever happens within the nest domains does not affect the host. With two-way communication, the predictions from the high-resolution model — potentially using better winds and better bathymetry — are shared with what could be considered the host domain and other high-resolution domains. Figure 11 illustrates this.

The current real-time configuration includes a global domain with 0.5° resolution and nine regional domains with resolutions of either 0.1° or 0.2°. Figure 12 illustrates the layout of all the domains. Winds forcing the global domain come from the Navy Global Environmental Model (NAVGEM) and the winds for the regional domains come from the Coupled Ocean/Atmosphere Mesoscale Prediction System (COAMPS™), both running at FNMOC. This modeling system now runs on an IBM iDataPlex Linux system at the Navy DoD Supercomputing Resource Center, where fore-

cast grids of significant wave height, wave direction, and wave period are produced automatically every 12 hours.

In addition, in a recent version developed at NRL, it is now possible that domains with dissimilar grid types (e.g., curvilinear grids and regular grids) can be run together, passing wave energy across the boundaries in both directions, as illustrated in Fig. 13. This removes the problem of running a regular latitude-longitude mesh too far north, decreasing the need to run a very small time step to accommodate for the convergence of the meridians. An Arctic curvilinear mesh can be incorporated into the operational system just like any of the other domains.

Implications and Conclusion: One advantage to running the multi-grid version of WW3 is that domain configuration is more efficient than in conventional methods, using computational resources more where needed, i.e., minimizing the redundancy. Any given geographic location is modeled by only one grid point except where there is overlap within buffer zones around boundaries. Compared to a conventional setup, the current configuration turnaround time has improved by about a factor of 3.

Since the multi-grid system runs multiple domains together instead of the traditional approach of running individual domains separately and sequentially, the model setup is less tedious, obviating the need to specify individual points in the host domain about the nest to which information is to be shared.

Comparisons of WW3 wave height output were made with in situ observations and altimeter measurements. Statistics from a number of buoy wave measurements provided by the NOAA Data Buoy Center (NDBC) and plotted in terms of mean bias, standard deviation, correlation coefficient, slope, and scatter index showed good results.

With the transition of the WW3 multi-grid system, wave modeling will be more streamlined, saving processing time, and forecast accuracy is expected to improve.

Acknowledgments: The authors thank Paul Wittmann for his advice during the WW3 transition. Funding provided by the Office of Naval Research through the National Oceanographic Partnership Program for continued development of WW3 is appreciated.

[Sponsored by ONR]

References

- ¹H.L. Tolman, B. Balasubramanian, L.D. Burroughs, D.V. Chalikov, Y.Y. Chao, H.S. Chen, and V.M. Gerald, "Development and Implementation of Wind-Generated Ocean Surface Wave Models at NCEP" *Weather and Forecasting (NCEP Notes)* 17, 311–333 (2002).

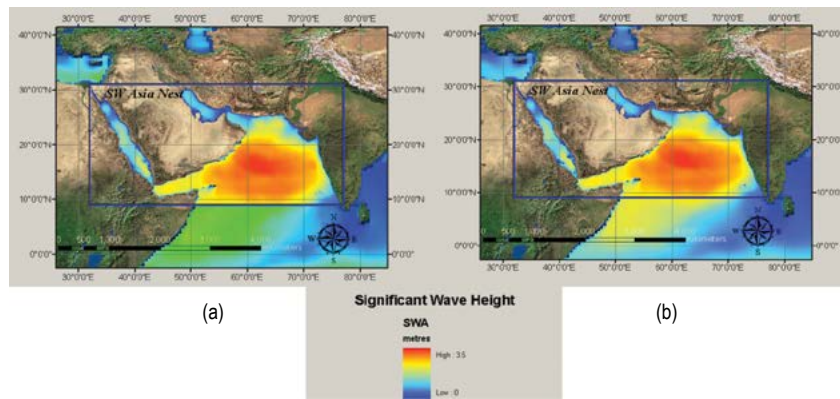


FIGURE 11
 Example of a domain where in (a) one-way nesting occurs, while in (b) two-way nesting is implemented in the multi-grid model.

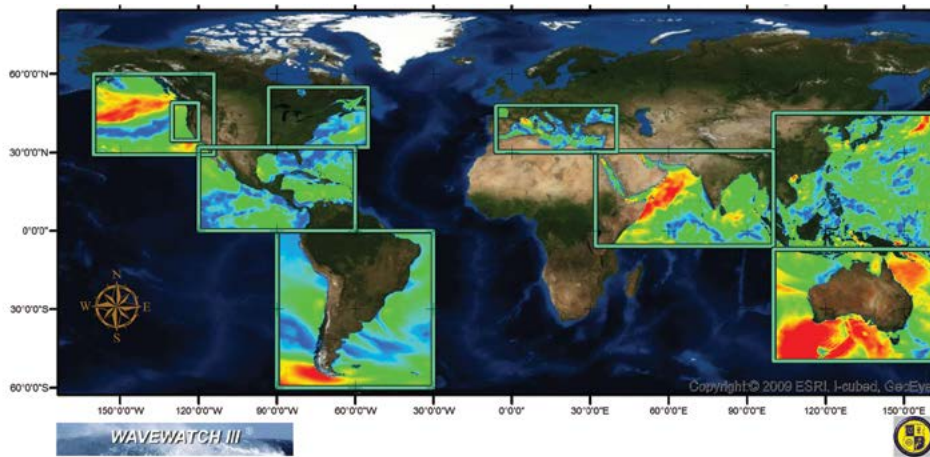


FIGURE 12
 Global and regional domains used primarily for providing boundary conditions for smaller scale models.

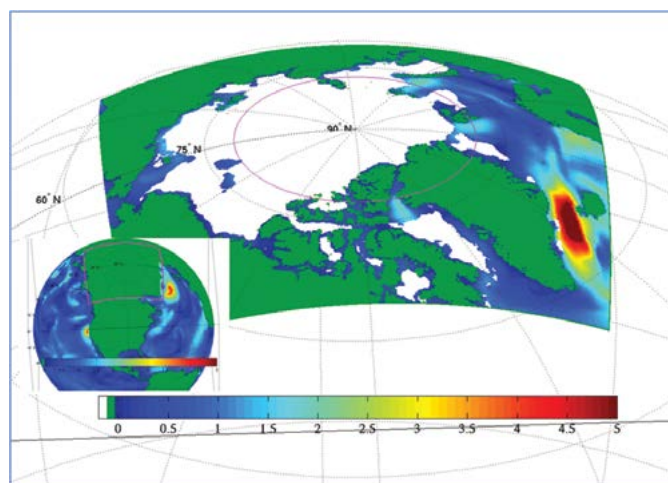
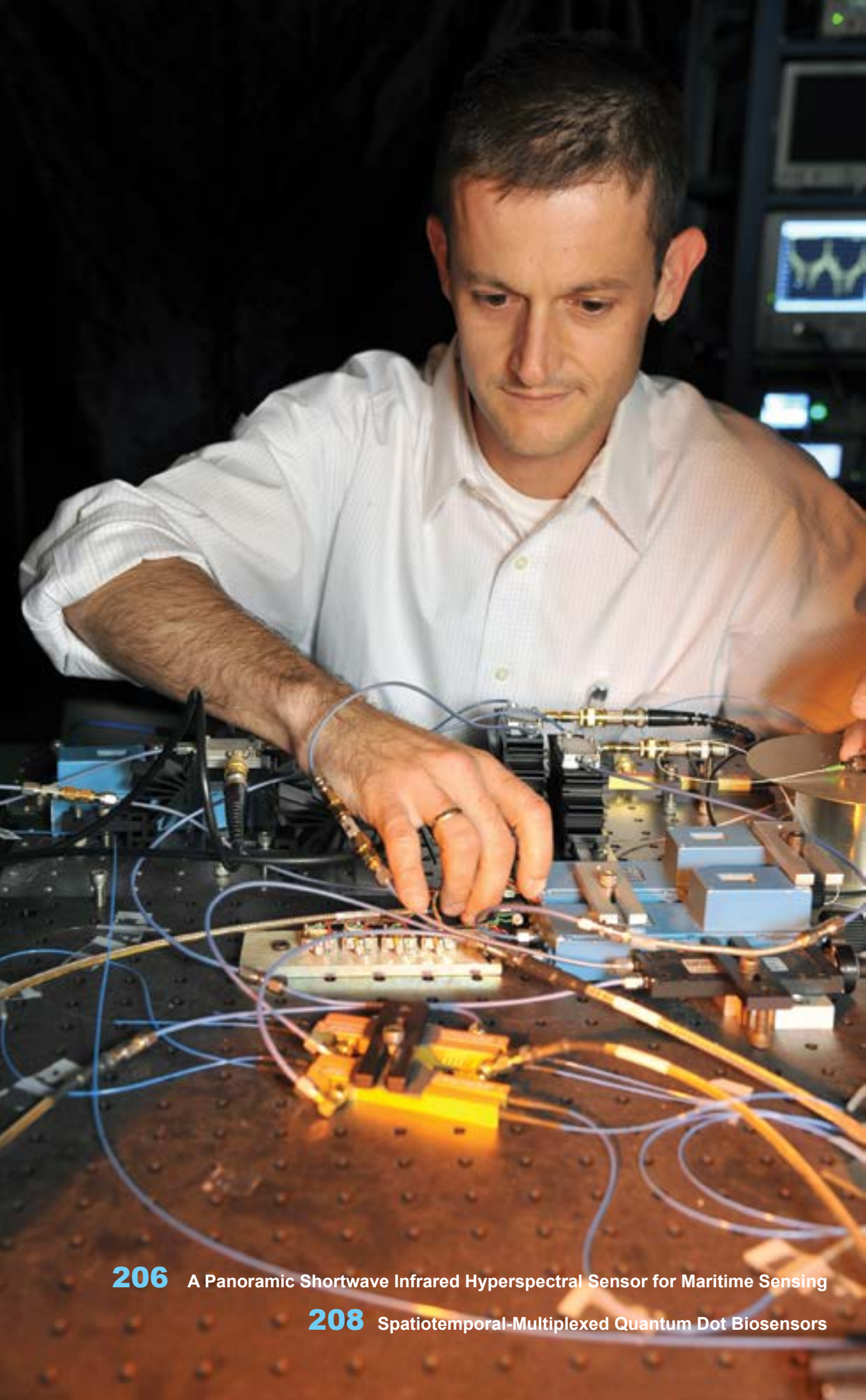


FIGURE 13
 Two-way nesting test with the curvilinear grid Arctic domain (~16 km resolution) and full (0.5°) global domain. Wave height is in meters. The regular global domain is plotted in the inset where masked areas shown in green include the land, ice, and the Arctic domain.

² H.L. Tolman, “User Manual and System Documentation of WAVEWATCH III® Version 3.14,” Tech. Note, NOAA/NWS/NCEP/MMAB, 220 pp. (2009).

³ F. Ardhuin, W.E. Rogers, A. Babanin, J.-F. Filipot, R. Magne, A. Roland, A. van der Westhuysen, P. Queffelec, J.-M. Lefevre, L. Aouf, and F. Collard, “Semi-empirical Dissipation Source Functions for Ocean Waves: Part I, Definitions, Calibration and Validations,” *J. Phys. Oceanogr.* **40**, 1917–1941 (2010). ◆



206 A Panoramic Shortwave Infrared Hyperspectral Sensor for Maritime Sensing

208 Spatiotemporal-Multiplexed Quantum Dot Biosensors

A Panoramic Shortwave Infrared Hyperspectral Sensor for Maritime Sensing

K.P. Judd,¹ J.M. Nichols,¹ J. Waterman,¹ C.C. Olson,²
K. Lee,³ and G. Scriven⁴

¹*Optical Sciences Division*

²*Sotera Defense Solutions, Inc.*

³*Thomas Jefferson High School for Science and Technology*

⁴*Opto-Knowledge Systems, Inc.*

Introduction: The U.S. Navy is exploring new technologies aimed at improving maritime electro-optic and infrared imaging systems. Specific goals include the enhancement of day/night, wide-area situational awareness; improved detection, identification, and tracking capabilities; and increased system reliability. Developing an imaging system that can accomplish these objectives is a tremendous design challenge, made even more difficult by the size, weight, and power limitations imposed on many shipboard and submarine imagers. In response to this challenge, the NRL Optical Sciences Division is leading the development of several compact, day/night imaging systems with resolution that supports detection and tracking of multiple contacts over a wide (360°) field of regard. The sensor system described here is one such example, driven by the Navy's Affordable Modular Panoramic Photonics Mast (AMPPM) program. The AMPPM program is aimed at creating several prototype imagers to serve as upgrades to the current *Virginia*-class submarine photonics masts.

Sensor System: In support of the AMPPM effort, the Maritime Sensing Section of the Applied Optics Branch, in collaboration with industry partners Brandywine Photonics and Smart Logic Inc., has developed a prototype hyperspectral shortwave infrared (SWIR) sensor for periscope applications. Current maritime imagers detect either the broadband emissive or reflective characteristics of an object; the resulting image data is then typically processed using either a point, blob (template matching), or more complex shape matching technique to automatically track the target. However, the image may not contain sufficient information to discriminate between true objects of interest and water- and land-based environmental clutter. The use of spectral imaging opens up the possibility of exploiting the unique optical characteristics that an object possesses to improve detection, identification, and tracking performance.¹ The shortwave infrared band, here defined as 0.9 to 1.7 micron, was selected as it has superior transmission characteristics through marine haze compared to the visible waveband and produces an image of comparable quality relative to visible sensor systems.

Ultimately, the limitation on physical space afforded a periscope imager dictates an aggressive optical design. This prototype therefore consists of a compact optical design Dyson spectrometer, a commercial 12-bit 640 × 512 InGaAs detector sensitive to radiation in the 0.9 to 1.7 micron waveband with thermoelectric cooling, and a commercial color-corrected 50 mm F/1.4 telescope (Fig. 1). The spatial data are aligned with the 640 pixel direction and the system has an instantaneous field of view (IFOV) of 0.5 mrad. The spectral resolution is ~8.7 nm with 111 bands illuminated. The sensor package is mounted to a variable speed pan/tilt unit that provides the scanning to generate the hyperspectral cube. Image acquisition, scanning, and real-time display of the data are computer controlled through a common graphical user interface (GUI). The scan speed and scan angle through which the sensor rotates determine the image width and final hyperspectral cube size.

Field Data and Processing: To examine the imaging quality, characteristics, and capabilities of the system, data were acquired of commercial and naval ship traffic through the port of San Diego from an elevated vantage point located at the tip of Point Loma in June 2012. During this time of year, a heavy marine layer persists until about mid-morning, producing challenging imaging conditions as can be seen in the visible quasi-stitched panoramic scene in the upper portion of Fig. 2. A typical maritime scene as represented by the false-color image of the hyperspectral data cube is shown at the bottom of the same figure. The bands chosen for the image are nominally the centers of the three major atmospheric transmission bandpass regions of the solar irradiance curve at sea level for the 0.9 to 1.7 micron waveband. A slow scan rate was used to create the high-fidelity image; however, slow scan rates translate into long scan periods and oversampling, which is not desirable for rapid object identification. Efforts are currently under way to minimize scan period while maximizing spatial and spectral content.

The processing effort is focused on determining the most efficient methods for classifying objects in the scene in real time so as to provide the operator with the most up-to-date information for rendering critical decisions. We have examined several such approaches, including creating spectral libraries for the maritime environment, applying matched filters to select spectral bands, creating models of relevant spectra using singular value decomposition (SVD) methods, and using more advanced techniques that leverage kernel principal component analysis (KPCA). Results of some recent studies are summarized in Fig. 3 using a standard receiver operating characteristic (ROC) curve. Current investigations are focused on incorporating

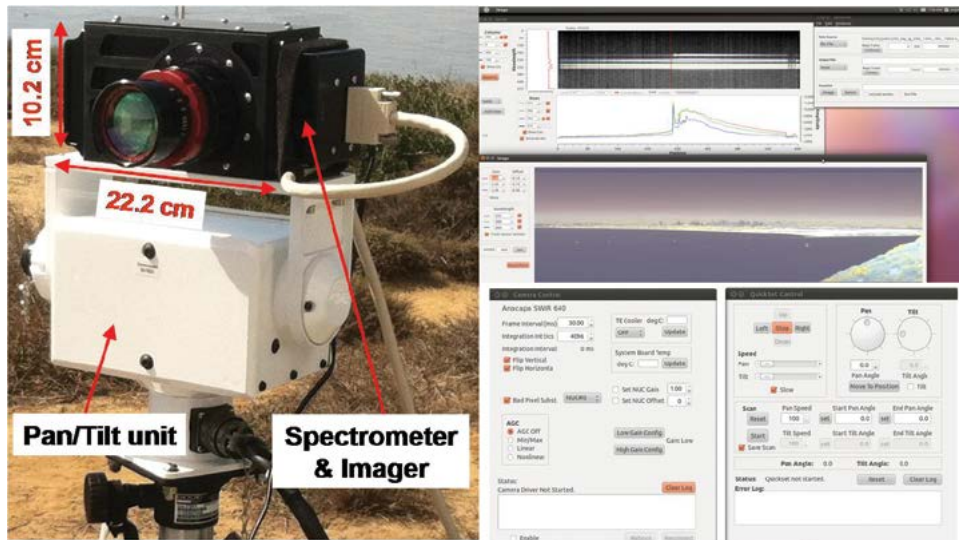


FIGURE 1
 On the left is the sensor (black enclosure) mounted to the pan/tilt drive (white). At top right is the spectral signature map for selected wavelengths and corresponding real-time image displayed by the GUI; below are the camera interface and pan/tilt control windows.



FIGURE 2
 The top image is a quasi-stitched visible image of the entrance to San Diego harbor as seen from Point Loma. Below is a typical false-color image generated by the sensor using the wavelengths labeled on the image to display the hyperspectral data. The red arrows point to common locations in both representations of the scene, a breakwater on the left and downtown San Diego on the right.

locally measured meteorological parameters into the algorithms to improve detection performance.

Summary: We have developed and field tested a compact SWIR hyperspectral sensor for maritime applications. Current efforts are directed at reducing the dimensionality of the data and determining the most efficient machine learning algorithm for rapidly classifying objects of interest within the marine environment while maintaining good classification performance.

This prototype is providing experience and laying the ground work for the future development of more advanced imaging systems.

Acknowledgments: We thank Dr. Costa Colbert of Smart Logic, Inc. and Dr. Dan Guerin of Brandywine Photonics for providing assistance during the field deployment.

[Sponsored by ONR]

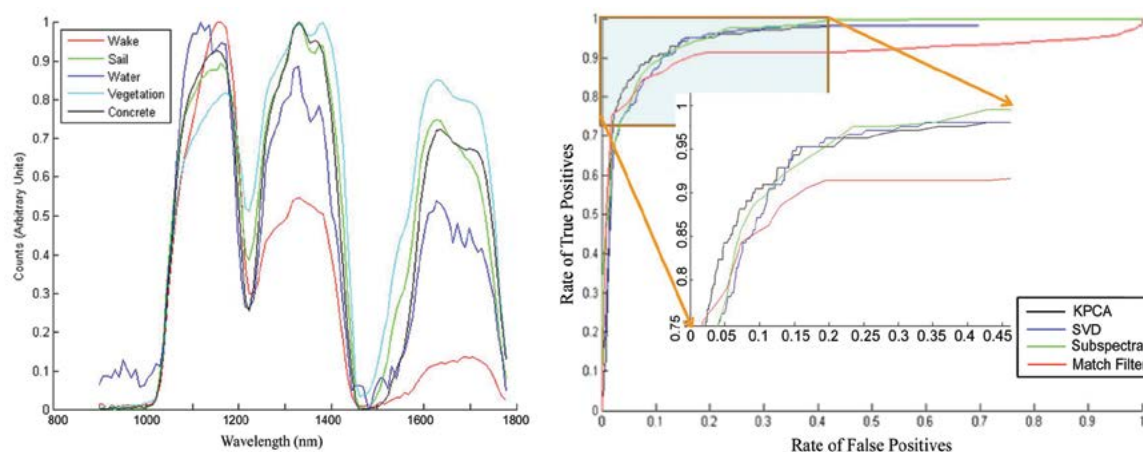


FIGURE 3 In the left panel are typical spectra of various objects of interest and clutter encountered in maritime environments. The right panel is an ROC curve for comparing the performance of several of the classification techniques. The inset is a magnification of the knee in the curve.

Reference

¹K.P. Judd, J.M. Nichols, J.G. Howard, J.R. Waterman, and K.M. Vilardebo, "Passive Shortwave Infrared Broadband and Hyperspectral Imaging in a Maritime Environment," *Optical Engineering* 51(1), 013202 (2012).



intermediary, where the QD functions as both acceptor and donor in a FRET relay.² We further show that such QD platforms allow spectral and temporal multiplexing (i.e., simultaneous detection of multiple analytes) utilizing a single QD color, which has significant advantages over current state-of-the-art color-multiplexed QD platforms.

Spatiotemporal-Multiplexed Quantum Dot Biosensors

M.H. Stewart,¹ W.R. Algar,² N. Hildebrandt,³ A. Huston,¹ and I. Medintz⁴

¹*Optical Sciences Division*

²*University of British Columbia*

³*Université Paris-Sud*

⁴*Center for Bio/Molecular Science and Engineering*

Introduction: Colloidal nanocrystalline semiconductor quantum dots (QDs) possess unique size-tunable electronic and photophysical properties that can be exploited for a variety of Department of Defense (DoD)-relevant technological applications, such as sensors for explosives and chem/bio threats, theranostics (therapeutics and diagnostics), taggants, and photovoltaics. All of these applications rely on the controlled transfer of energy between QDs and selected energy donors and energy acceptors via fluorescence resonance energy transfer (FRET) and/or charge transfer (CT).¹ QD-based sensors that consist of a central QD, surrounded by dye-labeled bioreceptors, can be designed to respond to specific analytes that produce changes in the FRET rate, and therefore, the relative fluorescence intensities of the QD donors and the proximal dye acceptors. We recently demonstrated a nanoconstruct in which a single QD acts as a FRET

QD FRET Relay Platforms: The QD FRET relay system is composed of three optical components, as seen in Fig. 4(a): (1) A long lifetime luminescent terbium(III) complex (Tb) that acts as a FRET donor (FRET₁) to a (2) 625 nm-emitting QD ground state acceptor, which subsequently transfers energy (FRET₂) to a terminal (3) fluorescent Alexa Fluor 647 (A647) acceptor dye. The absorbance and photoluminescence (PL) spectra of each platform component are shown in Fig. 4(b), illustrating the spectral overlap and potential for successive energy flow from higher energy (blue) to lower energy (red) directly and over a time-gated window.

The FRET relay system was fabricated using poly-histidine-peptide linkers, developed under a previous NRL Institute for Nanoscience project, to tether the A647 (PEP A) and Tb (PEP B) to the QD surface (Fig. 4(a)). Using a ratiometric mixing format, FRET relay platforms could be formulated to link specific numbers of Tb and A647 to the QDs to yield Tb_n-QD-A647_m assemblies. These platforms were developed in a collaborative effort between the Center for Bio/Molecular Science and Engineering, the Optical Sciences Division, and The Scripps Research Institute.

Time-Gated FRET: Short pulsed laser excitation of the FRET-relay system produces a mixture of excited-state QDs (QD*s) and Tb (Tb*) complexes. The shorter-lived QD*s (~50 ns) transfer energy rapidly to

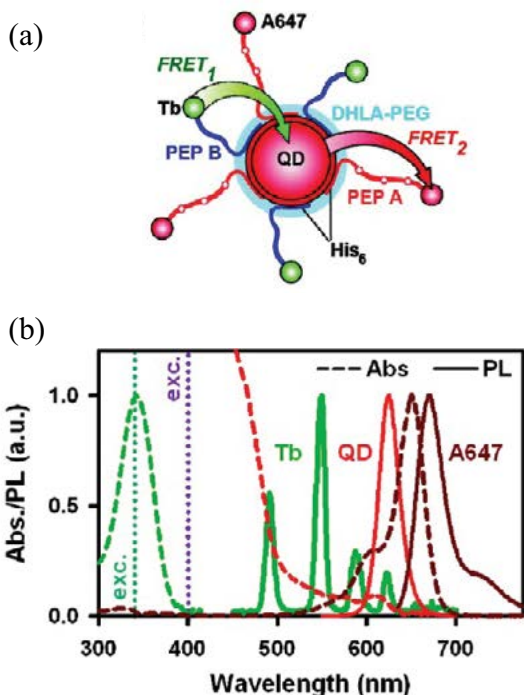


FIGURE 4
 (a) QD serves as a nanoplateform for the assembly of A647- and Tb-labeled peptides, PEP A and PEP B, respectively. QD functions as an acceptor via Tb-to-QD FRET₁ and a donor via QD-to-A647 FRET₂. (b) Absorbance and emission spectra for Tb, QD, and A647. Figure adapted from Ref. 2.

the A647 dyes that, in turn, rapidly relax via the emission of light at ~670 nm. The long-lived Tb* complexes (2.6 ms) then transfer energy via FRET₁ to the relaxed QDs, over an extended period of time, which subsequently transfer energy to the A647 dyes via FRET₂ (Fig. 5). The QD acts as a time-stable energy conduit between the Tb complex and the A647 dye. Time-

gating of the luminescence detection system allows one to utilize the immediate QD*-to-A647 FRET process independently from the time-delayed Tb*-QD-A647 FRET relay. The use of both the nongated and time-gated FRET provides two orthogonal FRET channels that can be used in a multiplexed format to detect two separate analytes within a single QD platform.

Two-plex DNA Hybridization Assay: To demonstrate this multiplexed format, a single QD platform was assembled to detect two separate nucleic acid hybridization events (Fig. 6(a)). QDs were conjugated with probe oligonucleotides, PRB A and PRB B, which capture the complementary target oligonucleotides TGT A-A647 and TGT B-Tb, respectively. The capture events were detected via nongated FRET₂ and time-gated FRET₁ and FRET₂ (Fig. 6(b)). The nongated ratio of A647/QD PL is proportional to the amount of hybridized TGT A-A647 and the time-gated sum of QD + A647 PL is proportional to the amount of hybridized TGT B-Tb per QD platform. This demonstrates that two orthogonal quantitative responses are detectable using a single QD platform.

Conclusions: NRL continues to develop powerful biosensors for DoD applications using energy transfer between QDs and peptide-linked donors and acceptors. We show that QDs can function as unique scaffolds and platforms to assemble FRET relays, where the QD behaves as both a FRET acceptor and donor in a time-gated format. Our work demonstrates that multiplexed sensing with a single QD color via spectrotemporal resolution of two orthogonal FRET processes is advantageous over current state-of-the-art QD multiplexing that relies on multiple QD colors. The time-gated FRET relay has been extended to multiplexed sensing of protease activity with a single QD vector, including the

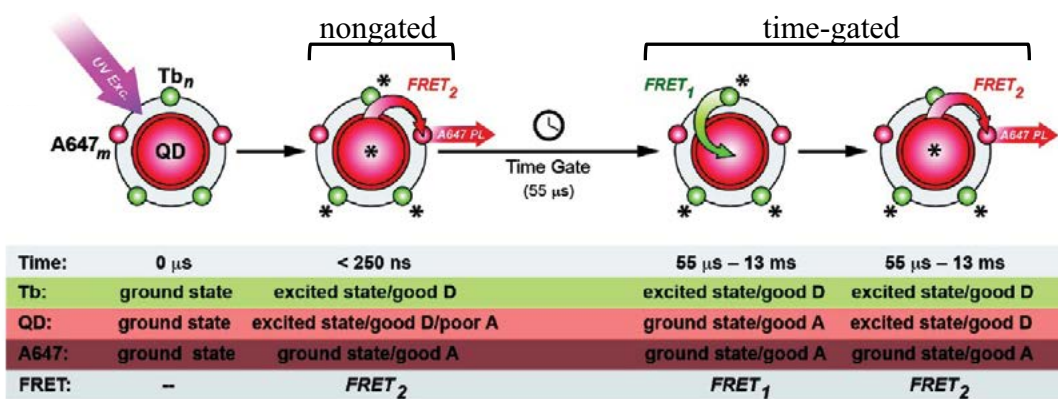


FIGURE 5
 Photophysical time-gated FRET relay process. Flash-excited QD*-to-A647 FRET₂ measured in nongated format. Excited state Tb* persists through microsecond delay (time gate). The ground state QD becomes a good FRET acceptor after a microsecond delay permitting the time-gated Tb*-to-QD FRET₁ and QD*-to-A647 FRET₂ energy cascade (D = donor, A = acceptor). Figure adapted from Ref. 2.

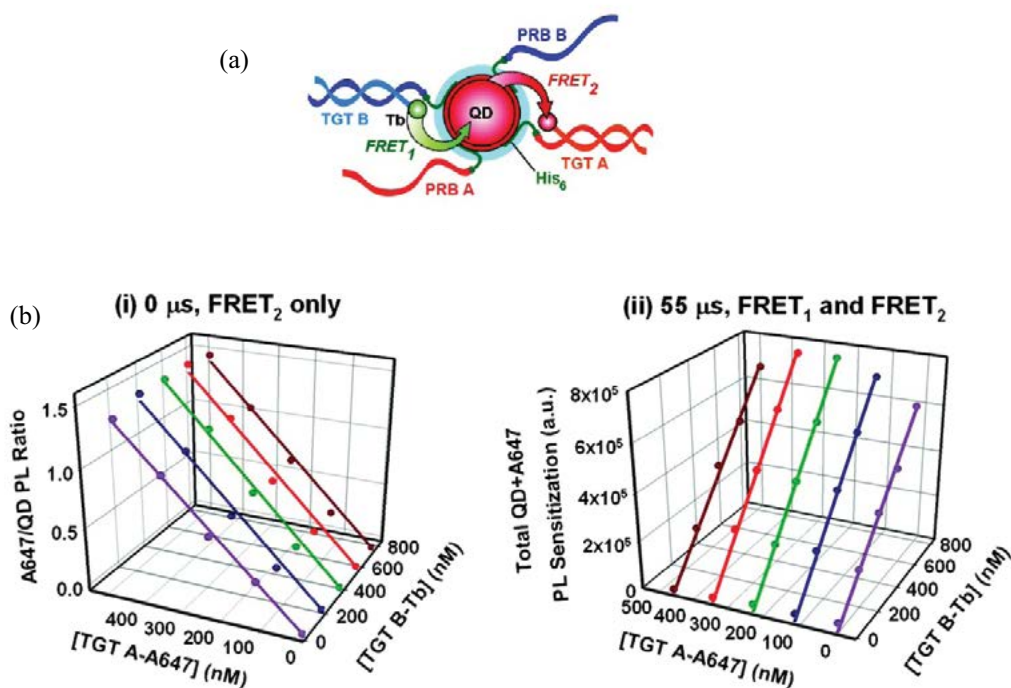


FIGURE 6

(a) Nucleic acid hybridization platforms. QDs conjugated with PRB A and PRB B engage in FRET upon capture of complementary TGT A–A647 and TGT B–Tb. (b) Orthogonal calibration curves for determining (i) TGT A–A647 hybridization via nongated FRET₂ data and (ii) TGT B–Tb via time-gated FRET₁ and FRET₂ data. Figure adapted from Ref. 2.

activation of an inactive pro-protease by another pro-protease, which is a significant advancement in nanoparticle-based biosensing.³

Acknowledgments: The authors thank Lumiphore, Inc., for providing the Tb complex and Invitrogen by Life Technologies for the QDs.

[Sponsored by DTRA, DARPA, ONR, NRL Base Program (CNR funded), NRL Institute for Nanoscience, Innovative Medicines Initiative, and European Commission FP7]

References

- ¹ M.H. Stewart, A.L. Huston, A.M. Scott, A.L. Efros, J.S. Melinger, K.B. Gemmill, S.A. Trammell, J.B. Blanco-Canosa, P.E. Dawson, and I.L. Medintz, “Complex Förster Energy Transfer Interactions between Semiconductor Quantum Dots and a Redox-Active Osmium Assembly,” *ACS Nano* **6**(6), 5330–5347 (2012).
- ² W.R. Algar, D. Wegner, A.L. Huston, J.B. Blanco-Canosa, M.H. Stewart, A. Armstrong, P.E. Dawson, N. Hildebrandt, and I.L. Medintz, “Quantum Dots as Simultaneous Acceptors and Donors in Time-Gated Förster Resonance Energy Transfer Relays: Characterization and Biosensing,” *J. Am. Chem. Soc.* **134**(3), 1876–1891 (2012).
- ³ W.R. Algar, A.P. Malanoski, K. Susumu, M.H. Stewart, N. Hildebrandt, and I.L. Medintz, “Multiplexed Tracking of Protease Activity Using a Single Color of Quantum Dot Vector and a Time-Gated Förster Resonance Energy Transfer Relay,” *Anal. Chem.* **84**(22), 10136–10146 (2012).

Remote Sensing

212 Electrochemical Detection of Nitroenergetics for Long Term Monitoring

214 Remote Sensing Signatures of Breaking Waves from Multi-Instrument Field Experiment on FLIP

216 Surprising Discoveries in Reflectance Properties of Complex Granular Sediments

Electrochemical Detection of Nitroenergetics for Long Term Monitoring

B.J. White,¹ B.J. Melde,¹ R.L. Siefert,² and M. Nasir³

¹Center for Bio/Molecular Science and Engineering

²U.S. Naval Academy

³Lawrence Technological University

Monitoring Contaminated Sites: U.S. Department of Defense activities related to ordnance manufacture, storage, disposal, and training have resulted in nitroenergetic contamination at a number of military installations. Monitoring and remediation of these sites is costly, leading to significant interest in more effective and efficient methods. Traditionally, monitoring is accomplished through collection of samples that are subsequently returned to a laboratory for analysis. This requires careful handling to protect against erroneous results and imposes a significant logistical burden. In situ monitoring offers flexibility in sampling frequency, improved information on system dynamics, and elimination of handling considerations. The use of electrochemical sensors offers the benefits of small size, low power requirements, and low cost to portable applications. Current commercially available sensors, however, do not provide sufficient sensitivity or selectivity to replace traditional methods.

Preconcentration for Improved Performance: Preconcentration by solid-phase extraction (SPE) involves adsorbing targets onto a solid support followed by desorption using a solvent. The result is more target in a smaller volume. Selective and semiselective adsorption can also help to eliminate nontarget compounds from the concentrated sample. Our effort is focused on developing the materials and systems necessary for inline preconcentration prior to analysis by electrochemical methods. The approach is intended to improve the detection limits for such a system and to eliminate potential inference by the sample matrix. The SPE sorbents developed are porous organosilicates providing semiselective binding of 2,4,6-trinitrotoluene (TNT), RDX, HMX, and dinitrotoluenes (DNT). These materials preconcentrate targets and eliminate nontarget contaminants as demonstrated by high performance liquid chromatography (HPLC) based studies.^{1,2} They show improved target retention and selectivity over commercially available SPE sorbents. The materials can be used repeatedly over periods of months with no degradation in performance and are applicable across a wide range of temperatures and chemical conditions.

The Inline System: The inline system is intended to provide sample collection, preconcentration, and

elution prior to analysis by an electrochemical detector (Fig. 1). Samples are pulled through a filter stack to eliminate particulates (size exclusion) using a peristaltic pump that also pushes the sample through the sorbent column. Once target is adsorbed, the precolumn valve is switched, and eluent is pushed through the column. The desorbed targets are then directed to the electrochemical detector after mixing with electrolyte solution. A single sorbent column was used for evaluation of more than 220 samples including deionized, ground, and surface water and soil extracts. The total time for processing using the prototype system (30 mL sample volume) was 45 min. During analysis of this sample series, it was necessary to replace the silicon tubing used in the peristaltic pump three times. Continued use of a single tubing set resulted in damage and eventual rupture of the tubing after 100 to 150 h of system use.

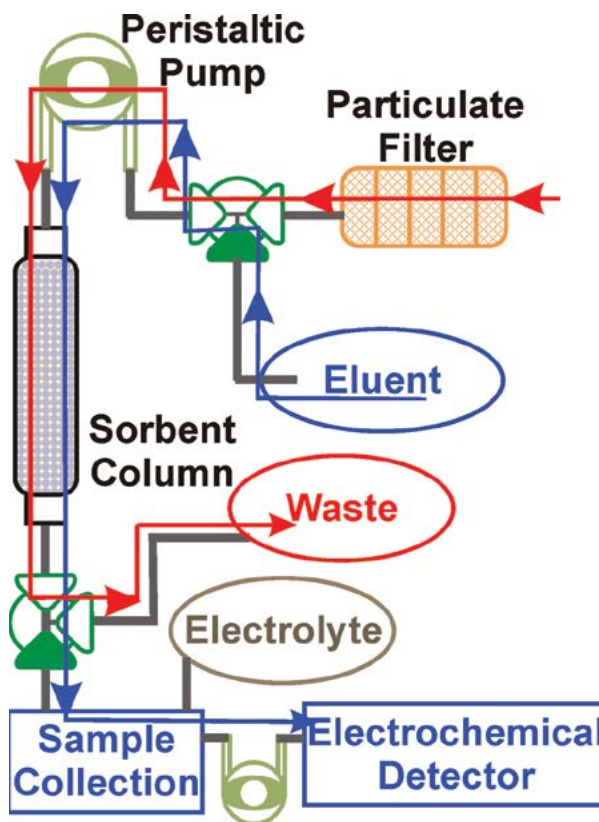


FIGURE 1

Preconcentration system. Shown here is a schematic of the prototype system developed by NRL. The red line indicates flow of the water sample through the system, entering at the particulate filter and exiting to waste. The blue line indicates the flow of eluent through the system, carrying concentrated target to the electrochemical detector.

System Performance: A PalmSens handheld potentiostat (PalmSens, Utrecht, The Netherlands) was selected for electrochemical (EC) measurements based on square wave voltammetry. Calibration of the EC

sensor indicated limits of detection at 250 ppb for TNT and 350 ppb for DNT. While RDX is of particular interest for in situ monitoring, the target does not lend itself to detection using commercially available components.³ Having established the performance of the EC system, the impact of preconcentration prior to EC analysis was evaluated. Samples in deionized water between 20 and 250 ppb were considered (30 mL). Samples of lower concentration were evaluated using larger sample volumes (300 mL). In the case of TNT, the variability between HPLC determined values and EC determined values is 26% on average with 23% for DNT data set. Evaluation of samples in ground water (Fig. 2(b)) indicated similar results for TNT and greater variation for DNT (40%), likely due to the analysis method utilized.

TNT detection using this method is encouraging. Discrimination of TNT from DNT and RDX was achieved without difficulty in blind sample analysis (Fig. 2(c)). Nitroglycerin presence was interpreted as low TNT concentrations by an operator with no knowledge of sample composition. While samples in ground water could not be analyzed by the EC system, use of inline preconcentration provided elimination of the interferents as well as enhanced target concentrations, resulting in performance similar to that in deionized water. Depending on the volume of sample used for preconcentration, detection limits for the electrochemical sensor could be reduced by up to two orders of magnitude (250 ppb to less than 3 ppb). While the approach was less successful for DNT, the study thoroughly demonstrates the potential of such a system. The use of modified electrodes, not currently commercially available, provides the potential for detection of additional targets, such as DNT and RDX.³

Acknowledgments: The authors would like to thank I.A. Leska, J.R. Taft, M.H. Moore, and A.P. Malanoski for their contributions to this effort. This research was sponsored by the Strategic Environmental Research and Development Program (SERDP, ER-1604) and conducted at the Naval Research Laboratory, Washington, DC.

[Sponsored by SERDP]

References

- ¹ B.J. Johnson, B.J. Melde, P.T. Charles, M.A. Dinderman, A.P. Malanoski, I.A. Leska, and S.A. Qadri, "Macroporous Silica for Concentration of Nitroenergetic Targets," *Talanta* **81**, 1454–60 (2010).
- ² B.J. Johnson, B.J. Melde, I.A. Leska, P.T. Charles, and A.D. Hewitt, "Solid-Phase Extraction Using Hierarchical Organosilicates for Enhanced Detection of Nitroenergetic Targets," *J. Environ. Monitor.* **13**, 1404–9 (2011).
- ³ S.Y. Ly, D.H. Kim, and M.H. Kim, "Square-Wave Cathodic Stripping Voltammetric Analysis of RDX Using Mercury-Film Plated Glassy Carbon Electrode," *Talanta* **58**, 919–926 (2002).

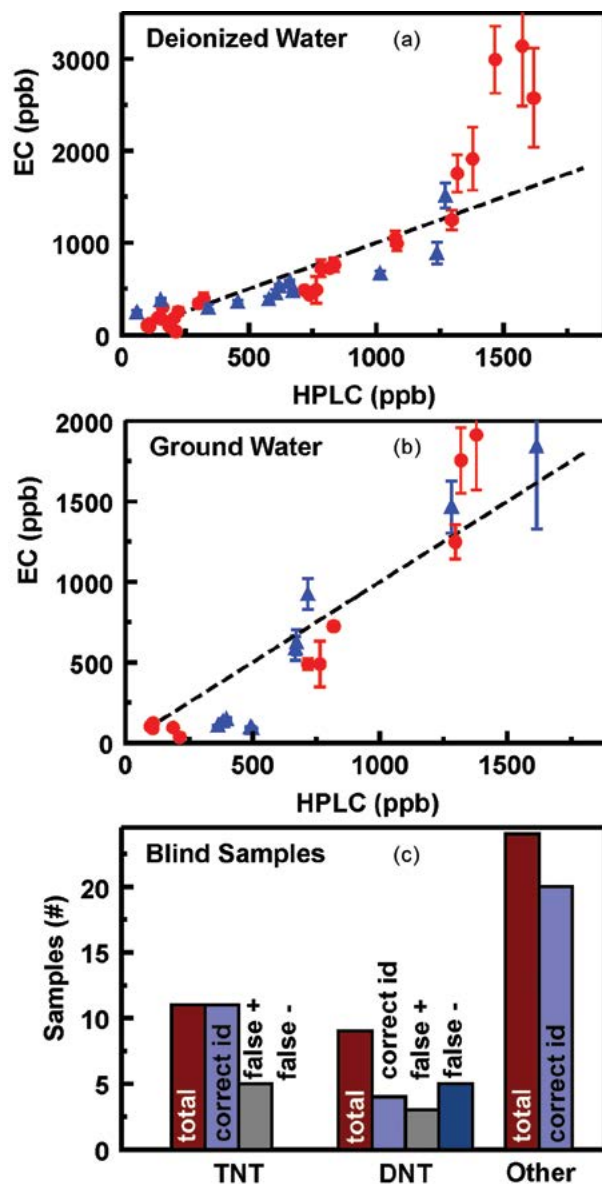


FIGURE 2 Preconcentration of targets. In (a) and (b), points here represent the results for quantification of targets from deionized water (a) and ground water (b) using the prototype system with analysis by HPLC (x-axis) and EC (y-axis): TNT (red) and DNT (blue). The line indicates the expected results based on HPLC analysis of the spiked samples. Error bars indicate the standard deviation in the measurements; where not visible, they are within the size of the symbol. Shown in (c) are results of blind sample analysis. The bars shown here indicate the total number of samples containing either TNT or DNT and the associated number of correct target identifications. Also shown are the number of false positive and negative responses. The third category of samples includes those with no target and those with targets not expected to be detected (RDX, nitroglycerin).

Remote Sensing Signatures of Breaking Waves from Multi-Instrument Field Experiment on FLIP

M.D. Anguelova,¹ D.J. Dowgiallo,¹ G.B. Smith,¹
S.L. Means,² I.B. Savelyev,¹ G.M. Frick,¹ C.M. Snow,¹
J.A. Schindall,² and J.P. Bobak¹

¹Remote Sensing Division

²Acoustics Division

Introduction: Oceanic whitecaps are the surface expression of breaking wind waves in the ocean. Whitecap fraction W , defined as the fraction of a unit surface covered with sea foam, quantifies wave breaking and is thus a suitable forcing variable for parameterizing and predicting air-sea interaction processes associated with breaking waves. Whitecaps in different lifetime stages have markedly different properties. Active whitecaps, formed at the moment of active breaking, are thick, comprise a wide range of bubble sizes, move along with the wave crest, and cover less surface area. Residual whitecaps, comprising decaying foam, are thinner, remain motionless behind the wave that has created them, and spread over a larger area. Total W (active plus residual whitecaps) is a useful predictor of bubble-mediated sea spray production and heat exchange.¹ More dynamical air-sea processes are better represented by active whitecap fraction W_A , e.g., production of spume droplets (important for tropical storms intensification), momentum flux, turbulent mixing, gas exchange, and generation of ambient noise in the ocean.²

A database of W from satellite-measured brightness temperature T_B of the ocean surface at microwave frequencies has been developed within the framework of the WindSat mission at NRL.³ This database is useful for studying and parameterizing W variability. However, to make this database useful for dynamic processes, it is necessary to find a way to extract W_A from W . We pursue separation of W_A from W both theoretically and experimentally. The physical basis for the experimental approach is that there are distinct signature differences between active and residual whitecaps at infrared (IR) wavelengths.⁴ To this end, we conducted a multi-instrument field campaign to collect data useful for identifying the signatures of breaking waves and whitecaps at different electromagnetic wavelengths, from visible, to IR, to microwave.

Field Campaign: We collected data from April 22 to 30, 2012, on the Floating Instrument Platform (FLIP) drifting along the coast of California from Monterey Bay south. FLIP is a unique vessel (<http://www-mpl.ucsd.edu/resources/flip.intro.html>) that provides a stable research platform for data collection on three

booms (port, starboard, and face). FLIP is towed to its operating area in a horizontal position and, through ballast changes, is “flipped” to a vertical position to become a stable spar buoy with a draft of 300 ft (Fig. 3(a)). The diameter of the hull tapers with depth, and this makes FLIP less responsive to wave motion.

Variations of ocean surface brightness temperature, T_B , caused by breaking waves and whitecaps were measured with microwave radiometers at frequencies of 10 and 37 GHz, vertical and horizontal (VH) polarizations. The radiometers, mounted on the port boom within a weather casing (Fig. 3(b)), looked at the ocean surface at an angle of 45°. The beamwidths of the 10- and 37-GHz horns are approximately 6°, giving an approximate footprint of 1.8 m in diameter for each instrument. The infrared imager used during this exercise was a Merlin-Mid (Indigo Systems, a division of FLIR). This system is sensitive to radiation in the 3 to 5 μm band (mid-wave infrared) and has a noise equivalent ΔT of approximately 0.017 K. Imagery was typically collected at a sampling rate of 10 Hz. The IR camera was mounted on top of the radiometers (Fig. 3(b)) to ensure the radiometer footprints fell within the

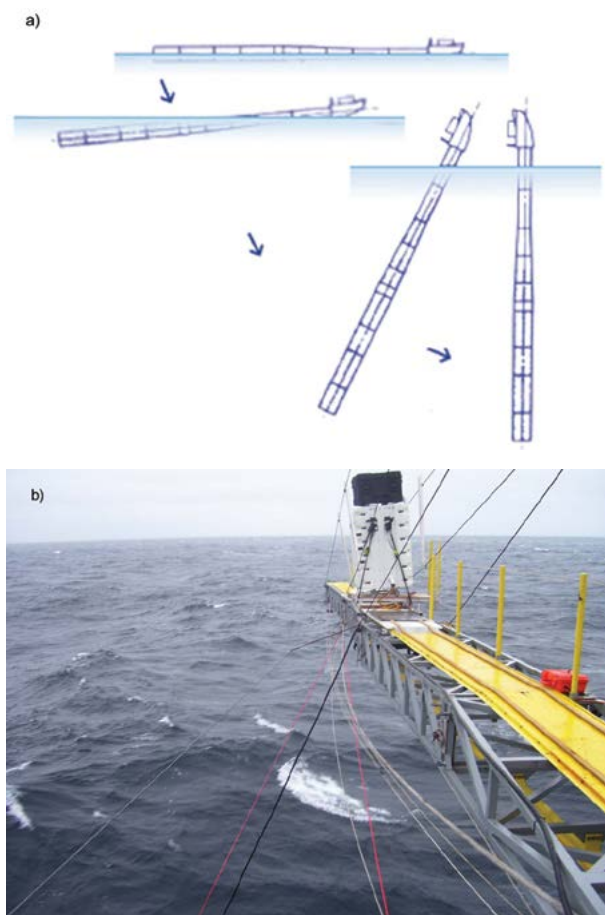


FIGURE 3 Research platform FLIP: a) controlled sinking to vertical position; b) instrumentation deployed on port boom.

16 × 12 m² field of view (FOV) of the IR camera. Three video cameras, positioned in different places, recorded visible images of whitecaps.

An acoustic vertical line array (VLA) provided data for the bubble-generated noise beneath breaking waves. The VLA was suspended between the face and port booms of FLIP. The array consisted of three nested apertures with hydrophones spaced at 1.25, 0.625, and 0.3125 m, yielding design frequencies of 600, 1200, and 2400 Hz, respectively. The VLA was deployed at a depth such that the upward endfire beam would isolate acoustic signatures from individual breaking waves, excluding FLIP-generated noise at all but the lowest frequencies.

The aerosol size distribution was measured with two instruments. A Particle Measuring Systems CSASP-100-HV, suspended from the starboard boom, measured aerosol from 0.25 to 23.5 μm radius. The NRL Differential Mobility Analyzer measured ducted and dried aerosol between 6 and 400 nm radii.

Various auxiliary data such as wind speed, air temperature, humidity, wave field, and water temperature profile characterize the experimental conditions. The conditions encountered ranged from wind speed of 2.8 to about 18 m s⁻¹, and significant wave height from 1 to ~5 m (Fig. 4).

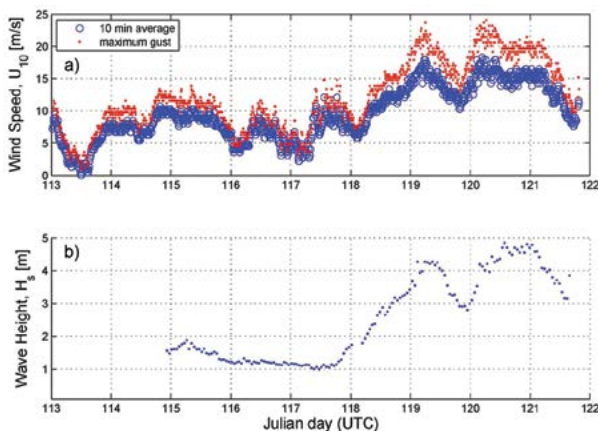


FIGURE 4
Experimental conditions: a) wind speed; b) significant wave height.

Data Collected: Figure 5 shows typical data collected from each instrument. A bright whitecap seen in the visible image (Fig. 5(a)) is identified by dark streaks at IR wavelengths (Fig. 5(b)). Spikes in T_b at 10 GHz, seen simultaneously in both H and V polarizations, mark whitecap signatures at microwave wavelengths (Fig. 5(c)). The observed increased noise level (in dB) is the whitecap acoustic signature (Fig. 5(d)).

IR images will help us identify active and residual foam as warm and cold patches, respectively. Matching these signals in time with radiometric, acoustic,

and aerosol data will help us identify the signatures of the two life stages at other wavelengths. We will then establish criteria for active vs residual separation for each type of data. Correlating radiometric, acoustic, and aerosol signature characteristics with each other, as well as with meteorological and oceanographic data, will yield empirical relationships useful for predicting breaking wave and whitecaps with observations from various sensors.

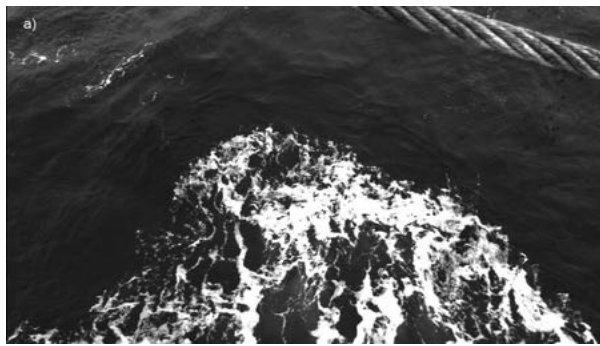
The impact of our findings will be the improvement of the current accuracy of predicting air-sea fluxes at the air-sea interface. More accurate air-sea fluxes will, in turn, reduce the uncertainty of weather forecasting, tropical cyclone intensification, wave forecasting, and climate prediction.

Acknowledgments: This work was sponsored by the Office of Naval Research (ONR), NRL Program element 61153N WU 4500. We highly appreciate the funding support for our use of FLIP by Robert Schnoor via the Naval Research Facilities Program at ONR, and by Dr. Joan Gardner and Dr. Edward Franchi via the NRL Platform Support Program. Captain William Gaines, FLIP program manager at Marine Physics Laboratory (MPL) at Scripps Institution of Oceanography, was indispensable in organizing the field campaign. We appreciate Tom Golfinos, Officer-in-Charge for FLIP, and crew members Johnny, Dave, Frank, and Jerry for their hard work, endurance, and camaraderie. We would also like to thank George Trekas and his colleagues at the MPL Machine Shop for their expertise and skills in devising the instrument deployment on the FLIP booms.

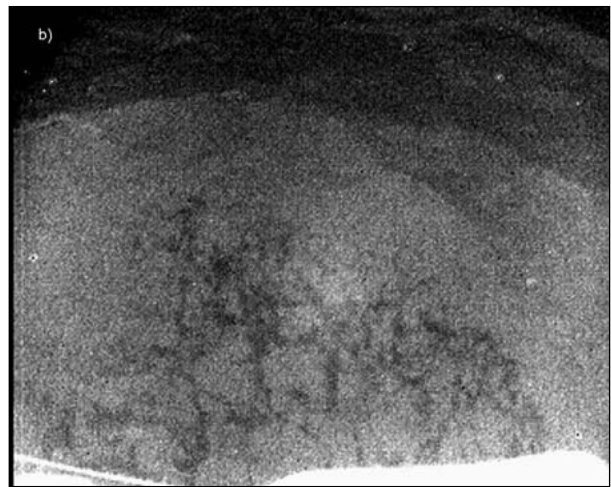
[Sponsored by ONR]

References

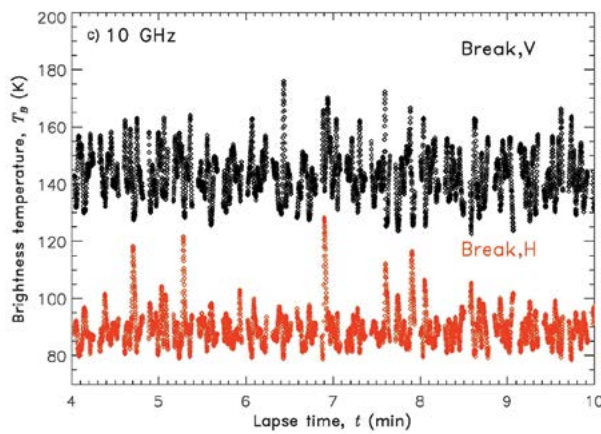
- ¹ G. de Leeuw, E. Andreas, M.D. Anguelova, C. Fairall, E. Lewis, C. O'Dowd, M. Schulz, and S. Schwartz, "Production Flux of Sea-Spray Aerosol," *Rev. Geophys.* **49** (2011).
- ² W.K. Melville, "The Role of Surface-Wave Breaking in Air-Sea Interaction," *Annu. Rev. Fluid Mech.* **28**, 279–321 (1996).
- ³ P.W. Gaiser, K.M. St Germain, E.M. Twarog, G.A. Poe, W. Purdy, D. Richardson, W. Grossman, W.L. Jones, D. Spencer, G. Golba, J. Cleveland, L. Choy, R.M. Bevilacqua, and P.S. Chang, "The WindSat Spaceborne Polarimetric Microwave Radiometer: Sensor Description and Early Orbit Performance," *IEEE Trans. Geosci. Rem. Sens.* **42**, 2347–2361 (2004).
- ⁴ G.O. Marmorino and G.B. Smith, "Bright and Dark Ocean Whitecaps Observed in the Infrared," *Geophys. Res. Lett.* **32**, L11604 (2005).



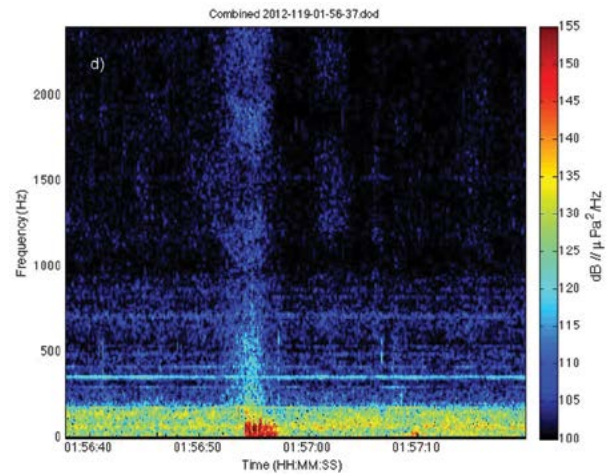
(a)



(b)



(c)



(d)

FIGURE 5 Breaking wave signatures at different wavelengths: a) visible; b) infrared; c) microwave (10 GHz); and d) acoustic.

Surprising Discoveries in Reflectance Properties of Complex Granular Sediments

A. Abelev¹ and C.M. Bachmann²

¹Marine Geosciences Division

²Remote Sensing Division

Introduction and Background: Terrestrial remote sensing applications are abundant in various fields of science and technology, applicable and currently in high demand in both the civilian and the military domains. One of the main goals of these applications is determination of the nature, properties, and composition of soils — natural and engineered alike. Multi- and hyperspectral measurements represent one of the main and quickly growing sectors of remote sensing, with

sensors deployed near the ground, in the air, and in Earth's orbit. The characteristic nature of the way that these sensors are used involves a phase angle dependence of measurements (angle between the line of sensor sight and the illumination line of the sun). This influence is expressed in models via a bidirectional reflectance distribution function (BRDF). Characteristics such as texture, grain-size distribution, and mineralogical composition are phase-angle dependent and represent the first level of complexity in characterizing soil properties and behaviors. These properties are features of the very surface of the soil, visible on the scale of the wavelength of a hyperspectral instrument spectrum, typically including some parts or all of the visible (VIS), near infrared (NIR), and shortwave IR (SWIR) ranges (0.4 to 2.5 μm). Additionally, some of the bulk properties of the soils are of great interest to the end-user and include, e.g., bulk density and porosity. Describing these properties involves the mechani-

cal characteristics of soils (and granular materials in particular), which rely on volume properties and are much harder to determine from overhead sensors. One of these volume properties is the relative density – i.e., the degree of grain packing in the range between the loosest (minimum density) and the densest (maximum) arrangement of grains a material can attain in the natural environment. The knowledge of this critical property leads to much higher levels of utility, up to and including certain soil strength parameters, such as a friction angle of the granular media.

Current state-of-the-art radiative transfer theories for granular media of a single constituent predicts increased reflectance with increased degree of material packing,^{1,2} or relative density. These theories have been validated using a variety of models and confirmed by experiments on assemblies of particles of the same mineralogical composition. These theories have also been applied to coastal soils, where some of the underlying principles may not hold true due to the typically very complex and heterogeneous mineralogical composition. In this work, we explore the directional reflectance dependence of a natural complex beach sand on its relative density. As a result of our experimental investigation,³ we uncovered some surprising effects that demonstrate a clear dependence of the reflectance on the relative density (or packing) of the material, but in exactly opposite form from that predicted by all current theories. We explain that the origin of these observations lies in the mineral complexity of the beach material.

Experimental Investigation and Discussion: The sand that was recovered from the Virginia Coast Reserve (VCR) during an experiment⁴ was reconstituted in the laboratory using an air-pluviation method⁵ that more closely represents the natural Aeolian formation processes than do the artificial compaction modes. The method involves sand air-pluviation through a series of sieves that serve as flow diffusers, dispensing from a calibrated height and at a given flow rate into a special mold. Various rates of deposition (and drop heights) result in a wide range of densities, from the very loose (for quick flows) to the very dense (for slow pours). The experimental apparatus for studying directional dependence of the reflectance was built (Fig. 6) and includes an Analytical Spectral Devices (ASD) spectrometer, recording radiance in the spectral range between 0.35 and 2.5 μm , with an 8° fore-optic, and an ASD lamp (as a light source), both mounted on booms and rotational stages with independent accurate positioning. This design allows for an exploration of reflectance values for a wide range of phase angles from 7° to 50° in the principal scattering plane. Select results from different ranges in the spectrum (VIS, NIR, SWIR) are

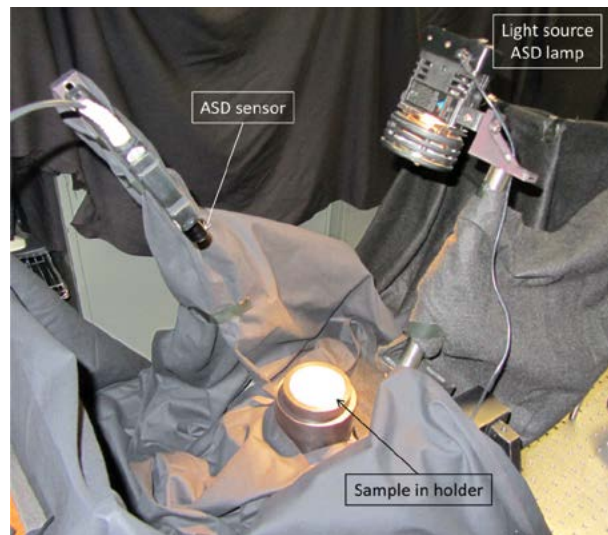


FIGURE 6 Experimental setup showing an ASD hyperspectral sensor (0.35 to 2.5 μm) with an 8° fore-optic and a light source, each mounted on a boom attached to a rotational stage with precise angular positioning. Reconstituted sample is shown in a Delrin holder. Black cloth shrouding covers reflective metal parts to minimize extraneous interference to measured sand surface reflectance.

shown in Fig. 7. These wavelengths were chosen at a few notable absorption features of the spectral curves. Additionally, surface images of the low and high density sand samples, taken at 4× magnification through a microscope, are shown as an inset in Fig. 7. The reflectance values for all phase angles plotted increase from high to low relative density, opposite of what might be expected and predicted with any of the current single-constituent theories. The source of this unexpected change lies in the complex mineralogical nature of the sample. Here, two distinct constituents can be found (Fig. 7, inset), a coarser fraction of larger (on average) and more translucent quartz grains and a finer fraction of darker magnetite mineral. When sieved into fractions, the optical difference between these two constituents is dramatic, with much of the finer fraction represented by the dark opaque mineral, and much of the larger fraction by the highly translucent quartz grains. Additionally, the differences in reflectance between the two densities increase at the larger phase angles. We explain these findings by the apparent filling of the smaller (and darker fraction) into the voids between the larger and more transparent grains, as the density increases. These filling and compaction effects result in progressive shutdown of the multiple scattering paths of the incident light and added absorption by the darker and more opaque fraction, resulting in the overall dramatic decline in surface reflectance. The reason that this effect is more pronounced at the higher wavelength has to do with the more dominant mineral absorption features in the SWIR range of the spectrum.

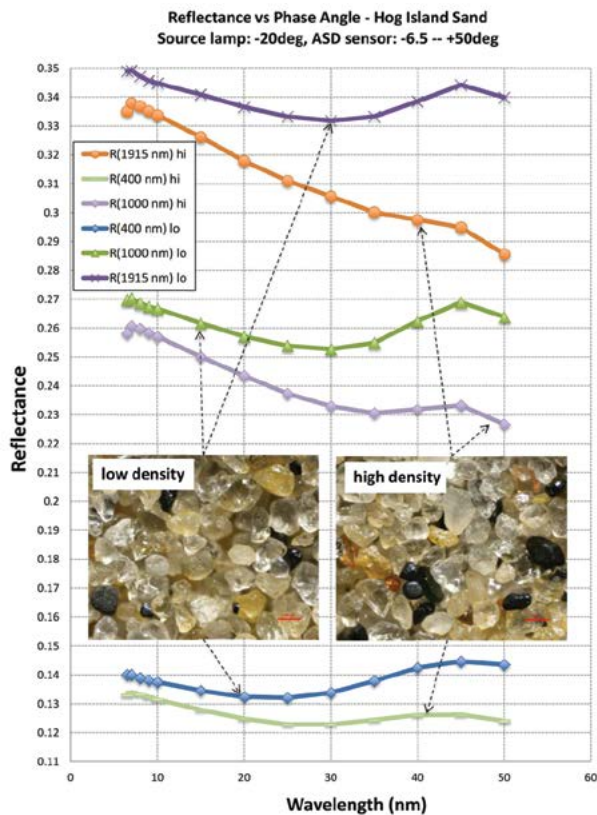


FIGURE 7
 Reflectance of sand samples of low and high relative density at several selected wavelengths. Lower densities display consistently increased reflectance values, especially at higher phase angles, due to mineral complexity, and contrary to current models. Inserts show microscope images (at 4x magnification) of the sand surface at both densities. Note the apparent increase in the darker (and smaller) mineral component at higher relative density.

Conclusions: Thus, we show in this work that if complex beach sands, often a product of many distinct sources of minerals in the coastal zone, contain minerals of distinctly different opacity, they may produce unexpected results in spectral reflectance that are not well characterized or explained by the current models. Moreover, our lab results are reinforced by the field data from other hyperspectral sensors^{4,6,7} collected at the VCR, including the NRL field goniometer hyperspectral tool (near-surface measurement) and the airborne sensors. Another consequence of these findings is that data collected at multiple phase angles in these complex sands may yield information on relative density, and, consequently, estimates of the friction angle of granular media.

[Sponsored by NRL Base Program (CNR funded)]

References

- ¹ B. Hapke, "Bidirectional Reflectance Spectroscopy: 6. Effects of Porosity," *Icarus* **195**(2), 918–926 (2008).
- ² P. Helfenstein and M.K. Shepard, "Testing the Hapke Photometric Model: Improved Inversion and the Porosity Correction," *Icarus* **215**, 83–100 (2011).
- ³ C.M. Bachmann, W. Philpot, A. Abelev, and D. Korwan, "Phase Angle Dependence of Sand Density Observable in Hyperspectral Reflectance," *Remote Sensing of the Environment* (in review).
- ⁴ C.M. Bachmann, A. Abelev, et al., "A Multi-Sensor Approach to Coastal Characterization," in *Optical Remote Sensing of the Environment, Sensor Fusion and Lidar I (RTu1E)* (Optical Society of America, 2012).
- ⁵ J. Kolbuszewski, L. Nadolski, and Z. Dydacki, "Porosity of Wind-deposited Sands," *Geological Magazine* **87**, 433–435 (1950).
- ⁶ C.M. Bachmann, D. Gray, A. Abelev, and W.D. Philpot, "Linking Goniometer Measurements to Hyperspectral and Multi-Sensor Imagery for Retrieval of Beach Properties and Coastal Characterization," in *SPIE Defense, Security, and Sensing: Algorithms, and Technologies for Multispectral, Hyperspectral, and Ultraspectral Imagery XVIII* **8390-48** (2012).
- ⁷ C.M. Bachmann, D. Gray, A. Abelev, et al., "A Field Portable Hyperspectral Goniometer for Coastal Characterization" (*IEEE Geoscience and Remote Sensing Society (GRSS)*, 2012). doi:WEPP.380.





Simulation, Computing, and Modeling

220 Robotic Multiaxial Testing and Constitutive Characterization of Composites

222 How Clutter and Expertise Affect Search in Geospatial Displays

Robotic Multiaxial Testing and Constitutive Characterization of Composites

J.G. Michopoulos,¹ J.C. Hermanson,² and A. Iliopoulos³

¹*Materials Science and Technology Division*

²*Forest Products Laboratory, USDA Forest Service*

³*George Mason University*

Introduction: Determining the constitutive response of polymer matrix composite materials is a critical requirement for using such materials in naval applications. This information is essential to structural design, material qualification and certification, material manufacturing, maintainability, and structural health monitoring. Over the past decade, we have been engaged in an effort to automate both the massive multiaxial testing of composite coupons required for constitutive characterization and the computational methodologies required for extracting the constitutive response from these tests. Here we report on the completion of the first recursively defined, custom-made, hexapod testing machine, capable of 6-degree-of-freedom (6-DoF) tests, and the first high-throughput, data-driven campaign of experiments for the purpose of constitutive characterization. Our approach is motivated by the data-driven requirements of employing design optimization principles for determining the constitutive behavior of composite materials.¹

NRL66.3 – NRL's Robotic Multiaxial Testing System: NRL's work in developing multi-degree-of-freedom automated mechatronic testing machines in conjunction with energy-based inverse characterization methodologies has culminated in the most recent advanced system, named NRL66.3, shown in Fig. 1(a). The NRL66.3 system has a recursive character; it has a hexapod configuration that is repeated six times. Details of the design reasoning, architecture, systemic requirements, and hardware and software prototyping are provided elsewhere.² The most critical recursion of this hexapod consists of the assembly connecting the bottom and top star-shaped frames with six linear actuators that are digitally controlled, through six spherical joints, which is known to the parallel robots community as a 6-6p parallel linkage mechanism. This configuration enables the conversion of the linear motion of the six actuators to the 6-DoF motion of a movable platform (upper section of the system with the associated upper grip). This motion corresponds to the three translations along the axes of an orthogonal Cartesian system located in the midpoint of the specimen between the grips, and three rotations about the same three axes. Therefore, a specimen gripped between the two grips as depicted in Fig. 1(b,c) can be tested in a loading path defined by the

evolution of any linear combination of these six motions, resulting in the most general possible multiaxial state of loading.

The other associated recursions consist of hexapods that contain in-line displacement and force sensors instead of linear actuators. Another critical feature of the system is the integration of two pairs of stereoscopic machine vision systems, custom developed for implementing the in-house developed full field displacement and strain measurement method known as Meshless (or Mesh Free) Random Grid Method (MRGM).³ Two additional collaborating serial robotic systems are used in a synergistic manner for inserting and extracting the specimens into and out of the grips before and after each testing sequence along a pre-defined loading path.

Computational Implementation of Constitutive Characterization: For the general case of a composite material system, we consider that a modified anisotropic hyperelastic strain energy density function can be constructed to encapsulate both the elastic and the inelastic responses of the material. However, certain classes of composite materials reach failure after small strains and some under large strains. For this reason, we developed two formalisms, one involving a small (infinitesimal) strain energy density (SSED) and another involving a finite (large) strain energy density (FSED). The material parameters to be determined are 9 elastic constants and potentially 12 damage constants, a total of 21.

To determine the material parameters that define the constitutive response, the inverse problem at hand is solved through a design optimization approach described by the iterative logic depicted in Fig. 2. The implementation of this logic employs a computational infrastructure controlled by a Matlab application, where the forward solution of the instantaneous finite element analysis (FEA) was accomplished by a computational customization and parallelization of the ANSYS commercial package.

The objective functions required for the optimization were constructed to express the difference between experimentally measured quantities and their analytical counterpart as predicted from the constitutive model under characterization. The required experimental values of the strains were measured via the REMDIS-3D software,³ developed by our group; one can obtain full field measurements of the displacement and strain fields over any deformable body. Thus, our experimental measurements for the formation of the objective functions were chosen to be the strains at the nodal points of the FEM discretization. The selected objective functions were implemented in Matlab, and we used a global Monte Carlo optimizer for determining the material parameters.

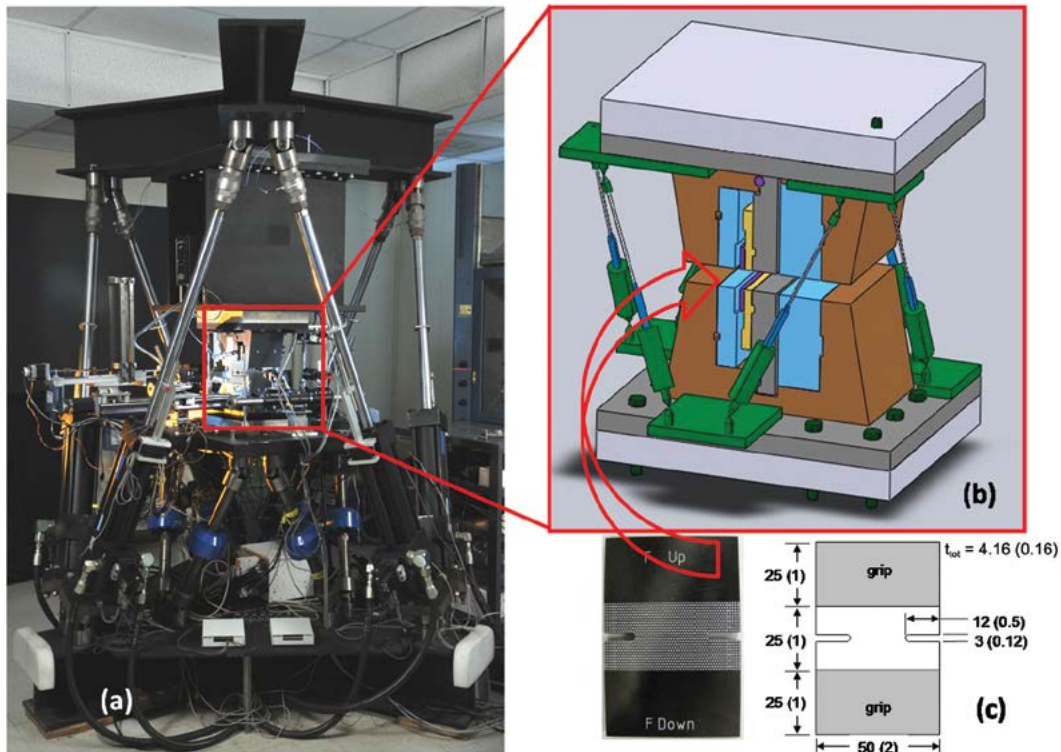


FIGURE 1
 (a) View of the NRL66.3, a 6-DoF mechatronically automated system for the multiaxial testing of composite materials; (b) schematic representation of the grip assembly; (c) typical specimen view with specifications in mm (inches).

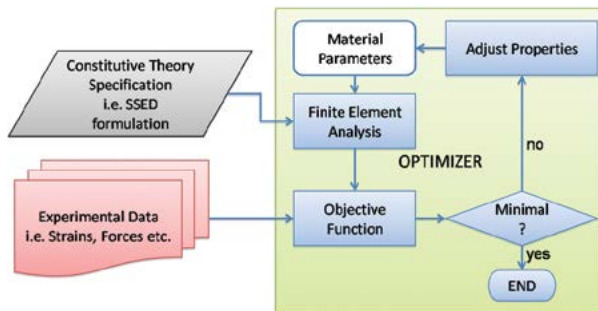


FIGURE 2
 Computational design optimization logic overview.

Experimental Campaign: We found that 72 proportional loading paths are required to sample homogeneously the 6-DoF space defined by the three translations and three rotations that can be applied by the moveable grip of the NRL66.3. We used a single specimen per loading path and then repeated the process, requiring 144 specimens per material system. Each material system was a balanced laminate with an alternating angle of fiber inclination per ply relative to the vertical axis of the specimen, which is perpendicular to the axis defined by the two notches of the specimen. Four angles were used (± 15 , ± 30 , ± 60 , ± 75 degrees), leading to $4 \times 144 = 576$ specimens. The ma-

terial was an AS4/3506-1 epoxy resin/fiber, the original material used for Navy's F/A-18 Hornet platform. Additional considerations raised the final specimen total to 1152. All specimens were tested using NRL66.3 on its inaugural run in May/June 2011. All tests were completed in 12 work days; peak throughput was 28 tests/hour. An example of the testing process can be viewed at <http://www.youtube.com/watch?v=Cp18y3HAqsM>. The tests yielded 13 TB of data from the sensors and cameras of the system. Using the collected data and the optimization approach outlined above for the case of the SSED, we identified all the material constants. By applying FEA for the cases that correspond to the specific loading path corresponding to a particular test, we compared the predicted distribution of any component of the strain or stress tensor to the experimental one. To demonstrate how well our identified constitutive model can capture the behavior of the coupons used to obtain the data used in the characterization process, we present in Fig. 3 a typical example of the distribution of ϵ_{yy} (strain) as measured by the MRGM (left column) and as predicted by the FSED theory (right column), for both the front (top row) and back (bottom row) of a specimen. The observed deviation between predicted and experimental strains never exceeded 3.5%.

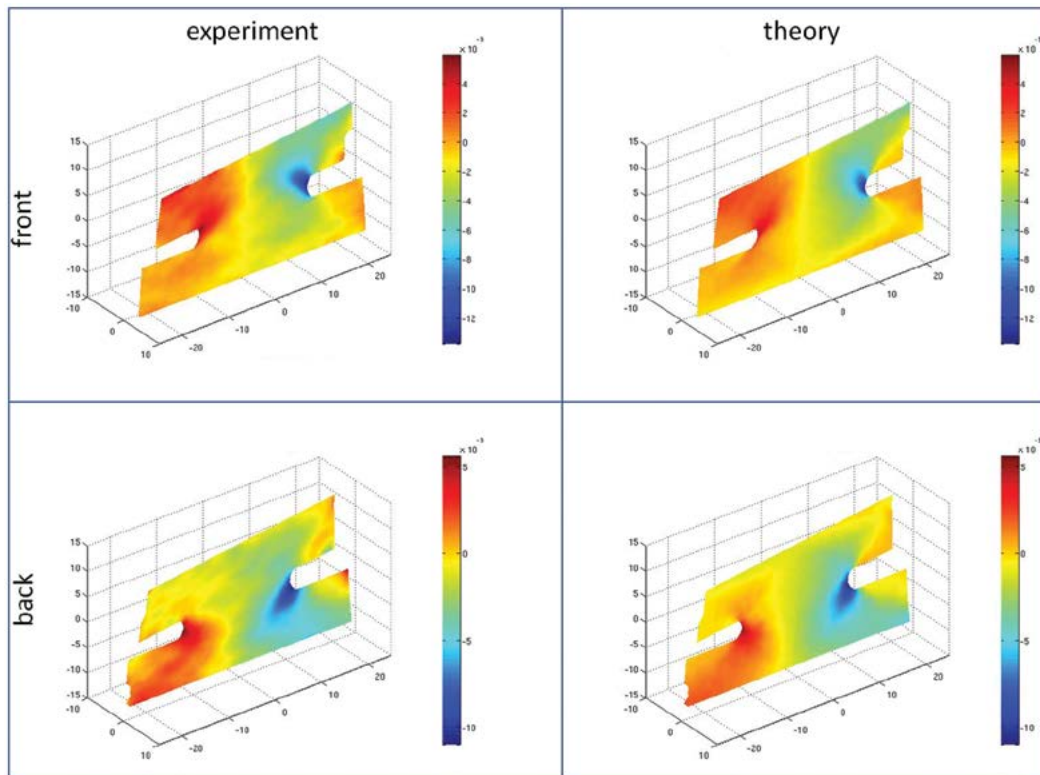


FIGURE 3 Comparison of ϵ_{yy} strain field as measured (left column) and as predicted by the identified model (right column) for the case of in-plane rotation and torsion of a ± 60 degree laminate for both the front side (top row) and the back side (bottom row) of a specimen.

Conclusions: The success of this approach provides closure to the problem of determining the constitutive response of anisotropic materials such as polymer matrix composites used in naval platforms. This approach opens the door for a new and fundamentally different look at the design of composite structures and the associated applications. The derived constitutive response is intrinsically validated because it is based on the measured multiaxial response of the material of interest. The potential for economic and optimally tailored designs of the future is limitless.

[Sponsored by ONR and the NRL Base Program (CNR funded)]

References

- ¹J.G. Michopoulos, J.C. Hermanson, A. Iliopoulos, S.G. Lambros, and T. Furukawa, "Data-Driven Design Optimization for Composite Material Characterization," *J. of Computing and Information Science in Engineering* **11**(2), 1–10 (2011).
- ²J.G. Michopoulos, J.C. Hermanson, and A. Iliopoulos, "Towards a Recursive Hexapod for the Multidimensional Mechanical Testing of Composites," Proceedings of the ASME 2010 International Design Engineering Technical Conferences and Computers and Information in Engineering Conference, no. DETC2010/CIE-28699, pp. 91–99 (2010).
- ³J.G. Michopoulos and A. Iliopoulos, "A Computational Workbench for Remote Full Field 3D Displacement and Strain Measurements," Proceedings of the ASME 2011 International

Design Engineering Technical Conferences and Computers and Information in Engineering Conference IDETC/CIE, August 29–31, 2011, Washington, DC, Vol. 2, pp. 489–498.



How Clutter and Expertise Affect Search in Geospatial Displays

M.E. Trenchard¹ and M.R. Beck²

¹Marine Geosciences Division

²Louisiana State University

Introduction: Clutter and expertise play significant roles in the search performance of users viewing complex geospatial displays.^{1,2} As geospatial displays become more complex in a networked battlespace environment, it is critical in both the design and assessment of these displays to ensure that warfighter performance is optimized. Using a quantitative measure of clutter (NRL's Color-Clustering Clutter (C3) algorithm¹), we can obtain a better understanding of how expertise affects performance at varying levels of clutter and use this information to assess geospatial display systems and improve training doctrine. Clutter may be mea-

sured both on a global basis (whole image), which relates favorably to set size (i.e., the number of distractors), and locally (area very near the target), which relates favorably to crowding effects. Increases in both types of clutter in geospatial displays lead to decreases in search performance for nonexpert participants.¹

Research has shown that experts perform better on tasks relevant to their area of expertise because they use a more efficient allocation of visual attention.² The current research extended this previous research by examining how clutter and expertise affect search performance.

Experimental Design: Thirty-one F/A-18 fighter pilots recruited from various squadrons stationed at Naval Air Station (NAS) Oceana, Virginia, served as our expert group. The pilots were primarily male (28 male, 3 female) with an average age of 30 (range: 25–38, standard deviation (SD) = 4.4) and had an average of 1390 flight hours and 242 combat flight hours. An age-matched control group included 18 NRL participants, primarily scientists. The NRL participants were primarily male (16 male, 2 female) with an average age of 31 (range: 20–49, SD = 6.9) with no flight or navigation background. The stimuli were 72 different base charts with 24 each of low, medium, and high global clutter as shown in Fig. 4. Three different versions of each base chart were created: a target was placed in a region of high local clutter or low local clutter, or the target was

absent. The same target symbol was used in each chart, varying only in color in an effort to make the target distinguishable yet similar to other colors in the chart. This control for target saliency is important because a high-contrast target is found quickly regardless of the amount of clutter in the chart.³

Participants were instructed to determine whether a target was present or absent in each chart. If a participant responded that the target was present, another screen was displayed that instructed him or her to click on the target with the mouse. The chart would appear again and the participant used the mouse to click on the target. If the participant indicated that the target was absent, or a one-minute time-out occurred, the trial ended.

Results: Responses were coded as accurate, inaccurate, or timeout. A $3 \times 3 \times 2$ mixed model analysis of variance (ANOVA) was conducted with three levels of global clutter (high, medium, low), three types of target presence (high, low, absent), and two levels of expertise (pilots, age-matched control) for accuracy and reaction time on accurate trials.

Accuracy: Accuracy was calculated by dividing the number of accurate trials by the number of trials for which a response was given within the one-minute time limit. Experts (i.e., pilots) were significantly more accurate than the control group on the high and medium global clutter trials when the target was in a high local clutter region. The control group was more accurate than the experts on the high global clutter/target absent trials. There were statistical main effects for global clutter and target presence, but not a main effect for expertise (see Fig. 5). However, there were significant interactions between global clutter and expertise, and target presence and expertise, and a three-way interaction among target presence, global clutter, and expertise.

Reaction Time: Experts were slower to respond for low global clutter/target absent trials and slower on the high local trials for both medium and low global clutter. While there were main effects for both global clutter and target presence, there was only a marginal main effect for expertise (see Fig. 6).

Conclusions: Our research indicates that both global and local clutter slow search performance and impair search accuracy. Search impairment is particularly prevalent for high and medium global/high local clutter conditions. Expertise did not improve performance across all trial types. However, when the target was present and difficult to find due to high local clutter and medium to high global clutter, experts were better able to accurately find the target. Although

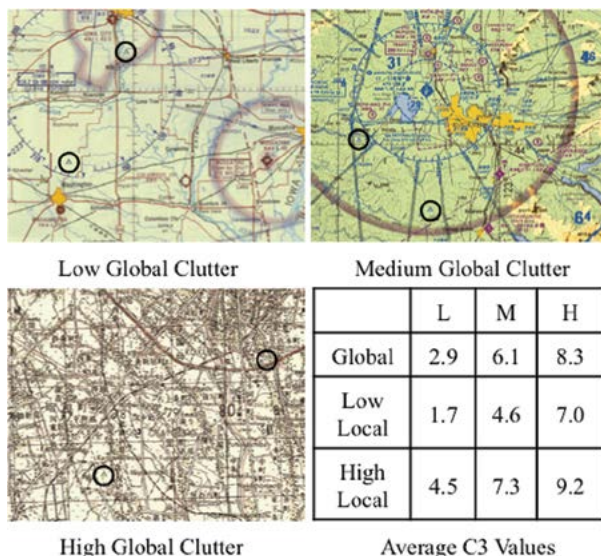


FIGURE 4
Examples of the low, medium, and high global clutter charts. Black circles indicate the location of high and low local clutter targets. In the versions used in the experiment, only one target was present or no target was present. The black circles are added here to draw attention to the target locations and were not present in the experiment. At bottom right is a table of the average global, low local, and high local C3 clutter values for the low (L), medium (M), and high (H) global clutter charts.

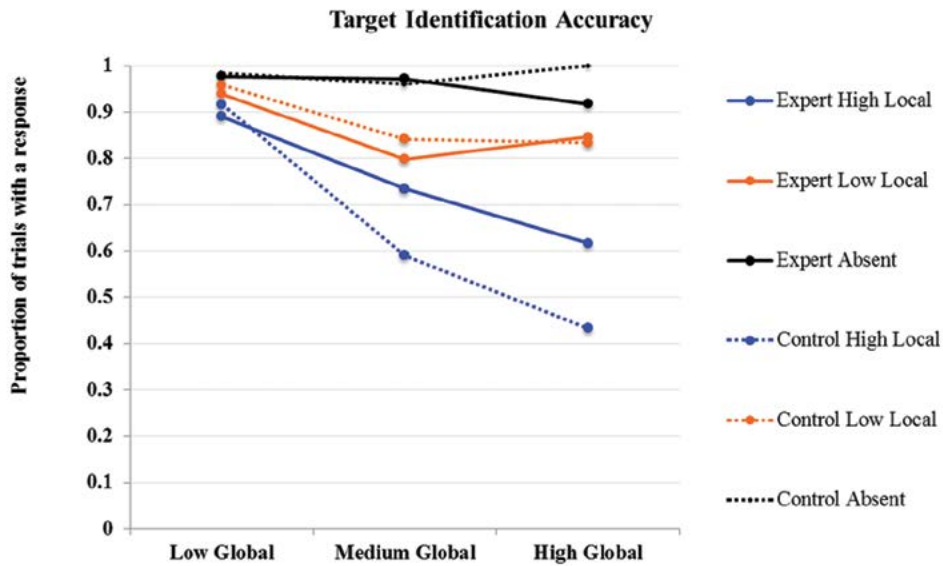


FIGURE 5
Trials in which an accurate response was given within the one-minute time limit.

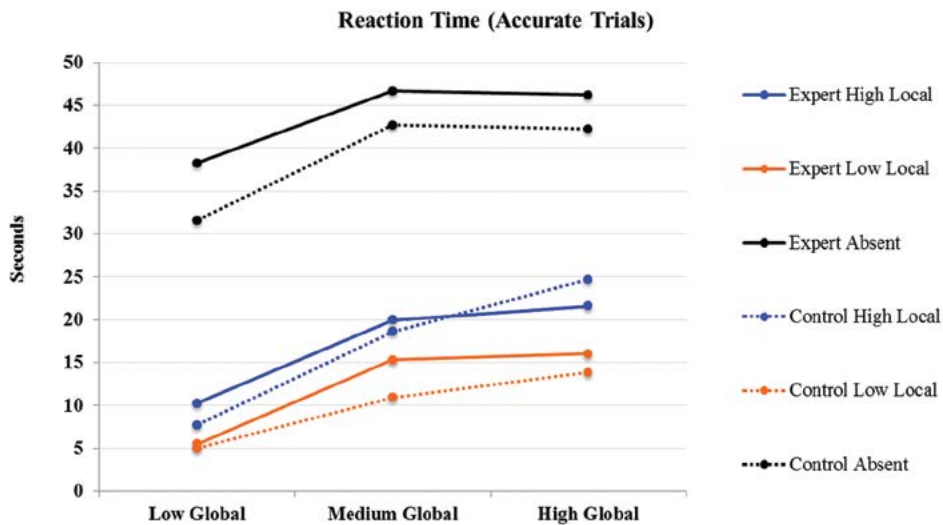


FIGURE 6
Reaction time for accurate trials only.

experts were also slower to respond on the low local/medium global clutter trials, suggesting performance may have improved due to spending more time looking, this was not the case in the high local/high global clutter trials, suggesting that something else may be driving the higher levels of performance on these trials. In addition, analysis of fixation durations and distances between fixations indicate that experts have slightly longer fixation durations, thus taking more time to process information in each fixation. It is not clear if this effect is primarily responsible for the performance improvement in high global/high local clutter conditions.

This research is an important step in deciphering what cognitive processes are at work when extracting information from complex geospatial displays. Further, expertise appears to play a greater role in information retrieval from these displays, particularly as clutter increases. Ultimately, this research can lead to improvements in geospatial display design and improved training doctrine for visual interpretation of these displays.

Acknowledgments: We thank the pilots and navigators at NAS Oceana and the scientists and support personnel at NRL who participated in these experiments. We also thank Ms. Amanda van Lamsweerde

and Ms. Rebecca R. Goldstein at Louisiana State University for their help in the gathering and analysis of this data. Finally, we thank Ms. Maura Lohrenz for her vision and guidance on this project as former principal investigator.

[Sponsored by the NRL Base Program (CNR funded)]

References

- ¹ M.R. Beck, M.C. Lohrenz, and J.G. Trafton, "Measuring Search Efficiency in Complex Visual Search Tasks: Global and Local Clutter," *Journal of Experimental Psychology: Applied* **16**(3), 238–250 (2010).
- ² H.J. Godwin, S.P. Liversedge, J.A. Kirkby, K. Cornes, M. Boardman, and N. Donnelly, "The Influence of Experience upon Threat Assessment and Visual Searching Complex Scenes," poster presented at the annual meeting of the Vision Sciences Society, Naples, FL, May, 2012.
- ³ M.R. Beck, M. Trenchard, A. Lamsweerde, R. Goldstein, and M. Lohrenz, "Searching in Clutter: Visual Attention Strategies of Expert Pilots," Proceedings of the Human Factors and Ergonomics Society 54th Annual Meeting, Boston, MA, October 2012, pp. 1411–1415.





228 Ground-Based Investigation of Near-Earth Space Plasma Processes in the NRL Space Physics Simulation Chamber

229 Artificial Ionospheric Plasma Clouds Using HAARP

232 Maritime Detection of Radiological/Nuclear Threats

233 RAIDER-M: Transitioning Space Systems Knowledge to Terrestrial Remote Sensing

235 Morphing Satellite Reflector Antennas Using Tensegrity Structures

Ground-Based Investigation of Near-Earth Space Plasma Processes in the NRL Space Physics Simulation Chamber

W.E. Amatucci,¹ D.D. Blackwell,¹ G.R. Gatling,¹
E.M. Tejero,¹ C.D. Cothran,² D.N. Walker,² and
E.D. Gillman³

¹Plasma Physics Division

²Sotera Defense Solutions, Inc.

³National Research Council Postdoctoral Fellow

Introduction: The NRL Space Physics Simulation Chamber Laboratory conducts a broad-based research program addressing near-Earth space plasma physics. The unique Space Chamber device (shown in operation in Fig. 1) produces large-volume, steady-state, space-like plasmas with conditions scaled to match various ionospheric and magnetospheric regions of interest. The program includes basic research illuminating the underlying physics driving key space plasma processes and applied research for understanding plasma effects on spacecraft systems, testing spacecraft hardware, and development of innovative plasma sensors.



FIGURE 1

The NRL Space Physics Simulation Chamber with the helicon plasma source in operation. The main chamber is 2 m in diameter and 5 m long, allowing for the creation of large-scale plasmas and accommodation of spacecraft hardware. The source chamber is 0.55 m in diameter and adds 2 m to the chamber length.

Simulating High-Altitude Space Physics: Recent Space Chamber investigations have addressed issues involving dynamic particle interactions in the radiation belts and the effects of discharges between rendezvousing spacecraft at geosynchronous orbit. The radiation belts are regions of space where high-energy particles remain trapped by the Earth's magnetic field, posing a

serious threat to the lifetime of orbiting satellites. In the natural environment, electromagnetic plasma whistler waves limit the number of high-energy particles by scattering them from their trapped orbits. NRL theorists have proposed techniques building on nature's example to protect space assets by generating whistler waves that enhance the scattering process.

Important aspects of these techniques are being tested in the Space Chamber. For example, under certain conditions, the radiation belt electron populations themselves can be used to amplify whistler waves, leading to accelerated loss of the dangerous particles. This depends upon having wave-particle interaction times sufficient for amplification to occur. However, the required interaction times are difficult to achieve in laboratory-scale devices, which cannot match the vast spatial and temporal scales of space. This limitation has been overcome in the Space Chamber by creation of high-Q standing whistler wave patterns.¹ By repeated reflection of antenna-driven whistler waves from controlled boundaries, long interaction times between a whistler wave and injected energetic electrons can be achieved, allowing for detailed comparisons with theory and simulation results.

The ability of the large-volume Space Chamber to precisely control conditions while being able to manipulate realistic spacecraft hardware was exploited recently in a joint NRL-NASA-DARPA project to investigate the effects of high-voltage discharges between rendezvousing spacecraft at geosynchronous orbital altitudes. Figure 2 shows examples of grippers from robotic arms being developed for the NRL SUMO/FREND program approaching target spacecraft hardware, which could be charged up to 10,000 V. The experiments demonstrated the current profile that can be expected in such discharges and the effects of repeated discharging, and tested possible mitigation methods.

Simulating Low-Altitude Space Plasmas: In an effort to understand space weather phenomena in the auroral ionosphere, Space Chamber research has produced the first observations of electromagnetic ion cyclotron (EMIC) waves driven by nonuniform, or sheared, plasma flows.² The origin of EMIC waves in the ionosphere is not known, but they can influence space weather through energy transport, ion heating, and outflow. In the Space Chamber, sheared plasma flows are driven by localized electric fields designed to match electric fields associated with EMIC waves in space. The threshold plasma conditions necessary for EMIC wave excitation in the presence of sheared flow and frequency and wave vector spectra have been identified in the laboratory. The discovery of a localized source of EMIC waves impacts the energy balance of space weather models since the waves can effectively

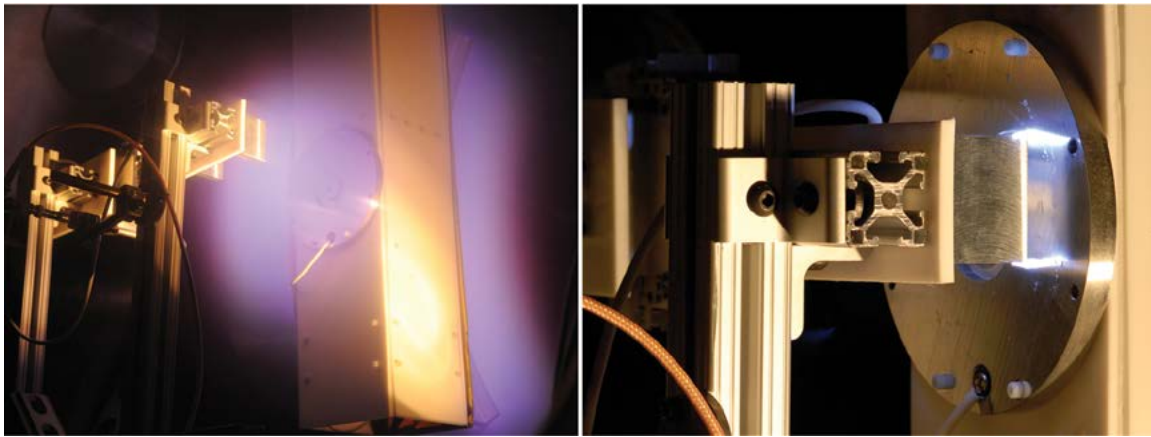


FIGURE 2

Photographs showing high-voltage discharges between simulated components of spacecraft rendezvousing at geosynchronous orbit. The photo on the left shows the dc glow discharge plasma that forms around the charged components when neutral gas is added to simulate the firing of thrusters. The photo on the right shows the arc discharge that occurs when the target and simulated gripper are brought within close proximity.

reflect back a portion of incident energy to the magnetosphere, while locally heating heavy ions and initiating bulk plasma transport.

Space Sensor Development: An innovative plasma impedance probe under development in the Space Chamber Laboratory shows promise for outperforming standard plasma parameter diagnostics.^{3,4} In laboratory testing, the NRL impedance probe has provided more accurate plasma density measurements than standard probe techniques, as well as accurate determination of plasma potential and electron temperature. Characterization of these basic plasma parameters is integral to nearly all laboratory plasma experiments and near-Earth space weather investigations. The laboratory investigations have also illustrated that the NRL impedance probe can yield useful data in operational regimes where other techniques are not feasible, opening up many new possibilities for making measurements in industrial processing plasmas and in atmospheric pressure discharge experiments. Additionally, in the space environment, there presently are no simple, dedicated sensors to monitor spacecraft charging, which can pose a serious threat to satellite operations. The sensitivity of the NRL plasma impedance probe response to slight changes in the sheath surrounding a charged object provides unique opportunities for early detection of the onset of hazardous levels of spacecraft charging.

A version of the probe that will focus on tracking plasma electron density will undergo its first space test flight aboard the NRL Tether Electrodynamics Propulsion CubeSat Experiment (TEPCE). The density measurements provided by the Space Plasma Diagnostic Suite (SPADE) will aid in the determination of TEPCE's efficiency for collection of ionospheric electrons and provide a key initial test of this emerging technology.

[Sponsored by the NRL Base Program (CNR funded), DTRA, NASA, and AFOSR]

References

- ¹W.E. Amatucci, D.D. Blackwell, E.M. Tejero, C.D. Cothran, L. Rudakov, G.I. Ganguli, and D.N. Walker, "Whistler Wave Resonances in Laboratory Plasma," *IEEE Trans. Plasma Sci.* **39**(2), 637–643 (2011).
- ²E.M. Tejero, W.E. Amatucci, G. Ganguli, C.D. Cothran, C. Crabtree, and E. Thomas, Jr., "Spontaneous Electromagnetic Emission from a Strongly Localized Plasma Flow," *Phys. Rev. Lett.* **106**(18), 185001 (2011).
- ³D.D. Blackwell, D.N. Walker, S.J. Messer, and W.E. Amatucci, "Characteristics of the Plasma Impedance Probe with Constant Bias," *Phys. Plasmas* **12**(9), 093510 (2005).
- ⁴D.N. Walker, R.F. Fernsler, D.D. Blackwell, W.E. Amatucci, and S.J. Messer, "On Collisionless Energy Absorption in Plasmas: Theory and Experiment in Spherical Geometry," *Phys. Plasmas* **13**(3), 032108 (2006).

Artificial Ionospheric Plasma Clouds Using HAARP

P.A. Bernhardt,¹ C.L. Siefring,¹ S.-M. Han,¹ D.L. Byers,¹ A. Fliflet,¹ S.C. Briczinski,² M. Wilkens,³ and E.G. Kendall⁴

¹Plasma Physics Division

²National Research Council Postdoctoral Fellow

³Sotera Defense Solutions

⁴SRI International

Introduction: Artificial balls of plasma have been produced in the upper atmosphere (160 to 200 km altitude) using the 3.6 MW high frequency (HF) transmitter facility known as HAARP (High frequency Active Auroral Research Program). These glow plasma

discharges were generated in November 2012 as a part of the Basic Research on Ionospheric Characteristics and Effects (BRIOCHE) campaign in Alaska. The plasma balls (or electron density enhancements) are being studied for use as artificial mirrors at altitudes 50 km below the natural ionosphere to be used for reflection of HF radar and communications signals. The density of these plasma clouds is proportional to the square of the transmission frequency, which is an integer harmonic of the electron cyclotron frequency.

Recent Accomplishments: NRL scientists in the Plasma Physics Division succeeded in producing artificial plasma clouds with densities exceeding 9×10^5 electrons per cm^3 using HAARP transmission at the 6th harmonic of the electron cyclotron frequency at 8.58 MHz. In previous work, lower density plasma density clouds at lower frequencies had lifetimes of only 10 minutes or less.¹ This higher density plasma density ball was maintained for over one hour by the HAARP transmissions and could have been sustained indefinitely by the ground HF radio transmissions. The NRL team is working on this project with collaborators at the Air Force Research Laboratory, SRI International, the University of Alaska in Fairbanks, the University of Florida, and BAE Systems.

The glow of artificial plasma clouds is directly detected with low light level cameras.² The optical images of the artificial plasma balls show that they are turbulent with dynamically changing density structures (Fig. 3). Electrostatic waves generated by the HAARP radio transmissions are thought to be responsible for accelerating electrons to high enough energy to produce the glow discharge in the neutral atmosphere.

Radio diagnostics of the artificial plasma clouds are (1) ground-based radio soundings and (2) reception of stimulated electromagnetic emissions (SEE).² Figure 4 illustrates the signature of an artificial plasma cloud near the 4th gyro harmonic resonance in the ionosphere. When the electromagnetic pump wave is tuned to the resonance, the electrostatic waves are generated by the parametric decay instability. These waves are converted to electromagnetic emissions to be detected on the ground as downshifted spectral features. These same electrostatic waves accelerate electrons to high enough energy for collisional ionization of the ambient neutral gas forming the plasma cloud. The ionospheric sounder detects this cloud as an apparent layer below the ambient ionosphere.

Theory and Modeling: The parametric interactions theory is being developed into a comprehensive model of the plasma cloud generation. High-power electromagnetic fields are propagated to the ionosphere using multidimensional magnetionic theory in both the ambient and modified plasma. At plasma resonance points in the atmosphere, different modes are excited including electron Bernstein, upper hybrid, and whistler waves. The waves with phase velocities that match the speeds of electrons transfer energy to the background electrons. Electrons with energies above the ionization potential of the ambient neutrals cause breakdown of these neutrals. The avalanche process that yields dense clouds of plasma is being investigated with a suprathermal electron source introduced into the NRL SAMI3 plasma transport model. The goal of the theoretical efforts is to develop techniques for the production of denser and more stable electron density clouds.

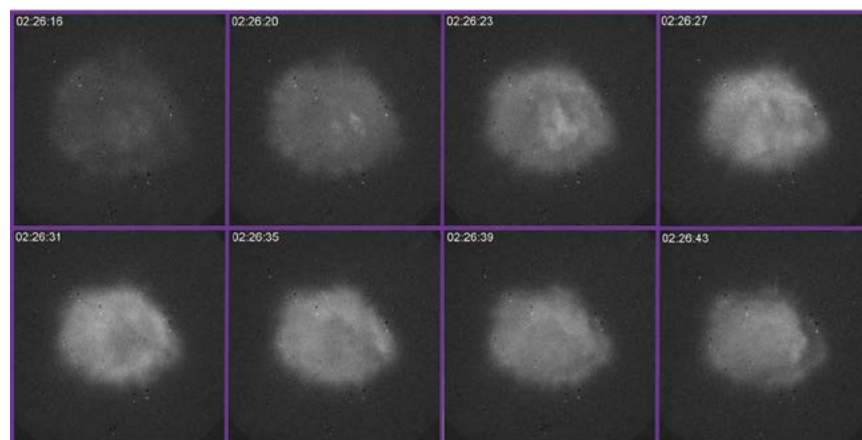


FIGURE 3 Sequence of images of the glow plasma discharge produced with transmissions at the 3rd electron gyro harmonic using the HAARP HF transmitter in Alaska. The 3rd harmonic artificial glow plasma clouds were obtained with HAARP using transmissions at 4.34 MHz. The resonant frequency yielded green line (557.7 nm) emission with HF on 12 November 2012 between the times of 02:26:15 and 02:26:45 GMT. (Images provided by Elizabeth Kendall of SRI International)

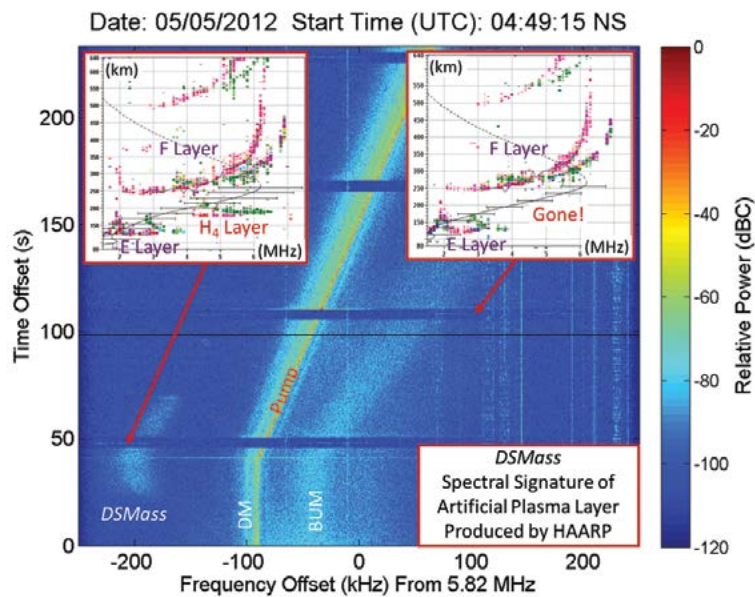


FIGURE 4

Radio frequency spectrograph showing the stimulated electromagnetic emissions from the ionosphere during times of artificial plasma cloud generation. The inset figures are ionosonde records of the ionosphere with (left) and without (right) a signature of an artificial plasma cloud. The H₄ layer is labeled to indicate the plasma cloud produced with an HF pump wave near the 4th gyro harmonic. This ionosonde feature is preceded by the DSMass spectral emissions centered 110 kHz below the transmitter frequency. Tuning the pump frequency away from the 4th harmonic resonance eliminates both the DSMass and the H₄ layer plasma cloud. (DSMass = downshifted mass; DM = downshifted maximum; BUM = broad upshifted maximum)

Laboratory Experiments: The HAARP experiments are being complemented with a series of laboratory studies using high-power electromagnetic waves to produce glow plasma discharges (Fig. 5). A microwave signal at 2.45 GHz is amplified using a porous spherical cavity resonator developed in the Plasma Physics Division to break down the neutral gas inside the resonator.³ A low-pressure chamber developed for microwave processing has been modified for these demonstrations of plasma ball creation. The microwave-driven plasma laboratory is being used as a surrogate for HAARP to study the role of initial plasma seeds for creation and maintenance of artificial plasma clouds. These experiments have shown that it is difficult to produce electron clouds with densities greater than the critical frequency

for reflection of the incident electromagnetic wave. Also, slow venting of neutral gases into the chamber has been used to study the effect of composition changes and neutral winds on the formation of the artificial plasma glow discharges.

Summary: By successfully making stable plasma clouds in both the upper atmosphere and the laboratory, NRL scientists are closer to producing artificial ionospheric mirrors with high-power radio waves. Breakthroughs in plasma cloud formation are accomplished by integrating HAARP upper atmospheric experiments, computer modeling with nonlinear plasma theory, and laboratory breakdown experiments.

Acknowledgments: Operations of the HAARP Ionospheric Research Instrument were provided by Marsh Creek LLC under support from the Air Force Research Laboratory.

[Sponsored by DARPA and the NRL Base Program (CNR funded)]

References

- ¹ E. Sergeev, S. Grach, A. Shindin, E. Mishin, P. Bernhardt, S. Briczinski, B. Isham, M. Broughton, J. LaBelle, and B. Watkins, "Artificial Ionospheric Layers During Pump Frequency Stepping Near the 4th Gyroharmonic at HAARP," *Phys. Rev. Lett.*, in press, 2013.
- ² E.G. Kendall, R. Marshall, R.T. Parriss, A. Bhatt, A. Coster, T. Pedersen, P. Bernhardt, and C. Selcher, "Decameter Structure in Heater-Induced Airglow at the High Frequency Active Auroral Research Program Facility," *J. Geophys. Res.* **115**, A08306 (2010), doi:10.1029/2009JA015043.
- ³ P.A. Bernhardt and R.A. Fernsler, "Electric Field Amplification Inside a Porous Spherical Cavity Resonator Excited by an External Plane Wave," *IEEE Trans. Ant. Prop.* **60**, 832-839 (2012).



FIGURE 5

Plasma ball generated inside a polyhedral cavity resonator with an external microwave field. The dynamics of the laboratory-generated glow plasma discharge are similar to those generated below the ionosphere by HAARP high-frequency transmissions.

Maritime Detection of Radiological/ Nuclear Threats

B. Philips, E. Wulf, L. Mitchell, A. Hutcheson, and W.N. Johnson
Space Science Division

Introduction: Improved detection of weapons of mass destruction is one of the seven critical capabilities identified in the most recent Quadrennial Defense Review (QDR). It is therefore also one of the science and technology (S&T) priorities of the Secretary of Defense for fiscal years 2013 to 2017. Unfortunately, the remote detection of special nuclear materials (fissile materials that can be used to make a nuclear weapon) is difficult because the materials are not very radioactive, and because the radiation signature decreases rapidly with distance. An additional problem is that there are many sources of naturally occurring and manmade radioactive materials that can cause confusion when looking for a faint source of radiation.

The Radiation Detection Section of NRL's High Energy Space Environment Branch has been developing gamma-ray detection instruments for ground-based and space-based applications for years. One such system, MISTI (Mobile Imaging and Spectroscopic Threat Identification), was developed for the Domestic Nuclear Detection Office (DNDO) of the Department of Homeland Security (DHS). The MISTI instrument¹ was mounted in a 20 ft box truck and was delivered to DHS in October 2009.

SuperMISTI: SuperMISTI^{2,3} is a follow-on instrument to the MISTI instrument and is designed for standoff detection in a maritime environment. It was developed as part of the Office of Naval Research (ONR) Maritime Weapons of Mass Destruction Detection program. The instrument consists of two standard refrigerated containers, each with its own power, communications, optical cameras, and GPS systems.

One container holds an array of high-purity germanium (HPGe) detectors (see Fig. 6). These cryogenic detectors can measure the energy of gamma rays with a high degree of accuracy, i.e., fine energy resolution. This accuracy helps solve the detection problem in two ways. First, the precise measurement of the energy provides unambiguous determination of the isotope emitting the gamma rays and allows the differentiation between isotopes of interest and other natural or manmade radioactive isotopes. The second advantage of the high energy resolution is that very little natural radiation background is exactly within the narrow energy band relevant for the isotopes of interest. The effective background is therefore quite low and the sensitivity of the system much improved.

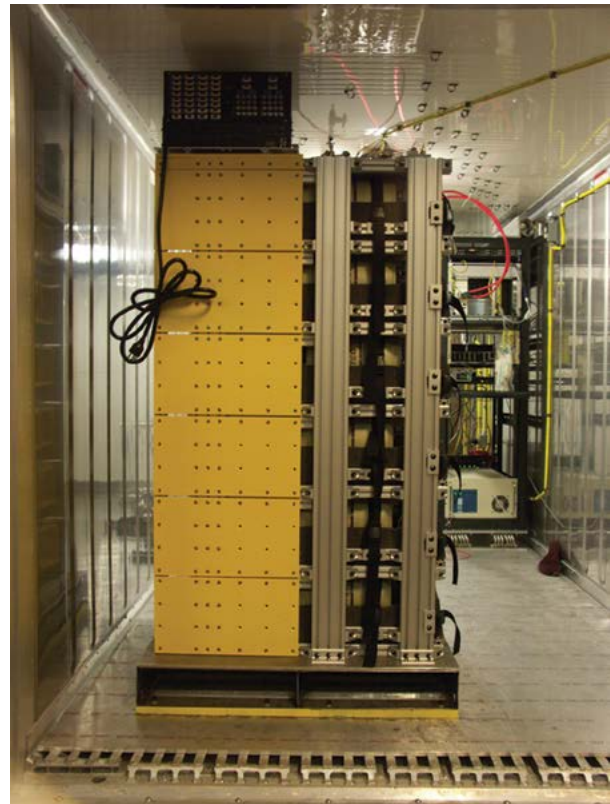


FIGURE 6
Photograph of the pallet containing high-purity germanium (HPGe) detectors.

The second container holds a gamma-ray imaging camera based on a two-dimensional array of sodium iodide detectors and a coded aperture camera. The sodium iodide detectors image the gamma rays that pass through the coded aperture. The coded aperture consists of a pattern of lead blocks that create a shadow on the detector array. The position of the shadow allows the position of the gamma-ray source to be reconstructed. The gamma-ray camera provides images but has a relatively poor energy measurement capability. The camera is therefore cued by the high-purity germanium array and together, the systems allow for sensitive detection, isotope identification, and three-dimensional localization of a source of gamma rays.

The MANTA Campaign: In July 2012, the SuperMISTI instrument was deployed at Norfolk Naval Station for the MANTA test campaign. The MANTA test campaign was organized by ONR to determine the on-water performance of different radiation detection systems. The deployed systems were tasked with detecting sources hidden in different types of vessels that were either docked at a pier or moored in open water. The two SuperMISTI containers were deployed on a 60 ft barge as shown in Fig. 7. The large cylindrical containers seen on the right-hand side of the photo-

graph were ballast tanks to keep the barge level. During the MANTA campaign, the barge was pushed by a tug at different speeds and standoff distances from vessels of interest. Some vessels contained radioactive sources. The task for SuperMISTI was to detect the sources, identify the isotopes, and localize the source on the vessel remotely.



FIGURE 7
Photograph of the two refrigerated containers on a barge at Norfolk Naval Station.

Results: The typical results for a pass of SuperMISTI by a vessel in open water are shown in Fig. 8. The photograph shows an optical photograph of the vessel being passed, and overlaid on it a gamma-ray image (blue rectangle) of the position of the radioactive source. While the position resolution of the gamma-ray



FIGURE 8
Photograph of the LCU-2000 target ship with the reconstructed radiation source position overlaid as the dark blue rectangle.

camera is quite coarse, it is sufficient to localize the position of the source on the vessel and to guide any potential boarding party. Not shown in the photograph is the spectroscopic data that allowed unambiguous identification of the isotope prior to the image reconstruction. During the MANTA test campaign, SuperMISTI correctly detected, identified, and localized all

sources it was exposed to from the standoff distances where detection was expected. SuperMISTI demonstrated the passive standoff detection of special nuclear materials in a maritime environment at operationally relevant distances.

[Sponsored by the Office of Naval Research Maritime Weapons of Mass Destruction Detection program]

References

- ¹ L.J. Mitchell et al., "Mobile Imaging and Spectroscopic Threat Identification (MISTI)," 2008 IEEE Nuclear Science Symposium Conference Record, Dresden, Germany, Oct. 2008, pp. 5575–5580.
- ² L.J. Mitchell, E.A. Wulf, B.F. Philips, A.L. Hutcheson, and B.E. Leas, "Cross Country Background Measurements with High Purity Germanium," 2011 IEEE Nuclear Science Symposium Conference Record, Valencia, Spain, Oct. 2011, pp. 319–323.
- ³ E.A. Wulf, A.L. Hutcheson, B.F. Philips, L.J. Mitchell, and B.E. Leas, "Stand-Off Detection with an Active Interrogation Photon Beam," 2011 IEEE Nuclear Science Symposium Conference Record, Valencia, Spain, Oct. 2011, pp. 315–318.

RAIDER-M: Transitioning Space System Knowledge to Terrestrial Remote Sensing

M. Haffner and C. Huffine
Space Systems Development Department

Overview: Terrestrial remote sensing systems and space-based systems face some of the same challenges. Both system classes require high reliability, autonomous operation, and remote management capability. The Advanced Systems Technology Branch of NRL's Space Systems Development Department has transitioned space system knowledge to a shipboard remote sensing platform, the RAIDER-M system. High-reliability design principles and rigorous component testing have allowed RAIDER-M to achieve continuous operation and reliable sensing and data reporting since deployment in the harsh environment at sea. Remote management principles used in space-based systems have been applied to the RAIDER-M design and have allowed the NRL team to push software updates improving the remote sensing capabilities without the need to have physical access to the fielded units.

Design for Reliability: The RAIDER-M project consists of a number of remote sensing nodes that relay data through the Iridium satellite network. Reliability was a prime consideration in designing the system, as a significant percentage of the lifecycle costs could be servicing of the deployed sensor units. Most units are deployed on ships at sea and we have only short

windows of opportunity to gain access to them once installed. With some vessels based outside the continental United States (OCONUS), servicing the units can be expensive. Also, RAIDER-M sensing units endure environmental extremes — arctic to Saharan temperatures, hurricanes, inches of ice accumulation, and the ever-present corrosive marine environment. Figure 9 shows an installed unit.



FIGURE 9
An installed RAIDER-M unit.

RAIDER-M units are constructed of all commercial off-the-shelf (COTS) components with a single-board ARM computer running Linux at the heart. To maintain operation in the field, the system is designed with a power-reset capability for all sensor and communication interfaces. The processor monitors data flow through the system and, if a problem is detected, has the ability to cycle power to any of the components. A watchdog timer capable of initiating a system reset in the event of a processor lockup also supervises the processor. Finally, there is a scheduled reboot of the system every 24 hours.

The Linux operating system running on an ARM processor provided a well-maintained and stable base upon which we were able to quickly build a remote

sensing platform. The system boots into a read-only file system stored on a secure digital (SD) card. A secondary copy of the file system is stored in on-board flash. If the primary file system is not bootable for any reason, the processor automatically boots from the secondary copy.

Components were selected based on their temperature range and power consumption specifications. Some components, most notably the Iridium modems, had limited options available that met our basic performance requirements. Many critical components underwent environmental testing to ensure they would operate over the range of extremes we expected to encounter.

All components are mounted in a watertight box constructed of marine grade stainless steel, and penetrations are limited to only environmentally sealed connectors or indicators. Penetrations are on the bottom of the unit to lessen the chance of water infiltration assisted by gravity. The units themselves are mounted to “marine board,” a noncorroding, nonrotting polymer that comes in sheets similar to plywood. A lesson learned after the initial deployment was that the relatively low reflectance of the stainless steel led to high temperatures inside the unit in warm locations, so an aluminum sunshade was designed for the enclosure to help maintain an acceptable internal temperature.

The resulting RAIDER-M units have low recurring engineering (RE) cost, with the Iridium modem being about 25% of the per-unit cost. Typical power consumption is approximately 10 W.

Software and Remote Management: While the RAIDER-M units operate autonomously in the field, they employ a remote management interface similar to that developed for satellite and aviation payloads. The RAIDER-M software is based around a Linux kernel running on the embedded single-board computer. We continued the UNIX development paradigm of implementing system functionality as small, single-purpose utility programs. We connect these small programs into a complete system through scripts written in bash shell. Embedded Linux systems with functionality built around shell scripting and these small utilities have been implemented in several other programs such as TacSat, GLADIS, Copperfield-2, and SRP.

The modular architecture provided by the bash script approach has several advantages. One advantage is the ability to easily apply the utilities to multiple portions of the overall system. If a program is written to send and receive data over a network socket, any portion of the system needing to access network sockets can use the same executable. In fact, we are able to use many of the same simple utilities developed in previous programs by simply compiling them for RAIDER-M’s

ARM architecture with no changes required in the underlying code.

Also, the use of a scripting environment allows reconfiguration of system functionality through a simple and reliable procedure. The RAIDER-M communication protocol allows us to upload and execute a script remotely. Since much of the functionality of RAIDER-M is implemented in scripts rather than large binary files, we are able to change system performance or apply bug fixes by sending small text files with new command logic. This is especially important in systems where high reliability is required and the data link bandwidth is low. The Iridium data link provides a link rate of 2.4 kbps data transfer; realistically, after protocols and packaging overhead, a 1 kbps rate is more typical.

A key to managing the “network” of the sensors is having a way to understand the health and status of individual units and the entire constellation at a single glance. A “dashboard” was developed to collect telemetry information and display it to the engineers (Fig. 10). Coupling that information with other tools such as Google Earth, LaTeX, and Gnuplot allows for instantaneous situational awareness and daily production reports. The constellation operates nearly 24/7 “lights-out” from a command and control and operations perspective.

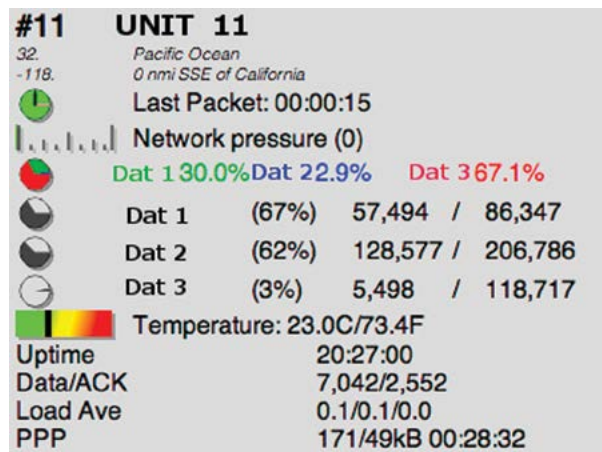


FIGURE 10
Unit dashboard display.

Summary: We have deployed approximately 16 RAIDER-M units across the globe. Several units have been operating autonomously for months and we have been able to apply software updates to fielded units remotely. The application of technology developed for high-reliability, reconfigurable space platforms has allowed us to rapidly create a reliable and reconfigurable terrestrial remote sensing system.

Acknowledgments: The authors would like to acknowledge RAIDER-M development team members Craig Wilson for layout and construction of the sensing units, Linda Summers for building all our RF cables, Brian Micek, consultant, for his work on the software system and communications protocols, and Dan Lizotte, consultant, for his help with installations.

[Sponsored by Navy TENCAP]

Morphing Satellite Reflector Antennas Using Tensegrity Structures

A. McKenna
Spacecraft Engineering Department

Introduction and Motivation: With the arrival of new communications and antenna technologies in the past few decades, requirements for antennas on Department of Defense satellites have increased in both complexity and scope. Modern military satellites may have extended lifetimes and require flexibility to fulfill ever-changing mission needs. A mechanically reconfigurable reflector would provide advanced beam forming and steering capabilities, which can increase or extend the usefulness of a satellite throughout its lifetime, as well as allow a single satellite design to be launched at different orbital locations. The design of the morphing reflector described here makes use of a unique light-weight structural configuration called tensegrity.¹

Tensegrity Structures Background: Tensegrity provides a unique approach to reducing weight. A tensegrity structure arranges the members in a specific geometric configuration to eliminate many typically found structural forces and to ensure that specific members remain in tension throughout a well-defined set of loading conditions. Replacing these tensional components (“strings”) with wires or cables greatly reduces weight.

One type of tensegrity unit that lends itself well to larger structure construction is the tensegrity prism, a three-bar example of which is shown in Fig. 11. Composed of three struts along with top and bottom polygons that are connected by strings, the tensegrity prism is one of the most stable units of tensegrity. Additionally, it can be modified to overcome one of tensegrity’s weakest elements, torsional force. The left image of Fig. 11 shows a minimal tensegrity prism, with the fewest number of strings needed for stability. The right image shows a nonminimal prism, with three extra strings for

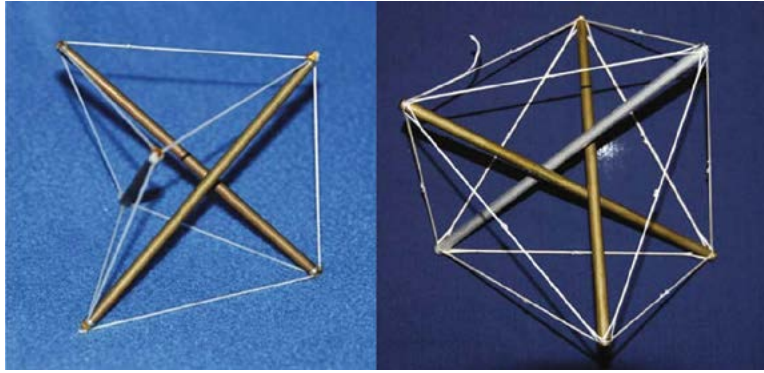


FIGURE 11

An example of three-bar tensegrity prisms. The left image is a three-bar minimal tensegrity prism with only nine strings, while the right has three additional strings to increase both tensional/compressive and torsional stiffness. Both structures are stable.

added stiffness. Increasing the prestress in the members will also increase the stiffness and the load capacity.

Tensegrity can be lightweight while still maintaining high strength. Also, morphing can take place by actuating the structure itself — the strings. Finally, tensegrity is a self-stabilizing structure, i.e., the structure will self-adjust its framework given a change in stress or length in one of the members. As long as the forces on the structure itself allow for a proper redistribution of internal forces so that all strings remain in tension, the structure will be stable.

Circular Multi-Cellular Tensegrity Antenna: The proposed concept of the morphing reflector makes use of six-bar tensegrity prisms arranged in concentric rings outward from a central point. This arrangement of cells is termed Circular Multi-Cellular Tensegrity (CMCT). A CMCT reflector antenna has several advantages. First, it is easily scalable, both by increasing string and strut lengths and by adding another ring of cells. Second, since it is composed of tensegrity units, shape changes can be created merely by changing the string lengths, which is a tremendous advantage over traditional morphing mechanisms, as only a linear wire actuator is needed. Additional research will investigate the possibility of using smart materials as the strings, allowing the structure to self-actuate. The CMCT structure creates control points at the ends of the struts and along the strings. A reflective antenna mesh attaches to these control points, creating a reconfigurable surface for beam shaping and steering.

Feasibility Results: With the goal of investigating the feasibility of constructing such a CMCT antenna and having it morph, NRL developed a program to calculate possible geometries. The equilibrium condition of tensegrity structures is subject to a form-finding problem in which an achievable configuration is found.

Using the properties of tensegrity prisms and the constraints of CMCT, the program searches for solutions of CMCT structures that could be suitable for reflector antennas.

The f/D ratio, which relates the focal length (f) to the antenna diameter (D), is an important variable in reflector antennas and plays a part in both design roles, such as focusing the antenna on a specific area of interest, and performance roles, such as increasing efficiency and decreasing polarization and sidelobes. The program was used to see if it was possible for a CMCT antenna to morph through a typical range of f/D values.

As Fig. 12 shows, stable and geometrically valid configurations for each ratio were found to be feasible. The conclusion is that mathematically, a tensegrity reflector antenna can morph through a series of stages to achieve a reasonable f/D range and fulfill multiple mission parameters. There are no morphing reflectors in orbit today, and none are being developed outside of NRL with this novel concept. Current usage of array-fed reflectors has disadvantages that could be eliminated or greatly reduced by the application of this morphing reflector.

[Sponsored by the NRL Base Program (CNR funded)]

Reference

¹ R.E. Skelton and M.C. De Oliveira, *Tensegrity Systems* (Springer, New York, 2009).

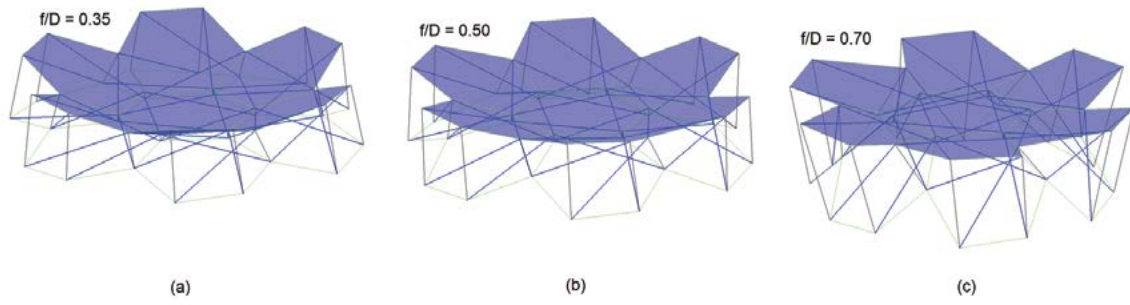


FIGURE 12

Morphing output over varying f/D ratios. Note that surfaces between control points are shown as planar, but in a finalized design would be a reflective, nonplanar mesh.





Programs for Professional Development

262 Programs for NRL Employees — Graduate Programs, Continuing Education, Professional Development, Equal Employment Opportunity (EEO) Programs, and Other Activities

264 Programs for Non-NRL Employees — Postdoctoral Research Associateships, Faculty Member Programs, Professional Appointments, and Student Programs

266 NRL Employment Opportunities

PROGRAMS FOR NRL EMPLOYEES

The Human Resources Office supports and provides traditional and alternative methods of training for employees. NRL employees are encouraged to develop their skills and enhance their job performance so they can meet the future needs of NRL and achieve their own goals for growth.

One common study procedure is for employees to work full time at the Laboratory while taking job-related courses at universities and schools local to their job site. The training ranges from a single course to undergraduate, graduate, and postgraduate course work. Tuition for training is paid by NRL. The formal programs offered by NRL are described here.

GRADUATE PROGRAMS

The **Advanced Graduate Research Program** (formerly the Sabbatical Study Program, which began in 1964) enables selected professional employees to devote full time to research or pursue work in their own or a related field for up to one year at an institution or research facility of their choice without the loss of regular salary, leave, or fringe benefits. NRL pays all travel and moving expenses for the employee. Criteria for eligibility include professional stature consistent with the applicant's opportunities and experience, a satisfactory program of study, and acceptance by the facility selected by the applicant. The program is open to employees who have completed six years of Federal service, four of which have been at NRL.

The **Edison Memorial Graduate Training Program** enables employees to pursue graduate studies in their fields at local universities. Participants in this program work 24 hours each workweek and pursue their studies during the other 16 hours. The criteria for eligibility include a minimum of one year of service at NRL, a bachelor's or master's degree in an appropriate field, and professional standing in keeping with the candidate's opportunities and experience.

To be eligible for the **Select Graduate Training Program**, employees must have a bachelor's degree in an appropriate field and must have demonstrated ability and aptitude for advanced training. Students accepted into this program receive one-half of their salary and benefits and NRL pays for tuition and travel expenses.

The **Naval Postgraduate School (NPS)**, located in Monterey, California, provides graduate programs to enhance the technical preparation of Naval officers and civilian employees who serve the Navy in the fields of science, engineering, operations analysis, and management. NRL employees desiring to pursue

graduate studies at NPS may apply; thesis work is accomplished at NRL. Participants continue to receive full pay and benefits during the period of study. NRL also pays for tuition and travel expenses.

In addition to NRL and university offerings, application may be made to a number of noteworthy programs and fellowships. Examples of such opportunities are the **Capitol Hill Workshops**, the **Legislative Fellowship (LEGIS) program**, the **Federal Executive Institute (FEI)**, and the **Executive Leadership Program for Mid-Level Employees**. These and other programs are announced from time to time, as schedules are published.

CONTINUING EDUCATION

Undergraduate and graduate courses offered at local colleges and universities may be subsidized by NRL for employees interested in improving their skills and keeping abreast of current developments in their fields.

NRL offers **short courses** to all employees in a number of fields of interest including administrative subjects, and supervisory and management techniques. Laboratory employees may also attend these courses at nongovernment facilities. HRO advertises training opportunities on the online *Billboard*, HRO website, and in the email newsletter, *HRO Highlights*.

For further information on any of the above Graduate and Continuing Education programs, contact the Employee Development and Management Branch (Code 1840) at (202) 767-8306 or via email at Training@hro.nrl.navy.mil.

The **Scientist-to-Sea Program (STSP)** provides opportunities for Navy R&D laboratory/center personnel to go to sea to gain first-hand insight into operational factors affecting system design, performance, and operations on a variety of ships. NRL is a participant of this Office of Naval Research (ONR) program. Contact (202) 767-7627.

PROFESSIONAL DEVELOPMENT

NRL has several programs, professional society chapters, and informal clubs that enhance the professional growth of employees. Some of these are listed below.

The **Counseling & Referral Service (C/RS)** helps employees improve job performance through counseling designed to resolve problems that may adversely affect job performance. Such problems may include family or work-related stress, relationship difficulties, or behavioral, emotional, or substance abuse problems.

C/RS provides confidential assessment, short-term counseling, training workshops, and referral to additional resources in the community. Contact (202) 767-6857.

The NRL chapter of **Women In Science and Engineering (WISE)** was established to address current issues concerning the scientific community of women at the NRL such as networking, funding, work-life satisfaction, and effective use of our resources. We address these issues by empowering members through the establishment of a supportive and constructive network that serves as a sounding board to develop solutions that address said issues, and then serve as a platform in which members work together to implement these solutions. The NRL chapter of WISE has started several new initiatives for the 2013-2014 year, including a seminar series entitled “Working Smarter Not Harder at NRL — Effective Use of Our Resources” and a Science as Art competition, which is open to all NRL sites. Membership is open to all employees. For more information, contact (202) 404-3355.

Sigma Xi, The Scientific Research Society, encourages and acknowledges original investigation in pure and applied science. It is an honor society for research scientists. Individuals who have demonstrated the ability to perform original research are elected to membership in local chapters. The NRL Edison Chapter, comprising approximately 200 members, recognizes original research by presenting annual awards in pure and applied science to two outstanding NRL staff members per year. In addition, an award seeking to reward rising stars at NRL is presented annually through the Young Investigator Award. The chapter also sponsors several lectures per year at NRL on a wide range of topics of general interest to the scientific and DoD community. These lectures are delivered by scientists from all over the world. The highlight of the Sigma Xi Lecture Series is the Edison Memorial Lecture, which traditionally is given by an internationally distinguished scientist. Contact (202) 767-5228.

The **NRL Mentor Program** was established to provide an innovative approach to professional and career training and an environment for personal and professional growth. It is open to permanent NRL employees in all job series and at all sites. Mentees are matched with successful, experienced colleagues having more technical and/or managerial experience who can provide them with the knowledge and skills needed to maximize their contribution to the success of their immediate organization, to NRL, to the Navy, and to their chosen career fields. The ultimate goal of the program is to increase job productivity, creativity, and satisfaction through better communication, understanding, and training. NRL Instruction 12400.1B provides policy and procedures for the program. For more information, please contact mentor@hro.nrl.navy.mil or (202) 767-6736.

Employees interested in developing effective self-expression, listening, thinking, and leadership potential are invited to join the Forum Club, a chapter of **Toastmasters International**. Members of this club possess diverse career backgrounds and talents and learn to communicate not by rules but by practice in an atmosphere of understanding and helpful fellowship. NRL's Commanding Officer and Director of Research endorse Toastmasters. Contact (202) 404-4670.

EQUAL EMPLOYMENT OPPORTUNITY (EEO) PROGRAMS

Equal employment opportunity (EEO) is a fundamental NRL policy for all employees regardless of race, color, national origin, sex, religion, age, sexual orientation, or disability. The NRL EEO Office is a service organization whose major functions include counseling employees in an effort to resolve employee/management conflicts, processing formal discrimination complaints, and requests for reasonable accommodation, providing EEO training, and managing NRL's affirmative employment recruitment program. The NRL EEO Office is also responsible for sponsoring special-emphasis programs to promote awareness and increase sensitivity and appreciation of the issues or the history relating to females, individuals with disabilities, and minorities. Contact the NRL Deputy EEO Officer at (202) 767-2486 for additional information on any of their programs or services.

OTHER ACTIVITIES

The award-winning **Community Outreach Program** directed by the NRL Public Affairs Office fosters programs that benefit students and other community citizens. Volunteer employees assist with and judge science fairs, give lectures, provide science demonstrations and student tours of NRL, and serve as tutors, mentors, coaches, and classroom resource teachers. The program sponsors student tours of NRL and an annual holiday party for neighborhood children in December. Through the program, NRL has active partnerships with three District of Columbia public schools. Contact (202) 767-2541.

Other programs that enhance the development of NRL employees include sports groups and the **Amateur Radio Club**. The **NRL Fitness Center** at NRL-DC, managed by Naval Support Activity Washington Morale, Welfare and Recreation (NSAW-MWR), houses a fitness room with treadmills, bikes, ellipticals, step mills, and a full strength circuit; a gymnasium for basketball, volleyball, and other activities; and full locker rooms. The Fitness Center is free to NRL employees and contractors. NRL employees are also eligible to participate in all NSAW-MWR activities held on Joint Base Anacostia-Bolling and Washington Navy Yard, less than five miles away.

PROGRAMS FOR NON-NRL EMPLOYEES

Several programs have been established for non-NRL professionals. These programs encourage and support the participation of visiting scientists and engineers in research of interest to the Laboratory. Some of the programs may serve as stepping-stones to Federal careers in science and technology. Their objective is to enhance the quality of the Laboratory's research activities through working associations and interchanges with highly capable scientists and engineers and to provide opportunities for outside scientists and engineers to work in the Navy laboratory environment. Along with enhancing the Laboratory's research, these programs acquaint participants with Navy capabilities and concerns and may provide a path to full-time employment.

POSTDOCTORAL RESEARCH ASSOCIATESHIPS

Every year, NRL hosts several postdoctoral research associates through the National Research Council (NRC) and American Society for Engineering Education (ASEE) postdoctoral associateship and fellowship programs. These competitive positions provide postdoctoral scientists and engineers the opportunity to pursue research at NRL in collaboration with NRL scientists and engineers. Research associates are guest investigators, not employees of NRL.

NRL/NRC Cooperative Research Associateship Program: The National Research Council conducts a national competition to recommend and make awards to outstanding scientists and engineers at recent postdoctoral levels for tenure as guest researchers at participating laboratories. The objectives of the NRC program are (1) to provide postdoctoral scientists and engineers of unusual promise and ability opportunities for research on problems, largely of their own choice, that are compatible with the interests of the sponsoring laboratories and (2) to contribute thereby to the overall efforts of the Federal laboratories. The program provides an opportunity for concentrated research in association with selected members of the permanent professional laboratory staff, often as a climax to formal career preparation.

NRL/NRC Postdoctoral Associateships are awarded to persons who have held a doctorate less than five years at the time of application and are made initially for one year, renewable for a second and possible third year. Information and applications may be found at <http://www.national-academies.org/rap>. To contact NRL's program coordinator, call (202) 404-7450 or email nrc@hro.nrl.navy.mil.

NRL/ASEE Postdoctoral Fellowship Program:

The ASEE program is designed to significantly increase the involvement of creative and highly trained scientists and engineers from academia and industry in scientific and technical areas of interest and relevance to the Navy. Fellowship awards are based upon the technical quality and relevance of the proposed research, recommendations by the Navy laboratory, academic qualifications, reference reports, and availability of funds.

NRL/ASEE Fellowship awards are made to persons who have held a doctorate for less than seven years at the time of application and are made for one year, renewable for a second and possible third year. Information and applications may be found at <http://www.asee.org/nrl/>. To contact NRL's program coordinator, call (202) 404-7450 or email asee@hro.nrl.navy.mil.

FACULTY MEMBER PROGRAMS

The **Office of Naval Research Summer Faculty Research and Sabbatical Leave Program** provides for university faculty members to work for ten weeks (or longer, for those eligible for sabbatical leave) with professional peers in participating Navy laboratories on research of mutual interest. Applicants must hold a teaching or research position at a U.S. college or university. Contact NRL's program coordinator at sfrp@hro.nrl.navy.mil.

The **NRL/United States Naval Academy Cooperative Program for Scientific Interchange** allows faculty members of the U.S. Naval Academy to participate in NRL research. This collaboration benefits the Academy by providing the opportunity for USNA faculty members to work on research of a more practical or applied nature. In turn, NRL's research program is strengthened by the available scientific and engineering expertise of the USNA faculty. Contact NRL's program coordinator at usna@hro.nrl.navy.mil.

PROFESSIONAL APPOINTMENTS

Faculty Member Appointments use the special skills and abilities of faculty members for short periods to fill positions of a scientific, engineering, professional, or analytical nature at NRL.

Consultants and experts are employed because they are outstanding in their fields of specialization or because they possess ability of a rare nature and could not normally be employed as regular civil servants.

Intergovernmental Personnel Act Appointments temporarily assign personnel from state or local governments or educational institutions to the Federal Government (or vice versa) to improve public services rendered by all levels of government.

STUDENT PROGRAMS

The student programs are tailored to high school, undergraduate, and graduate students to provide employment opportunities and work experience in naval research.

The **Naval Research Enterprise Intern Program (NREIP)** is a ten-week summer research opportunity for undergraduate juniors and seniors, and graduate students. The Office of Naval Research (ONR) offers summer appointments at Navy laboratories to current college sophomores, juniors, seniors, and graduate students from participating schools. Application is online at www.asee.org/nreip through the American Society for Engineering Education. Electronic applications are sent for evaluation to the point of contact at the Navy laboratory identified by the applicant. Contact NRL's program coordinator at nreip@hro.nrl.navy.mil.

The **National Defense Science and Engineering Graduate Fellowship Program** helps U.S. citizens obtain advanced training in disciplines of science and engineering critical to the U.S. Navy. The three-year program awards fellowships to recent outstanding graduates to support their study and research leading to doctoral degrees in specified disciplines such as electrical engineering, computer sciences, material sciences, applied physics, and ocean engineering. Award recipients are encouraged to continue their study and research in a Navy laboratory during the summer. Contact NRL's program coordinator at (202) 404-7450 or ndseg@hro.nrl.navy.mil.

The **Pathways Intern Program** (formerly STEP and SCEP) provides students enrolled in a wide variety of educational institutions, from high school to graduate level, with opportunities to work at NRL and explore Federal careers while still in school and while getting paid for the work performed. Students can work full-time or part-time on a temporary or non-temporary appointment. Students must be continuously enrolled on at least a half-time basis at a qualifying educational institution and be at least 16 years of age. The primary focus of our **Non-temporary** intern appointment is to attract students enrolled in undergraduate and graduate programs in engineering, computer science, or the physical sciences. Student on non-temporary appointments are eligible to remain on their appointment until graduation and may be noncompetitively converted to a permanent appointment within 120 days after completion

of degree requirements. Conversion is dependent on work performance, completion of at least 640 hours of work under the intern appointment before completion of degree requirements, and meeting the qualifications for the position. The **Temporary** intern appointment is up to one year in duration and may be extended for one additional year. This program enables students to earn a salary while continuing their studies and offers them valuable work experience. NRL's Pathways Intern Program opportunities are announced on USAJOBS four times per year. Visit USAJOBS at <https://www.usajobs.gov/> to create an account, search for jobs, set up an e-mail notification alert of when positions of interest are posted (see "Saved Searches") and apply for our intern opportunities when posted. For additional information on NRL's Intern Program, contact (202) 767-8313.

The **Student Volunteer Program** helps students gain valuable experience by allowing them to voluntarily perform educationally related work at NRL. Applications are accepted year-round. For additional information, contact (202) 767-8313.

The **Department of Defense Science and Engineering Apprenticeship Program (SEAP)** provides an opportunity for high school students who have completed at least Grade 9, and are at least 15 years of age, to serve as junior research associates. Under the direction of a mentor, for eight weeks in the summer, students gain a better understanding of research, its challenges, and its opportunities through participation in scientific, engineering, and mathematics programs. Criteria for eligibility are based on science and mathematics courses completed and grades achieved; scientific motivation, curiosity, the capacity for sustained hard work; a desire for a technical career; teacher recommendations; and exceptional test scores. The NRL program is the largest in the Department of Defense. For detailed information visit <http://seap.asee.org/>, or call (202) 767-8324, or email seap@hro.nrl.navy.mil.

NRL EMPLOYMENT OPPORTUNITIES

for Highly Innovative, Motivated, and Creative Professionals

NRL offers a wide variety of challenging S&T positions that involve skills from basic and applied research to equipment development. The nature of the research and development conducted at NRL requires professionals with experience. Typically there is a continuing need for electronics, mechanical, aerospace, and materials engineers, metallurgists, computer scientists, and oceanographers with bachelor's and/or advanced degrees and physical and computer scientists with Ph.D. degrees.



■ **Biologists.** Biologists conduct research in areas that include biosensor development, tissue engineering, molecular biology, genetic engineering, proteomics, and environmental monitoring.

■ **Chemists.** Chemists are recruited to work in the areas of combustion, polymer science, bioengineering and molecular engineering, surface science, materials synthesis, nanostructures, corrosion, fiber optics, electro-optics, microelectronics, electron device technology, and laser physics.

■ **Electronics Engineers and Computer Scientists.** These employees may work in the areas of communications systems, electromagnetic scattering, electronics instrumentation, electronic warfare systems, radio frequency/microwave/millimeter-wave/infrared technology, radar systems, laser physics technology, radio-wave propagation, electron device technology, spacecraft design, artificial intelligence, information processing, signal processing, plasma physics, vacuum science, microelectronics, electro-optics, fiber optics, solid-state physics, software engineering, computer design/architecture, ocean acoustics, stress analysis, and expert systems.

■ **Materials Scientists/Engineers.** These employees are recruited to work on materials, microstructure characterization, electronic ceramics, solid-state physics, fiber optics, electro-optics, microelectronics, fracture mechanics, vacuum science, laser physics and joining technology, and radio frequency/microwave/millimeter-wave/infrared technology.

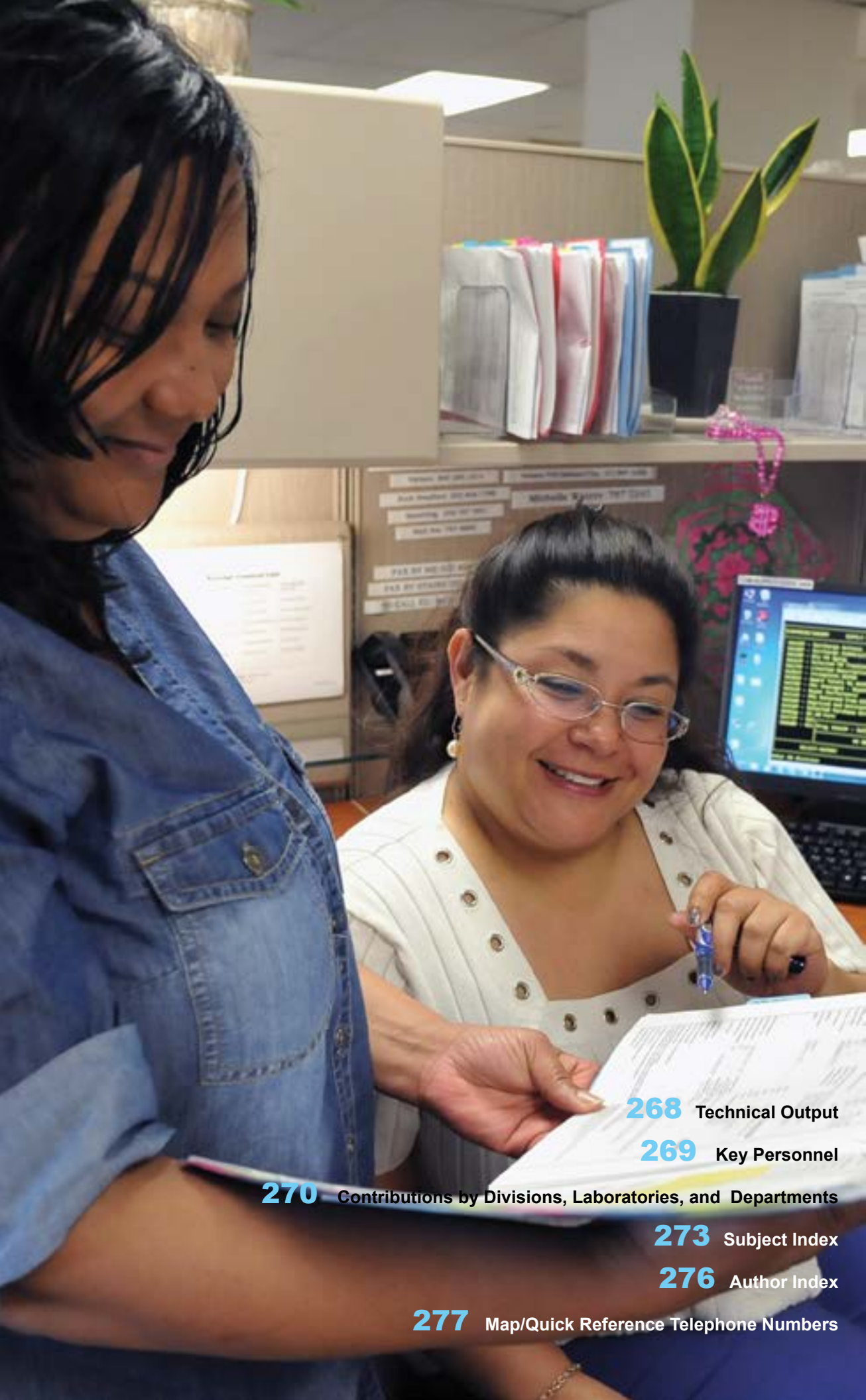
■ **Mechanical and Aerospace Engineers.** These employees may work in areas of spacecraft design, remote sensing, propulsion, experimental and computational fluid mechanics, experimental structural mechanics, solid mechanics, elastic/plastic fracture mechanics, materials, finite-element methods, nondestructive evaluation, characterization of fracture resistance of structural alloys, combustion, CAD/CAM, and multifunctional material response.

■ **Oceanographers, Meteorologists, and Marine Geophysicists.** These employees work in the areas of ocean and atmospheric dynamics, air-sea interaction, upper-ocean dynamics, oceanographic bio-optical modeling, oceanic and atmospheric numerical modeling and prediction, data assimilation and data fusion, retrieval and application of remote sensing data, benthic processes, aerogeophysics, marine sedimentary processes, advanced mapping techniques, atmospheric physics, and remote sensing. Oceanographers and marine geophysicists are located in Washington, DC, and at the Stennis Space Center, Bay St. Louis, Mississippi. Meteorologists are located in Washington, DC, and Monterey, California.

■ **Physicists.** Physics graduates may concentrate on such fields as materials, solid-state physics, fiber optics, electro-optics, microelectronics, vacuum science, plasma physics, fluid mechanics, signal processing, ocean acoustics, information processing, artificial intelligence, electron device technology, radio-wave propagation, laser physics, ultraviolet/X-ray/gamma-ray technology, electronic warfare, electromagnetic interaction, communications systems, radio frequency/microwave/millimeter-wave/infrared technology, computational physics, radio and high-energy astronomy, solar physics, and space physics.

For more information and current vacancy listings,
visit <http://hroffice.nrl.navy.mil/>

General Information



268 Technical Output

269 Key Personnel

270 Contributions by Divisions, Laboratories, and Departments

273 Subject Index

276 Author Index

277 Map/Quick Reference Telephone Numbers

TECHNICAL OUTPUT

The Navy continues to be a leader in initiating new developments and applying these advancements to military requirements. The primary method of informing the scientific and engineering community of the advances made at NRL is through the Laboratory's technical output — reports, articles in scientific journals, contributions to books, papers presented to scientific societies and topical conferences, patents, and inventions.

The figures for calendar year 2012 presented below represent the output of NRL facilities in Washington, D.C.; Bay St. Louis, Mississippi; and Monterey, California.

In addition to the output listed, NRL scientists made more than 1159 oral presentations during 2012.

<u>Type of Contribution</u>	<u>Unclassified</u>	<u>Classified</u>	<u>Total</u>
Articles in periodicals, chapters in books, and papers in published proceedings	1473*	0	1473*
NRL Formal Reports	7	4	11
NRL Memorandum Reports	61	1	62
Books	1	0	1
U.S. patents granted	90	0	90
Foreign patents granted	14		14
U.S. Trademark Registrations	3		3

*This is a provisional total based on information available to the Ruth H. Hooker Research Library on January 28, 2014. Additional publications carrying a 2012 calendar year publication date are anticipated. Total includes refereed and nonrefereed publications.

KEY PERSONNEL

Area Code (202) unless otherwise listed
 Personnel Locator - 767-3200
 DSN-297 or 754

Code	Office	Phone Number
EXECUTIVE DIRECTORATE		
1000	Commanding Officer	767-3403
1000.1	Inspector General	767-3621
1001	Director of Research	767-3301
1001.1	Executive Assistant for the Director of Research	767-2445
1002	Chief Staff Officer	767-3621
1004	Head, Technology Transfer Office	767-3083
1006	Head, Office of Program Administration and Policy Development	767-3091
1008	Office of Counsel	767-2244
1030	Public Affairs Officer	767-2541
1100	Director, Institute for Nanoscience	767-3261
1200	Head, Command Support Division	767-3621
1220	Head, Information Assurance and Communications Security	767-0793
1400	Head, Military Support Division	767-2273
1600	Commander, Scientific Development Squadron One	301-342-3751
1700	Director, Laboratory for Autonomous Systems Research	767-2684
1800	Director, Human Resources Office	767-3421
1830	Deputy EEO Officer	767-5264
3005	Deputy for Small Business	767-6263
3540	Head, Safety Branch	767-2232
BUSINESS OPERATIONS DIRECTORATE		
3000	Comptroller/Associate Director of Research	767-2371
3200	Head, Contracting Division	767-5227
3300	Head, Financial Management Division	767-3405
3400	Head, Supply and Information Services Division	767-3446
3500	Director, Research and Development Services Division	404-4054
SYSTEMS DIRECTORATE		
5000	Associate Director of Research	767-3425
5300	Superintendent, Radar Division	404-2700
5500	Superintendent, Information Technology Division/ NRL Chief Information Officer*	767-2903
5600	Superintendent, Optical Sciences Division	767-7375
5700	Superintendent, Tactical Electronic Warfare Division	767-6278
MATERIALS SCIENCE AND COMPONENT TECHNOLOGY DIRECTORATE		
6000	Associate Director of Research	767-3566
6040	Director, Laboratories for Computational Physics and Fluid Dynamics	767-2402
6100	Superintendent, Chemistry Division	767-3026
6300	Superintendent, Materials Science and Technology Division	767-2926
6700	Superintendent, Plasma Physics Division	767-2723
6800	Superintendent, Electronics Science and Technology Division	767-3693
6900	Director, Center for Bio/Molecular Science and Engineering	404-6000
OCEAN AND ATMOSPHERIC SCIENCE AND TECHNOLOGY DIRECTORATE		
7000	Associate Director of Research	404-8690
7100	Superintendent, Acoustics Division	767-3482
7200	Superintendent, Remote Sensing Division	767-3391
7300	Superintendent, Oceanography Division	228-688-4670
7400	Superintendent, Marine Geosciences Division	228-688-4650
7500	Superintendent, Marine Meteorology Division	831-656-4721
7600	Superintendent, Space Science Division	767-6343
NAVAL CENTER FOR SPACE TECHNOLOGY		
8000	Director	767-6547
8100	Superintendent, Space Systems Development Department	767-0410
8200	Superintendent, Spacecraft Engineering Department	404-3727

*Additional Duty

CONTRIBUTIONS BY DIVISIONS, LABORATORIES, AND DEPARTMENTS

Radar Division

- 154 High Frequency Vector Sensor Design and Testing
W.W. Lee, M. Parent, and G.S. San Antonio

Information Technology Division

- 164 Stable Throughput Tradeoffs in Cognitive Radio Networks
S. Kompella, G.D. Nguyen, J.E. Wieselthier, and A. Ephremides
- 165 X-Band Airborne Satellite Communications
T.R. Husson and M.A. Rupar
- 169 Dynamic Network Analysis for Mobile (DyNAMo) Adaptation
J. Macker, J. Dean, and D. Claypool

Optical Sciences Division

- 81 Sputtered Thin Film Absorbers for Flexible Photovoltaics
J.A. Frantz, J.D. Myers, R.Y. Bekele, V.Q. Nguyen, and J.S. Sanghera
- 190 A Micromechanical Analogue to Optical Lasers
M.W. Pruessner, J.B. Khurgin, T.H. Stievater, and W.S. Rabinovich
- 206 A Panoramic Shortwave Infrared Hyperspectral Sensor for Maritime Sensing
K.P. Judd, J.M. Nichols, J. Waterman, C.C. Olson, K. Lee, and G. Scriven
- 208 Spatiotemporal-Multiplexed Quantum Dot Biosensors
M.H. Stewart, W.R. Algar, N. Hildebrandt, A.L. Huston, and I.L. Medintz

Tactical Electronic Warfare Division

- 136 High-Altitude Flight Control of a Micro Air Vehicle Using Only Two Sensors
A. Kahn and D. Edwards
- 171 Frequency Position Modulation
J. Goodman, C. Bertoini, B. Nousain, and G. Cowart

Laboratories for Computational Physics and Fluid Dynamics

- 176 The Physics of the Unconfined Deflagration-to-Detonation Transition
A.Y. Poludnenko, V.N. Gamezo, and E.S. Oran

Chemistry Division

- 88 Single-Component Polysiloxane Coating for Navy Topsides
E. Iezzi, J. Martin, J. Tagert, P. Slebodnick, J. Wegand, and E. Lemieux
- 148 Barnacle Adhesion Two-Step
K.J. Wahl, C.M. Spillmann, D.E. Barlow, R.K. Everett, B. Orihuela, D. Rittschof, and D.K. Burden
- 178 Failure of Classical Elasticity
C.M. Roland, J. Roh, and P. Mott
- 180 Synfuel from Seawater
H.D. Willauer, D.M. Drab, F. DiMascio, D.R. Hardy, R. Ananth, and F.W. Williams
- 188 Measuring Protein Secretions from Individual Live Cells
M.P. Raphael, J.A. Christodoulides, J.B. Delehanty, J.P. Long, P.E. Pehrsson, and J.M. Byers

Materials Science and Component Technology Division

- 96 Graphene as a Tunnel Barrier
O. van 't Erve, E. Cobas, A.L. Friedman, C.H. Li, J.T. Robinson, and B.T. Jonker
- 148 Barnacle Adhesion Two-Step
K.J. Wahl, C.M. Spillmann, D.E. Barlow, R.K. Everett, B. Orihuela, D. Rittschof, and D.K. Burden
- 176 The Physics of the Unconfined Deflagration-to-Detonation Transition
A.Y. Poludnenko, V.N. Gamezo, and E.S. Oran
- 180 Synfuel from Seawater
H.D. Willauer, D.M. Drab, F. DiMascio, D.R. Hardy, R. Ananth, and F.W. Williams
- 181 Relationship of Grain Boundary Microchemistry with Stress Corrosion Susceptibility in Aircraft Aluminum Alloys
R. Goswami, P.S. Pao, and R.L. Holtz

- 188 Measuring Protein Secretions from Individual Live Cells
M.P. Raphael, J.A. Christodoulides, J.B. Delehan-ty, J.P. Long, P.E. Pehrsson, and J.M. Byers
- 220 Robotic Multiaxial Testing and Constitutive Characterization of Composites
J.G. Michopoulos, J.C. Hermanson, and A. Iliopoulos

Plasma Physics Division

- 150 Pulsed Electron Beam Driven Chemistry
J.D. Sethian, M. Wolford, M. Myers, and F. Hegeler
- 228 Ground-Based Investigation of Near-Earth Space Plasma Processes in the NRL Space Physics Simulation Chamber
W.E. Amatucci, D.D. Blackwell, G.R. Gatling, E.M. Tejero, C.D. Cothran, D.N. Walker, and E.D. Gillman
- 229 Artificial Ionospheric Plasma Clouds Using HAARP
P.A. Bernhardt, C.L. Siefring, S.-M. Han, D.L. Byers, A. Fliflet, S.C. Briczinski, M. Wilkens, and E.G. Kendall

Electronics Science and Technology Division

- 96 Graphene as a Tunnel Barrier
O.M.J. van 't Erve, E. Cobas, A.L. Friedman, C.H. Li, J.T. Robinson, and B.T. Jonker
- 156 Intrinsically Switched Varactor-Tuned Filters and Filter Banks
A.C. Guyette
- 159 Thermoelectroelastic Simulation of GaN Devices
M.G. Ancona, S.C. Binari, and D.J. Meyer
- 183 A New Annealing Technique — Multicycle Rapid Thermal Annealing (MRTA)
B.N. Feigelson, T.J. Anderson, J.A. Freitas, J.K. Hite, C.R. Eddy, Jr., and F.J. Kub

Center for Bio/Molecular Science and Engineering

- 106 Molecular Epidemiology of Global Antimicrobial Resistance
C.R. Taitt, T.A. Leski, and G.J. Vora
- 121 Low Power Microrobotics Utilizing Biologically Inspired Energy Generation
G.P. Scott, S.P. Arnold, C.E. Person, L.M. Tender, and K.P. Gregoire
- 148 Barnacle Adhesion Two-Step
K.J. Wahl, C.M. Spillmann, D.E. Barlow, R.K. Everett, B. Orihuela, D. Rittschof, and D.K. Burden

- 188 Measuring Protein Secretions from Individual Live Cells
M.P. Raphael, J.A. Christodoulides, J.B. Delehan-ty, J.P. Long, P.E. Pehrsson, and J.M. Byers

- 208 Spatiotemporal-Multiplexed Quantum Dot Biosensors
M.H. Stewart, W.R. Algar, N. Hildebrandt, A. Huston, and I. Medintz

- 212 Electrochemical Detection of Nitroenergetics for Long Term Monitoring
B.J. White, B.J. Melde, R.L. Seifert, and M. Nasir

Acoustics Division

- 128 Controlling Sonar Clutter via Higher-Order Statistics
R.C. Gauss and J.M. Fialkowski
- 130 Transition and Optimization of a Fast Broad-band Pulse Propagation Algorithm for Fleet Use
R.A. Zingarelli
- 132 Range-Dependent Seismo-Acoustics
M.D. Collins
- 196 A Target Depth Classification Method for Autonomous Passive Acoustic Surveillance Systems in Littorals
A. Turgut and L.T. Fialkowski
- 214 Remote Sensing Signatures of Breaking Waves from Multi-Instrument Field Experiment on FLIP
M.D. Anguelova, D.J. Dowgiallo, G.B. Smith, S.L. Means, I.B. Savelyev, G.M. Frick, C.M. Snow, J.A. Schindall, and J.P. Bobak

Remote Sensing Division

- 194 Turbulence Production by Nonbreaking Waves
I. Savelyev, E. Maxeiner, and D. Chalikov
- 214 Remote Sensing Signatures of Breaking Waves from Multi-Instrument Field Experiment on FLIP
M.D. Anguelova, D.J. Dowgiallo, G.B. Smith, S.L. Means, I.B. Savelyev, G.M. Frick, C.M. Snow, J.A. Schindall, and J.P. Bobak
- 216 Surprising Discoveries in Reflectance Properties of Complex Granular Sediments
A. Abelev and C.M. Bachmann

Oceanography Division

- 199 Maximizing Effectiveness of Autonomous Underwater Vehicles
L.F. Smedstad, C.N. Barron, K.D. Heaney, G. Peggion, and E.M. Coelho
- 201 WAVEWATCH III® Transition to Naval Operations
J.D. Dykes and W.E. Rogers

Marine Geosciences Division

- 216 Surprising Discoveries in Reflectance Properties of Complex Granular Sediments
A. Abelev and C.M. Bachmann
- 222 How Clutter and Expertise Affect Search in Geospatial Displays
M.E. Trenchard and M.R. Beck

Marine Meteorology Division

- 138 The Navy Global Environmental Model
T. Hogan, M. Peng, N. Baker, C. Reynolds, B. Ruston, M. Liu, J. Ridout, S. Eckermann, J. Moskaitis, T. Whitcomb, K. Viner, J. McLay, P. Pauley, L. Xu, R. Langland, M. Flatau, J. McCormack, and S. Chang
- 143 Smart Voyage Planning — Saving Fuel by Using Environmental Forecasts to Aid in Ship Routing
J. Cook and J. Hansen

Space Science Division

- 114 The Stuff Coronal Mass Ejections Are Made Of
A. Vourlidas
- 138 The Navy Global Environmental Model
T. Hogan, M. Peng, N. Baker, C. Reynolds, B. Ruston, M. Liu, J. Ridout, S. Eckermann, J. Moskaitis, T. Whitcomb, K. Viner, J. McLay, P. Pauley, L. Xu, R. Langland, M. Flatau, J. McCormack, and S. Chang
- 140 Long-Range, Low-Frequency Atmospheric Sound Propagation Physics
D.P. Drob and M.A. Hedlin
- 232 Maritime Detection of Radiological/Nuclear Threats
B. Philips, E. Wulf, L. Mitchell, A. Hutcheson, and W.N. Johnson

Space Systems Development Department

- 168 GLADIS Hosted Payload Demonstrates Nano-Satellite Technology
J. Middour, I. Galysh, K. Clark, T. Rodillo, M. Haffner, C. Belmonte, R. Baummer, J. Graham, and J. Tugman
- 233 RAIDER-M: Transitioning Space System Knowledge to Terrestrial Remote Sensing
M. Haffner and C. Huffine

Spacecraft Engineering Department

- 121 Low Power Microrobotics Utilizing Biologically Inspired Energy Generation
G.P. Scott, S.P. Arnold, C.E. Person, L.M. Tender, and K.P. Gregoire
- 235 Morphing Satellite Reflector Antennas Using Tensegrity Structures
A. McKenna

SUBJECT INDEX

- Acoustic Reverberation Simulation Facility, 71
Acoustics Division, 56
Acoustics, 140, 199
Activation, 183
Active sonar, 128
Adhesion, 148
Administrative Services Branch, 73
Advanced Graduate Research Program, 262
Advanced Multifunction Radio Frequency Concept (AMRFC), 37
Advanced Optical Materials Fabrication Laboratory, 40
Advanced Silicon Carbide Epitaxial Research Laboratory (ASCERL), 52
Air-pluviation, 216
Aluminum alloys, 181
Amateur Radio Club, 263
Antibiotic resistance, 105
Antifouling, 148
Atmospheric acoustics, 140
Atmospheric Science and Technology, 136
Atmospheric science, 143
Atomic Layer Deposition System (ALD), 52
Atomic Layer Epitaxy System, 52
Audio Laboratory, 39
Autonomous networks, 169
Autonomous Systems and Robotics Laboratory, 39
Autonomous underwater vehicles, 199
Auxetic foam, 178
Barnacles, 148
Behavior Detection Laboratory, 39
Bio-inspired underwater vehicle, 54
Bioadhesion, 148
Biologically inspired, 121
Biosensing, 208
Biosensor, 188
Blossom Point Satellite Tracking and Command Facility, 77
Breaking waves, 214
Bubble acoustics, 214
Capitol Hill Workshops, 262
Carbon dioxide, 180
Cavity optomechanics, 190
Cell secretion, 188
Center for Bio/Molecular Science and Engineering, 54
Center for Computational Science (CCS), 38
Chemical Vapor and Plasma Deposition Facility, 47
Chemistry Division, 46
Chesapeake Bay Detachment (CBD), 75
Class 1000 clean room, 48
Classical elasticity, 178
Clutter, 128, 222
Cognitive radio networks, 164
Community Outreach Program, 263
Compact Antenna Range, 36
Compact CORonograph (CCOR), 66
Composite materials, 220
Compound Semiconductor Processing Facility (CSPF), 52
Constitutive characterization, 220
Cooperative Aircraft Identification system, 37
Cooperative communications, 164
Copper indium gallium diselenide (CIGS), 80
Coronal mass ejections, 113
Counseling & Referral Service (C/RS), 262
Cryptographic Technology Laboratory, 38
Cyber Defense Development Laboratory, 39
Data assimilation, 138
Data exfiltration, 168
Department of Defense Science and Engineering Apprenticeship Program (SEAP), 265
Detonations, 176
DNA, 105
Dynamic Spectrum Allocation/Cognitive Radio Technology Test Lab, 38
Dynamic topology, 169
Edison Memorial Graduate Training Program, 262
Electra, 50
Electrical, Magnetic, and Optical Measurement Facility, 48
Electromagnetic vector sensor, 154
Electron beam, 150
Electronic charts, 222
Electronics and electromagnets, 136
Electronics Science and Technology, 52
Ensembles, 143
Environmental monitoring, 212
Environmental Prediction System Development Laboratory, 64
Epicenter, 52
ex-USS *Shadwell* Research Platform, 47, 78
Executive Leadership Program for Mid-Level Employees, 262
Explosions, 176
Federal Executive Institute (FEI), 262
Field experiment, 214
Flames, 176
Focal Plane Array Evaluation Facility, 41
Forster resonance energy transfer, 208
Fouling, 148
Fourier transform, 130
Free Surface Hydrodynamics Laboratory (FSHL), 59
Freespace Laser Communications Laboratory, 38
Frequency position modulation, 171
Fuel efficiency, 143
Fuel reformation, 150
Gamble II, 50
GaN, 159, 183
Geospatial displays, 222
Geospatial hub (GHub), 63
Gliders, 199
Global weather prediction, 138
Glow plasma discharges, 229
Granular media, 216
Graphene, 95
Gravity waves, 140
High data rate communications, 171
High Energy Laser Lab, 50
High Pressure Multi-Anvil System (HPMAS), 52
Higher-order statistics, 128
Hybridization, 208
Hydrogen, 180
Hyperspectral Imager for the Coastal Ocean (HICO), 58
Hyperspectral imaging, 206
Hyperspectral sensor, 216
Imaging, 188
Immersive Simulation Laboratory, 39
Implantation, 183
Information Technology Division, 38
Infrared Materials and Detectors Characterization Laboratory (IR Characterization Lab), 52
Infrasound, 140
Institute for Nanoscience, 34
Integrated optics, 190
Ionospheric modification, 229
IR camera, 214
IR Missile-Seeker Evaluation Facility, 41
Karles Invitational Conference, 10
Label free, 188
Laboratories for Computational Physics and Fluid Dynamics, 44
Laboratory for Advanced Materials Synthesis (LAMS), 52
Laboratory for Structural Acoustics, 57
Laboratory plasma, 228
Laminar Flow Clean Room, 71
Large Angle Spectrometric and Coronographic Telescope (LASCO), 67
Large Area Plasma Processing System (LAPPS), 51
Legislative Fellowship (LEGIS) program, 262
Locomotion, 120
Low power, 120
LPI/LPD, 171
Magnetic Resonance Facility, 46
Magneto-electronics Fabrication Facility, 48
Marine Coatings Facility, 47, 78
Marine Corrosion Facility, 47, 78

Marine Geosciences Division, 62
 Marine Meteorology Center, 14
 Marine Meteorology Division, 64
 Maritime sensing, 206
 Maritime detection, 233
 Materials Processing Facility, 48
 Materials Science and Technology Division, 48
 Materials Synthesis/Property Measurement Facility, 46
 Materials Testing Facility, 50
 Mechanical Characterization Facility, 48
 Mercury, 50
 Meteorology, 143
 Michelson Interferometer for Global High-Resolution Thermospheric Imaging (MIGHTI), 67
 Micro-electro-mechanical systems (MEMS), 190
 Micro/Nanostructure Characterization Facility, 49
 Microarray, 105
 Microbial fuel cell, 120
 MicroSTAR-H X-ray generator, 54
 Microstructures, 181
 Microwave Microscope (MWM), 37
 Midway Research Center, 76
 Millimeter-Wave Vacuum Electronics Fabrication Facility (MWVEFF), 52
 Mobile Ad Hoc Networking (MANET), 38, 169
 Mobile Atmospheric Aerosol and Radiation Characterization Observatories (MAARCO), 65
 Mobile wireless, 169
 Modeling, 159
 Molecular epidemiology, 105
 Monterey (NRL-MRY), 74
 Morphing, 235
 Multiaxial testing, 220
 Multiplexing, 208
 Nano-satellite technology, 168
 Nanometer Characterization/Manipulation Facility, 46
 NASA NIAC, 120
 National Defense Science and Engineering Graduate Fellowship Program, 265
 National Medal of Technology and Innovation, 8
 Naval Key Management Laboratory, 39
 Naval Postgraduate School (NPS), 262
 Naval Research Enterprise Intern Program (NREIP), 265
 Navy Fuel Research Facility, 47
 Network modeling, 169
 Nike, 50
 Nitroenergetic, 212
 Non-linear dynamics, 140
 Non-Rayleigh statistics, 128
 NO_x removal, 150
 NRL Fitness Center, 263
 NRL Focused Phased Array Imaging Radar (NRL FOPAIR), 58
 NRL Mentor Program, 263
 NRL/ASEE Postdoctoral Fellowship Program, 264
 NRL/NRC Cooperative Research Associateship Program, 264
 NRL/United States Naval Academy Cooperative Program, 264
 NRLFCU, 33
 Nuclear magnetic resonance (NMR) spectroscopy, 54
 Ocean acoustics, 132
 Ocean data telemetry microsatellite link (ODTML), 168
 Ocean Dynamics and Prediction Computational Network Facility, 60
 Ocean modeling, 199
 Ocean remote sensing, 214
 Oceanography Division, 60
 Oceanography, 143
 Office of Naval Research Summer Faculty Research and Sabbatical Leave Program, 264
 Optical Fiber Preform Fabrication Facility, 40
 Optical Sciences Division, 40
 Optoelectronic Scanning Electron Characterization Facility (OSECF), 52
 Organosilica, 212
 p-type, 183
 Panoramic, 206
 Parabolic equation, 130
 Parabolic wave equation, 132
 Passive radiometry, 214
 Passive, 196
 Pathways Intern Program, 265
 Phase angle, 216
 Piezoelectric, 159
 Plasma diagnostics, 228
 Plasma Physics Division, 50
 Plasma waves, 228
 Plasmonics, 188
 Poisson-Rayleigh, 128
 Poisson's ratio, 178
 Polysiloxane, 87
 Pomonkey Facility, 77
 Porosity, 216
 Precision Clock Evaluation Facility (PCEF), 69
 Preconcentration, 212
 Quantum dot, 208
 Queueing theory, 164
 Radar Division, 36
 Radar Test Facility, 36
 Radar, 12
 Radio mirrors, 229
 Radiological/nuclear weapons of mass destruction (WMD), 232
 Range dependence, 132
 Reflectance, 216
 Reflector antennas, 235
 Relative density, 216
 Reliant unmanned underwater vehicle, 56
 Remote Sensing Division, 58
 Remote sensing, 136
 RF Communications Laboratory, 38
 Robotic testing, 220
 Robotics, 120
 Ruth H. Hooker Research Library, 73
 Salt water tank facility, 57
 Satellite antenna, 165
 Satellite communications, 165
 Satellite Data Processing Laboratory, 65
 Satellite modem, 165
 Scanfish, 61
 Scientific Development Squadron One (VXS-1), 76
 Scientist-to-Sea Program (STSP), 262
 Sea spray, 214
 Seawater, 180
 Seismo-acoustics, 132
 Seismology, 132
 Select Graduate Training Program, 262
 Semi-Lagrangian, 138
 Sensor Exploitation Lab (SEALAB), 59
 Service Oriented Architecture Laboratory, 39
 Ship routing, 143
 Shortwave infrared, 206
 Sigma Xi, 263
 Silicon photonics, 190
 Silicon, 95
 Single-component, 87
 Slocum gliders, 61
 Small antenna array, 168
 Solar Cell Characterization Laboratory (SCCL), 52
 Solar corona, 113
 Solar Coronagraph Optical Test Chamber (SCOTCH), 66
 Sonomagnetic measurement facility, 57
 Sorbent, 212
 Space Physics Simulation Chamber, 50
 Space plasma, 228
 Space Science Division, 66
 Space Systems Development Department, 68
 Space weather, 113
 Space, 120
 Spacecraft Engineering Department, 70
 Spacecraft Robotics Engineering and Control Laboratory, 71
 Special Sensor Ultraviolet Limb Imager (SSULI), 67
 Spin Test Facility, 71
 Spintronics, 95
 Stable throughput region, 164
 Standoff nuclear detection, 232
 Static Loads Test Facility, 71
 Stennis Space Center (NRL-SSC), 74
 Stress corrosion cracking, 181
 Stress, 159
 Student Volunteer Program, 265
 Sun-Earth Connection Coronal Heliospheric Investigation (SECCHI), 67
 Surface Characterization Facility, 40
 Surface waves, 194
 Surveillance, 196
 Synfuel, 180
 Synthetic fuels, 150
 Tactical decision aids, 199
 Tactical Electronic Warfare Division, 42
 Technical Information Services Branch, 72
 Technology Transfer Office, 72
 Tensegrity, 235
 Terbium, 208

Thermal Fabrication and Test Facility, 71
Thin film photovoltaics, 80
Thin-Film Materials Synthesis and Processing Facility, 49
Time domain, 130
Time-gated, 208
Toastmasters International, 263
Topside coating, 87
TORPEDO, 73
Transmission electron microscopy, 181
Multicycle rapid thermal annealing, 183
Tunable filters, 156
Tunnel barrier, 95
Turbulence, 176, 194
Ultra-Violet Photolithography Laboratory for Submillimeter-Wave Devices (UV-PL), 52
Ultrafast Laser Facility (ULF), 52
Ultralow-loss Infrared Fiber-Optic Waveguide Facility, 41
Ultrashort-Pulse, High-Intensity Laser Facility, 50
Ultrasonic measurements laboratory, 57
Unmanned aerial vehicles, 136
Upper ocean, 194
Varactor-tuned filters, 156
Vertical Microstructure Profiler (VMP), 61
Vibration Test Facility, 71
Visual Analytics Laboratory, 39
Voice Communications Laboratory, 38
W-band Advanced Radar for Low Observable Control (WARLOC), 37
Warfighter Human System Integration Laboratory, 39
Water Vapor Millimeter-wave Spectrometer (WVMS), 59
Wave forecast, 201
Wave models, 201
Waveguide invariance, 196
WAVEWATCH III, 201
Weapons of mass destruction (WMD) detection, 232
Women in Science and Engineering (WISE), 263
X-band, 165

AUTHOR INDEX

- Abelev, A., 216
Algar, W.R., 208
Amatucci, W.E., 228
Ananth, R., 180
Ancona, M.G., 159
Anderson, T.J., 183
Anguelova, M.D., 214
Arnold, S.P., 121
Bachmann, C.M., 216
Baker, N., 138
Barlow, D.E., 148
Barron, C.N., 199
Baummer, R., 168
Beck, M.R., 222
Bekele, R.Y., 80
Belmonte, C., 168
Bernhardt, P.A., 229
Bertoncini, C., 171
Binari, S.C., 159
Blackwell, D.D., 228
Bobak, J.P., 214
Briczinski, S.C., 229
Burden, D.K., 148
Byers, D.L., 229
Byers, J.M., 188
Chalikov, D., 194
Chang, S., 138
Christodoulides, J.A., 188
Clark, K., 168
Claypool, D., 169
Cobas, E., 96
Coelho, E.M., 199
Collins, M.D., 132
Cook, J., 143
Cothran, C.D., 228
Coward, G., 171
Dean, J., 169
Delehanty, J.B., 188
DiMascio, F., 180
Dowgiallo, D.J., 214
Drab, D.M., 180
Drob, D.P., 140
Dykes, J.D., 201
Eckermann, S., 138
Eddy, Jr., C.R., 183
Edwards, D., 136
Ephremides, A., 164
Everett, R.K., 148
Feigelson, B.N., 183
Fialkowski, J.M., 128
Fialkowski, L.T., 196
Flatau, M., 138
Fliflet, A., 229
Frantz, J.A., 80
Freitas, J.A., 183
Frick, G.M., 214
Friedman, A.L., 96
Galysh, L., 168
Gamezo, V.N., 176
Gatling, G.R., 228
Gauss, R.C., 128
Gillman, E.D., 228
Goodman, J., 171
Goswami, R., 181
Graham, J., 168
Gregoire, K.P., 121
Guyette, A.C., 156
Haffner, M., 168, 233
Han, S.-M., 229
Hansen, J., 143
Hardy, D.R., 180
Heaney, K.D., 199
Hedlin, M.A., 140
Hegeler, F., 150
Hermanson, J.C., 220
Hildebrandt, N., 208
Hite, J.K., 183
Hogan, T., 138
Holtz, R.L., 181
Huffine, C., 233
Husson, T.R., 165
Huston, A., 208
Hutcheson, A., 232
Iezzi, E., 88
Iliopoulos, A., 220
Johnson, W.N., 232
Jonker, B.T., 96
Judd, K.P., 206
Kahn, A., 136
Kendall, E.G., 229
Khurgin, J.B., 190
Kompella, S., 164
Kub, F.J., 183
Langland, R., 138
Lee, K., 206
Lee, W.W., 154
Lemieux, E., 88
Leski, T.A., 106
Li, C.H., 96
Liu, M., 138
Long, J.P., 188
Macker, J., 169
Martin, J., 88
Maxeiner, E., 194
McCormack, J., 138
McKenna, A., 235
McLay, J., 138
Means, S.L., 214
Medintz, I., 208
Melde, B.J., 212
Meyer, D.J., 159
Michopoulos, J.G., 220
Middour, J., 168
Mitchell, L., 232
Moskaitis, J., 138
Mott, P., 178
Myers, J.D., 80
Myers, M., 150
Nasir, M., 212
Nguyen, G.D., 164
Nguyen, V.Q., 80
Nichols, J.M., 206
Nousain, B., 171
Olson, C.C., 206
Oran, E.S., 176
Orihuela, B., 148
Pao, P.S., 181
Parent, M., 154
Pauley, P., 138
Peggion, G., 199
Pehrsson, P.E., 188
Peng, M., 138
Person, C.E., 121
Phlips, B., 232
Poludnenko, A.Y., 176
Pruessner, M.W., 190
Rabinovich, W.S., 190
Raphael, M.P., 188
Reynolds, C., 138
Ridout, J., 138
Rittschof, D., 148
Robinson, J.T., 96
Rodilloso, T., 168
Rogers, W.E., 201
Roh, J., 178
Roland, C.M., 178
Rupar, M.A., 165
Ruston, B., 138
San Antonio, G., 154
Sanghera, J.S., 80
Saveljev, I.B., 194, 214
Schindall, J.A., 214
Scott, G.P., 121
Scriven, G., 206
Sethian, J.D., 150
Siefert, R.L., 212
Siefing, C.L., 229
Sleboznick, P., 88
Smedstad, L.F., 199
Smith, G.B., 214
Snow, C.M., 214
Spillmann, C.M., 148
Stewart, M.H., 208
Stievater, T.H., 190
Tagert, J., 88
Taitt, C.R., 106
Tejero, E.M., 228
Tender, L.M., 121
Trenchard, M.E., 222
Tugman, J., 168
Turgut, A., 196
Van 't Erve, O.M.J., 96
Viner, K., 138
Vora, G.J., 106
Vourlidas, A., 114
Wahl, K.J., 148
Walker, D.N., 228
Waterman, J., 206
Wegand, J., 88
Whitcomb, T., 138
White, B.J., 212
Wieselthier, J.E., 164
Wilkins, M., 229
Willauer, H.D., 180
Williams, F.W., 180
Wolford, M., 150
Wulf, E., 232
Xu, L., 138
Zingarelli, R.A., 130

NAVAL RESEARCH LABORATORY

4555 Overlook Ave., SW • Washington, DC 20375-5320

LOCATION OF NRL IN THE CAPITAL AREA



Quick Reference Telephone Numbers

	NRL Washington	NRL- SSC	NRL- Monterey	NRL CBD	NRL VXS-1 Patuxent River
Hotline	(202) 767-6543	(202) 767-6543	(202) 767-6543	(202) 767-6543	(202) 767-6543
Personnel Locator	(202) 767-3200	(228) 688-3390	(831) 656-4763	(410) 257-4000	(301) 342-3751
DSN	297- or 754-	828	878	—	342
Direct-in-Dialing	767- or 404-	688	656	257	342
Public Affairs	(202) 767-2541	(228) 688-5328	(202) 767-2541	—	(202) 767-2541

Additional telephone numbers are listed on page 269.

General information on the research described in this *NRL Review* can be obtained from the Public Affairs Office, Code 1030, (202) 767-2541. Information concerning Technology Transfer is available from the Technology Transfer Office, Code 1004, (202) 767-7230. Sources of information on the various educational programs at NRL are listed in the *NRL Review* chapter entitled “Programs for Professional Development.”

For additional information about NRL, the *NRL Fact Book* lists the organizations and key personnel for each division. It contains information about Laboratory funding, programs, and field sites. The *Fact Book* can be obtained from the Technical Information Services Branch, Code 3430, (202) 404-4963. The web-based *NRL Major Facilities* publication, which describes each NRL facility in detail, can be accessed at <http://www.nrl.navy.mil>.

ON THE COVER

Front cover (left to right):

A huge flux rope coronal mass ejection (CME) imaged on November 27, 2013 by the LASCO C3 telescope.

Researchers use the Mobile, Dexterous, Social (MDS) robot Lucas in studies of embodied cognition, voice and gesture recognition, and dynamic autonomy.

Vanguard Program — the Rocket

Electromagnetic railgun

Deployment of a remotely operated vehicle (ROV) to recover a bottom mounted mooring off the coast of Kayak Island, Alaska.

Drs. Jerome and Isabella Karle

Back cover (top left, clockwise):

USNS *Lorenzen*

Aqueous film-forming foam

TacSat-4

Ex-USS *Shadwell*

A rare display of cloud-to-ground lightning over Monterey Bay, California that lasted for over three hours.

GRAB – America’s first operational intelligence satellite

A 246 million pixel display wall enables users to focus on one region of data while maintaining the global context and offers a facility for collaborative data exploration.

Far-Ultraviolet Camera/Spectrograph

Bio-inspired deformable fin unmanned underwater vehicle (UUV)

Unmanned air vehicle flying in the prototyping high bay inside the Laboratory for Autonomous Systems Research.

WINDSAT polarimetric radiometer

Early airborne radar

HICO images taken over Lake Erie, PA, Great Barrier Reef, Australia, and Bubaque, Guinea Bissau

Clementine satellite

Ion Tiger unmanned air vehicle

First operational radar aboard the battleship USS *New York*

Dispersion plumes displayed using the CT-Analyst program.

Field testing an oceanographic mooring powered by a benthic microbial fuel cell.

Photograph of aircraft carrier USS *Hancock*, with crew in positions spelling out “Moon Relay,” was first to be transmitted by radio facsimile via Moon bounce (radio energy reflected from the Moon).

In Memory of

Jerome Karle, Nobel Prize Laureate and Navy Scientist



Dr. Jerome Karle, former Naval Research Laboratory scientist and Nobel Prize laureate, died on June 6, 2013, at the age of 94. Dr. Karle shared the 1985 Nobel Prize in Chemistry for developing a theoretical technique in X-ray crystallography, known as the “Direct Method” that is used by scientists the world over to determine the structures and shapes of complex molecules. His discovery paved the way for important advances in medicine and many other scientific fields.

Dr. Karle shared both his work and his life with his wife Dr. Isabella Karle, who worked alongside him at the Naval Research Laboratory. At NRL, Dr. Karle held the Chair of Science as Chief Scientist of the Laboratory for the Structure of Matter. Dr. Karle came to NRL in 1944; his wife joined him in 1946. At their retirement in 2009, they held a combined 127 years of Federal service.

Jerome Karle, along with Herbert Hauptman, was awarded the Nobel Prize for Chemistry in 1985 for devising direct methods of determining complex crystal structures by using X-ray diffraction analysis. At the time Karle and Hauptman tackled the challenge of discerning the structure of three-dimensional molecules, it was a problem that scientists had struggled with for years—a process that could take scientists months or years to complete. With the technique they developed, Jerome Karle and Herbert Hauptman solved the problem so that the lengthy, tedious process could now be completed precisely and quickly.

